THEME C

Theme C

Computational Challenges in Consequence Estimation for Risk Assessment: Numerical Modelling, Uncertainty Quantification, and Communication of Results

Part 1 – Hydraulic Modelling and Simulation

Sponsoring Organizations:

U.S. Army Corps of Engineers (USA)
U.S. Department of Homeland Security (USA)

Formulators:

Yazmin Seda-Sanabria (Formulation Team Co-Chair)

National Program Manager, Critical Infrastructure Protection & Resilience Program, U.S. Army Corps of Engineers, Headquarters, 441 G Street NW (ATTN: CECW-HS), Washington, DC 20314 (USA), Email: yazmin.seda-sanabria@usace.army.mil

Enrique E. Matheu (Formulation Team Co-Chair)

Chief, Critical Lifelines Branch, Sector Outreach and Programs Division, Office of Infrastructure Protection, U.S. Department of Homeland Security, 245 Murray Lane Arlington, VA 20598-0608 (USA), Email: enrique.matheu@hq.dhs.gov

Timothy N. McPherson (Formulation Team Technical Lead)

R&D Group Leader, Energy and Infrastructure Analysis, Los Alamos National Laboratory, Los Alamos, New Mexico 87544 (USA), Email: tmac@lanl.gov

Mustafa Altinakar

Director and Research Professor, National Center for Computational Hydroscience and Engineering, The University of Mississippi, Brevard Hall Room 327, P.O. Box 1848, University, MS 38677-1848 (USA), Email: altinakar@ncche.olemiss.edu

Mark Jourdan

Research Hydraulic Engineer, Coastal and Hydraulics Laboratory, U.S. Army Engineer Research and Development, 3909 Halls Ferry Road, Vicksburg, Mississippi 39180 (USA), Email: mark.r.jourdan@usace.army.mil

Michael K. Sharp

Technical Director, Geotechnical and Structures Laboratory, U.S. Army Engineer Research and Development, 3909 Halls Ferry Road, Vicksburg, Mississippi 39180 (USA), Email: michael.k.sharp@usace.army.mil

For technical information, please contact Dr. Tim McPherson at tmac@lanl.gov

Introduction

In the last decade, computational capacity has grown dramatically such that multiprocessor computing techniques are now widely available. This increase in resource availability has allowed the development of a vast array of new models for flooding and consequence assessment. Many of these models are computing flood wave propagation at extremely high temporal and spatial resolutions. When these models are coupled to equally complex models of population mobility, infrastructure impact and economic consequence, simulation frameworks are created that can support a paradigm shift from standard approaches to dam risk analysis.

Although computational advances have increased the availability and applicability of novel tools, there is a deficiency in benchmarks on the use of those tools in risk assessments. An obvious application of increased availability and efficiency of computational resources is to conduct probabilistic risk assessments using Monte Carlo techniques, but the application of such approaches entails a wide range of assumptions and technical decisions regarding the management of uncertainty such as variable uncertainty, parameter uncertainty, uncertainty in probabilistic sub-model, measurement error, computational errors, and numerical approximation to name a few.

Universities, engineering companies and regulatory bodies are invited to contribute to the benchmark and take part in the discussion of results gained.

This document is part 1 in a 2-part series for Theme C. Part 1 pertains to the hydraulic modelling and simulation of the dam breach and subsequent flood wave and provides details regarding the available data, dam geometry and failure, and expected modelling and simulation solution requirements. Part 2 primarily focuses on consequence estimation using the modelling and simulation results from Part 1.

Benchmark Focus

The numerical problem proposed for the workshop consists of estimating the consequences of failure of a dam near populated areas with complex demographics, infrastructure and economic activity. The dam in question will be near the city of Hydropolis, a virtual testbed for flood risk analysis to be built in preparation for the benchmark study.

Theme C participants are free to select the type and sophistication of the simulation engines used to solve the problem, including 1-d, 2-d and 3-d flood simulation tools, Population at Risk (PAR) and Loss of Life (LOL) estimation techniques, and infrastructure and consequence assessment models.

Flood Modelling and Simulation

The following sections are intended to provide information regarding the data provided for the dam failure modelling and simulation benchmark. Specifically this information includes the topographic data and dam geometric and construction information. It is not
the intent of this benchmark to set requirements as to which modelling and simulation environment should be used. Therefore, the descriptions and data provided are intended to be useful to a wide range of modelling and simulation environments at many levels of fidelity.

Dam Information

A hypothetical embankment dam was constructed in a mountainous region. The high- hazard dam sits directly above a lightly populated area and 3.5 kilometres away from an urban environment. The front and rear views of this dam are shown in Figure 2-1 and 2-2, respectively.

The primary function of the dam is flood control for heavy snowmelt and strong monsoonal weather patterns. In addition, the reservoir provides some water supply and recreational activities to nearby communities. The following sections provide more detail regarding the geometry and the construction of the hypothetical dam.
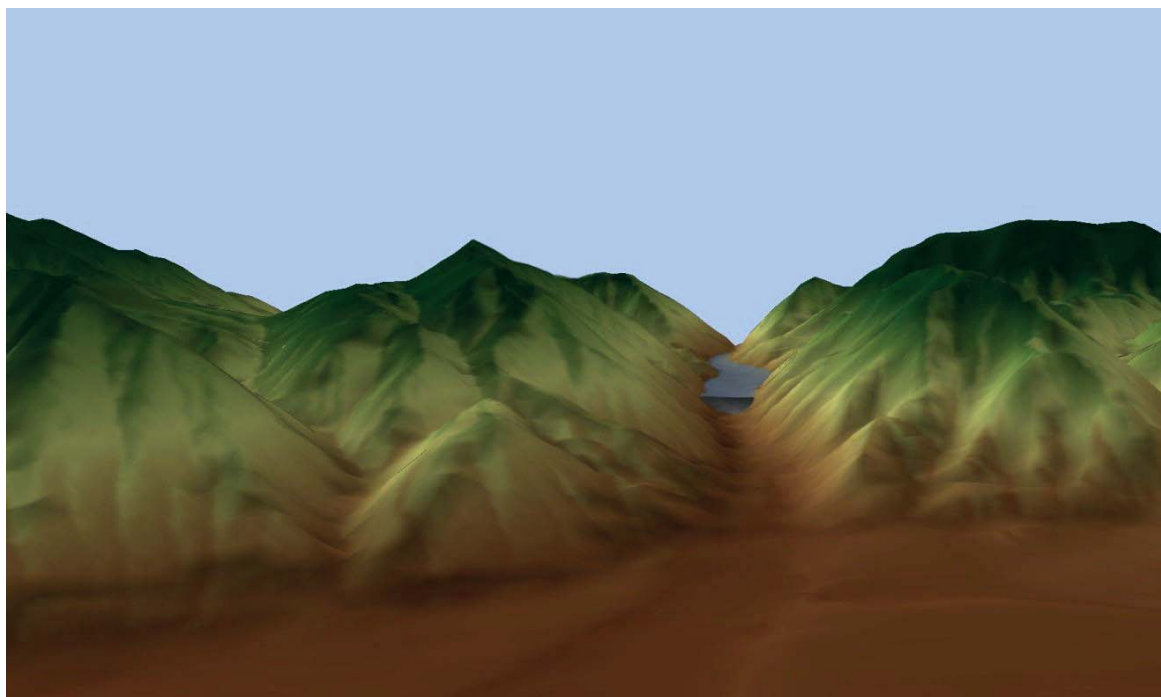
Figure 1: Front view of dam and surrounding topography
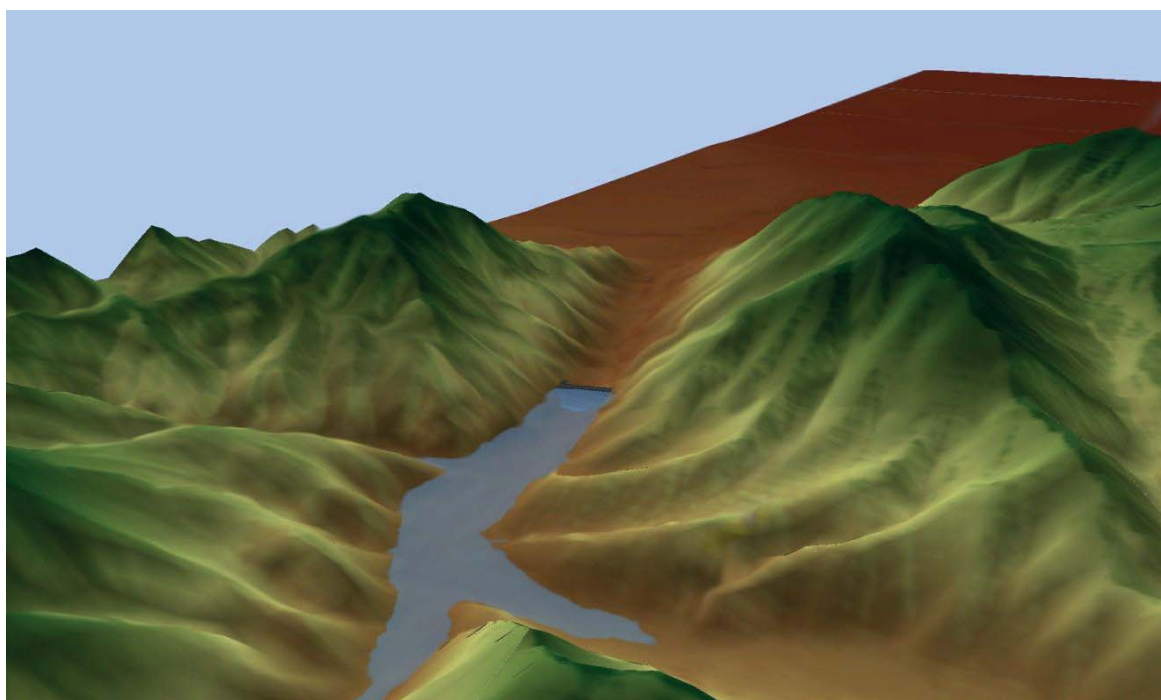
Figure 2: Rear view of dam, reservoir, and surrounding topography

Dam Geometry

The hypothetical embankment dam is considered high head (61 m) with moderate storage (38 million cubic meters). An overview of the dam geometry is provided in Table 5 and a cross-sectional profile is shown in Figure 3.

Table 5: Dam geometric parameters

Parameter Description	Value
Dam Location (x, y)	4499.66, 6681.57
Crest Length (m)	360
Crest Width (m)	24
Crest Elevation (m)	272
River Bed Elevation (m)	211
Upstream Embankment Slope (?H:1V)	3
Downstream Embankment Slope (?H:1V)	3
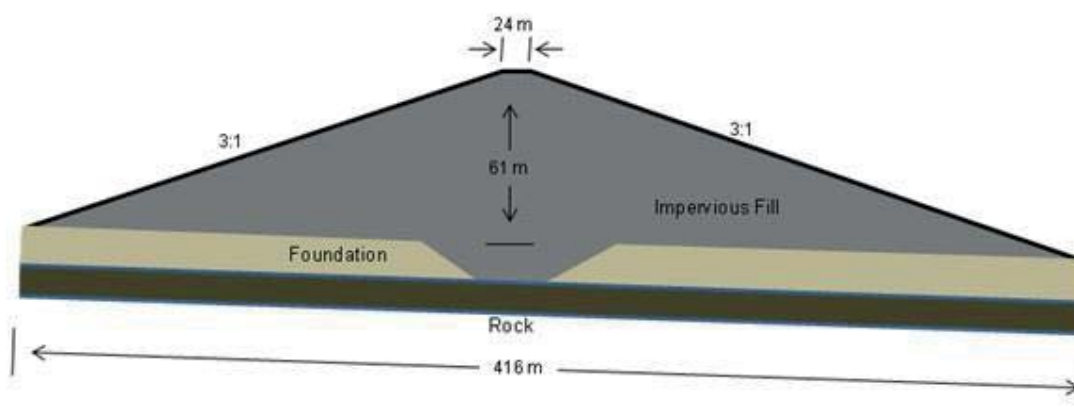
Figure 3: Cross-sectional view of the hypothetical dam

The storage capacity at crest elevation is more than 38 million cubic meters. The stage-volume curve for the reservoir is shown in Table 6.

Table 6: Reservoir stage-volume curve

Elevation (m)	Surface Area (m²)	Volume (m³)	Elevation (m)	Surface Area (m²)	Volume (m³)
211	0	0	243	605,559	6,214,463
213	898	266	245	682,169	7,500,447
215	7,812	7,432	247	762,461	8,944,612
217	25,502	39,871	249	848,052	10,553,044
219	43,821	109,250	251	916,938	12,322,332
221	62,409	216,078	253	978,640	14,218,482
223	85,038	364,294	255	1,035,581	16,233,223

225	117,544	565,695	257	1,094,197	18,365,080
227	153,732	836,860	259	1,155,316	20,614,116
229	190,728	1,181,477	261	1,216,975	22,987,820
231	222,068	1,594,314	263	1,278,543	25,483,100
233	252,239	2,067,481	265	1,338,586	28,100,382
235	294,797	2,613,155	267	1,398,359	30,837,356
237	351,808	3,254,198	269	1,467,826	33,701,532
239	461,611	4,084,756	271	1,543,126	36,712,416
241	531,463	5,077,507	272	1,584,052	38,276,344

Dam Construction Information

Homogenous Dam

The dam is a rolled earth fill structure composed of predominantly sandy clays and clayey sands. Compaction was achieved using 4 passes of a 50-ton pneumatic-tired roller on 0.3-meter loose lifts.

Strength properties for the dam were developed from results from undrained triaxial strength tests. The drained strength parameters were based on 5% axial strain and were selected to represent initial confining stresses up to 478 kPa. The undrained strengths were interpreted from an approximate evaluation of S_u/σ'_{mc} ratios estimated from the reported undrained tests. The undrained strength S_u was taken as one-half the maximum deviator stress for axial strains up to 10%. The estimated strengths are summarized in Table 7.

Table 7: Selected parameters for dam

Parameter Description		Value
Strength Parameters:		
c′	Effective (drained) cohesion in kPa	19.15 kPa
ϕ′	Effective (drained) friction angle	14°
S_u	Undrained strength in kPa	43.09+ 0.175·σ'_{mc}
Stiffness Parameters:		
V_{s1}	Shear wave velocity at $\sigma'_v = 1$ atm	152.4 m/s
$G_{max,1}$	Maximum shear modulus at $\sigma'_v = 1$ atm	46443 kPa
Others:		
γ_{sat}	Saturated unit weight	2002 kg/m³
k	Permeability	$1.9 \cdot 10^{-6}$ cm/s

Foundation

Foundation stiffness parameters were based on shear wave velocity values without reduction for strain level or changes in effective stress. A simplified stiffness distribution was used to reflect the gradual increase in stiffness with depth. The selected properties are summarized in Table 8.

Table 8: Selected parameters for foundation

Parameter Description		Value	
		Base of dam to depth of 3.6 m	Foundation below 3.6 m
Stiffness Parameters:			
V_s	Shear wave velocity	167 m/s	185 m/s
G	Shear modulus	$6.75 \cdot 10^5$ kPa	$8.33 \cdot 10^6$ kPa
ν	Poisson's ratio	0.25	0.25
Others:			
γ	Unit weight	2,242kg/m³	2,402 kg/m³
K	Permeability	$9.5 \cdot 10^{-7}$ cm/s	$9.5 \cdot 10^{-7}$ cm/s

Dam Failure Guidance

The dam failure for this benchmark takes place when the pool elevation is at crest elevation. The mode of failure will be assumed as an overtopping failure. While it is open for participants to conduct detailed (physically-based) modelling of the breaching process as part of the benchmark, several breach parameter estimation approaches available in the literature are summarized in the appendix of this document.

Data Provided

In addition to the information provided in this document, gridded data representing the topography and the land use classification are provided. All gridded datasets conform to the same domain and cellsize. The resolution of data provided is considered a base dataset and may be altered if required by the modelling and simulation environment used by the participant.

Digital Elevation Data

Two digital elevation models (DEM) are provided to benchmark participants:
- DEM representing pre-dam construction.
- DEM representing post-dam construction.

Participants in the benchmark may decide which DEM is more appropriate for use based on individual requirements for modelling and simulation.

Land Use/Cover

Benchmark participants are provided a gridded dataset representing the hypothetical land use/cover for the simulation region. These data follow the classification guidance and values provided in the National Land Cover Dataset (NLCD). For completeness, a description of land use classifications is provided in Table 9.

Table 9: Land use/cover classifications and descriptions

NLCD Class	Description
11	Open Water
12	Perennial Ice/Snow
21	Developed-Open Space
22	Developed- Low Intensity
23	Developed- Med. Intensity
24	Developed- High Intensity
31	Barren Land
41	Deciduous Forest
42	Evergreen Forest
43	Mixed Forest
52	Shrub/Scrub
71	Grassland/Herbaceous
81	Pasture/Hay
82	Cultivated Cropland

Correlation of these classifications to surface roughness for modelling and simulation should be reported by the participant.

Flood Modelling and Simulation Reporting Requirements
For consistency between benchmark participants, each participant is requested to generate information described in Table 10 from the results of the flood simulation. These data focus on the hydraulics of the simulation.

Table 10: Reporting requirements for flood modelling and simulation

Required Data	Data Description
Breach Discharge	This hydrograph should show the discharge rate from pre-failure to empty reservoir, in units of m3/
Cross-Section Discharge	These shall consist of a complete hydrograph for unsteady simulation environments and peak discharges for steady-state simulation environments
Peak Flood Depths	Gridded dataset representing the peak flood depth, units of meters
Flood Wave Arrival Time	Gridded dataset with flood wave arrival time in 5-minute intervals
Peak Unit Flow Rate	Gridded dataset with a value representing the peak unit flow rate in units of m²/s
Flooded Area	Summation of the total flooded area, units of m². In addition, participants will provide flooded area categorized by range of flood depths at .5 meter intervals

The locations in which participants should provide hydrographs are shown in Table 11

Table 11: Cross-section locations

Cross Section ID	X Location (m)	Y Location (m)
1	4737.18	6755.39
2	5971.79	7053.10
3	7486.60	7582.85
4	9100.84	7773.91
5	10716.96	7397.67

Solution Metadata

As described above, Participants are expected to provide gridded data for some of the reporting requirements. These gridded data files must conform to the metadata of the original data provided in the benchmark. These are summarized in Table 12.

Table 12: Gridded data metadata requirements

Metadata Parameter	Value
Left Extent	0
Bottom Extent	0
Right Extent	25831.81905
Top Extent	9930.941439
Cellsize	9.4760892
Columns	2726
Rows	1048

Acronyms and Abbreviations

DEM   Digital Elevation Model
NLCD   National Land Cover Dataset
kPa   Kilopascal

Theme C
Computational Challenges in Consequence
Estimation for Risk Assessment: Numerical Modelling, Uncertainty
Quantification, and Communication of Results

Part 2 – Consequence Estimation

Sponsoring Organizations:

U.S. Army Corps of Engineers (USA)
U.S. Department of Homeland Security (USA)

Formulators:

Yazmin Seda-Sanabria (Formulation Team Co-Chair)

National Program Manager, Critical Infrastructure Protection & Resilience Program, U.S. Army Corps of Engineers, Headquarters, 441 G Street NW (ATTN: CECW-HS), Washington, DC 20314 (USA), Email: yazmin.seda-sanabria@usace.army.mil

Enrique E. Matheu (Formulation Team Co-Chair)

Chief, Critical Lifelines Branch, Sector Outreach and Programs Division, Office of Infrastructure Protection, U.S. Department of Homeland Security, 245 Murray Lane Arlington, VA 20598-0608 (USA), Email: enrique.matheu@hq.dhs.gov

Timothy N. McPherson (Formulation Team Technical Lead)

R&D Group Leader, Energy and Infrastructure Analysis, Los Alamos National Laboratory, Los Alamos, New Mexico 87544 (USA), Email: tmac@lanl.gov

Mustafa Altinakar

Director and Research Professor, National Center for Computational Hydroscience and Engineering, The University of Mississippi, Brevard Hall Room 327, P.O. Box 1848, University, MS 38677-1848 (USA), Email: altinakar@ncche.olemiss.edu

Mark Jourdan

Research Hydraulic Engineer, Coastal and Hydraulics Laboratory, U.S. Army Engineer Research and Development, 3909 Halls Ferry Road, Vicksburg, Mississippi 39180 (USA), Email: mark.r.jourdan@usace.army.mil

Michael K. Sharp

Technical Director, Geotechnical and Structures Laboratory, U.S. Army Engineer Research and Development, 3909 Halls Ferry Road, Vicksburg, Mississippi 39180 (USA), Email: michael.k.sharp@usace.army.mil

For technical information, please contact Dr. Tim McPherson at tmac@lanl.gov

Introduction

In the last decade, computational capacity has grown dramatically such that multiprocessor computing techniques are now widely available. This increase in resource availability has allowed the development of a vast array of new models for flooding and consequence assessment. Many of these models are computing flood wave propagation at extremely high temporal and spatial resolutions. When these models are coupled to equally complex models of population mobility, infrastructure impact and economic consequence, simulation frameworks are created that can support a paradigm shift from standard approaches to dam risk analysis.

Although computational advances have increased the availability and applicability of novel tools, there is a deficiency in benchmarks on the use of those tools in risk assessments. An obvious application of increased availability and efficiency of computational resources is to conduct probabilistic risk assessments using Monte Carlo techniques, but the application of such approaches entails a wide range of assumptions and technical decisions regarding the management of uncertainty such as variable uncertainty, parameter uncertainty, uncertainty in probabilistic sub-model, measurement error, computational errors, and numerical approximation to name a few.

Universities, engineering companies and regulatory bodies are invited to contribute to the benchmark and take part in the discussion of results gained.

This document is part 2 in a 2-part series for Theme C. Part 1 pertains to the hydraulic modelling and simulation of the dam breach and subsequent flood wave and provides details regarding the available data, dam geometry and failure, and expected modelling and simulation solution requirements. Part 2 focuses on the consequences of the flood using the modelling and simulation results from Part 1.

Benchmark Focus

The numerical problem proposed for the workshop consists of estimating the consequences of failure of a dam near populated areas with complex demographics, infrastructure and economic activity. The dam in question will be near the city of Hydropolis, a virtual testbed for flood risk analysis to be built in preparation for the benchmark study.

Theme C participants are free to select the type and sophistication of the simulation engines used to solve the problem, including 1-d, 2-d and 3-d flood simulation tools, Population at Risk (PAR) and Loss of Life (LOL) estimation techniques, and infrastructure and consequence assessment models.

Consequence Estimation

A full consequence assessment for dam failure generally includes four main categories- public health and safety, economic impact, psychological impact, and governance/mission impact. At a minimum, the consequence assessment should focus on
impacts related to human consequences and direct economic impact. This document outlines the requirements for consequence assessment within Theme C of the benchmark, addressing human consequences (e.g., population at risk and loss of life) and direct economic impact. The intent is not to limit the approaches or techniques used by participants but to guide the assessment into categories for comparison. Additional consequence assessments are also encouraged, but will not be used in the assessment of uncertainty.

Dam Failure Assumptions

Over a series of fall rainfall events, the reservoir slowly approaches crest elevation. Due to the frequency of fall rainfall events, there are few people recreating at or near the facility. At 11:00 pm on Saturday evening, the dam fails, releasing a torrent of water through the canyon and towards Hydropolis. The failure was sudden and unexpected, and for those in the canyon witnessing the failure, there are no mobile phone services. The reservoir and dam does not have a completed emergency action plan, thus the potential impact related to failure is unknown to residents in Hydropolis.

Data Provided

Participants are requested to evaluate the downstream consequences as it relates to population at risk, loss of life and direct economic impact. Participants in Benchmark Theme C are provided additional data to assist in consequence assessment. This data includes Hydropolis census information in shapefile format and parcel data in shapefile format.

Census Data

Participants are provided with a shapefile representative of census data for the city of Hydropolis. This data includes information regarding the population and the economic activity. Table 5 and Table 2 provide attribution information for these data.

Table 1: Population data field names and descriptions

Field Names	Description
Total	Total Male and Female
Male	Total Male
Munder5	Male: Under 5 years
M5to9	Male: 5 to 9 years
M10to14	Male: 10 to 14 years
M15to17	Male: 15 to 17 years
M18to19	Male: 18 and 19 years
M20	Male: 20 years
M21	Male: 21 years
M22to24	Male: 22 to 24 years
M25to29	Male: 25 to 29 years
M30to34	Male: 30 to 34 years
M35to39	Male: 35 to 39 years
M40to44	Male: 40 to 44 years
M45to49	Male: 45 to 49 years
M50to54	Male: 50 to 54 years
M55to59	Male: 55 to 59 years
M60to61	Male: 60 and 61 years
M62to64	Male: 62 to 64 years
M65to66	Male: 65 and 66 years
M67to69	Male: 67 to 69 years
M70to74	Male: 70 to 74 years
M75to79	Male: 75 to 79 years
M80to84	Male: 80 to 84 years
M85over	Male: 85 years and over

Female	Total Female
Funder5	Female: Under 5 years
F5to9	Female: 5 to 9 years
F10to14	Female: 10 to 14 years
F15to17	Female: 15 to 17 years
F18to19	Female: 18 and 19 years
F20	Female: 20 years
F21	Female: 21 years
F22to24	Female: 22 to 24 years
F25to29	Female: 25 to 29 years
F30to34	Female: 30 to 34 years
F35to39	Female: 35 to 39 years
F40to44	Female: 40 to 44 years
F45to49	Female: 45 to 49 years
F50to54	Female: 50 to 54 years
F55to59	Female: 55 to 59 years
F60to61	Female: 60 and 61 years
F62to64	Female: 62 to 64 years
F65to66	Female: 65 and 66 years
F67to69	Female: 67 to 69 years
F70to74	Female: 70 to 74 years
F75to79	Female: 75 to 79 years
F80to84	Female: 80 to 84 years
F85over	Female: 85 years and over

Table 2: Economic table field names and descriptions

Field Names	Description
jobs11	Agriculture, Forestry, Fishing and Hunting
jobs21	Mining, Quarrying, and Oil and Gas Extraction
jobs22	Utilities
jobs23	Construction
jobs3133	Manufacturing
jobs42	Wholesale Trade
jobs4445	Retail Trade
jobs4849	Transportation and Warehousing
jobs51	Information
jobs52	Finance and Insurance
jobs53	Real Estate and Rental and Leasing
jobs54	Professional, Scientific, and Technical Services
jobs55	Management of Companies and Enterprises
jobs56	Administrative and Support and Waste Management and Remediation Services
jobs61	Educational Services
jobs62	Health Care and Social Assistance
jobs71	Arts, Entertainment, and Recreation

jobs72	Accommodation and Food Services
jobs81	Other Services (except Public Administration)
jobs92	Public Administration

Parcel Data

Benchmark participants are provided parcel data in shapefile format. This includes information regarding the zoning (e.g., residential, commercial, etc.) and the structure (e.g., stories, basement, quality). Table 3 provides a description of the zone classification provided in this data.

Table 3: Parcel descriptions for zone classifications

Code	Description
A-1	Rural Agricultural—1-Acre Minimum Zone
A-2	Rural Agricultural—2-Acre Minimum Zone
AP	Airport Protection Overlay Zone
C-1	Neighborhood Commercial Zone
C-2	Community Commercial Zone
C-3	Heavy Commercial Zone
IP	Industrial Park Zone
M-1	Light Manufacturing Zone
O-1	Office & Institutional Zone
P	Parking Zone
P-R	Reserve Parking Zone
R-1	Residential Zone: Houses
R-1	Single Family Residential Zone
R-2	Residential Zone: Houses, Townhomes & Medium Density Apartments
R-3	Residential Zone: Houses, Townhomes & High Density Apartments
RA-1	Residential and Agricultural Zone, Semi-Urban Area
RA-2	Residential and Agricultural Zone
R-D	Residential and Related Uses Zone, Developing Area
R-LT	Residential Zone: Houses & Limited Townhomes
RO-1	Rural and Open Zone
RO-20	Rural and Open Agricultural Zone
R-T	Residential Zone: Houses & Townhomes
SD-LC-1	Limited Neighborhood Commercial Zone
SD-RO	Residential/Office Zone
SU-1	Special Use Zone
SU-2	Special Neighborhood Zone, Redeveloping Area
SU-3	Special Center Zone
UCO	Urban Conservation Overlay Zone
WO	Wall Overlay Zone

Consequence Assessment Reporting Requirements

All participants should summarize methods, techniques, assumptions, and key results in a paper not to exceed 15 pages. In addition, each participant is requested to generate the information described in Table 4 using results of the consequence assessment. These data focus on the consequences of failure.

Table 4: Reporting requirements for consequence assessment

Required Data	Data Description
Population at Risk	Participants should use the provided consequence results spreadsheet to populate the requested information. This information includes age demographic break-downs by time to flooding and depth of flooding. A gridded dataset indicating the spatial variability of population at risk (regardless of age) is also requested.
Loss of Life	Participants should use the provided consequence results spreadsheet to populate the requested information. The loss of life estimation includes break-downs by time from breach failure. A gridded dataset indicating the spatial variability of loss of life is requested.
Flood Severity Grid	Gridded dataset representing the peak flood severity, classified as low, medium and high (e.g., 1, 2, 3) severity. Participants are expected to describe the assumptions used in categorizing flood severity in the submitted paper.
Direct Economic Impact	Participants should use the provided consequence results spreadsheet to populate the requested information. This information includes break-downs by time from dam failure. A gridded dataset indicating the spatial variability of direct economic impact is also requested.

Consequence Metadata

As described above, participants are expected to provide gridded data for some of the reporting requirements. These gridded data files must conform to the metadata of the original data provided in the benchmark. These are summarized in Table 5.

Table 5: Gridded data metadata requirements

Metadata Parameter	Value
Left Extent	0
Bottom Extent	0
Right Extent	25831.81905
Top Extent	9930.941439
Cellsize	9.4760892
Columns	2726
Rows	1048

RESULT COMPARISON OF THE PARTICIPANTS

THEME C

Results Comparison

Theme C
Computational Challenges in Consequence Estimation for Risk Assessment

Introduction

Theme C of the 12th International Benchmark Workshop on the Numerical Analysis of Large Dams involved 8 participants who submitted at least partial solutions of the Hydropolis Dam Break Case Study. This synthesis is not a complete representation of each solution. In many cases, participants conducted their own sensitivity/uncertainty analyses. For brevity, this synthesis document considered only one set of solutions from each participant. Full description of solutions can be found in the papers authored by each participant team.

This synthesis of results is based on statistical methods to facilitate comparison to the greatest extent possible. The Kappa statistic is used to quantify the similarities among the participants' study results. Kappa corresponds to a numerical rating of the degree of agreement between two raters, which in this case are the outputs (e.g., gridded data peak flood depths) of two participant models. Kappa is calculated in Equation 1.

$$kappa = \frac{P(a) - P(e)}{1 - P(e)} \qquad (1)$$

where *P(a)* is the relative observed agreement between the two models and *P(e)* is the probability that the agreement is due to chance. Kappa ranges from -1 to 1. If the two models are in perfect agreement then Kappa equals 1, whereas if there is no agreement among the models except what would be expected by chance. A Kappa value less than 0 indicates more disagreement than what one can expect by chance. A commonly cited scale for interpreting Kappa values is given by Landis and Koch[1] and reported in the following Table 1. The Kappa statistic quantifies the aggregate agreement between two different spatial grids, but does not provide any spatial information about where the two models differ more or less.

Table 1: Kappa value interpretation as proposed by Landis

Kappa	Agreement Interpretation	Agreement Index (used in Results Tables)
< 0	Less than chance agreement	**Chance**
0.01-0.20	Slight agreement	**Slight**
0.21-0.40	Fair agreement	**Fair**
0.41-0.60	Moderate agreement	**Moderate**
0.61-0.80	Substantial agreement	**Substantial**
0.81-0.99	Almost perfect agreement	**Almost perfect**

---

[1] Landis J.R., and Koch G.G., *The measurement of observer agreement for categorical data.* 1977 Biometrics 33, 159-174

Overview of Participation

The benchmark case includes a diverse set of analyses and several participants only submitted results against a subset of the complete problem. Table 2 lists each of the lead authors, an ID assigned to the participant team for solution comparison, and an indication of submission completion for topics of comparison.

Table 2: Summary of Participant Submissions

Authors	ID	Hydraulic Solution	Population at Risk Solution	Loss of Life Solution	Economic Solution
Davison et al.	HRW	Yes	Yes	Yes	Yes
Bent et al.	LANL	Yes	Yes	Yes	Yes
Mancusi et al.	MANC	Yes	Yes	Yes	Yes
Williams & Buchanan	MMC	Yes	Yes	Yes	Yes
Thames & Kalyanapu	TK	Yes	Yes	Yes	Yes
Altinakar et al.	MUST	Yes	Yes	Yes	No
Saberi et al.	SAB	Yes	No	No	No
McVan et al.	MCV	Yes	Yes	No	No

Discussion

Breach formulation

Participants used a range of models, including physics-based breach models using dam material information and regression equations based on previous dam failures. Figure 1 shows the breach hydrographs produced by each team. It is clear that choice of model, method, and parameters can significantly affect the timing and the magnitude of the peak discharge. In general, models using regression equations had a much earlier peak than physics-based models. The SAB and HRW hydrographs were shifted in time to better illustrate the data for comparison. The peak discharge ranges in time from under 0.5 hours to more than 18 hours and the magnitude of peak discharge ranges from near 10,000 cubic meters per second (cms) to more than 40,000 cms. SAB, MMC, LANL, MANK, and TK all have peak discharges above 20,000 cms, while MCV, MUST, and HRW have peaks below 20,000 cms.
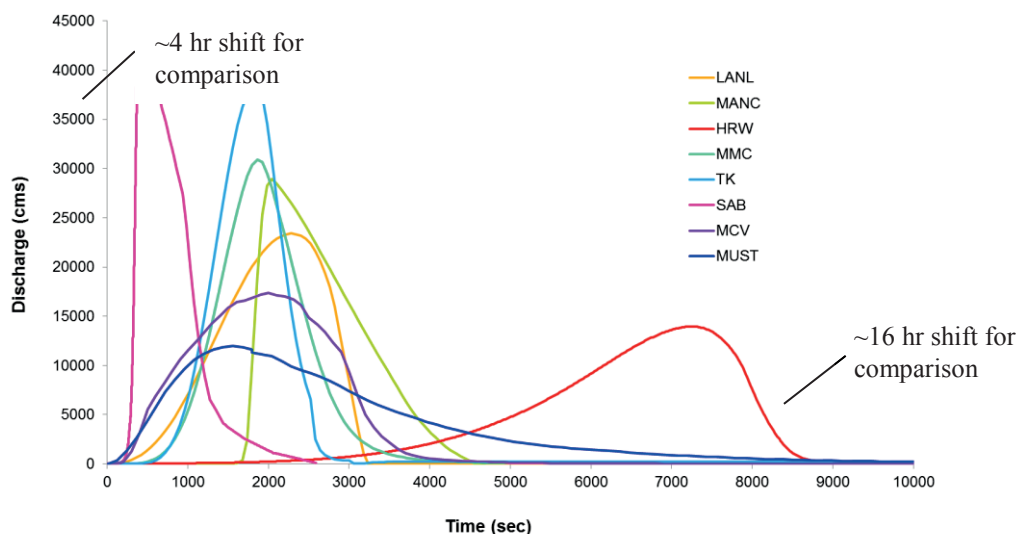
Figure 1: discharge hydrographs

Hydrodynamics

Each participant used different models, which solve the same equations using different numerical schemes. The most notable difference between models appeared to be the difference in mesh or grid type used. Models using structured grids tended to have more similar results relative to peak depths than models using irregular meshes. This may be a result of interpolation between the two types of meshes for comparison. A wide variety of techniques were used by the participant teams to produce the necessary flood output data for consequence analyses. Each participant submission details the methods used. These differences can be a strong explanatory variable in the comparison of consequence results. For example, dam failure hydrodynamic simulation results are dependent on the input datasets (e.g., breach discharge, topography, roughness) and modeling\method approach. Participants used different approaches to estimate roughness coefficients. Each participant was required to interpret the roughness coefficient associated with an NLCD land use type. Because there isn't a single accepted dataset, there were a range of coefficients used by participants.

Cross Sections

The participants were provided a single point location for each section, and the participants estimated the line upon which flow should be summed. Figure 2 shows the hydrographs submitted by each of the participants for all cross sections. SAB and HRW have the same time shifts as previously noted.
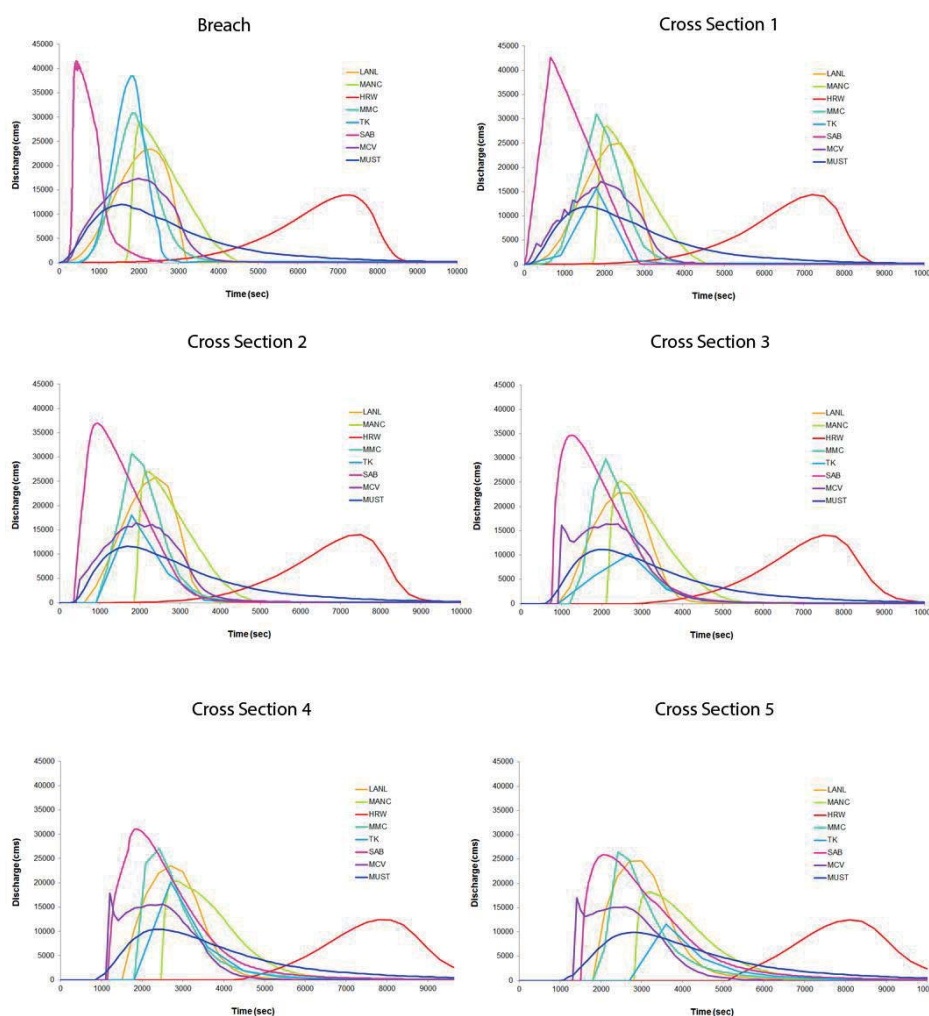
Figure 2: Hydrographs for all cross sections submitted by benchmark participants

Peak Flood Depths

The peak flood depth was defined by all participants as the peak depth at every cell regardless of the time at which it occurred. The maximum flooded area and flooded area categorized in half-meter increments of peak depths are summarized in Figure 3 and Figure 4. The total flooded area ranges from near 47 km² to just under 30 km².

The Kappa statistic was applied to the gridded peak flow depths. A Kappa value was calculated for each unique combination of two models. The results of the peak flood depth Kappa analysis are summarized in Table 3. There is generally strong agreement between the models. The chance and moderate differences between MCV and SAB and other models is likely due to interpolation of the irregular mesh output from those submissions to a new mesh for comparison with other models.

Figure 3: Summary of total flooded area
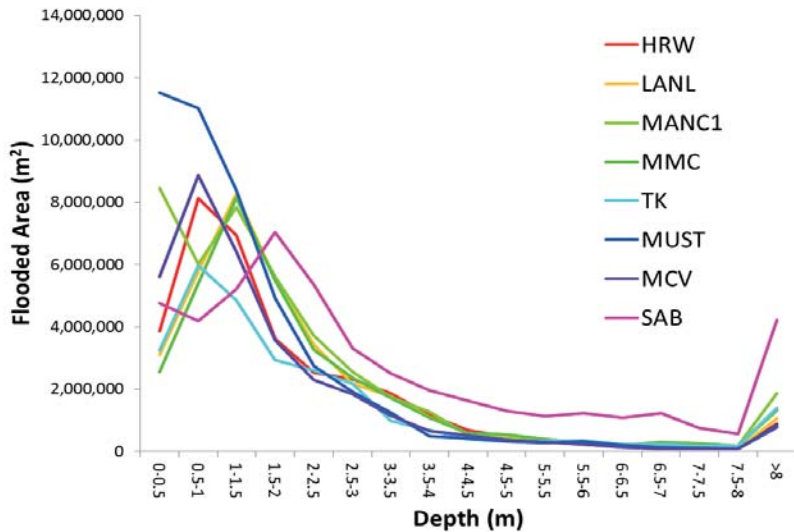
Figure 4: Flood area summarized by half-meter increments of peak depth

Table 3: Kappa statistic (model similarity) for peak flood depth

	HRW	LANL	MANC	MMC	TK	MUST	MCV	SAB
HRW		Substantial	Substantial	Substantial	Substantial	Substantial	Moderate	Chance
LANL	Substantial		Substantial	Substantial	Substantial	Substantial	Moderate	Chance
MANC	Substantial	Substantial		Substantial	Substantial	Substantial	Moderate	Chance
MMC	Substantial	Substantial	Substantial		Substantial	Substantial	Moderate	Chance
TK	Substantial	Substantial	Substantial	Substantial		Substantial	Moderate	Chance
MUST	Substantial	Substantial	Substantial	Substantial	Substantial		Moderate	Chance
MCV	Moderate	Moderate	Moderate	Moderate	Moderate	Moderate		Chance
SAB	Chance	Chance	Chance	Chance	Chance	Chance	Chance	

Flood Wave Arrival Time

There were differences among participants in defining thresholds for determining when the flood wave arrived. For example, LANL and MUST defined the flood wave arrival as the time at which a grid cell becomes wet without implying a threshold. MMC defined the flood wave arrival as the time in which the depth of water in a grid cell reaches 0.6 meters. Agreement between participants was assessed using the Kappa Statistic and are shown in Table 4. The results indicate that the level of agreement between any two models varies more for the flood wave arrival time than for the peak flood depths. It is noted again that HRW used a breach hydrograph with a much longer lag time to peak discharge than other participants.

Table 4: Kappa statistic (model agreement) for flood wave arrival time

	HRW	LANL	MANC	MMC	TK	MUST	MCV	SAB
HRW		Chance	Chance	Chance	Chance	Chance	Chance	Chance
LANL	Chance		Slight	Substantial	Slight	Fair	Substantial	Moderate
MANC	Chance	Slight		Slight	Chance	Fair	Slight	Fair
MMC	Chance	Substantial	Slight		Slight	Moderate	Substantial	Substantial
TK	Chance	Slight	Chance	Slight		Slight	Slight	Slight
MUST	Chance	Fair	Fair	Moderate	Slight		Fair	Substantial
MCV	Chance	Substantial	Slight	Substantial	Slight	Fair		Moderate
SAB	Chance	Moderate	Fair	Substantial	Slight	Substantial	Moderate	

Peak Unit Flow Rate

Table 5 shows the level of agreement between participants for Peak Unit Flow Rate as determined by the Kappa analysis. The results show less agreement between two models for the peak unit flow rate than for peak flood depth and flood wave arrival.

Table 5: Kappa statistic (model agreement) for peak unit flow rate

	HRW	LANL	MANC	MMC	TK	MUST	MCV	SAB
HRW		Fair	Moderate	Slight	Slight	Substantial	Fair	Fair
LANL	Fair		Fair	Substantial	Chance	Fair	Slight	Slight
MANC	Moderate	Fair		Fair	Slight	Moderate	Slight	Slight
MMC	Slight	Substantial	Fair		Chance	Fair	Slight	Slight
TK	Slight	Chance	Slight	Chance		Slight	Slight	Chance
MUST	Substantial	Fair	Moderate	Fair	Slight		Fair	Fair
MCV	Fair	Slight	Slight	Slight	Slight	Fair		Slight
SAB	Fair	Slight	Slight	Slight	Chance	Fair	Slight	

Consequences

Population

The spatial distribution of population within the flooded area varied among the participants. MCV, MANC, and MUST uniformly distributed the population available in the census blocks to properly sum the affected population within partially flooded census blocks. HRW, TK, and MMC redistributed the population to the parcel data provided. MMC additionally accounted for residential population and workforce population within the parcels. Finally, LANL used imperviousness defined by developed areas in the NLCD to distribute the population from each census block.

Population at Risk

Population results include total PAR and PAR by age (e.g., under 14 and over 65 years). These are summarized in Figure 5 and Figure 6.
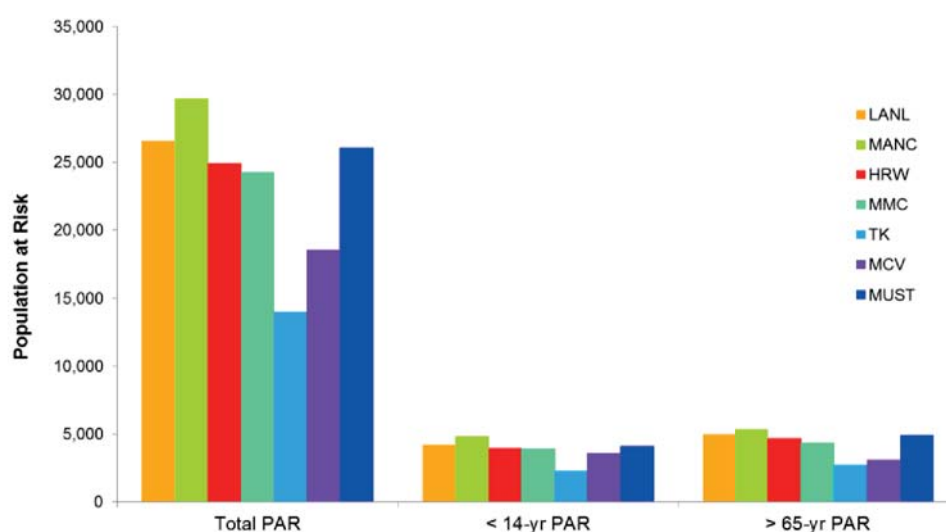
Figure 5: Summary of total, under 14-yr, and over 65-yr PAR

Despite the wide range of peak discharges and subsequent flooded areas, the total sum of PAR is fairly consistent among participants. In addition, the participants consistently indicate that the majority of the PAR is located in flood water less than 2 meters deep. While there is consistency in total population by depth, PAR is less consistent with respect to flood arrival time. This indicates that PAR is perhaps sensitive to breach formulation. For example, HRW had nearly a 16-hour lag time for peak discharge. Therefore, the PAR in their solution is not generally at risk until more than 3 hours. This information is likely to have an impact on loss of life models that take into account warning time and evacuation plans.
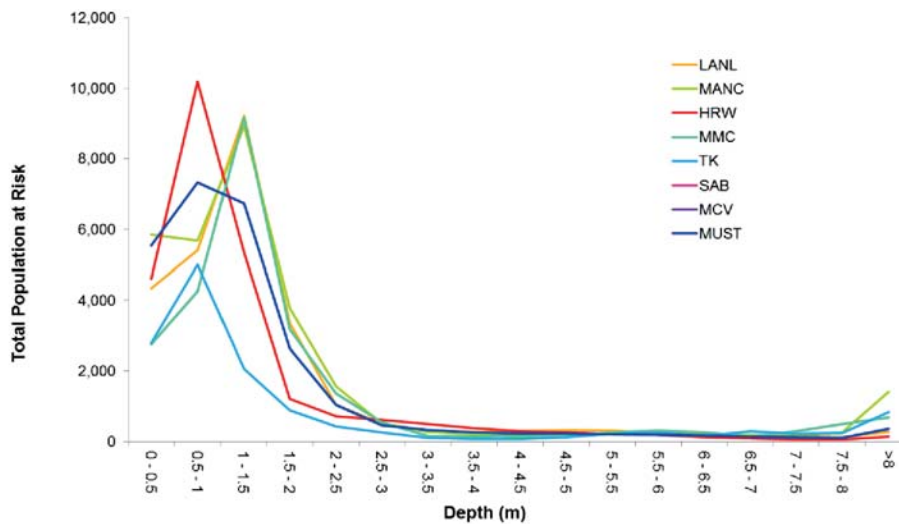
Figure 6: PAR by peak depth

Flood Severity

Figure 1-7 shows the standard deviation among the different flood severity calculations.
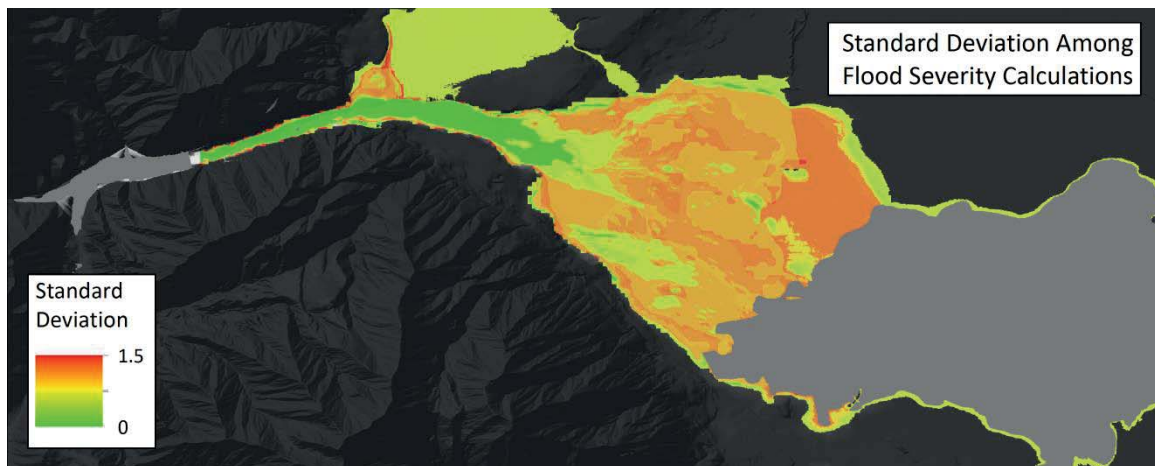
Figure 7: Flood severity standard deviation

There are significant differences on how the flood severity is defined across the participants. The methods used by TK and MMC were not described. HRW defined flood severity based on effects to population who are exposed (i.e., not within buildings) to the flood waters. LANL, MUST, and MANC used the U.S. Department of Homeland Security's Dam Sector

consequence estimation guidelines.[2] These classifications are based more on structural stability and population within buildings than people directly exposed to the flood. There is complete agreement between the models on the severity assigned within the canyon (standard deviation of 0). Differences in severity classification are noted within the floodplain area, which the area where population in this case study is located.

Loss of Life

The total loss of life is shown in Figure 8. Although the method in which the loss of life was estimated varied between participants, the majority of estimates for loss of life was approximately 2,000 people. HRW's loss of life estimate was the same order of magnitude as the other teams, but nearly twice as great. An explanatory factor in this difference could be the different technique used to calculate flood severity.
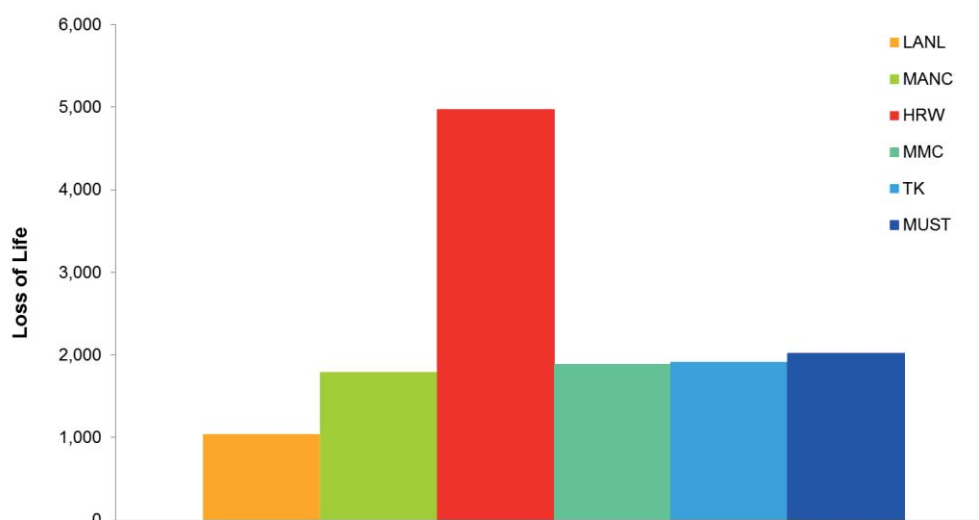
Figure 8: Total loss of life

Economics

There were differences in definition of direct economic impact. For example, LANL defined the direct economic impact as lost jobs, wages, and business outputs. LANL was the only participant to use business gross domestic product (GDP) per employee, but they did not include structural damage, which they defined as an insurable loss and not a direct economic impact. As such, LANL economic results are reported on a $/day basis, but did not estimate the duration of the impact. MAN, MMC, TK, and HRW all evaluated structural damages using the provided parcel information. The key challenge using the parcel data was assigning values to the occupancy classes. Because this information was not provided by the formulation team, each participant had to assume this information. The data used by participants ranged from available data in models, economic subject matter experts, and values reported in the literature. Figure 9 shows the total economic impact. Because of the difference in methods (e.g., GDP vs. insurable losses), and the assumption regarding asset value, the economic impact values range significantly. LANL reported $665,000/day, but the duration of the event is unknown. At the high end, MANC reported $2.6 Billion based on insurable losses.

---

[2] Department of Homeland Security, 2011. "Estimating loss of life for dam failure scenarios."

Figure 9: Summary economic impact submitted by the participants

Conclusion

In general, the results from each participant team are similar in terms of hydrodynamics. However, flood wave arrival times were different between teams. This is attributable to differences in the calculation of the breach hydrograph and differences in regression and physics-based formulations in addition to definition of thresholds used to quantify the arrival of the flood. The largest differences in peak flood depths were likely due to the requirement for the teams using irregular meshes to report output in a structured grid format.

PAR estimates were also similar across teams. Differences are primarily due to different methods used by participants to spatially distribute population. The methods included uniform distribution of the population within the census block, uniform distribution of the population among parcels within the census blocks, and uniform distribution of the population among develop land within the census block. The most significant differences in the population estimates appeared to be the time after failure at which population is at risk. This has significance relative to flood wave warning time and potential evacuations.

Finally, there were some significant differences in the economic impact. First, there were differences in interpretation of direct economic impact. This was either interpreted as business losses based on GDP or structural damage/insurable losses using parcel data. In addition, within the insurable loss estimation, there were significant differences in assessing the value of structures within parcels.

PAPERS

THEME C

A Benchmark study on dam breach and consequence estimation using EMBREA and Life Safety Model

M. Davison[1], M. Hassan[1], O. Gimeno[1], M. van Damme[1] and C. Goff[1]

[1] HR Wallingford, Howbery Park, Wallingford, Oxfordshire, OX10 8BA, United Kingdom

E-mail: m.davison@hrwallingford.com

Abstract

This paper presents the modelled consequences of a hypothetical dam breach as laid out in Theme C of the 12th international Benchmark Workshop on Numerical Analysis of Dams. The EMBREA model was used to model the failure of the dam due to headcut erosion and to derive a breach hydrograph which was then used in InfoWorks ICM to model the 2D flood spreading. The results of the flood model have been used to calculate how severe the flood would be in terms of the total population at risk, loss of life using the Life Safety Model and economic impact. The paper shows that the consequences of the hypothetical flood will be severe in terms of casualties and economic damage.

Introduction

This paper presents the modelling of a potential breach of a hypothetical dam and the estimation of the consequences in the populated areas and economic activities downstream, within Theme C of the 12th International Benchmark Workshop on Numerical Analysis of Dams [1]. The paper is structured in three sections. Section 1 describes the dam breach model, which provides indicative predictions of a number of breach scenarios; Section 2 focuses on the flood wave propagation and Section 3 presents the human consequences and direct economic impact of the dam failure.

Dam Breach Modelling

Choice of Breach Model

During the last 15 years, HR Wallingford has undertaken the development of a new breach model, called EMBREA (previously known as HR BREACH). The IMPACT project [2] in 2005, Peeters et al. [3] in 2011, and Morris et al [4] in 2012 have demonstrated that EMBREA performs the best among the available breach models. On that basis, EMBREA was used to undertake the modeling for this benchmark work.

Selection of Failure Modes

EMBREA can simulate breach failure by overtopping and piping. For this study overtopping is considered to be the main dam failure mode, but piping was also investigated in one of the scenarios.

Overtopping failure results in breach formation either due to headcut erosion or surface erosion. With headcut formation the erosion of material forms steps in the downstream face of the embankment which progressively grow in size and cut through the embankment. When the retreating headcuts reach the upstream side of the crest, the hydraulic control rapidly reduces in height and rapid failure ensues. With surface erosion, material is eroded from the embankment face and the crest area more smoothly leading to a reduced cross sectional embankment profile.

The dominant process depends mainly on the material used in the dam construction. The hypothetical dam in this instance is a rolled earth fill structure composed of predominantly sandy clays and clayey sands with a relatively low permeability (1.9×10^{-6} cm/s). Based on the type of soil and the permeability provided, and using Shevnin et al. [5], its clay content is estimated to be more than 25%. In addition to the clay content, the matric suction in unsaturated soils adds to the cohesive properties of soils. The low permeability of the embankment soil indicates the high likelihood of the presence of an added cohesion due to matric suction throughout the erosion process. The overall cohesive properties make headcut erosion the most likely erosion mode during overtopping failure.

The headcut erosion process is modeled in EMBREA using an erodibility coefficient (K_d), and a headcut migration coefficient (C). These parameters are usually measured on site or in a soil laboratory, but as the dam on this study is hypothetical, they were estimated based upon the soil clay content and compaction effort. To assess their uncertainty, the Monte Carlo analysis feature in EMBREA was used as described in below.

A number of modeling runs were undertaken to establish the potential worst case scenarios for the hypothetical dam failure. Within these runs, consideration was given to the uncertainty and sensitivity of results to various aspects such as material erodibility, failure mode and erosion processes, as follows:

- Runs 1, 2 and 3. In these runs EMBREA was used to perform a Monte Carlo analysis to the overtopping failure with headcut (1000 runs with a triangular probability distribution for K_d and corresponding C values as given in Table 4). The output of the Monte Carlo run analysis was a frequency distribution of the peak breach outflow. The median value of this distribution was taken as the base run (Run 1). The corresponding values of the 75 % (Run 2) and 25 % (Run 3) exceedance probabilities were taken as the lower and upper limits respectively.
- Run 4. In this run, the erosion process was changed to overtopping through surface erosion rather than headcut to assess the impact of a different erosion process on the breach hydrograph. Other inputs were identical to Run 1.
- Run 5: In this run, a good grass protection is assumed to be present on the downstream face of the embankment to assess its impact on delaying the breach initiation and hence the wave arrival time at downstream locations. Other inputs were identical to Run 1.
- Run 6: In this run, the failure mode was changed to piping rather than overtopping to assess the impact of a different failure mode on the breach hydrograph. It should be noted that surface erosion is used in the model once the top of the pipe becomes unstable and fails (i.e. failure mode changes from piping to overtopping). Other inputs were identical to Run 1.

Model set up

This section provides a description of the model set up, including modeling boundary conditions, initial conditions, dam geometry and soil properties. The selection of such data was mainly based upon the data provided to participants in [1]. Due to the size of the reservoir, any inflow into the reservoir during the breach event has a negligible effect on the reservoir water levels, and has therefore not been included. Based on investigation of the immediate reach downstream of the dam, a low tailwater level was assumed meaning that the breach flow was not 'drowned'. The dam geometry data is given in Table 1. Table 2 shows

the initial conditions used in each series of runs. The dam failure for this benchmark takes place when the pool elevation is at crest elevation. Table 3 shows soil properties used in each series of runs and Table 4 shows K_d and C values for each run. The K_d values and C values were obtained from the qualitative relationships for different soil types provided in the EMBREA user manual version 1.3.

Table 1: Dam geometry

Crest level	Foundation level	Crest Width	Crest length	Upstream slope	Downstream slope
272 mAD	211 mAD	24m	360m	1:3	1:3

Table 2: Initial conditions

Run No.	Pipe diameter (m)	Pipe Level (mAD)	Initial water level (mAD)	Initial breach depth (m)	Initial breach width (m)
1-5	NA	NA	272	0.25	0.5
6	0.03	212	272	NA	NA

Table 3: Soil properties

Porosity	0.40	Friction Angle (degrees)	14
Unit Wt (KN/m^3)	19.64	Cohesion (KN/m^2)	19.15
Manning's n	0.025	Plasticity Index	10

Table 4: K_d and C values

Run No.	Erodibility coefficient, K_d (cm^3/N-s)	Headcut migration coefficient, C (s$^{-2/3}$)
Monte Carlo	Triangular probability distribution with a lower value of 1, mid value of 5 and an upper value of 10	Values calculated from K_d values based on EMBREA user manual version 1.3
1, 5 and 6	5.5	0.0032
2	4.3	0.0026
3	6.8	0.0040
4	5.5	NA

Modelling results, observations and conclusions

Figure 1 shows a comparison of the breach outflow results for Runs 1 to 6. Runs 1, 2 and 3 hydrographs show that K_d and C values have a significant effect on the breach peak outflow and initiation time in the case of overtopping failure due to headcut formation. Increasing them by a factor of 1.3 (Run 1) and 1.6 (Run 3) has increased the breach peak outflow by about 40 and 100% compared to run 2 respectively. Run 4 shows that changing the type of erosion process results in a significant reduction in the peak breach outflow and initiation time. The peak outflow was reduced by about 78% compared to Run 1 with less than one hour of initiation time. Run 5 shows that for the case considered, a grass protection increases the initiation time of the breach with a negligible change in the peak breach outflow compared to Run 1. Run 6 shows that changing of the failure mode on breach formation to piping

significantly reduces the peak breach outflow and initiation time. The peak outflow was reduced by about 30 % compared to Run 1, with the shortest initiation time of all the runs.
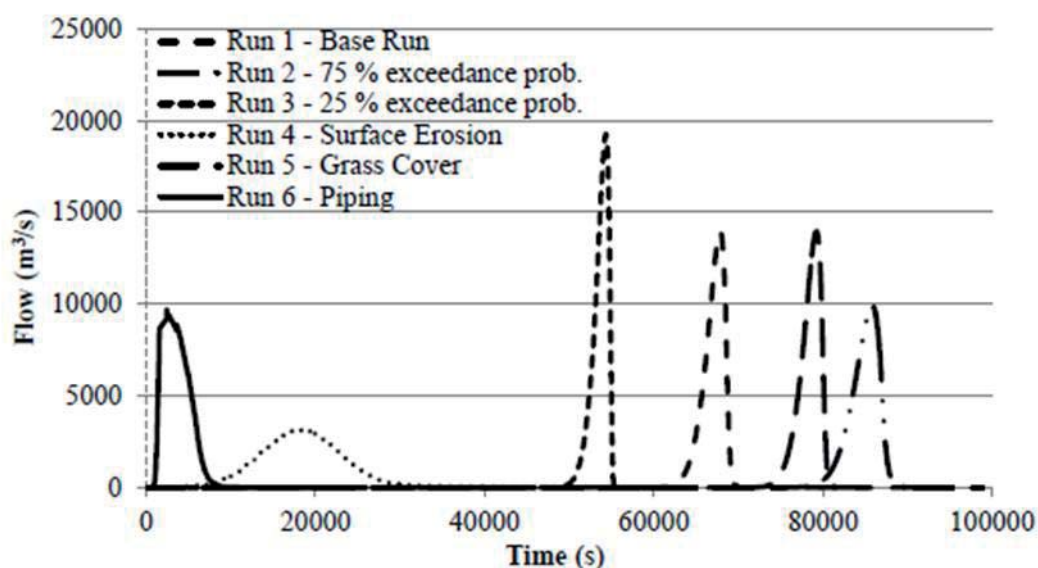
Figure 1: Breach outflow hydrograph for Runs 1 to 6

Flood Modelling

Data provided
The data provided for the flood model to participants was:
- digital elevation model (DEM) representing pre-dam and post-dam construction
- gridded dataset of land use/cover

The horizontal resolution of both datasets is about 9.5m. The land use/cover data follows the classification guidance and values provided in the National Land Cover Dataset (NLCD), 2006.

Roughness estimation
Surface roughness values for the flood simulation were estimated for each land use/cover class using the Conveyance and Afflux Estimation System (CES/AES) software [6]. The tool provides a database of roughness values extracted from various sources in the literature and given as mid, upper and lower estimates covering the range of roughness values expected within each system. This provides some measure of the uncertainty associated with the estimation of roughness by deriving an upper and a lower roughness credible scenario. The values assigned to each land use/cover class are shown in Table 5, as well as the total areas covered in the test bed region. For the developed areas, the low and high roughness values correspond to the lowest and highest values derived from the possible share between pervious/impervious areas given in the descriptions.

Table 5: Land use/cover estimated roughness

Class	ID	Description	Area	Winter			Summer		
				Mid	Low	High	Mid	Low	High
Water	11	Open Water	16.9%	0.010	0.010	0.010	0.010	0.010	0.010
Developed	21	Developed, Open Space	5.2%	0.029	0.025	0.034	0.029	0.025	0.034
	22	Developed, Low Intensity	10.7%	0.030	0.026	0.035	0.030	0.026	0.035
	23	Developed, Medium Intensity	5.1%	0.031	0.026	0.036	0.031	0.026	0.036
	24	Developed High Intensity	0.5%	0.032	0.025	0.036	0.032	0.025	0.036
Barren	31	Barren Land (Rock/Sand/Clay)	0.2%	0.022	0.017	0.028	0.022	0.017	0.028
Forest	41	Deciduous Forest	28.4%	0.073	0.049	0.112	0.102	0.072	0.162
	42	Evergreen Forest	7.9%	0.251	0.151	0.341	0.251	0.151	0.341
	43	Mixed Forest	0.1%	0.142	0.091	0.205	0.142	0.091	0.205
	52	Shrub/Scrub	20.9%	0.073	0.048	0.112	0.102	0.072	0.162
Herbaceous	71	Grassland/ Herbaceous	3.5%	0.046	0.027	0.083	0.046	0.027	0.083
Planted/ Cultivated	81	Pasture/Hay	0.4%	0.046	0.027	0.083	0.046	0.027	0.083
Wetlands	90	Woody Wetlands	0.2%	0.054	0.039	0.064	0.054	0.039	0.064

Flood model

The 2D Infoworks ICM software was used to simulate spreading of the flood given by the breach hydrograph into the valley downstream of the dam. Three roughness scenarios were considered that correspond with the mid, low and high roughness values for each land use class. For each roughness scenario, the model was run for each of the six dam breach hydrographs from the breach model. The hydrographs were used as an inflow boundary condition for the flood model. This was represented using the breach width and depth corresponding to the maximum breach outflow in combination with the post-dam construction digital elevation model.

Results

The results of the flood model presented in this section correspond to the overtopping failure with headcut failure mechanism only, as this is the most likely failure mode for the dam. The results for other failure modes can be provided upon request.

Figure 3 shows the attenuation of the breach hydrograph of the median scenario (Run 1) between the five cross sections on Figure 2. As shown, the peak flow is reduced by 10% when the flood arrives at cross section 5, which takes about 14 min from the moment of the peak breach discharge. In the scenario with 75% exceedance probability (Run 2), the peak flow attenuation is of a similar amount (9%), but the wave takes 10 min to reach cross section 5. Finally, for the scenario with 25% exceedance probability (Run 3), the peak flow hardly decreases (see Table 6).

The flood extents for the three scenarios are very similar, with the flood spreading to the valley on the north between sections 3 and 4 for the median and 75% scenarios (see Figure 2).

The peak flood depths for the 25%, the Median, and 75% exceedance probability scenarios are given in Table 7. Flood depths are mostly below 2m for all three scenarios, and below 4m for more than 90% of the flooded area. The spatial variability of the peak flood depths is shown in Figure 4 at 0.5m intervals for the median scenario. The higher flood depths in the city occur between cross sections 3 and 5 and also along the south end of the flood extent downstream section 5. That is also the main flowpath through the plain, with unit flow rates mainly between 4 and 10 m^2/s (Figure 5), increasing to 30m^2/s near section 5. The area of the city with higher unit flow rates –up to 80m^2/s- is between cross sections 4 and 5.

The arrival time of the first inundation relative to the time at which a breach flow initiates is shown in Figure 6. The flood reaches the populated area after 1.5h to 2h, but the majority of the city starts flooding after 2h. That is the arrival time of the small flow at the beginning of the dam breach initiation. However, the peak flow travel time in Figure 7 shows that the flood wave peak travels from the dam to the city in less than 15min, reaching the further edge in less than 90min, and hence the peak flow travel time is the travel time to consider.
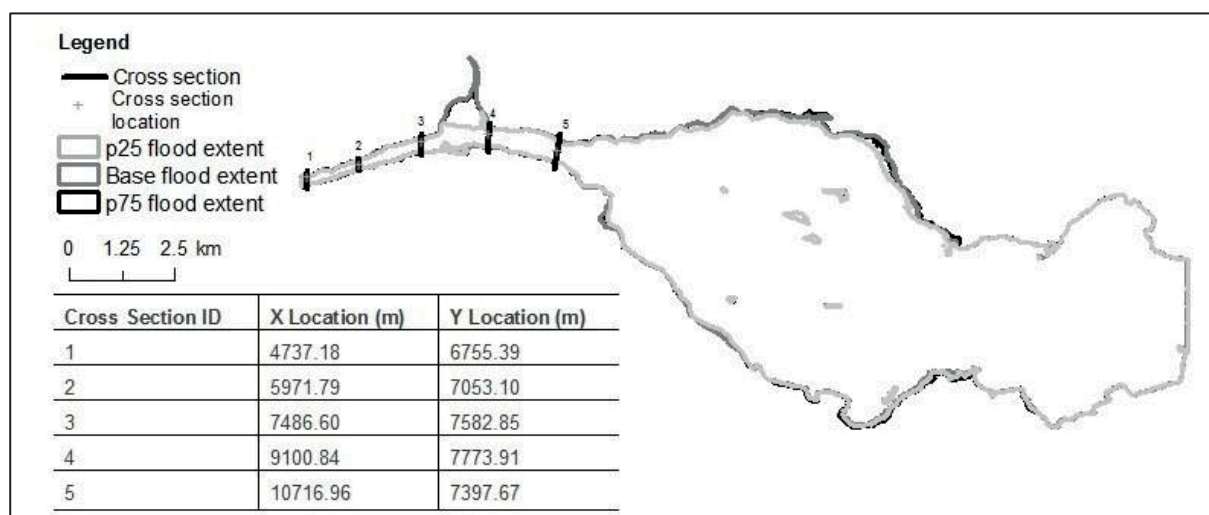
Figure 2: Cross-section locations and flood extent
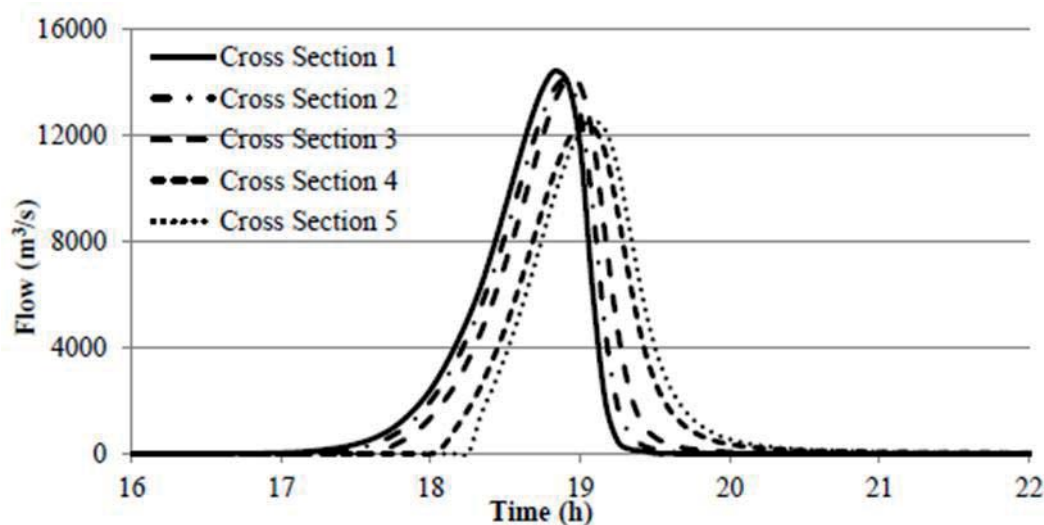
Figure 3: Cross section discharges median run

Table 6: Cross section discharges

Scenario	Breach		Cross Section 5	
	Peak flow (m^3/s)	Time	Peak flow (m^3/s)	Time
Median	13,956	18:51	12,540 (-10.1%)	19:05 (14min)
75% Exc. Prob.	19,257	15:05	17,537 (-8.9%)	15:15 (10min)
25% Exc. Prob.	9,908	23:51	9,877 (-0.3%)	24:05 (14min)
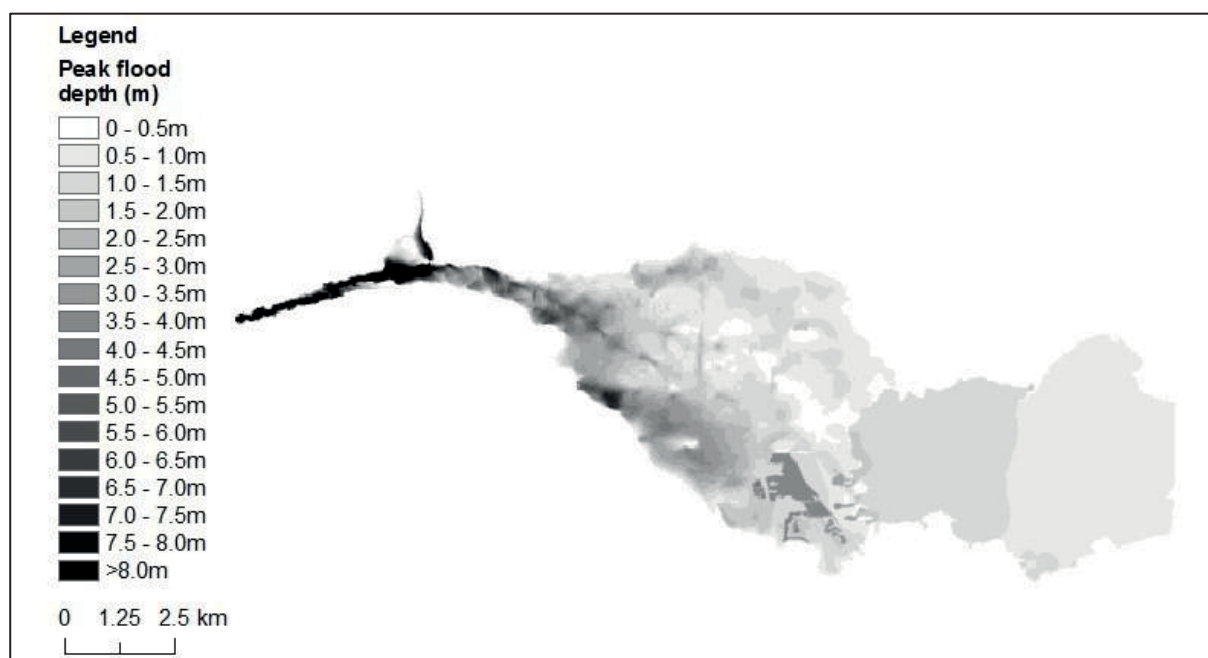
Figure 4: Peak flood depths (m) for the median scenario

Table 7: Flooded area (m^2)

Peak Flood Depth Range (m)	Flooded area (m^2)		
	25% exceedance probability	Median	75% exceedance probability
0 - 0.5	7,684,136	3,842,921	3,776,472
0.5 - 1	9,977,083	8,084,897	8,525,347
1 - 1.5	5,110,216	6,912,247	7,732,446
1.5 - 2	3,012,575	3,611,785	4,025,567
2 - 2.5	2,115,959	2,523,993	2,710,321
2.5 - 3	1,231,376	2,305,789	1,967,706
3 - 3.5	515,700	1,875,305	1,380,169
3.5 - 4	355,773	1,185,490	696,280
4 - 4.5	186,327	683,978	424,916
4.5 - 5	136,850	463,618	386,304
5 - 5.5	143,135	354,426	256,907
5.5 - 6	95,004	222,336	162,801
6 - 6.5	61,959	151,037	150,050
6.5 - 7	57,559	131,372	140,801
7 - 7.5	61,421	113,772	82,433
7.5 - 8	58,368	86,025	71,119
>8	522,524	900,657	973,392
TOTAL	31,325,966	33,449,648	33,463,027
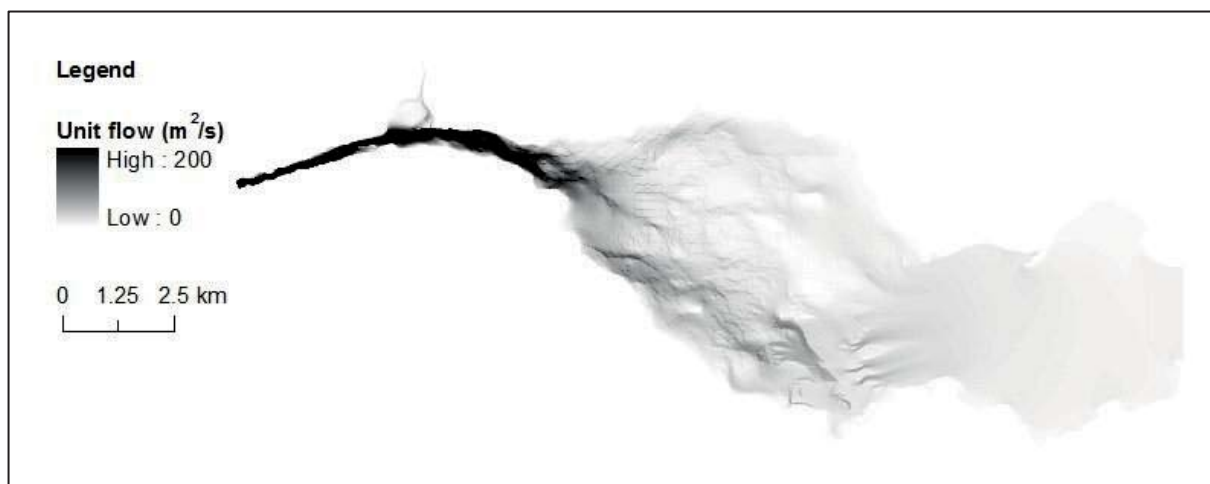
Figure 5: Peak unit flow rate in m²/s for the median scenario
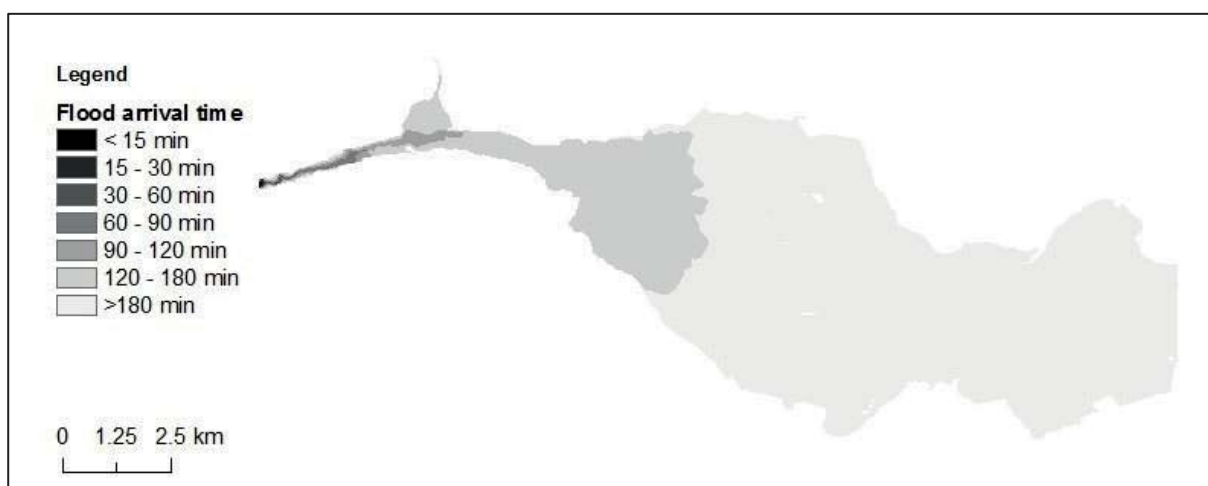
Figure 6: Inundation arrival time from initiation time for the median scenario
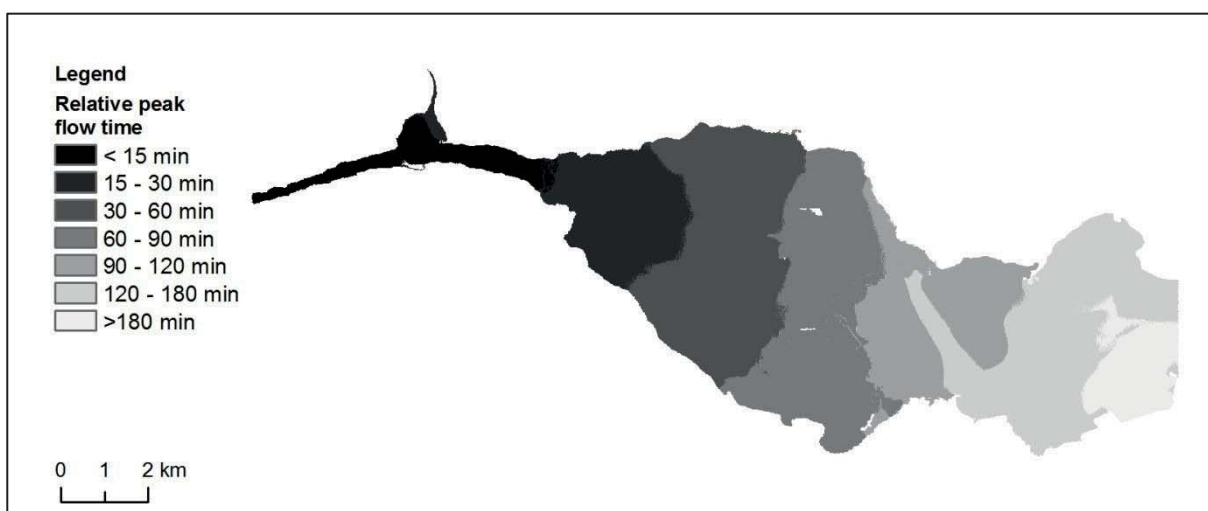
Figure 7: Peak flow travel time

Consequence Estimation

Flood severity

Flood Severity has been classified according to the Defra methodology presented in technical reports [7, 8]. The method describes the flood hazard as a function of velocity, depth and the presence of debris as

$$HR = d \times (v + 1.5) + DF$$

(1)

Where, HR is the (flood) Hazard Rating, d is the Depth of flooding (m), v is the velocity of the floodwater in (m/s), and DF is the debris factor (assumed to be 0.5 for depths <0.25m, and 1.0 for depths >0.25m).

Four flood hazard classes were established based on the thresholds of flood hazard rates (HR) that cause people to lose stability. Thresholds are derived from the experiments on people with different height multiplied by mass values. For this study, a 3 class categorization (low, medium and high) was required. Therefore the thresholds have been redefined as in Table 8. Figure 8 shows that the flood severity is mostly high in the flooded area.

Table 8: Flood Severity classification

ID	Class	Flood Hazard Rate (HR)	Description
1	Low	< 0.75	Caution. Flood zone with shallow flowing water or deep standing water"
2	Medium	0.75 - 1.25	Dangerous for some (i.e. children, the elderly and the infirm). Danger: Flood zone with deep or fast flowing water
3	Significant to high	>1.25	Dangerous for most people to all people. Danger to extreme danger: flood zone with deep fast flowing water
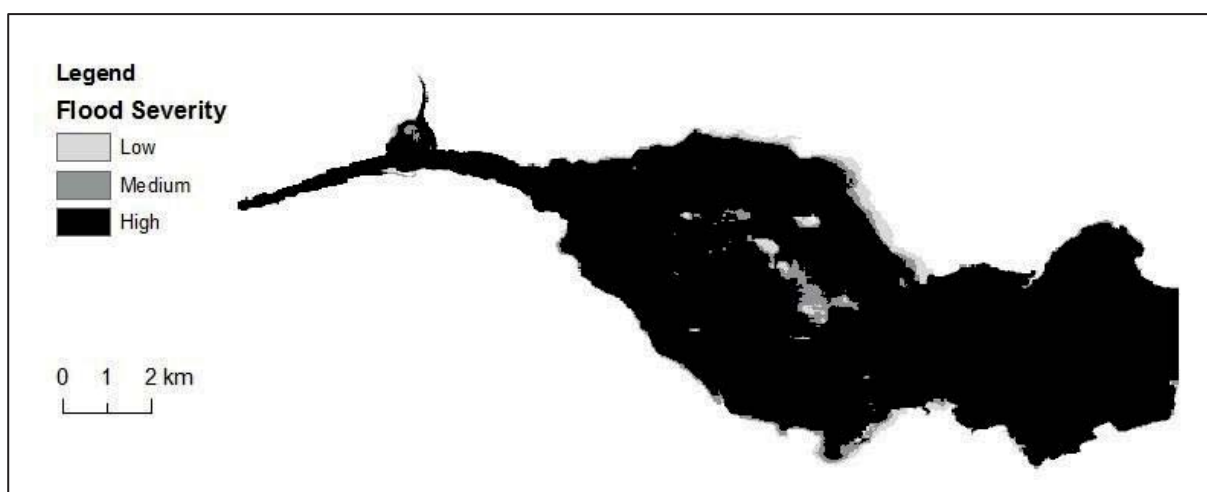
Figure 8: Flood severity

People at risk

Given the reporting requirements of the people at risk by time intervals and flood depths, the calculation of the number of people at risk was based on the flood extent from the hydraulic model and the population from the census data and the buildings. The average number of people in a building was calculated by dividing the total population by the number of buildings for each census zone. To calculate the number of people at risk from flooding the number of buildings in the maximum flood extent was determined from GIS and the population summed. Table 9 shows the total number of people at risk per age group and flood depth. Most of the people are at areas with flood depth below 1.5m.

Table 9: Number of people at risk per age group and flood depth

Peak Flood Depth Range (m)	Total Population At Risk	12-yr and Under Population at Risk	65-yr and Over Population at Risk
0 - 0.5	4,608	693	841
0.5 - 1	10,189	1,528	1,878
1 - 1.5	5,336	763	1,139
1.5 - 2	1,209	146	326
2 - 2.5	710	113	163
2.5 - 3	621	118	111
3 - 3.5	497	106	72
3.5 - 4	369	93	28
4 - 4.5	283	71	21
4.5 - 5	252	63	21
5 - 5.5	211	55	17
5.5 - 6	182	47	13
6 - 6.5	123	33	7
6.5 - 7	91	23	8
7 - 7.5	52	13	4
7.5 - 8	43	11	3
>8	128	37	6
Total	24,904	3,913	4,658

Loss of life

As with the number of people at risk from flooding, the calculation of loss of life uses the same population distribution. There are a number of methods to calculate loss of life. Brown and Graham [9] is a very simple method where the population at risk is multiplied by a factor depending on the length of time between the breach and flood warning. DeKay and McClelland [10] use a simple method that uses different equations for high and low force flooding. Graham [11] expands on the simple methods of Brown and Graham [9] and DeKay and McClelland [10] using the concept of flood severity, flood warning and the understanding of the exposed population to vary the fatality rate. The UK Flood Risk to People methodology [7] calculates the loss of life based on the hazard rating, the type of people exposed and the sensitivity of the area. This is similar to the method of Graham [11] used in the US, although it is more advanced because it uses the magnitude of the flood expressed by the spatially variable hazard rating to define fatality rate rather than a global fatality rate. The sensitivity of the area is defined by the time of travel of the flood wave, type of housing, and the presence of flood warning and evacuation plans. This calculation is most appropriate for large areas for

example census zones. Finally, the Life Safety Model [12] is an agent based model that determines the fate of each person that is exposed to the flood in a dynamic way through time and space. The model is designed for improving evacuation plans. The loss of life function in the model is based on the water depth and velocity. This function can be used in a static way to calculate loss of life from the maximum DV (Depth x Velocity).

After consideration of all the above methodologies, the approach taken was to primarily use the loss of life function from the Life Safety Model (LSM) to provide an estimate of loss of life based on people distributed in buildings. This has been chosen ahead of the UK Risk to People (UK R2P) method because of the requirement to produce gridded output at a high resolution.

The Theme C2 information [13] states that the dam fails at 11pm on Saturday night with no witnesses that are able to raise an alarm, and that there is no evacuation plan in place. It has therefore been assumed that the total population are in their homes and receive no warning for the loss of life calculations. The loss of life estimated for this pilot from the Life Safety Model approach is 4,966. That is based on conservative assumptions that a) people are on the ground, and b) take no measures to avoid the flood. The spatial variability of fatalities in Figure 9 show that the area between cross sections 3 and 5 is the most affected. All fatalities are after 3h of the breach initiation.

An alternative scenario where people shelter in buildings has been performed with the Life Safety Model where loss of life occurs if the building is submerged or collapsed. Assuming that people shelter in buildings the number of fatalities is estimated to be 3,075. A more realistic estimate can be produced assuming that people take refuge in multi-storey buildings or respond to a warning and evacuate the area, for which the dynamic Life Safety Model would be appropriate. A comparison of the methods is shown in Table 10.

The UK R2P method was used as a secondary check of LLOL. It is an area wide calculation which uses a simple vulnerability measure multiplied by the Hazard Rating to define the number of people at risk. The number of injuries is then estimated as 2 times the number of old and sick people as a proportion of the number at risk. The fatality rate is 2 times the Hazard Rating, and the number of fatalities is the number of injured multiplied by the fatality rate. This produces a significantly lower estimate of loss of life than the LSM because it assumes that young and healthy people can escape the flood. In this case the lack of flood warning means that the whole population should be considered at risk. The calculation has been modified so that the whole population is exposed producing an estimate of loss of life of 4,134.

Table 10: Loss of life

Estimation method	Life Safety Model approach 1	Life Safety Model approach 2 (people shelter in buildings)	UK Risk to people methodology	Modified UK Risk to people methodology
Loss of life	4,966	3,075	1,150	4,134
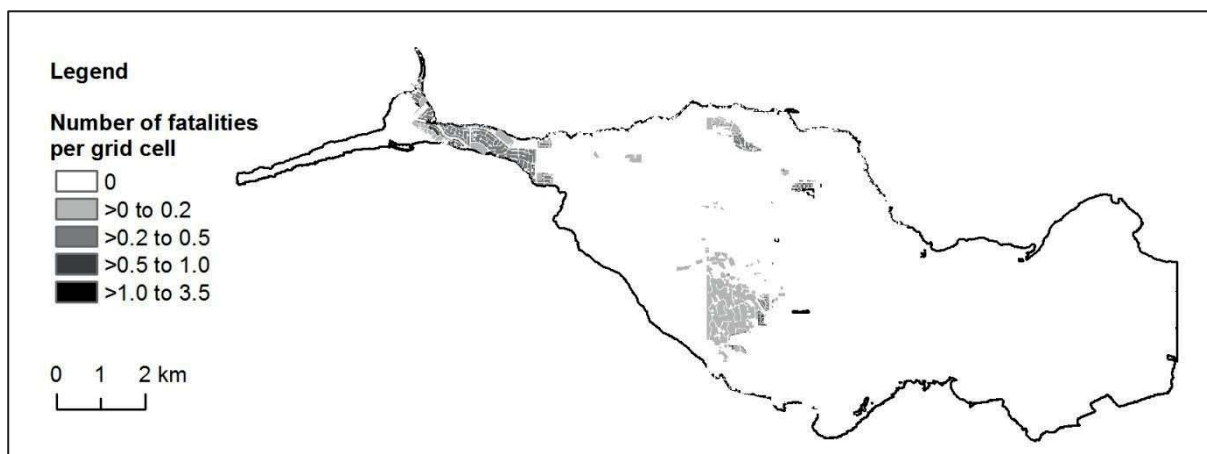
Figure 9: Loss of life from Life Safety Model, cell size ~9.5m x 9.5m

Economic damage

Depth damage curves have been taken from the MCM [14] 2010 update for residential and non-residential properties that are similar to the description given in the building data provided. These curves were developed for UK properties. The damages have been converted to US$ using an exchange rate of 1.51, but no other adjustments have been made to account for differences in US and UK properties. Alternatively there is a US method that relates the damage as a percentage of the building value for given water depths [15], but this method could not be used because building values were not provided in the building data.

The total economic damage for the base dam breach has been estimated as US$1,237,582,738. The spatial variability of the economic impact is shown in Figure 10, the commercial buildings having the higher damage per grid cell (~89.8m^2).
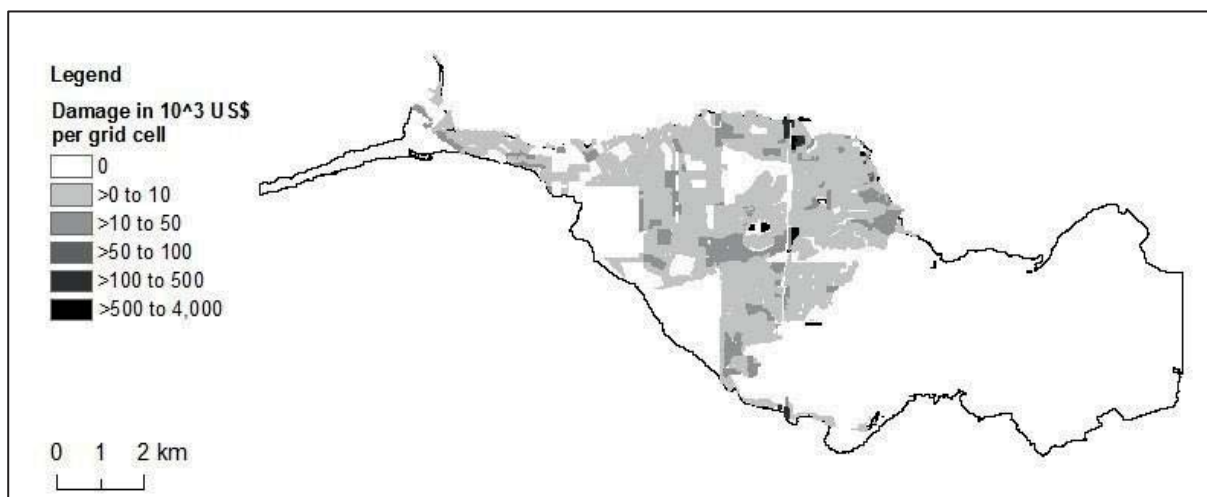
Figure 10: Direct economic impact

Observations

It would have been preferable to distribute the number of people across the residential buildings based on knowledge of household groupings. However, the census data provided was not detailed enough. In addition the building data provided contained the overall footprint rather than the number of individual properties (in the case of flats). This meant that some census zones had large population with little or no residential buildings. For example census zone 30 has 3 large properties classified as commercial but a population of 565. To reduce

uncertainty in the distribution of people within a census area, more detail is required on the demographics and number and type of buildings. The LSM can also model the behaviour of people in a flood situation as they seek to avoid the flood, thereby reducing the predicted loss of life.

Conclusions

The paper presents the consequences of the breach of the hypothetical dam as described in Theme C of the 12th International Benchmark Workshop on Numerical Analysis of Dams.

The dam breach analysis undertaken using EMBREA highlights the importance of choosing the correct erosion method and the impact of choosing the correct erodibility of the soil. Based on the data provided, it was estimated that the embankment fails according to headcut erosion leading to a steep hydrograph with a high peak discharge, the consequences of which are more severe than when an embankment fails due to surface erosion or piping.

The effects of the different roughness scenarios considered on the flood model was negligible compared to the impact of the different hydrographs used as input, emphasizing again the need for a good dam breach model. The flood model results provide useful information for warning and evacuation planning. The model indicates that the first flow from the dam breach reaches the populated area 1.5h to 2h after the breach initiates, but the peak flow travels from the dam to the city in less than 15min, reaching the further edge in less than 90min.

The total direct economic impact is estimated at more than US$1.24b. The loss of life calculations performed with the static Life Safety Model show a loss of life of 4,966, which represents nearly the 20% of the total people at risk.

References

[1] 12th International Benchmark workshop on numerical analysis of dams, "THEME C: Computational Challenges in Consequence Estimation for Risk Assessment: Numerical modelling, Uncertainty Quantification, and Communication of Results. Part 1- Hydraulic Modelling and Simulation," ed: International Commission on Large Dams (ICOLD), 2013.

[2] M. W. Morris, M. A. A. M. Hassan, and K. A. Vaskinn, "*Conclusions and recommendations from the IMPACT Project: WP2 Breach Formation*," 2004.

[3] P. Peeters, T. Van Hoestenberghe, L. Vincke, and P. Visser, "SWOT analysis of breach models for common dike failure mechanisms," presented at the 34th IAHR World Congress - Balance and Uncertainty, 33rd Hydrology & Water Resources Symposium, 10th Hydraulics Conference, Brisbane Australia, 2011.

[4] M. W. Morris, M.A.A.M. Hassan, T.L. Wahl , R.D. Tejral, G.J. Hanson, and D.M.

[5] Temple, "Evaluation and development of physically-based embankment breach models," presented at the 2nd European Conference on Flood Risk Management, Rotterdam, The Netherlands, 2012.

[6] V. Shevnin, O. Delgado-Rodríguez, A. Mousatov, and A. Ryjov, "Estimation of hydraulic conductivity on clay content in soil determined from resistivity data," *Geofisica Internacional,* vol. 45, 2006.

[7] Defra and Environment Agency, "Reducing uncertainty in river flood conveyance, phase 2, Conveyance manual," Environment Agency, report2004.

[8] Defra and Environment Agency, "R&D outputs: Flood Risk to People Phase 2.

[9] Guidance Document," 2006.

[10] Defra and Environment Agency, "Framework and guidance for Assessing and Managing Flood Risk Development, Flood Risk Assessment Guidance for New Development," Technical report2005.

[11] C. A. Brown and W. J. Graham, "Assessing the Threat to Life from Dam Failure,"

[12] *Water Resources Bulletin,* vol. 24, pp. 1303-1309, 1988.

[13] M. L. DeKay and G. H. McClelland, "Predicting Loss of Life in Cases of Dam Failure and Flash Flood," *Risk Analysis,* vol. 13, pp. 193-205, 1993.

[14] W. J. Graham, "A Procedure for Estimating Loss of Life Caused by Dam Failure," ed.

[15] Denver, Colorado: U.S. Department of Interior, Bureau of Reclamation, Dam Safety

[16] Office, 1999.

[17] BC Hydro, "Dam Safety, BC Hydro Life Safety Model: Formal model description," ed: BC Hydro,, 2004.

[18] I. B. w. o. n. a. o. dams, "THEME C: Computational Challenges in Consequence Estimation for Risk Assessment: Numerical modelling, Uncertainty Quantification, and Communication of Results. Part 2- Consequence Estimation," International Commission on Large Dams (ICOLD) ed, 2013.

[19] E. Penning-Rowsell, C. Johnson, S. Tunstall, S. Tapsell, J. Morris, J. Chatterton*, et al.*, "The benefits of Flood and Coastal Risk Management: A manual of assessment techniques," ed. Middlesex: Middlesex University Press., 2005.

[20] C. Scawthorn, P. Flores, N. Blais, H. Seligson, E. Tate, S. Chang*, et al.*, "HAZUS-MH flood loss estimation methodology. II. Damage and loss assessment," *Natural Hazards Review,* vol. 7, pp. 72-81, 2006.

Uncertainty in Two-Dimensional Dam-Break Flood Modeling and Consequence Analysis

M.S. Altinakar[1], M.Z. McGrath[1], V.P. Ramalingam[1], D. Shen[1], Y. Seda-Sanabria[2] and E.E. Matheu[3]

[1] National Center for Computational Hydroscience and Engineering, The University of Mississippi, Brevard Hall Room 327, P.O. Box 1848, University, MS 38677-1848, USA

[2] Critical Infrastructure Protection and Resilience Program, Office of Homeland Security, U.S. Army Corps of Engineers, Headquarters, Washington, DC 20314, USA

[3] Critical Lifelines Branch, Sector Outreach and Programs Division, Office of Infrastructure Protection, National Protection and Programs Directorate, Washington, DC 20528, USA

E-mail: altinakar@ncche.olemiss.edu

Abstract

This paper presents the preliminary results of an extensive study to evaluate and quantify uncertainty in two-dimensional numerical dam-break flood modeling and consequence analysis based on a benchmark test case. The benchmark problem consists of a hypothetical 61m-high embankment dam in a mountainous region with lightly populated urban areas located downstream. Although the benchmark problem was intended mainly for estimating the uncertainty in the evaluation of the consequences of failure of a dam near populated areas with complex demographics, infrastructure and economic activity, the present study also investigated the uncertainty in two-dimensional numerical modeling based on three control variables. DSS-WISE™ numerical model was used to calculate dam-break flood and potential loss-of-life for a total of 120 cases, which represented 40 random pairs of breach width and breach formation time, each computed with three different sets of Manning's coefficients defined based on land use/cover type. Computed results include raster maps of maximum flood depth, maximum flood discharge per unit width and flood arrival time as well as hydrographs at 7 cross sections. Analysis of population at risk (PAR) impacted by the flood and loss-of-life were also computed for all 120 simulations. The paper presents some preliminary results based on the statistical analysis of results.

Introduction

Test case consists of synthetic data specially designed for the benchmark study. A hypothetical 61m-high embankment dam located in a mountainous area impounds a reservoir having a normal storage of 38 million cubic meters. A lightly populated urban area, called Hydropolis, is located about 3.5 km downstream from the dam. The benchmark test case data for hydrodynamic simulation consists of (1) digital elevation model (DEM) of the area of interest with and without the dam; (2) dam geometric characteristics; (3) reservoir stage-volume and stage surface area curves; (4) dam and foundation material; (5) dam failure scenario and conditions ate the time of failure; and (6) gridded data of land use/cover.

In addition the following data is provided for consequence estimation: (1) shapefile of the census data for Hydropolis with breakdown into various age and gender classes; (2) shapefile for twenty economic activity classes; (3) shapefile for parcel data with 28 zone classes (residential, commercial, etc.). The complete dataset and supporting documents have been published on the conference website under Theme-C and will not be repeated here. It is

assumed that the dam fails without warning when the water surface in the reservoir is at the crest elevation and the population downstream cannot be warned.

Two-Dimensional Dam-Break Flood Simulation Model

Two dimensional simulations of dam-break flood were performed using the DSS-WISE™ software developed by the National Center for Computational Hydroscience and Engineering (NCCHE), The University of Mississippi. DSS-WISE™ is an integrated platform, which couples a state-of-the-art two dimensional numerical model with GIS-based pre- and post-processors, that are developed as an extension to ArcGIS® software developed and commercialized by ESRI. Its numerical solver – CCHE2D-FLOOD – solves the conservative form of the two-dimensional shallow water equations, given as

$$U_t + [F(U)]_x + [G(U)]_x = S(U) \tag{1}$$

in which, U is the vector of conserved variables, $F(U)$ and $G(U)$ are flux vectors in x and y directions, and $S(U)$. These are defined as

$$U = \begin{bmatrix} h \\ hu \\ hv \end{bmatrix} \quad F(U) = \begin{bmatrix} h \\ huu + \frac{gh^2}{2} \\ huv \end{bmatrix} \quad G(U) = \begin{bmatrix} h \\ hvu \\ hvv + \frac{gh^2}{2} \end{bmatrix} \quad S(U) = \begin{bmatrix} q_v \\ -ghS_{fx} - gh\left(\frac{\partial z_b}{\partial x}\right) \\ -ghS_{fy} - gh\left(\frac{\partial z_b}{\partial y}\right) \end{bmatrix} \tag{2}$$

where, h is the flow depth, hu and hv components of unit discharge in x and y directions, z_b the bed elevation, q_v the net source/sink mass flux per cell area per unit time, and g the gravitational acceleration. The slopes of energy grade line are given by Manning's equation

$$S_{fx} = \frac{un^2\sqrt{u^2 + v^2}}{h^{4/3}} \; ; \; S_{fy} = \frac{vn^2\sqrt{u^2 + v^2}}{h^{4/3}} \tag{3}$$

with n as the Manning's coefficient of roughness. Note that hu and hv correspond to the components of the unit discharge in x and y directions, respectively, i.e., q_x and q_y . Finite volume discretization of Equation (1) over a regular Cartesian mesh provides an explicit equation for advancing the values of the conserved variables in time:

$$U_{i,j}^{m+1} = U_{i,j}^m - \left(\frac{\Delta t}{\Delta x}\right)\left(F_{i+\frac{1}{2},j} - F_{i-\frac{1}{2},j}\right) - \left(\frac{\Delta t}{\Delta y}\right)\left(G_{i,j+\frac{1}{2}} - G_{i,j-\frac{1}{2}}\right) + \Delta t S_{i,j} \tag{4}$$

In Equation (4), Δx and Δy define the cell size in x and y directions, and Δt the time step size. The intercell fluxes are computed using the first order Harten-Lax-van Leer-Contact (HLLC) approximate Riemann solver by Toro et al. (1994), which was implemented following the methodology described by Kim et al. (2007). The details can be found in Altinakar et al. (2013a), Altinakar (2012) and Altinakar and McGrath (2012). The DSS-WISE software and its solver CCHE2D-FLOOD have been fully verified using analytical solutions and validated using laboratory and field data. Blind tests have also been undertaken in collaboration with U.S. Army Corps of Engineers (Altinakar et al., 2012).

Data for Benchmark Test Case

Figure 1 shows the digital elevation model without dam. Open water surface to the East of the area of interest was converted into "NoData". The numerical model treats NoData cells as an

internal free outflow boundary. This prevents flood propagating over the open water surface, which would otherwise be perceived as bed topography. The dam is represented in the DEM as an idealized structure representing a wall of constant thickness. The embankment dam has a crest width of 24m and the upstream and downstream slopes of 3H:1V. Considering that the dam has a height of 61m, the width of the idealized wall was chosen as 207m, which corresponds to the average width of the embankment dam. The overtopping failure was assumed to take place when the reservoir reaches crest elevation. Thus, the initial condition models the reservoir as a stagnant water body with surface elevation equal to crest elevation.
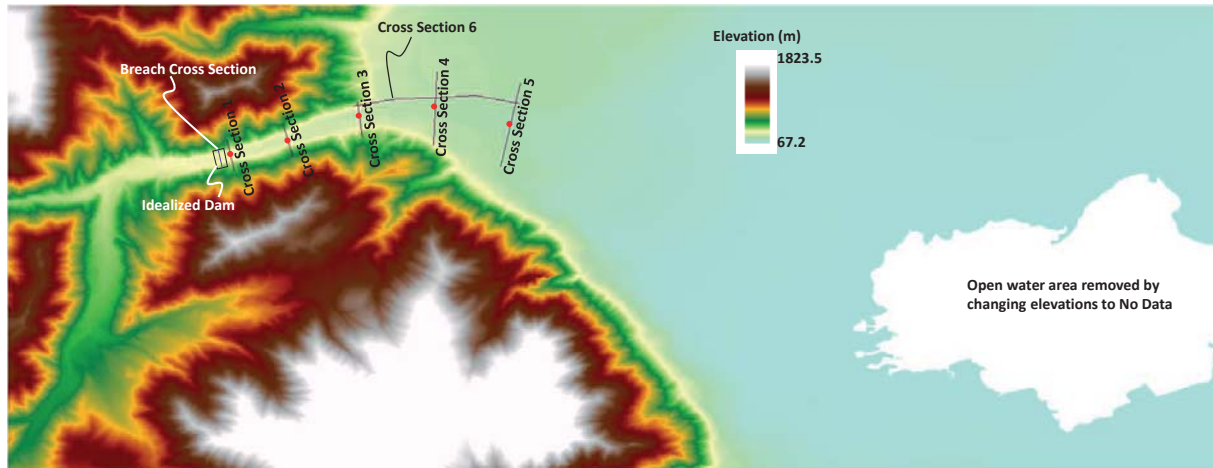
Figure 1: DEM without the dam (pre-construction) with open water area removed.

Selection of Test Cases

Three parameters were chosen to investigate the uncertainty of unsteady hydrodynamic simulations: (1) bottom breach width, W_b; (2) breach formation time, t_f; and (3) the set of Manning's coefficient of roughness, n.

Prediction of Breach Parameters

Empirical equations have been developed to estimate breach parameters based on the analysis of the data from historic dam failures (Wahl, 2004). The present study uses the empirical equations given by Froehlich (1995) to compute the breach width and breach formation time

$$B_{avg} = 0.1803 \, K_o \, V_w^{0.32} \, h_b^{0.19} \tag{5}$$

$$t_f = 0.00254 \, V_w^{0.32} \, h_b^{-0.9} \tag{6}$$

where B_{avg} is the average breach width (m), i.e. the breach width at half of the breach height h_b (m), K_o is a constant equal to 1.4 for overtopping failures, and V_w is the reservoir volume at the time of failure (m3). Equations (5) and (6) were obtained based on data from past failures of zoned earthen, earthen with a clay core, and rockfill embankment dams. The dam heights ranged from 3.66m to 92.6m (with 90%<30m and 76%<15m), the volume of water in the reservoir ranged from 0.0130×106 m3 to 660.0×106 m3 (with 87%<25.0×106 m3 and 76%<15.0×106 m3) and the lake surface areas ranged from 0.045km2 to 2,165km2. The data for the benchmark test case (61m, 38×106 m3, and 1.584 km2), which is well within the range of cases used to establish Equations (5) and (6). Thus, the average breach width and breach formation time are calculated as $\overline{B_{avg}} = 147m$ and $\overline{t_f} = 0.7hr$, respectively. Considering the

side slopes of 1.4H:1V [6], the bottom with and top width of the trapezoidal breach cross section are $\overline{W_b} = 62m$ and $\overline{B_t} = 233m$, respectively.

Uncertainty of prediction of breach parameters for embankment dams was investigated by Wahl (2004) [12]. It was shown that the prediction errors using empirical equations, including Froehlich (1995) [6], exhibit a lognormal probability distribution (base 10) defined by a mean value, μ, and a standard deviation, σ. Table 1 summarizes the uncertainty estimates of the breach parameters predicted using Froehlich (1995). Using the values given in Table 1, the 95% confidence interval for the breach bottom width extends from 25m to 146m whereas the 95% confidence interval for breach formation time extends from 0.3hr to 4.9hr.

Table 1: Uncertainty Estimates for Froehlich (1995) Equations (taken from Wahl, 2004).

Parameter	Equation	Number of Cases		μ (log cycles)	σ (log cycles)	95% Confidence interval*
		Before outlier exclusion	After outlier exclusion			
Breach width	Eq. (5)	77	75	+0.01	±0.195	0.40 – 2.4
Breach formation time	Eq. (6)	34	33	-0.22	±0.32	0.38 – 7.3

*95% confidence interval is given around a hypothetical predicted value of 1.0

Manning's Coefficients

Manning's coefficients were assigned based on the given land use/cover data with 16 size classes that follow the classification guidance and values provided in the U.S. National Land Cover Dataset (NLCD). The land use/cover classes for the area of interests are shown in Figure 2. Table 2 shows the three sets of Manning's coefficient used in the present study. It should be noted that the area of interest does not have classes 12 and 95. Figure 3 provides a visual comparison of the three sets of Manning's coefficients for each land use/cover class.
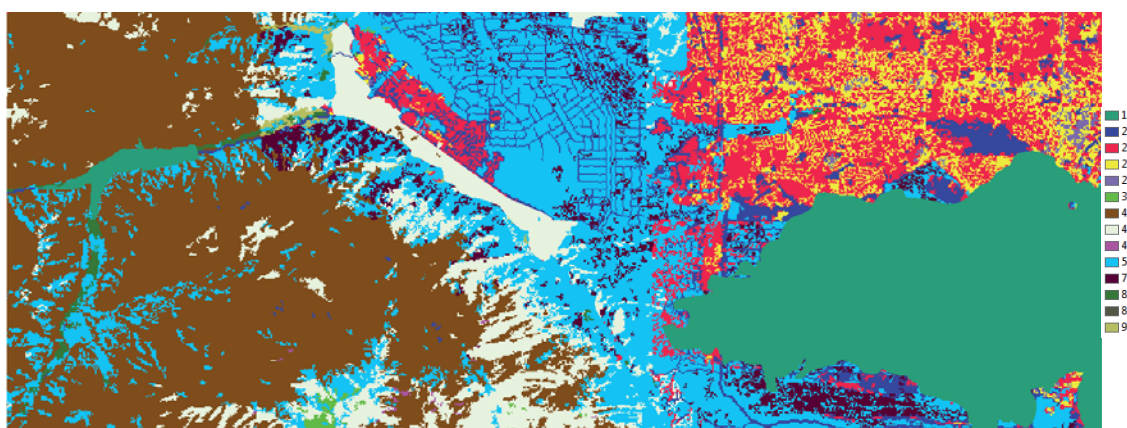
Figure 2: Map of land use/cover classifications.

Latin Hypercube Sampling for Breach Parameters

Latin Hypercube Sampling (LHS) method was used to select 40 random pairs of bottom breach width, W_b and breach formation time, t_f. LHS is a stratified-random method which provides an efficient way of sampling variables from their distributions (Iman et al. 1981). The cumulative distribution (normal distribution of logarithms) of both variables were divided into 40 intervals of equal probability. For each variable, a value is randomly selected from every interval. The selected values are paired randomly to achieve an optimal filling of the parameter-uncertainty space defined by the 40×40 matrix of W_b and t_f. Design of the LHS was accomplished using the "lhsdesign" function in Matlab® software using an option that

maximizes the minimum distance between the pairings. Figure 4a shows the LHS design used in the present study. Since W_b and t_f have lognormal distributions (base 10), the probability values, p_{norm}, used in LHS were converted into real values using the following expressions:

Table 2: Land Use/Cover Classes and Three Sets of Corresponding Manning's Coefficients.

NLCD Class	Description	$n\ (m^{-1/3}s)$					
		DSS-WISE[(1)]	FEMA HAZUS[(2)]	NOAA C-CAP[(3))]	Min. Value	Average Value	Max. Value
11	Open Water	0.0330	0.0010	0.0250	0.0010	0.0197	0.0330
12	Perennial Ice/Snow	0.0100	0.0100	0.0100	0.0100	0.0100	0.0100
21	Developed-Open Space	0.0404	0.0200	0.0350	0.0200	0.0318	0.0404
22	Developed- Low Intensity	0.0678	0.0500	0.1200	0.0500	0.0793	0.1200
23	Developed- Med. Intensity	0.0678	0.1000	0.1200	0.0678	0.0959	0.1200
24	Developed- High Intensity	0.0404	0.1500	0.1200	0.0404	0.1035	0.1500
31	Barren Land	0.0113	0.0900	0.0300	0.0113	0.0438	0.0900
41	Deciduous Forest	0.1000	0.1000	0.1600	0.1000	0.1200	0.1600
42	Evergreen Forest	0.1000	0.1100	0.1800	0.1000	0.1300	0.1800
43	Mixed Forest	0.1200	0.1000	0.1700	0.1000	0.1300	0.1700
52	Shrub/Scrub	0.0400	0.0500	0.0800	0.0400	0.0567	0.0800
71	Grassland/Herbaceous	0.0400	0.0340	0.0350	0.0340	0.0363	0.0400
81	Pasture/Hay	0.0350	0.0330	0.0500	0.0330	0.0393	0.0500
82	Cultivated Cropland	0.0700	0.0370	0.1000	0.0370	0.0690	0.1000
90	Woody Wetlands	0.1500	0.1000	0.1500	0.1000	0.1333	0.1500
95	Herbaceous Wetlands	0.1825	0.0450	0.0500	0.0450	0.0925	0.1825

[(1)]Altinakar et al. (2013b); [(2)]Luettich and Westerink (2009); [(3)]ARCADIS (2011)
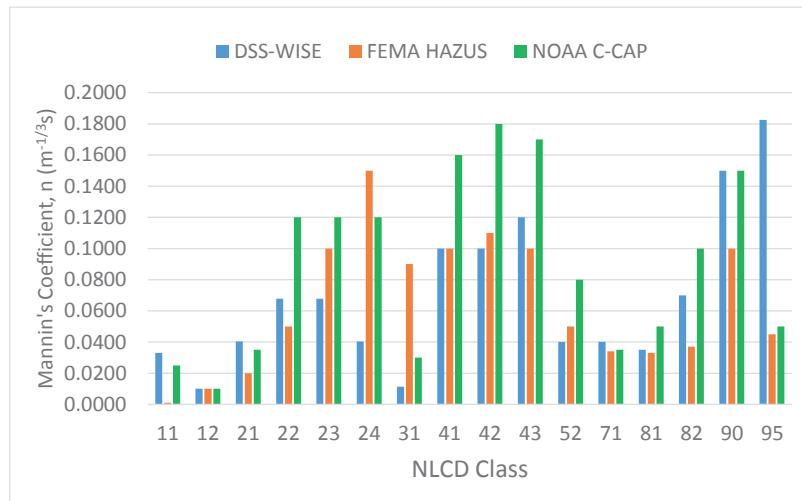
Figure 3: Comparison of three sets of Manning's coefficients assigned to NLCD classes.

$$W_b = \overline{W_b}\ 10^{[-\mu+norminv(p_{norm},0,1)*\sigma]}\ ;\ t_f = \overline{t_f}\ 10^{[-\mu+norminv(p_{norm},0,1)*\sigma]} \qquad (7)$$

In the above expression, $norminv(p_{norm},0,1)$ stands for the inverse of the cumulative distribution function of standard normal distribution, with mean equal to zero and standard deviation equal to 1, at the probability value of p_{norm}. For each variable, i.e. W_b or t_f, its corresponding μ and σ values were used. The selected 40 pairs are provided in Table 3. In Figure 4a, the numbers for the data points correspond to combination numbers in Table 3. Figure 4b and Figure 4c show that the randomly selected of W_b and t_f values display a lognormal probability distribution, as expected.

Assumptions Regarding the Progression of the Breach Geometry

Froehlich (1995) expression, used for estimating breach characteristics, assumes that the final breach cross section for overtopping failures is a trapezoidal with side slopes of 1.4H:1V. Figure 5a shows the mean, minimum and maximum breach sizes selected by LHS. The elevations of the cells under the footprint of the idealized dam were initially raised to the level of the crest. As soon as the simulation starts, the breach occurs by gradually bringing down these cells to the original valley elevation during the breach formation time, t_f, as shown in Figure 5b. The cell elevations are not permitted to go below the original bed elevation.

(a)   (b)   (c)
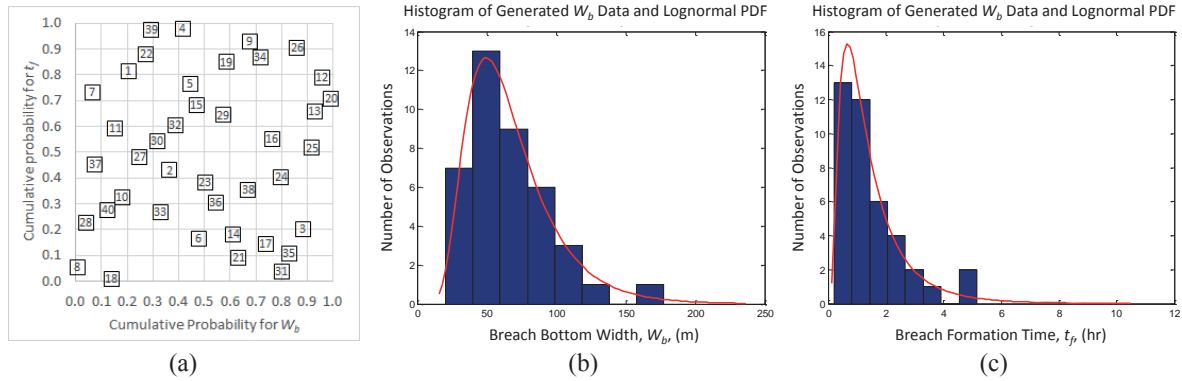
Figure 4: (a) LHS design obtained by maximizing minimum distance between data pairs; (b) Histogram of randomly selected breach widths and the fitted lognormal distribution; (c) Histogram of randomly selected breach formation times and the fitted lognormal distribution.

Table 3: List of 40 pairs of breach width and breach formation time selected using LHS.

Pair No	W_b (m)	t_f (hr)	Pair No	W_b (m)	t_f (hr)	Pair No	W_b (m)	t_f (hr)	Pair No	W_b (m)	t_f (hr)
1	41.9	2.2	11	38.3	1.4	21	70.6	0.4	31	88.4	0.3
2	51.8	1.0	12	130.3	2.1	22	46.2	2.8	32	53.2	1.4
3	103.5	0.6	13	116.9	1.6	23	60.7	0.9	33	49.6	0.7
4	55.1	5.2	14	68.8	0.6	24	88.0	1.0	34	78.4	2.6
5	57.0	2.0	15	58.6	1.7	25	113.1	1.2	35	92.9	0.5
6	59.0	0.6	16	83.6	1.3	26	98.5	3.0	36	63.6	0.8
7	30.6	1.8	17	80.6	0.5	27	44.7	1.1	37	31.8	1.1
8	20.0	0.4	18	37.2	0.2	28	27.4	0.7	38	73.8	0.9
9	74.4	3.4	19	66.7	2.5	29	65.7	1.5	39	47.5	4.9
10	40.1	0.8	20	177.3	1.7	30	48.9	1.3	40	36.0	0.7

(a)   (b)
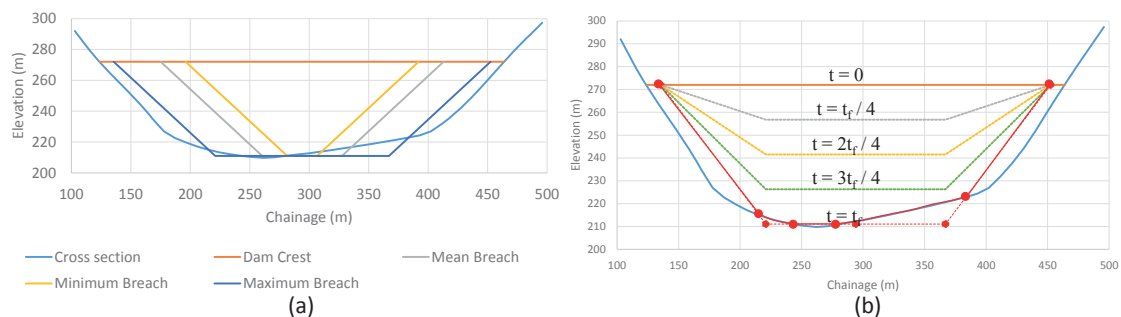
Figure 5: (a) Breach geometry for mean, minimum and maximum breach bottom widths; and (b) Linear progression of the breach geometry assumed in the numerical model.

Results of Hydrodynamic Simulations

A total of 120 numerical simulations were performed by combining 40 randomly chosen pairs of breach width and breach formation time with three sets of Manning's coefficients. Each simulation provided three raster files (maximum flow depth, h_{max}, flood arrival time, t_{arr}, and maximum specific discharge, q_{max}), and discharge hydrographs at seven cross sections (dam crest, five pre-defined cross sections along the main downstream flow, and one cross section to capture the flows towards north) recorded with a time interval of two minutes.
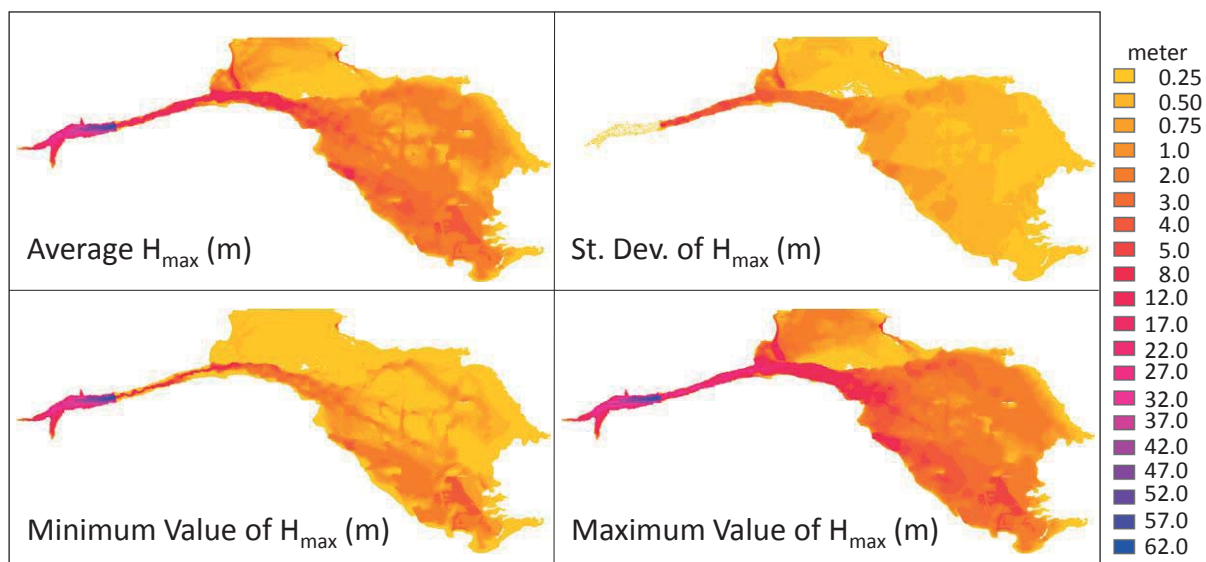
Figure 6: Statistics of maximum flood depth, $\boldsymbol{h_{max}}$ (m), based on 120 simulations.

Maps of Maximum Depth, Flood Arrival Time and Maximum Discharge per Unit Width
The set of 120 raster files were used to calculate maps of ensemble average, standard deviation, and minimum and maximum values of the maximum flood depth (Figure 6), the flood arrival time (Figure 7), which is defined as the time at which the dry computational cell becomes wet, regardless of the depth, and the maximum discharge (Figure 8). In these maps, cells with a null value are not displayed. As expected, the highest flow depths and unit discharges occur in the narrow valley immediately downstream of the dam. Comparison of minimum and maximum value maps of these three variables indicate that large differences exist between individual runs. The largest standard deviations of maximum flood depth and maximum unit discharge occur in the narrow valley downstream of the dam whereas the largest standard deviation values for the arrival time are observed farthest from the dam. The area on the northern part is inundated only for certain simulations. The longest time arrival and largest standard deviations of arrival time are observed in this area (Figure 7).

An understanding of the sensitivity of results to different parameters can be gained by analyzing and comparing results files of individual simulations. Figure 9 shows a comparison of the flood maps of selected pairs of breach width and breach formation time with all three sets of Manning's coefficients. The upper right hand corner shows a plot of all 40 random pairs selected with LHS in terms of real values of W_b and t_f. This should be compared with the plot in probability space shown in Figure 4a. As shown, there are no simulations in the upper right corner of the plot corresponding to large breach widths with long formation times.

The inspection of Figure 9 shows that the area on the north part of the DEM is inundated only for certain combinations of parameters. In $W_b - t_f$ space, the simulations with inundation of

north part correspond to small breach formation times and large breach widths. In addition, higher Manning's values favor inundation of the north part of the DEM. The main land use/cover types in the narrow valley are pasture/hay, woody wetlands, and evergreen forest. The n-values from NOAA C-CAP for these land use/cover types are the highest resulting in higher flow depths and, thereby spilling of the flood into northern region of the DEM for pair numbers 3, 6. 8, 18, and 31.
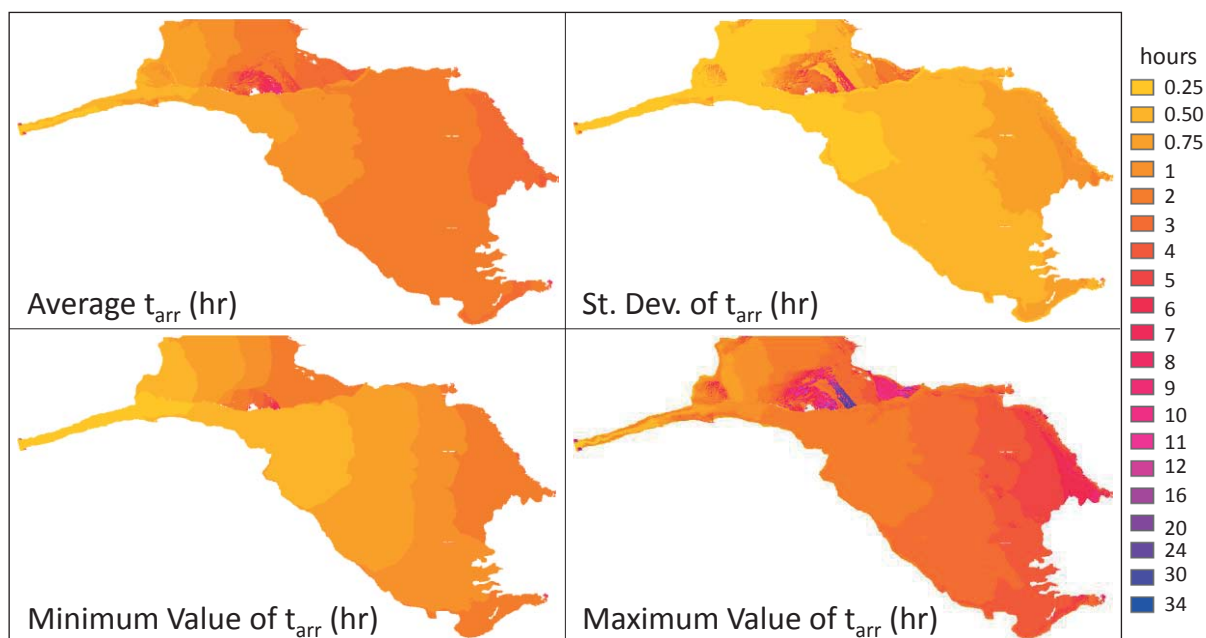
Figure 7: Statistics of flood arrival time, t_{arr} (hr), based on 120 simulations.
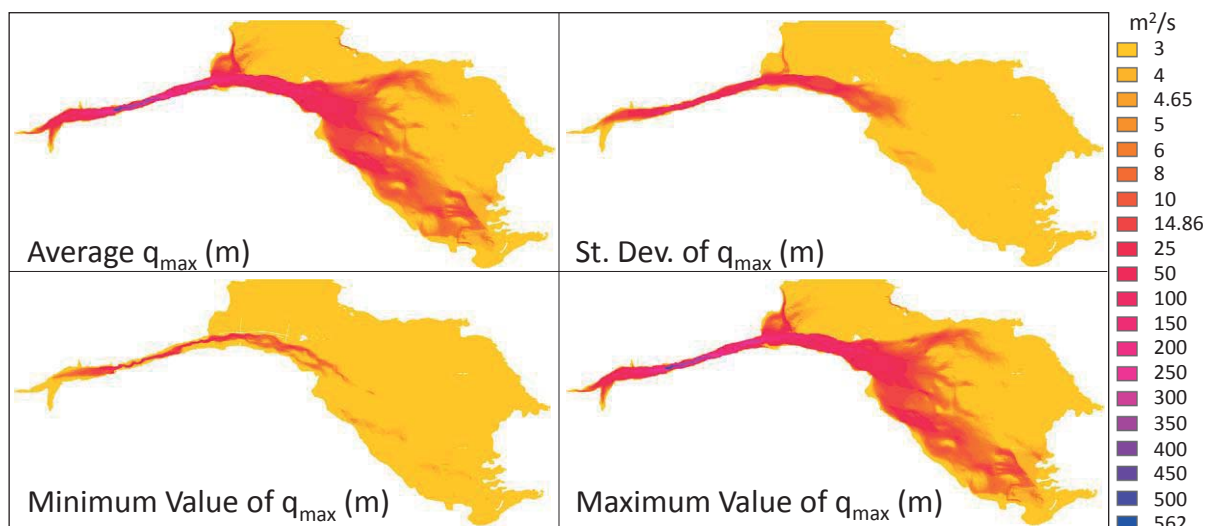
Figure 8: Statistics of maximum discharge per unit width, q_{max} (m^2/s), based on 120 simulations.

Hydrographs

Discharge hydrographs were recorded at seven cross sections. These include the breach cross section and five cross sections specified in the benchmark test case formulation. An additional cross section was also introduced in order to measure the flood discharge propagating to the north of the DEM under certain combinations of control parameters (see Figure 9). Due to the

lack of space, only limited number of results will are presented in this paper. Additional details will be provided in subsequent publications.

Figure 10 shows the discharge hydrographs at the breach cross section (left plot) and the relationship between peak discharge and the control parameters W_b (middle plot) and t_f (right plot). Runs with different n-values are distinguished with different symbols/colors. Since at the breach cross section the influence of the Manning's coefficient is not fully felt, for a given W_b and t_f pair, the hydrographs obtained with different n-values coincide fairly well. The peak discharge does not seem to be highly correlated with the breach width (middle plot) but rather with the breach formation time (right plot). The peak discharge is inversely proportional with the breach formation time and all the data collapses onto a single curve.

A similar plot is shown for cross section 5 in Figure 11. The peak discharges of hydrographs are attenuated. For a given W_b and t_f pair, the hydrographs computed with different sets of n-values have different arrival times. The peak discharges are not correlated with the breach width (middle plot) but they still show a relatively good correlation with the breach formation time (right plot) despite the fact that the differences in the peak discharge for simulations with different n-values are larger for W_b and t_f pairs.
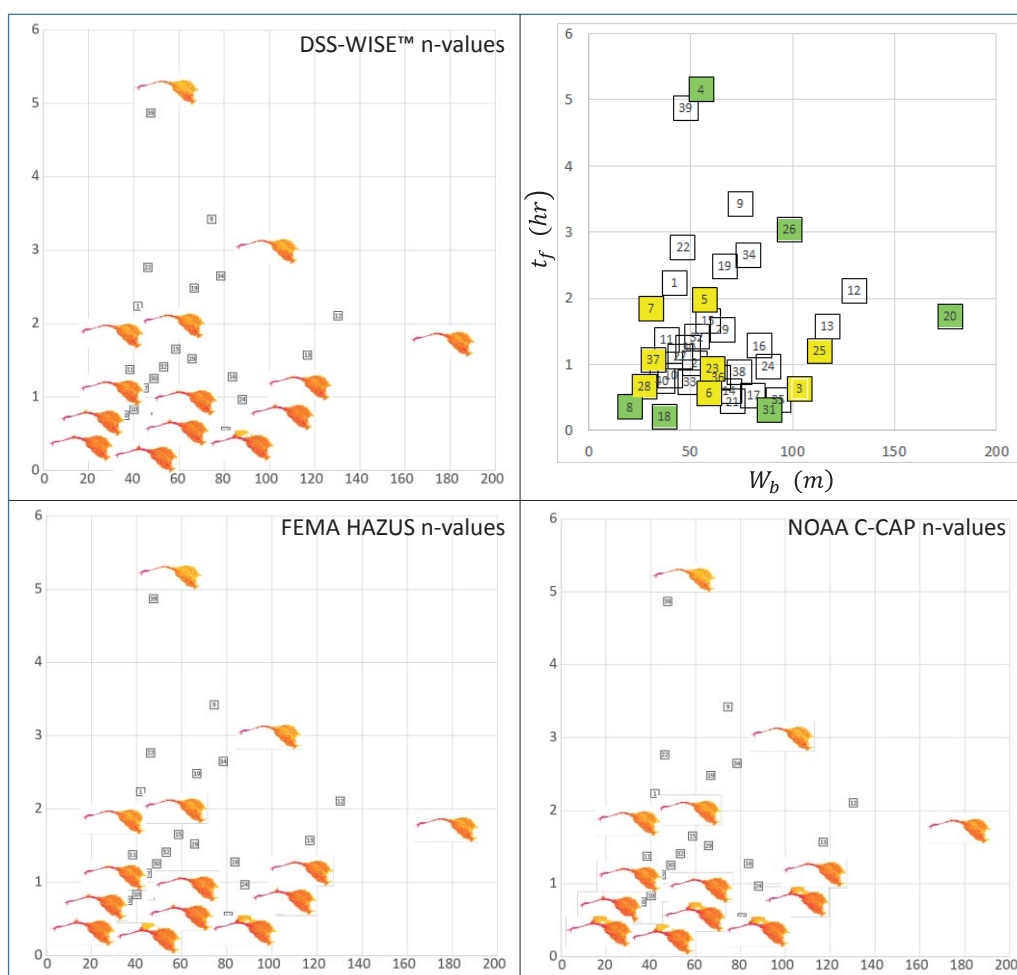
Figure 9: Comparison of flood depth maps for selected simulations.
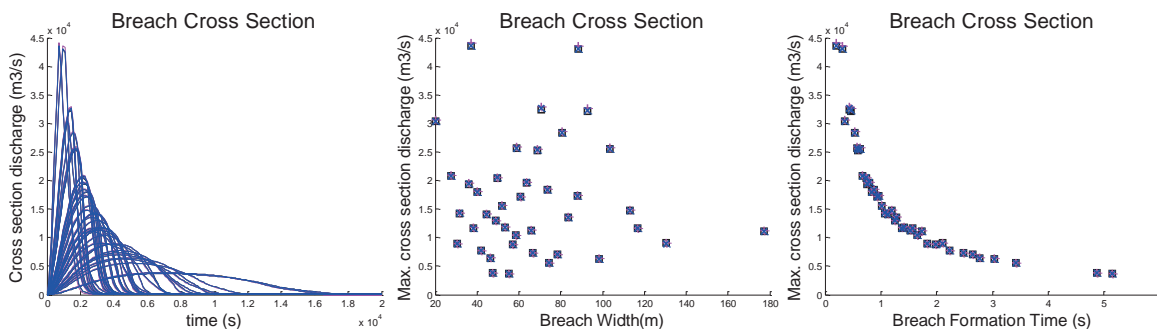
Figure 10: Discharge hydrographs and the peak discharge at the breach cross section (DSS-WISE: black squares, FEMA HAZUS: red "plus" signs, and NOAA C-CAP: blue crosses).
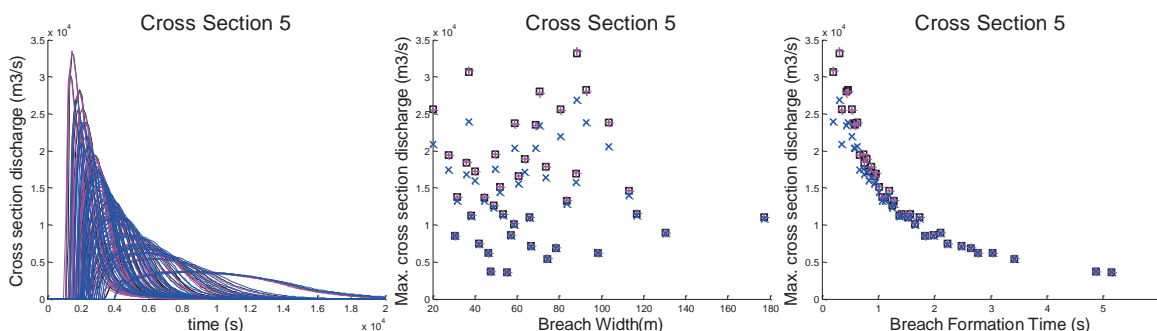
Figure 11: Discharge hydrographs and the peak discharge at cross section 5 (DSS-WISE: black squares, FEMA HAZUS: red "plus" signs, and NOAA C-CAP: blue crosses).

Consequence Analysis

In the present study the consequence analyses were restricted to the analysis of population at risk (by age group) to be affected by flood based on flood arrival time and peak discharges per unit width. Direct or indirect economic analyses were not performed.

Population by Census Block and PAR Distribution

Census block polygons for Hydropolis, colored by total population, are shown in Figure 12. Other polygon attributes include population by age and gender group and jobs in 20 different classes. The loss of life analysis in the present study was based only on total population. The map of population at risk per computational cell shown in Figure 13 was computed by assuming a uniform distribution of population in each census block. As it can be seen, there are two major urban areas (see also Figure 2). The urban area on the west is located in the narrow valley downstream of the dam and directly on the path of the flow. The urban area on the north east corner of the map is farther from the dam and located on a relatively flat area.
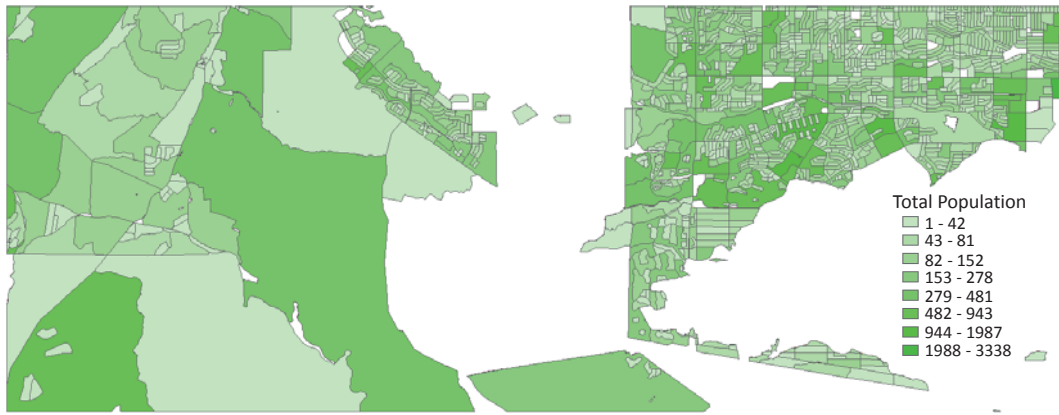
Figure 12: Total population by census block (only census blocks with population are shown).

PAR Analysis

The number of PAR by age group for each one of the 120 simulations were counted for 7 flood arrival-time intervals and for 17 depth intervals and recorded in tables.

shows the average value, standard deviation, minimum and maximum values of PAR numbers by arrival time interval. Some of the information listed in

is summarized in Figure 14. The plot on the right hand side of Figure 14 shows that the range between cumulative values of minimum and maximum PAR can be significant. Final minimum and maximum cumulative PAR values correspond to 4.4% of 268% of the final average cumulative PAR.

Figure 13: PAR distribution per computational cell (10m×10m).

Table 4: Statistics of PAR numbers by age group and flood arrival time interval.

Age	Value	0-15min	15-30min	30-60min	60-90min	90-120min	120-180min	>180min
Total PAR	Average	0.186	12.782	38.370	75.021	65.333	54.556	14.201
	St. Dev.	0.548	14.597	28.768	47.800	25.632	39.032	26.624
	Min.	0.043	0.019	8.566	1.110	0.532	1.210	0.087
	Max.	5.110	52.346	144.341	148.087	95.128	119.794	132.010
PAR ≤ 14	Average	0.035	3.296	7.584	10.381	9.437	7.987	2.037
	St. Dev.	0.147	3.802	3.101	6.789	4.100	6.049	4.041
	Min.	0.006	0.002	2.014	0.286	0.140	0.157	0.010
	Max.	1.286	13.409	19.903	21.096	14.424	18.265	20.306
14<PAR < 65	Average	0.129	8.623	25.142	48.743	42.874	35.977	9.376
	St. Dev.	-	-	-	-	-	-	-
	Min.	0.031	0.014	5.926	0.746	0.346	0.853	0.061
	Max.	3.507	35.341	93.943	96.662	59.286	77.542	87.380
PAR ≥ 65	Average	0.021	0.862	5.644	15.898	13.022	10.592	2.789
	St. Dev.	0.030	0.986	7.590	10.011	4.963	7.275	4.983
	Min.	0.007	0.004	0.625	0.078	0.046	0.200	0.016
	Max.	0.317	3.597	30.495	30.329	21.418	23.987	24.324
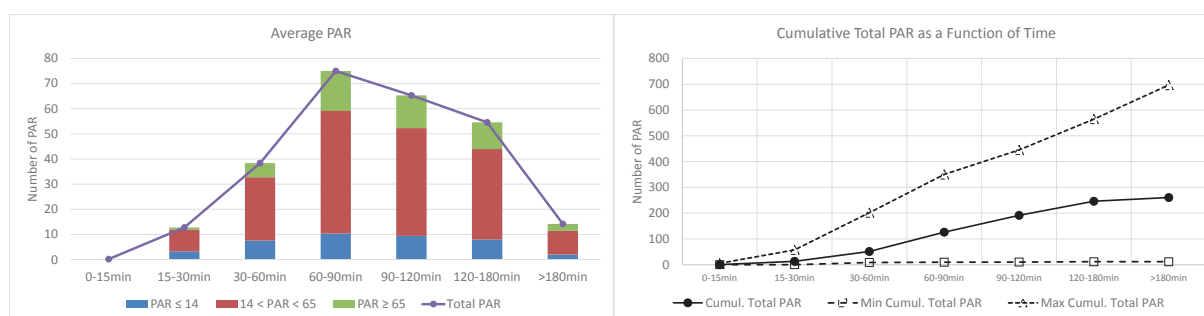
Figure 14: (Left) Average PAR by age group and by arrival time; (Right) Cumulative values of average, minimum and maximum total PAR impacted by the flood as a function of time.

and Table 6 show the average value, standard deviation, minimum and maximum values of PAR numbers by flood depth interval in two separate tables. Some of the PAR information listed in Table 5 and Table 6 is summarized in Figure 14. The plot on the right hand side of Figure 14 shows that the range between cumulative values of minimum and maximum PAR can be significant. This figure shows that majority of PAR impacted by the flood (93.5%) will be subjected to a maximum flood depth of 3.5m. The range between minimum and maximum PAR values is significant. The largest differences are observed for the depth interval 0.0-0.5m. Minimum (98.6% PAR in less than 3.5m depth) and maximum (87.8% PAR in less than 3.5m depth) PAR both show the same tendency as the average PAR. The average, minimum and maximum values of the inundated area listed in Table 5 and Table 6 are plotted in Figure 16 as a function of flow depth. As it can be seen most of the inundated area (95.1%) will be subjected to water depths less than or equal to 5m. The largest differences between minimum and maximum values occur for the depth interval 0.0-0.5m.

Table 5: Average and standard values of PAR numbers by age group and depth interval.

Depth (m)	Total PAR		PAR $\leq$ 14		14 < PAR < 65		PAR $\geq$ 65		Inundated Area (m2)	
	Min	Max	Min	Max	Min	Max	Min	Max	Min	Max
0.0m-0.5m	55.53	19.25	8.21	2.91	37.03	-	10.29	3.48	7,333,416	3,206,673
0.5m-1.0m	73.38	15.41	11.10	2.16	48.74	-	13.54	3.29	9,018,780	1,693,804
1.0m-1.5m	67.36	23.75	9.97	3.68	44.20	-	13.19	4.05	8,709,363	1,270,547
1.5m-2.0m	26.36	12.31	3.63	1.83	16.67	-	6.06	2.33	5,856,884	1,471,850
2.0m-2.5m	10.30	4.18	1.37	0.43	6.23	-	2.70	1.27	3,358,918	1,008,449
2.5m-3.0m	4.65	0.87	0.81	0.15	2.83	-	1.01	0.41	2,018,934	709,981
3.0m-3.5m	3.23	0.47	0.67	0.19	2.02	-	0.54	0.24	1,453,657	533,611
3.5m-4.0m	2.57	0.67	0.62	0.20	1.67	-	0.28	0.14	1,337,561	659,157
4.0m-4.5m	2.24	0.83	0.58	0.21	1.50	-	0.16	0.06	674,860	362,878
4.5m-5.0m	2.18	0.85	0.56	0.21	1.46	-	0.16	0.07	325,181	106,113
5.0m-5.5m	2.02	0.90	0.52	0.23	1.35	-	0.15	0.07	260,150	95,178
5.5m-6.0m	1.81	0.95	0.46	0.24	1.22	-	0.13	0.08	218,419	85,614
6.0m-6.5m	1.63	1.08	0.41	0.27	1.10	-	0.12	0.09	185,084	79,717
6.5m-7.0m	1.41	1.09	0.36	0.27	0.95	-	0.10	0.09	161,414	73,249
7.0m-7.5m	1.17	1.06	0.30	0.27	0.79	-	0.08	0.08	137,548	63,610
7.5m-8.0m	1.03	1.13	0.26	0.28	0.70	-	0.08	0.09	119,563	57,089
>8.0m	3.55	4.92	0.92	1.21	2.40	-	0.23	0.36	2,226,929	550,383

Table 6: Minimum and maximum values of PAR numbers by age group and depth interval.

Depth (m)	Total PAR		PAR $\leq$ 14		14 < PAR < 65		PAR $\geq$ 65		Inundated Area (m2)	
	Min	Max	Min	Max	Min	Max	Min	Max	Min	Max
0.0m-0.5m	38.76	134.98	5.33	20.13	25.84	89.84	7.59	25.01	3,502,773	17,674,779
0.5m-1.0m	49.03	102.42	7.00	15.17	33.25	67.26	8.78	19.99	6,067,713	11,718,682
1.0m-1.5m	12.73	92.40	2.05	14.09	7.80	61.01	2.88	17.30	4,253,739	10,358,269
1.5m-2.0m	7.50	45.04	1.32	6.95	4.98	29.01	1.20	9.09	2,131,314	7,690,691
2.0m-2.5m	3.93	19.90	0.80	2.95	2.82	12.39	0.30	4.56	740,011	5,280,020
2.5m-3.0m	2.59	7.23	0.54	1.09	1.84	4.38	0.21	1.76	422,222	3,035,832
3.0m-3.5m	1.25	4.61	0.30	1.15	0.85	2.59	0.10	0.87	447,365	2,560,271
3.5m-4.0m	0.67	3.63	0.16	0.93	0.46	2.08	0.05	0.62	171,062	2,481,161
4.0m-4.5m	0.29	4.16	0.07	1.02	0.20	2.78	0.02	0.36	95,543	1,333,115
4.5m-5.0m	0.28	4.03	0.08	1.00	0.19	2.70	0.01	0.33	78,662	521,537
5.0m-5.5m	0.23	3.65	0.07	0.93	0.16	2.42	0.01	0.31	73,453	442,965
5.5m-6.0m	0.17	3.69	0.06	0.91	0.11	2.45	0.00	0.33	74,621	418,002
6.0m-6.5m	0.02	4.07	0.01	1.01	0.01	2.71	0.00	0.35	66,539	330,630
6.5m-7.0m	0.00	4.05	0.00	1.00	0.00	2.70	0.00	0.35	59,984	298,393
7.0m-7.5m	0.00	4.10	0.00	1.02	0.00	2.72	0.00	0.35	44,808	276,752
7.5m-8.0m	0.00	4.26	0.00	1.05	0.00	2.84	0.00	0.36	39,151	277,381
>8.0m	0.02	20.47	0.00	5.10	0.01	13.92	0.00	1.44	1,409,981	3,827,117

Loss of Life Analysis

The loss of life is computed using the U.S. Bureau of Reclamation DSO-99-06 Procedure (Graham, 1999). In this method, the fatality rate of PAR in a given area, which in the case of a two dimensional numerical simulation can be taken as the computational cell, is computed from Table 6 based on three parameters: flood severity, warning time, and flood severity understanding. Warning time can be computed as the time difference between the time the warning issued and the arrival time of the flood. Flood severity understanding is a parameters that must be appreciated based on the characteristics of the population in the inundation area. Since in the benchmark test case it is assumed that the population cannot be warned, the flood severity understanding is no longer applicable, and Table 6 reduces to the three highlighted lines. There are no clear guidelines for estimating flood severity. In the present study, the flood severity was computed based on maximum specific discharge, q_{max}, which is equal to the product of depth and flow speed. The limits of high, medium, and low flood severity

shown in Table 7 are taken from guidelines published by the U.S. Department of Homeland Security (DHS, 2011).
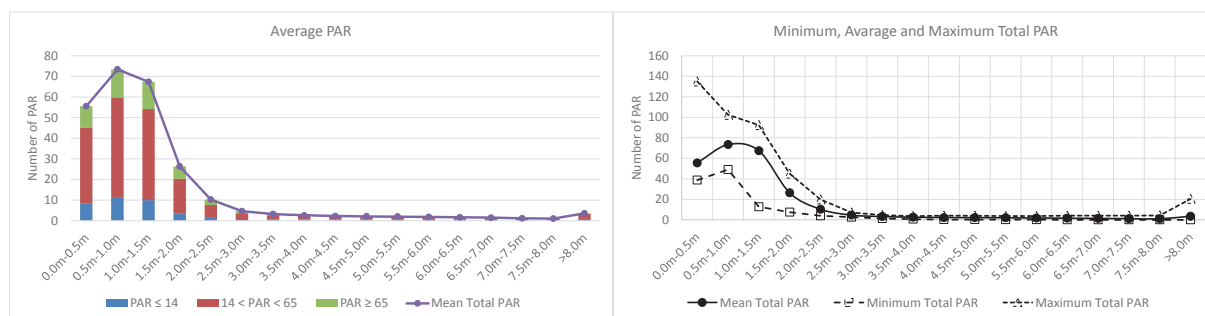
Figure 15: (Left) Average PAR by age group and by flood depth; (Right) Average, minimum and maximum total PAR impacted by the flood as a function of depth.
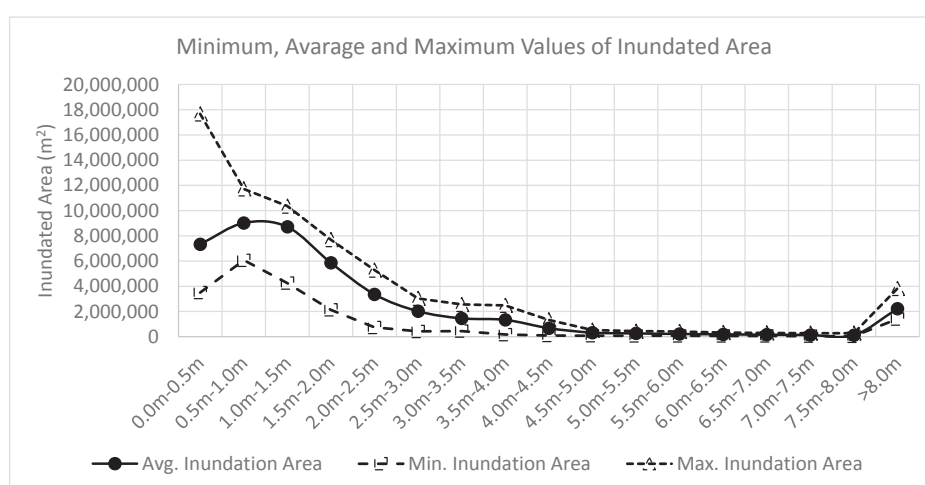
Figure 16: Average, minimum and maximum values of inundated area as a function of depth.

Based on the flood severity criteria given in Table 8 and the fatality rates in Table 7, the loss-of-life (LOL) maps for each simulation was established using the corresponding q_{max} raster. The average value, standard deviation, and minimum and maximum values of loss of life for each computational cell were then computed from 120 loss-of-life maps. Figure 17 shows the average value, standard deviation, minimum and maximum values of estimated loss of life (LOL) based on 120 simulations. As expected, the largest loss of life numbers are observed in the western urban area located in the narrow valley. This area is closer to the dam and directly on the path of the dam-break flood. The q_{max} values are much larger. The urban area on the north eastern corner of the map has relatively small values of LOL due to lower values of q_{max}. It is important to note that the areas with no loss of life and with zero standard deviation are not displayed. Looking at the standard deviation map, one can observe that there are areas with zero standard deviation. These areas can be regarded as areas where the LOL has highest likelihood.

Table 7: Fatality rates for loss-of-life estimation from dam failure (Graham, 1999).

Flood Severity	Warning Time (Minutes)	Flood Severity Understanding	Fatality Rate (Fraction of PAR projected to die)	
			Suggested Value	Suggested Range
HIGH		Not applicable	0.75	0.30 – 1.00
	15 to 60	Vague	Apply the values shown above to the PAR values who remain in the dam failure floodplain after warnings are issued. No guidance is provided on how many people will remain in the flood plain.	
		Precise		
	More than 60	Vague		
		Precise		
MEDIUM		Not applicable	0.15	0.03 – 0.35
	15 to 60	Vague	0.04	0.01 – 0.08
		Precise	0.02	0.005 – 0.04
	More than 60	Vague	0.03	0.005 – 0.06
		Precise	0.01	0.002 – 0.02
LOW		Not applicable	0.01	0.0 – 0.02
	15 to 60	Vague	0.007	0.0 – 0.015
		Precise	0.002	0.0 – 0.004
	More than 60	Vague	0.0003	0.0 – 0.0006
		Precise	0.0002	0.0 – 0.0004

Table 8: Flood severity criteria used for loss of life analysis.

Flood severity	Criteria in SI Units	Criteria in US Customary Units
LOW	$0 < q_{max} \leq 4.65\ m^2/s$	$0 < q_{max} \leq 50\ ft^2/s$
MEDIUM	$4.65\ m^2/s < q_{max} \leq 14.86\ m^2/s$	$50\ ft^2/s < q_{max} \leq 160\ ft^2/s$
HIGH	$q_{max} > 14.86\ m^2/s$	$q_{max} > 160\ ft^2/s$
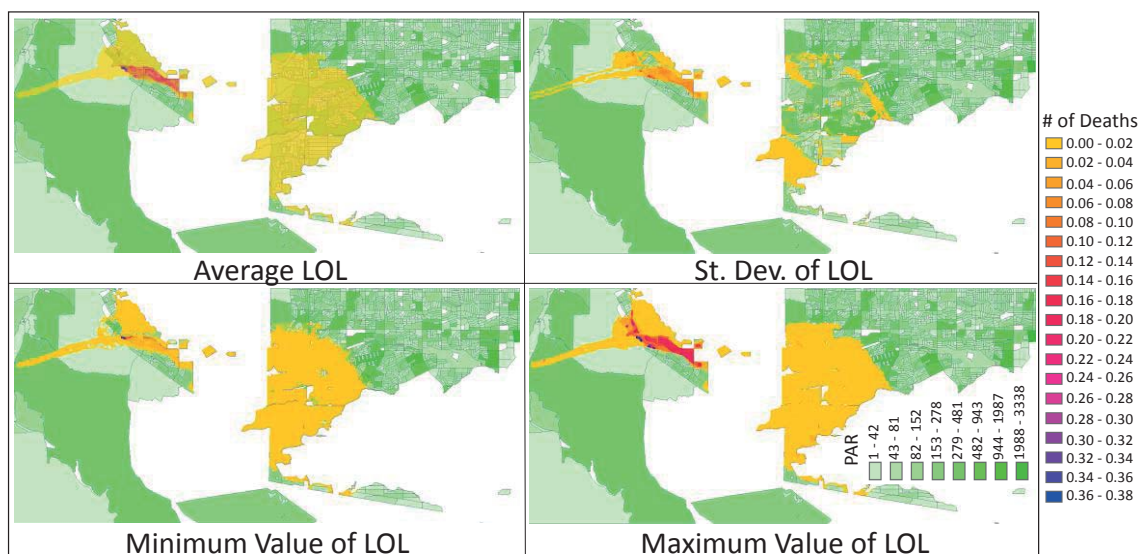
Figure 17: Average value, standard deviation, minimum and maximum values of estimated loss of life (LOL) based on 120 simulations.

Conclusion

The uncertainty in 2D numerical modeling of dam-break flood and the resulting loss of life were studied using 120 simulations representing 40 random pairs of breach width and breach formation time calculated with three different sets of Manning's coefficients. The results show that large variations in the extent of the inundated area, water depths, and loss-of-life occur based on the particular combination of control parameters. The paper presents the average value and standard deviation of selected computed results as well as their upper and lower bounds. Peak discharge at the breach cross section and the cross sections downstream seem to be highly correlated with the breach formation time rather than the breach width.

Only part of the results could be presented. Additional findings will be presented in subsequent publications.

Acknowledgements

References

[1]   Altinakar, M.S., McGrath, M.Z., Yucel, O., and Ger, M. (2013a). Simulation of Super-critical Flow in an Open Channel Bend Using Cut-Cell Boundary Method. 6th Int. Perspective on Water Res. and Env. (IPWE 2013), January 7-9, 2013, Izmir Turkey.

[2]   Altinakar, M.S., McGrath, M.Z., Ramalingam, V.P., Strati, O. (2013b). Dam Break Flood Simulation – Doing It Faster and Simpler: DSS-WISE™, DSS-WISE™ Lite, and DSAT. 1-day Short Course, ASDSO West Regional Conf., May 8, 2013, Seattle, Washington.

[3]   Altinakar, M.S. (2012). Advances in Numerical Modeling and Simulation of Floods, Inundation Mapping and Consequence Analysis. Keynote Lecture presented at the 10th International Congress on Advances in Civil Engineering (ACE 2012), October 17-19, 2012, Middle East Technical University (METU), Ankara, Turkey.

[4]   Altinakar, M.S., McGrath, M.Z., Matheu, E.E., Ramalingam, V.P., Seda-Sanabria, Y. Breitkreutz, W., Oktay, S., Zou, J.Z., Yezierski, M. (2012): Validation of Automated Dam-Break Flood Simulation and Assessment of Computational Performance, Proc. Dam Safety 2012, September 16-20, Denver, Colorado.

[5]   Altinakar, M.S. and McGrath, M.Z. (2012). Parallelized Two-Dimensional Dam-Break Flood Analysis with Dynamic Data Structures. ASCE-EWRI, 2012 World Environmental & Water Resources Congress, May 20-24, 2012, Albuquerque, New Mexico.

[6]   ARCADIS (2011). ADCIRC Based Storm Surge Analysis of Sea Level Rise in the Galveston Bay and Jefferson County Area in Texas. Report prepared for The Nature Conservancy, Nov 28, 2011.

[7]   DHS (2011). Estimating Loss of Life for Dam Failure Scenarios. U.S. Department of Homeland Security, September 2011. Washington DC.

[8]   Froehlich, D.C. (1995a). Embankment Dam Breach Parameters Revisited. Water Res. Engineering, Proc. 1995 ASCE Conf. on Water Res. Eng., New York, pp. 887-891.

[9]   Graham, Wayne J. (1999). A Procedure for Estimating Loss of Life Caused by Dam Failure. DSO-99-06, U.S. Bureau of Reclamation, Denver, Colorado, September 1999.

[10] Iman, R.L.; Helton, J.C.; and Campbell, J.E. (1981). An Approach to Sensitivity Analysis of Computer Models, Part 1. Introduction, Input Variable Selection and Preliminary Variable Assessment. Journal of Quality Technology, Vol. 13, No. 3, pp. 174–183.

[11] Kim, D.-H., Cho, Y.-S., and Yi, Y.-K. (2007). Propagation and Run-up of Nearshore Tsunamis with HLLC Approximate Riemann Solver. Ocean Engineering, Volume 34, Issues 8-9, June 2007, pp. 1164-1173.

[12] Luettich, R. and Westerink, J. Storm Surge Inundation Modeling: State of Science. Hurricane Surge Workshop, February 11, 2009, St. Petesburg, Florida

[13] Toro, E. F., Spruce, M., Speares, W. (1994). Restoration of the Contact Surface in the HLL-Riemann Solver. Shock Waves, Vol. 4, No. 1, pp. 25-34.

[14] Wahl, T.L. (2004). Uncertainty of Predictions of Embankment Dam Breach Parameters. Journal of Hydraulic Engineering, Vol. 130, No. 5, pp. 389-397.

Risk assessment for hypothetical dam break
A method for the rapid and consistent evaluation

L.Mancusi[1], L.Giosa[2], A.Cantisani[2], A.Sole[2] and R.Albano[2]

[1] Sustainable Development and Energy Resources Department, Research on Energy Systems (RSE) Spa, via R. Rubattino 54, 20134 Milano, Italy

[2] School of Engineering, University of Basilicata, viale dell'Ateneo Lucano 10, 85100 Potenza, Italy

E-mail: leonardo.mancusi@rse-web.it

Abstract

This paper details the technical contribution to the theme of flood risk analysis as consequence of a dam failure. According to the numerical problem proposed for the workshop, the analysis consists of the evaluation of the dam break and its consequences. The simulation includes two scenarios of dam breach: the scenario 1 that represents the case of an easy erodible dam and the scenario 2 the case of an erosion resistant dam. For each scenario, a dam failure discharge hydrograph was calculated and the subsequent flood wave and consequences have been evaluated.

The methodology adopted involves, for a first part, the use of standard models for the hydraulic modelling of the dam breach and flood wave propagation. For the second part, a set of GIS scripts was written, tested and developed using the python scripting language to obtain a rapid appraisal of consequences for the population and to assess the direct economic damages for residential, commercial, and industrial buildings.

Since the latter elaboration depends greatly on the type and the level of detail of available data, in this study we have been used data as generic as possible and GIS scripts that allow, for a great variety of cases, a rapid initial assessment.

Introduction

Modern society considers it essential to increase the safety of the infrastructure. Risk analysis is a helpful tool for the evaluation and management of risks which can affect people, environment and human development. The purpose of this paper was to demonstrate the application of an example of quantitative risk assessment technique that consists of estimating the consequences of failure of a dam near populated areas with complex demographics, infrastructure and economic activity.

The first chapter concerns the hydraulic modelling and simulation of the dam breach, the second the subsequent flood wave propagation and the last focuses on consequence estimation.

Dam failure

This section includes the description of modelling of the breaching process and the subsequent discharge hydrograph for the hypothetical overtopping of the dam.

Two methods have been adopted and the results are named respectively scenario 1 and 2.

Scenario 1

In this case were used, a statistical method available in the literature for the dam failure peak-discharge estimation of and a physically based mathematical model for calculating the total discharge hydrograph.

P. Molinaro [1] utilised 31 data sets (predominantly earthfill and some rockfill) extracted from the report of J. E. Costa [2] to develop a relationship from the peak-discharge, the height of dam and the reservoir volume at time of failure.

$$\frac{Q_{max}}{\sqrt{g}H^{5/2}} = 0.116\left(\frac{V}{H^3}\right)^{0.221} \tag{1}$$

Where:
Qmax = peak-discharge (m^3/s)
g = gravity of Earth that has an approximate value of 9.81 m/s^2
H = height of the dam (m)
V = volume of water at breach time (m^3)

Applying the formula (1) for this case (H=61 m and V=30.3*10^6 m^3) we obtain:
$$Q_{max} = 32800 \ m^3/s$$

The latter value was used to calibrate parameters of the mathematical model.

The mathematical model was developed by Molinaro [3] and simulates the breach development process through an earthen dam due to overtopping.

The model is developed by coupling the conservation of mass of the reservoir inflow, spillway outflow, and breach outflow with the sediment transport capacity of the quasi-steady uniform flow along an erosion-formed breach channel. The rate at which the breach is eroded is evaluated using the Engelund and Hansen [4] sediment transport relation.

The dam is modeled as an isosceles triangle formed by a noncohesive material of uniform diameter D. The storage characteristics of the reservoir are described by specifying a table of volume vs. water elevation.

The overtopping failure simulation starts by assigning a small initial breach whose bottom elevation must be below the reservoir water level. The first stages of erosion are along the downstream face of the dam while the breach bottom erodes vertically downward. An erosion triangular channel is gradually cut into the downstream face of the dam. The sides of the breach channel has a constant angle (α) with the vertical which is a function of the internal friction (φ) of dam's material. The flow into the channel is determined by the broad-crested triangular weir relationship.

The breach bottom is allowed to progress downward until it reaches the bottom elevation of the dam, subsequently the channel becomes trapezoidal with the sides that maintain the same slope α of the previous triangle.

The following figure Figure 1 shows the sequence of the simulation of the breach formation.
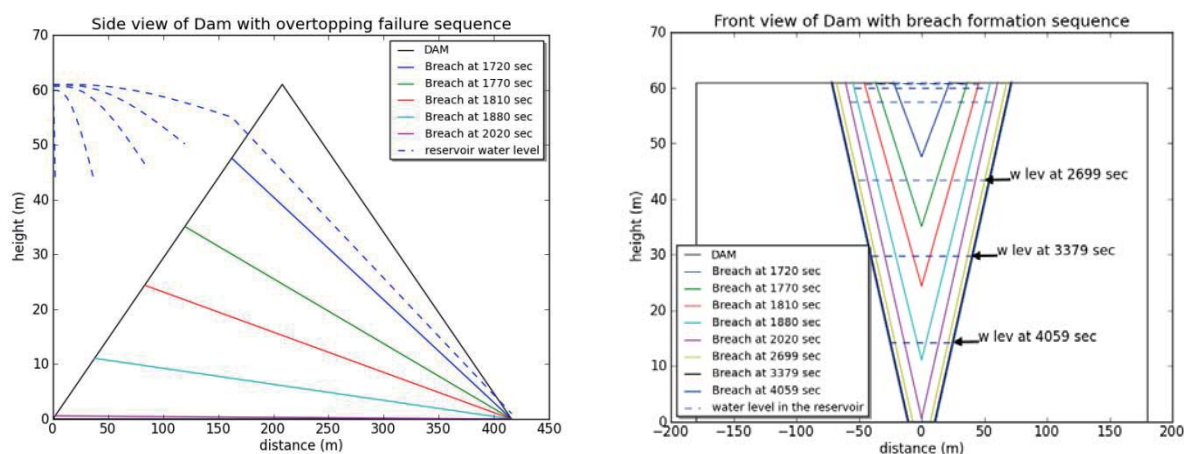
Figure 1: Breach formation sequence

The most important parameter for model calibration is the characteristic diameter D. In this case, taking into account the result of the equation 1, we have adopted the value D = 0.01 m. The discharge hydrograph obtained is shown in the Figure 3.

This hydrograph was used for the first propagation of a flood wave referred to the next chapter. It is characterized by Q_{max} =28936 m³/s and a breach formation time of 2040 sec (0.57 hrs).

Scenario 2

In addition to the above, a second method was applied for the evaluation of failure discharge hydrograph. Even in this case a regression equations was used for the estimation of dam breach parameters, and then a mathematical model was applied.

Table 1 summarizes the resulting breach parameters (*Wb*: bottom width of the breach and *tf*: breach formation time) computed by several approaches available in the literature.

Table 1: Breach Parameters

Method	Wb (m)	tf (hrs)
MacDonald and Langridge - Monopolis (1984)	167	1.99
Floehlich (1995a)	147	0.66
Floehlich (2008)	110	0.57
Von Thun and Gillette (1990)	207	1.47

In the last column you can see that the breach formation time ranges from 0.57 to 2 hours. As in scenario 1 the resulting time corresponds with the minimum, then for this scenario the case of the maximum value of tf=2 hours was investigated.

For performing the dam breach outflow hydrograph computation, HEC-RAS model was adopted. The implementation of these breach parameters in the HEC-RAS modelling system is depicted on Figure 2. The resulting discharge hydrograph compared to the previous scenario is depicted in Figure 3. As can be seen in the latter figure, the second hydrograph, having the same volume, is characterized by a peak value cut in half compared to the first, but a duration in time approximately double.

For further analysis, we can consider the two hydrographs: the first as representing of a easy erodible dam and the second an erosion resistant dam.
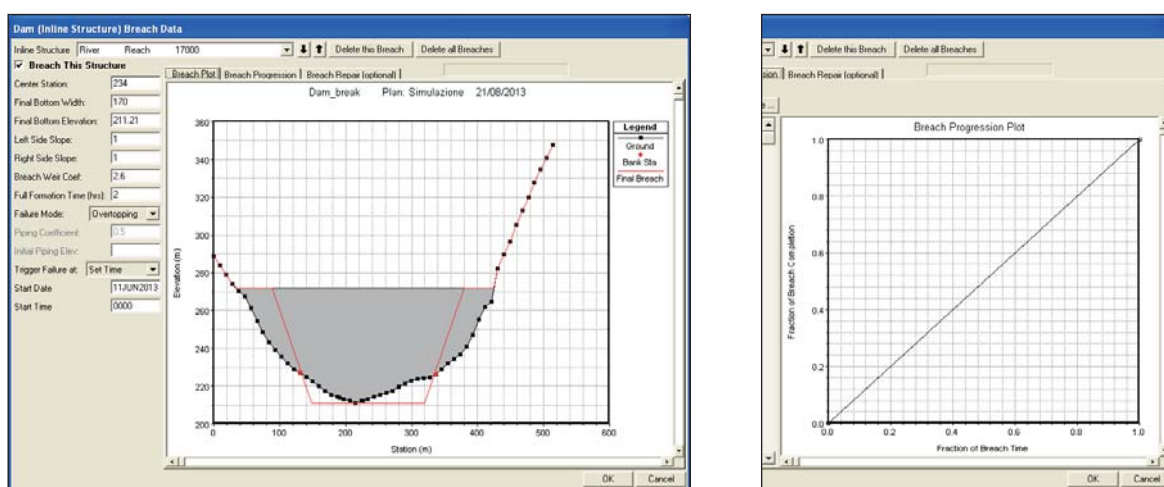
Figure 2: HEC-RAS Dam Breach Model of scenario 2

Dam Failure discharge hydrographs for scenario 1 and 2
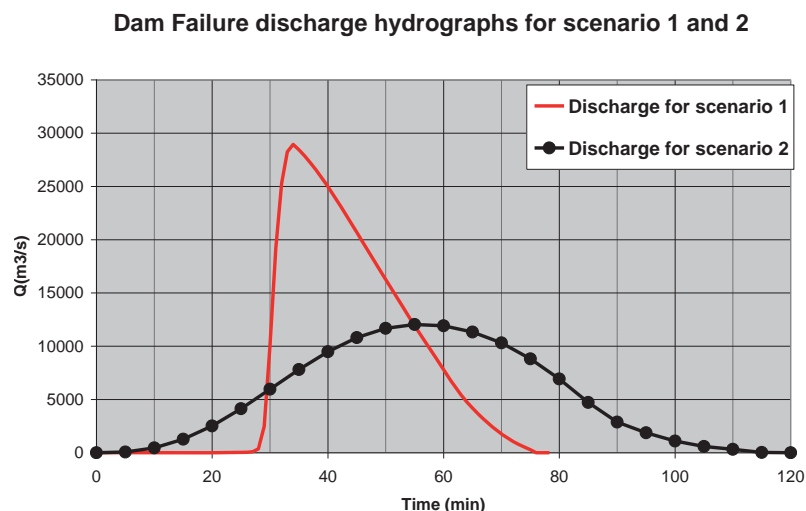
Figure 3: Discharge hydrograph of scenario 2 compared with scenario 1

Flood simulation

Hydraulic modelling has carried out using the MIKE 21 software by the DHI Water Environment Health to simulate flood wave propagation in the river and to describe the inundation on the floodplain. This software solves the shallow water equations by means of a finite difference scheme. For each scenario, the simulation has been constructed using, as upstream boundary condition, the corresponding discharge hydrograph for the hypothetical overtopping of the dam.

According to Bunya et al. [5], the Manning n coefficient is spatially assigned associating the value of n with the land cover definition of 2001 from the USGS National Land Cover Data (NLCD) (Table 2), These values are selected or interpolated from standard hydraulic literature.

Table 2: Manning n value for 2001 NLCD classification

Lu Code	Description	n Mann. $(s/m^{1/3})$	Lu Code	Description	n Mann. $(s/m^{1/3})$
11	Open Water	0.020	42	Evergreen Forest	0.180
12	Perennial Ice/Snow	0.022	43	Mixed Forest	0.170
21	Developed-Open Space	0.050	52	Shrub/Scrub	0.070
22	Developed-Low Intensity	0.120	71	Grassland/Herbaceous	0.035
23	Developed-Med Intensity	0.120	81	Pasture/Hay	0.033
24	Developed-Hight Intensity	0.121	82	Cultivated Cropland	0.040
31	Barren Land	0.040	90	Woody Wetlands	0.140
41	Deciduous Forest	0.160	95	Herbaceous Wetlands	0.035

The results of flood modelling consist of values, for each grid cell in the study area, depth (m) and the two components of the vector unit flow rate (m²/s) for 15 minute intervals and the envelope of their maximum. Using a GIS scripts, hydrographs flow at different cross sections were extracted. Some of these are shown in Figure 4.

**Comparison of hydrographs of the two scenarios
at different cross sections**
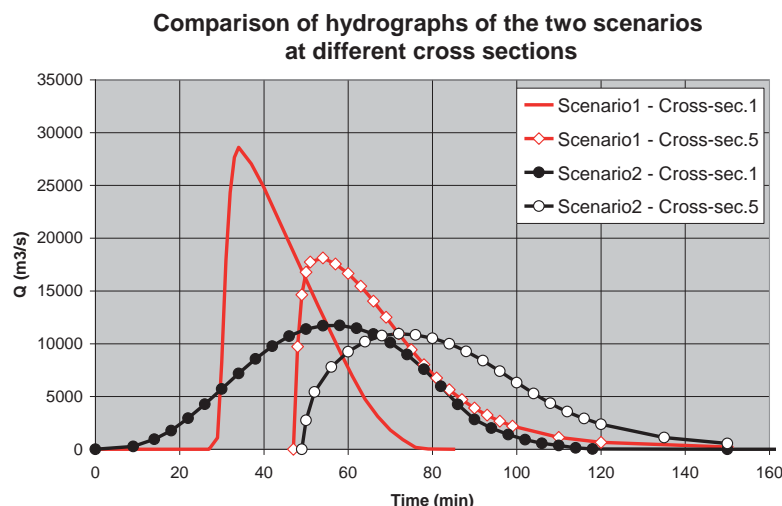
Figure 4: Discharge hydrographs of the two scenarios at different cross sections

Comparing the hydrographs of two scenarios in different cross sections we may note that: while having at the initial cross-section a large difference in peak flow rate, however, during the process of propagation downstream, an attenuation of the difference occurs.

Impacts assessment

The potential risks associated with the failure or disruption of dams could be considerable and potentially result in significant destruction, including loss of life, massive property damage, and severe long-term consequences. The following sections contain the analysis of two categories: public safety and direct economic impact.

Population at Risk and Loss of Life estimation
The analyzes described in this section have been carried out by adopting the published guidelines of the report [6] that provides guidelines and recommendations for estimating loss of life resulting from dam failure or disruption.
The results of flood modelling and the data from the population census are used. Geographic analyzes were carried out using Map Algebra techniques implemented in a set of scripts written, tested and developed using the python scripting language and the Open Sources GDAL libraries and NumPy Python module. To combine multiple maps in Map Algebra all data have been converted into grid format.
The outputs of the hydrodynamic model have been processed to derive the information required for the analysis. Using a GIS scripts, a **Flood Wave Arrival Time** grid was obtained, in addition the two components of the vector unit flow rate are combined to obtain the maximum **Peak Unit Flow Rate** values (m^2/s). These values, called parameter DV, are representative of the general level of destructiveness that would be caused by the flooding. The DV values are then categorized, as suggested in the Figure 5 extracted from guidelines, into ranges of values which define low, medium, and high severity zones.

Table 8. Flood Severity Rating Criteria for Use with 2D Modeling Output (Source: LSM Users Guide)

Flood Severity Rating	Rating Criteria
Low	DV less than 50 ft²/s
Medium	DV equal to or greater than 50 ft²/s and less than 160 ft²/s
High	DV equal to or greater than 160 ft²/s combined with rate of rise of at least 10 feet in 5 minutes

Figure 5: Flood severity rating criteria reported in the guidelines

The vector polygons of the population census block were converted into grid format: the hypothesis assumed for the different values of the fields is that their distribution within the polygon is homogeneous.

By overlaying grid maps of flood with the grid of the population is achieved as a result the map of Population at Risk (PAR).

The estimate of loss of life is finally obtained by multiplying the PAR with the Fatality Rate (Fraction of people at risk projected to die).

The latter was obtained by using the values of the Table 3 (from tab. 4 of guidelines) as a function of warning time and flood severity.

Table 4 shows the results for the two scenarios for the hypothesis of event occurred at night (understanding=vague). In the case of the first scenario, there is a population at risk greater than 11 percent, while the estimate of the largest loss of life is almost 30 percent. The last result is mainly caused by the shorter warning time of the first scenario.

It should be noted that in each case that the differences in terms of the consequences are less than the differences of the peak discharge of the two scenarios at the breach of the dam, . This result is due to the fact that the volume released from the dam is still the same.

Table 3: Recommended Fatality Rates for Estimating Loss
of Life as reported in the guidelines

Flood Severity	Warning Time (min)	Understanding	Fatality Rate
HIGHT	Not applicable	Not applicable	0.75
MEDIUM	No warning	Not applicable	0.15
	15 to 60	Vague	0.04
		Precise	0.02
	More then 60	Vague	0.03
		Precise	0.01
LOW	No warning	Not applicable	0.01
	15 to 60	Vague	0.007
		Precise	0.002
	More then 60	Vague	0.0003
		Precise	0.0002

Table 4: Population at Risk and Loss of Life estimation

Time Interval (min)	Total Population At Risk		14-yr and Under Population at Risk		65-yr and Over Population at Risk		Loss of Life	
	Scen. 1	Scen. 2	Scen. 1	Scen. 2	Scen. 1	Scen. 2	Scen. 1	Scen. 2
0-15	0	3	0	0	0	0	0	2
15-30	2	4	0	0	0	1	2	2
30-60	4 529	2 794	1 169	732	308	196	1 783	1 262
60-90	5 111	641	721	110	1 057	105	2	0
90-120	10 411	8 529	1 491	1 084	2 163	1 996	0	0
120-180	8 935	12 346	1 350	1 899	1 662	2 290	0	0
>180	688	1 911	85	265	121	360	0	0
Total	**29 676**	**26 228**	**4 816**	**4 090**	**5 311**	**4 948**	**1 787**	**1 266**

Peak Flood Depth Range (m)	Flooded Area (m^2)		Total Population At Risk		14-yr and Under Population at Risk		65-yr and Over Population at Risk	
	Scen. 1	Scen. 2	Scen. 1	Scen. 2	Scen. 1	Scen. 2	Scen. 1	Scen. 2
0.0-0.5	8 308 132	4 088 784	5 854	4 825	915	706	1 017	937
0.5-1.0	6 025 869	7 190 976	5 683	6 770	895	1 021	987	1 237
1.0-1.5	7 854 660	7 858 701	8 937	7 769	1 373	1 164	1 664	1 453
1.5-2.0	5 612 806	5 141 466	3 768	2 879	543	391	781	676
2.0-2.5	3 711 550	2 970 641	1 562	1 038	197	118	404	304
2.5-3.0	2 547 251	1 901 885	510	380	72	60	137	98
3.0-3.5	1 746 448	1 453 532	274	292	43	49	68	70
3.5-4.0	1 279 417	711 995	209	220	37	53	49	28
4.0-4.5	546 680	392 859	125	228	35	62	8	17
4.5-5.0	391 332	310 246	153	237	43	65	11	17

5.0-5.5	380 736	209 944	211	216	57	54	15	13
5.5-6.0	242 630	250 352	190	271	51	67	15	16
6.0-6.5	201 323	294 532	194	346	53	90	14	25
6.5-7.0	192 882	221 527	162	337	44	83	9	30
7.0-7.5	176 180	128 947	176	154	44	37	11	11
7.5-8.0	186 417	101 919	254	84	61	18	16	7
>8	1 880 693	850 640	1 414	182	353	52	104	9
Total	**41 285 006**	**34 078 946**	**29 676**	**26 228**	**4 816**	**4 090**	**5 311**	**4 948**

Direct Economic Impact estimation

Methods and values of the parameters used in this section are drawn mostly from the report [7]. They concern the assessment of the direct economic damages for residential, commercial, and industrial buildings. The input data consist of map of land use and parcel zone map of the study area. As in the previous paragraph, for the analysis, all the data are preliminarily converted into grid format.

The following assessments do not take into account Agricultural, Roads, Infrastructure and Vehicles damages. The assessment however allows the estimation of the damage to buildings and their contents, and when applied to different scenarios allows an effective comparison of the impact.

The extent of damage to the buildings and its contents is estimated from the depth of flooding by the application of a depth-damage curve associated with each occupancy type.

Depth damage curves demonstrate the relationship between the depth of the flood relative to the first finished floor level of buildings and the damage caused to the structures and contents. Damages are typically expressed as a percentage of depreciated building replacement value. Adopting a non-traditional approach, the adopted method models directly the content damage as a percentage of structure value rather than using a content-to structure value ratio.

Not having a map of buildings, the area covered by the buildings has been derived from the land use map according to the hypothesis of Building Coverage shown in the following table.

Table 5: Relationship between Land Use and Building Coverage

Lu Code	Description	Building Cover. %	Lu Code	Description	Building Cover. %
11	Open Water	0%	42	Evergreen Forest	0%
12	Perennial Ice/Snow	0%	43	Mixed Forest	0%
21	Developed-Open Space	**10%**	52	Shrub/Scrub	0%
22	Developed-Low Intensity	**20%**	71	Grassland/Herbaceous	0%
23	Developed-Med Intensity	**35%**	81	Pasture/Hay	0%
24	Developed-Hight Intensity	**50%**	82	Cultivated Cropland	0%
31	Barren Land	0%	90	Woody Wetlands	0%
41	Deciduous Forest	0%	95	Herbaceous Wetlands	0%

To calculate damages, each structure must be assigned to a structure occupancy type. For each structure occupancy type an estimated replacement value and a structure depth-damage and a content depth-damage relationship must be defined.

In our case, replacement values were extracted from the "*Table C-3 Estimated Replacement Value*", depth-damage relationship from "*Table C-1 Depth Damage Curves, Defining Damages as a Percentage of Depreciated Building Value for Depth of Flooding Above Floor*

Height" and the height of the floor of buildings from the ground level was taken from "*Table C-2 Foundation Heights*" of report [7]. The following table contains the list of occupancy type categories adopted.

Table 6: Occupancy types

Occup. Type	Description	Unit Cost ($US/sqm)	Origin data of Depth Damage Curve
RES1	Residential One Story, No Basement	1711	USACE Generic Depth Damage Curves for residential buildings
RES2	Residential Two or more Stories, No Basement	3336	"
COM	Commercial buildings	1528	USACE depth damage, as used in Ford (2005) [8]
IND	Industrial buildings	1528	"
PUB	Public buildings	1711	"
FAR	Homestreads	1711	"

The Figure 6 below shows the graph of the depth-damage curves.
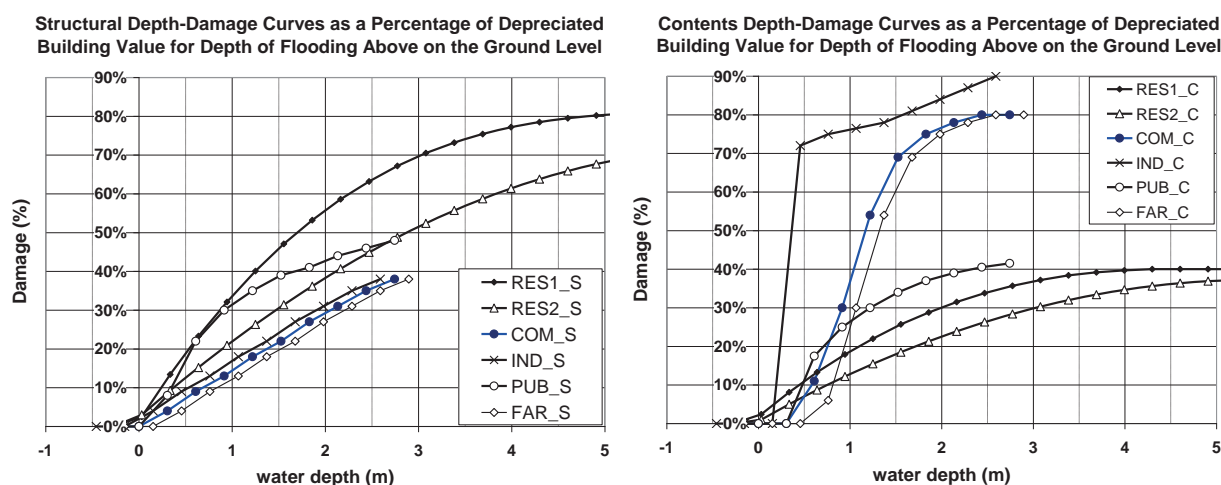
Figure 6: Depth damage curves

To assign at each parcel the occupancy type we chosen the values according to the Table 7.

Table 7: Reclassify table: from parcel ZONINGCATE to occupancy type

ZONINGCATE	Stories	Occupancy Type
COMMERCIAL	any	COM
INDUSTRIAL / WHOLESALE / MANUFACTURING	any	IND
INSTITUTIONAL / GOVERNMENT	any	PUB
OFFICE	1	RES1
OFFICE	2	RES2
OFFICE	3	RES2
OPEN SPACE / RECREATION / AGRICULTURAL	any	FAR
RESIDENTIAL	1	RES1
RESIDENTIAL	2	RES2
RESIDENTIAL	3	RES2

| RESIDENTIAL / AGRICULTURAL | any | FAR |
| UTILITIES / TRANSPORTATION | any | RES1 |

The results of applying the method for the two scenarios are listed in the following table.

Table 8: Direct Economic Impact

Time Interval (min)	Direct Economic Impact ($US)	
	Scenario 1	Scenario 2
0-15	0	0
15-30	0	0
30-60	499 417 507	333 141 773
60-90	671 323 845	151 037 801
90-120	839 403 518	854 746 410
120-180	577 769 953	822 621 093
>180	12 807 947	64 207 745
Total	**2 600 722 770**	**2 225 754 822**

The results show that the total damage, in the case of the first scenario, are greater than 14% and that difference occurs in the first 120 minutes. Also in terms of economic loss the difference between the two scenarios are less than the differences of the peak discharge in the breach of the dam.

Conclusion

In this paper we present the results of the analysis of a possible dam failure. The development of a dam break is a complex process involving numerous uncertainties: the methodology adopted in this work is a medium-scale approach type and can be used for the rapid and consistent evaluation of consequences for the population and to assess the direct economic damages for residential, commercial, and industrial buildings. Rapidity is allowed by using aggregate data: maps of land-use, population census and parcel zone. Consistency is required to ensure comparability between evaluations. For that reason the method can be used to prioritize corrective actions to achieve the greatest and quickest possible risk reduction or for identification of the most effective and better-justified measures of risk mitigation.

The comparison carried out for the two scenarios is an example of use of the methodology to estimate the sensitivity of results with respect to an uncertain parameter which is the breach formation time.

Acknowledgements

References

[1] Molinaro P. (1990). Metodi statistici per la stima della portata di picco defluente in una valle per la rottura di una diga in materiale sciolto. ENEL DSR-CRIS Milano.
[2] Costa J. E. (1995). Floods from dam failures. U.S. Geological Survey, Open-File Report 85-560 Denver Colorado.

[3] Molinaro P. (1986). Modello matematico della breccia che si sviluppa in uno sbarramento in materiale sciolto per tracimazione. ENEL DSR-CRIS Milano.

[4] Engelund F., and E. Hansen (1972). A Monograph on Sediment Transport in Alluvial Streams, Teknisk Folag, Copenhagen.

[5] S. Bunya, J. C. Dietrich, J. J. Westerink, B. A. Ebersole, J. M. Smith, J. H. Atkinson, R. Jensen, D. T. Resio, R. A. Luettich, C. Dawson, V. J. Cardone, A. T. Cox, M. D. Powell, H. J. Westerink, H. J. Roberts. (2010). A High-Resolution Coupled Riverine Flow, Tide, Wind, Wind Wave, and Storm Surge Model for Southern Louisiana and Mississippi. Part I: Model Development and Validation. Monthly Weather Review 138:2, 345-377.

[6] Dams Sector. Estimating Loss of Life for Dam Failure Scenarios. U.S. Department of Homeland Security, Washington, D.C. , September 2011.

[7] Department of Water Resources Division of Flood Management (2008). Flood Rapid Assessment Model (F-RAM) Development 2008, State of California, The Resources Agency

[8] David Ford Consulting Engineers (2005). Urban flood scenario: Sacramento area levee breach scenario, report prepared for California Department of Water Resources, December 5th 2005.

2-D hydraulic modelling of a dam break scenario

O. Saberi[1] , C. Dorfmann[2] and G.Zenz[3]

[1, 2]PhD student, Institute of Hydraulic Engineering and Water Resources Management, Stremayrgasse 10/2, A-8010 Graz, AUSTRIA

[3]Univ. Prof. Institute of Hydraulic Engineering and Water Resources Management, Stremayrgasse 10/2, A-8010 Graz, AUSTRIA

E-Mail: omid.saberi@student.tugraz.at

Abstract

Dam failure is a catastrophic event, and study on the structure of dam is important in the field of water resource engineering. The reason is the risk to life and property below the dam structure. The dam failure occur due to many reasons, some of these reasons are related to structural problems while others are related to the hydraulic conditions. For embankment dams, main reasons are overtopping and piping through the dam body or foundation. However there are some situations that make dam failure happen suddenly, like earthquakes, landslides or wars.

This study provides a two-step numerical simulation of dam failure analysis for an embankment dam which its failure happened in overtopping conditions. First step is about simulating breach of the dam and calculating breach hydrograph, maximum discharge of breach, initial time of the breach formation, and time of maximum breach discharge and other parameters of breach. BREACH GUI software was used for this step. The second part simulates flood after dam break. TELEMAC2D software was used for simulating the flood. The results include the travel time (warning time) of the flood wave to various locations in the downstream valley and the representative valley cross-sections depicting flow depth and unit flow rates. Furthermore the results of this paper can provide information to build an inundation map which can help to develop risk management analyzes.

Introduction

A hypothetical embankment dam was constructed in a mountainous region. This high hazard dam sits directly above a lightly populated area which is 3.5 kilometers away from an urban environment. The primary function of this dam is flood control for heavy snowmelt and strong monsoonal weather patterns. In addition, the reservoir provides some water supply and recreational activities to nearby communities. The dam failure for this dam takes place when the pool elevation is at crest elevation. The mode of failure is assuming an overtopping failure [6].

Two primary tasks in the analysis of a potential dam failure are the prediction of the reservoir outflow hydrograph and the routing of that hydrograph through the downstream valley to determine the dam failure consequences. When populations are located close to a dam, it is important to accurately predict the breach outflow hydrograph and its timing relative to events in the failure process that could trigger the start of evacuation efforts.

Breach Parameter Estimation

Empirical Method
The empirical method are used to predict breach parameters estimation and breach peak discharge and breach hydrograph estimation including geometry of breach, time to reach failure and peak flow discharge, the empirical methods are get from documented failures.
The recommended empirical method for predicting dam breach parameters are MacDonald&langridge-Monopolis (1984), Froehlich (2008), Froehlich (1995 a) and Von Thun and Gillite. In this paper we calculate the dam breach parameters with Froehlich (2008) Formula. For more details we refer to the 12th International Benchmark Workshop [6].
Froehlich (2008) is depending only on the height of breach (h_b), the reservoir volume(v_w) and the breach side-slope, also we have the failure mode factor (k_0) in the Froehlich (2008) for distinguish between overtopping and piping failure.
After put mentioned parameters in the Froehlich (2008) formula we have breach hydrograph in the below shape:

Table 1: Results of the Froehlich (2008)

	$Q_p(m^3/s)$	$t_f(hr)$	$B_{ave}(m)$
Froehlich (2008)	39500	0.57	110
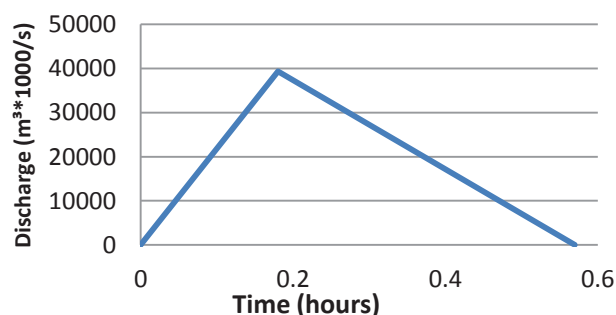
Figure 1: Outflow hydrograph from the Froehlich (2008)

BREACH modelling
In this project we use the National Weather Service (NWS) software Brach GUI for predicting the breach parameters and the resulting outflow hydrograph of an earthen dam [1]. BREACH model was primarily developed by Fread [9] from the National Weather Services. Since 1988 it has been used broadly. This software use a physically-based mathematical model using the principles of hydraulics, sediment transport, soil mechanics, the geometric and material properties of the dam, and the reservoir properties [1]. Furthermore it uses critical properties which are measurable from dam material descriptions. Therefore it considers a more robust model. However it is the responsibility of the engineer to determine the appropriate combination of values as the measure characteristic are normally changing with in a wide range.

Available parameter of breach hydrograph
The dam used in this study is a homogenous embankment dam which is a rolled earth fill structure and composed of predominantly sandy clays and clayey sands. It is located in a

mountain region. The width of crest is 24 m, the length of crest is 360 m and the height of the dam is 61m. The total water volume of water behind the dam is 38,276,344 m³. The distance from this dam to the population area is 3.5 km. The dam failure will take place when the water level behind the dam is at crest elevation and the mode of failure will be over topping failure. For more details we refer to the 12th International Benchmark Workshop [6]. As base inflow we assumed a discharge equal to 100 m³/s. In Table 1 the main physical parameters of the dam are listed.

Table 2: Strength parameters of soil [6]

Effective cohesion (KPa)	$C´$	19.15
Effective friction angle	$Ø´$	14°
Undrained strength (KPa)	Su	$43.09+0.175× \sigma_{mc}$
Shear Wave velocity (m/s)	v	152.4
Maximum shear modulus (KPa)	G	46443
Saturated unit weight (kg/m3)	γ_{sat}	2002
Permeability (cm/s)	K	$1.9*10^{-6}$

Calculating input parameter for Breach software

For start a simulation with the BREACH software we need to calculate some parameters as input data. The most important input parameters to be provided in the BREACH software are the mean grain size D50 (mm), the initial elevation of water surface, the elevation of the top of the dam, the elevation of the bottom of the dam, the average plasticity index (PI), the critical shear stress coefficient, the slope of the upstream and downstream faces of the dam (1:3), the base inflow hydrograph, the surface area behind the dam vs. the elevation of the dam, the porosity specifications of the dam material and the breach parameter. Table 1 and the equations 1-4 according to [5] can help with defining these input parameters:

$$V = \sqrt{G/\rho} \tag{1}$$

where V is the shear wave velocity (m/s), ρ is the density of material (kg/m3) and G is the shear modulus (KPa)

$$G_s = \frac{\gamma}{\gamma_w} \tag{2}$$

where G_s is the specific gravity, γ is the unit weight of soil (N/m³) and γ_w is the unit weight of water (N/m³)

$$\gamma sat = \frac{(G_s+e)}{1+e} \times \gamma w \tag{3}$$

where G_s is the specific gravity, γ_w is the unit weight of water (N/m³) and e is the void ratio

$$n = \frac{e}{1+e} \tag{4}$$

where e is the void ratio (%) and n is the porosity (%).

With the parameters in Table 1 and the equations 1-4 the porosity n is calculated as 49%. D50 can be considered approximately equal to 0.066 mm [4]. The basis for this approximation comes from soils mechanics fields.

When the diameter of Clay soil is less than 0.002 mm and the diameter of sand soil is between and 0.05 and 2.00 mm then sandy clay is a soil with 33 percent till 55 percent clay and up to 65 percent sand [5].

The average plasticity index (PI) is calculated according to the USCS plasticity chart and the relationship equations of Skempton and Henkel (1953) [3], Psterman (1959) [3] and Bjerum(1960) [3] which is equal to 42%. Furthermore PI will be used in the following formulation to calculate two more parameters required by BREACH software (CA, CB) [1]:

$$\tau_{cr} = (CA \times PI)^{CB} \tag{5}$$

where τ_{cr} is the critical shear stress (kPa), PI is the plasticity index (%) and CA, CB are the critical shear stress parameters. Having PI=42% and τ_{cr} derived from Table 1, CA and CB are calculated as $CA = 0.02$ and $CB = 0.835$.

Output of the BREACH software

Having all the above inputs into the software we can run the BREACH model to calculate the outflow hydrograph given in Figure 1.
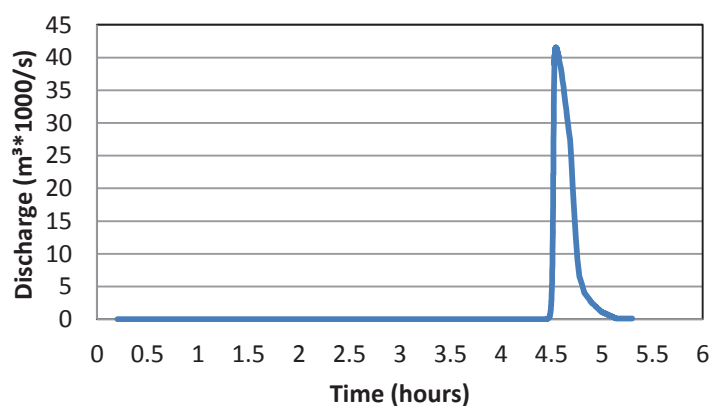
Figure 2: Outflow hydrograph from the breach software

Furthermore the software output provides some other parameters which can be used in risk management studies. These parameters are given in Table 2:

Table 3: Results of the BREACH software

Maximum discharge of breach (m3/s)	41600
Time for peak out flow (hours)	4.62
Time for starting outflow (hours)	4.44
Final depth of breach (m)	61
Top width of breach at peak breach flow (m)	250
Time to reach final breach bottom elevation (hours)	4.97
Bottom width of breach at peak breach flow (m)	15

Comparison between result of Froehlich (2008) and BREACH modelling

After calculating breach hydrograph from Froehlich (2008) and breach modeling in follow picture, we find out all the dam breach parameters including the failure time, the peak discharge outflow and the average of breach width of Froehlich less than BREACH software.
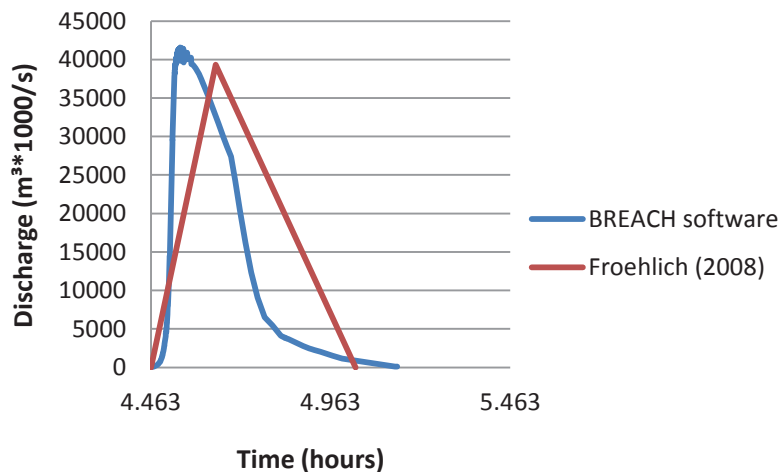
Figure 3: merged discharge of cross sections (m3)/s

2-D hydrodynamic flood with Telemac-2D

The flood from dam break can go to downstream valley and in this part we are going to determine dam failure consequences and calculating the water surface, the water depths, the unit flow rates as well as the flow rates in various cross sections. The TELEMAC-2D modelling software is used for this purpose. TELEMAC-2D is a numerical simulation software and belongs as module to the open source Telemac-Mascaret suite for the simulations of hydrodynamic flow, contaminant and sediment transport. It solves the two-dimensional depth-averaged Saint Venant equations for free surface flow. A detailed description of the Telemac System is given in Hervouet's book (2007)[7]. The main results of Telemac-2D are the water depths and the depth- averaged velocity components.

The original geometry provided by the ICOLD benchmark specifications was modified by deleting a priori non flooded mesh areas in order to save computation time. Table 3 shows the resulting mesh properties:

Table 4: Mesh properties

Number of element:	213750
Interior elements:	210652
Edge elements:	3038
Number of nodes:	108433
Edge nodes:	3114
Interior nodes:	105319

The upstream boundary condition is located at the dam and the hydraulic boundary condition is the unsteady flow hydrograph from the BREACH software, see Figure 1. The downstream boundary condition is a free outflow.

Results overview

The results of TELEMAC-2D are stored in the binary SEARAFIN format which can be analyzed and visualized by using the free software Fudaa or BlueKenue [8]. In this project BLUE KENUE software was used.

In the following the results are shown graphically for breach discharge, cross section discharge, peak flood depth, flood wave arrival time, peak unit flow rate and flooded area. Furthermore interpretation on each subject is given along with the output figure.

Breach Discharge

This result was calculated in the first part with BREACH GUI software (shown in Figure 1). Also from the calculated breach hydrograph we find out:

- With the inflow of 100 m³/s into the dam reservoir it takes 4.36 hours for the dam breach initiation.
- The maximum discharge takes place after 648 s after the breach initiation.
- The duration of flood is 2844 s.

Cross-Section Discharge

For the calculation of the cross section discharge the following steps are performed:

- First the unit flow rates are calculated (m²/s)
- Second the unit flow rates are integrated along the cross section width

Figure 2 shows the discharges in various cross sections and the reduction of the peak flows going downstream from cross section 1 to 5.
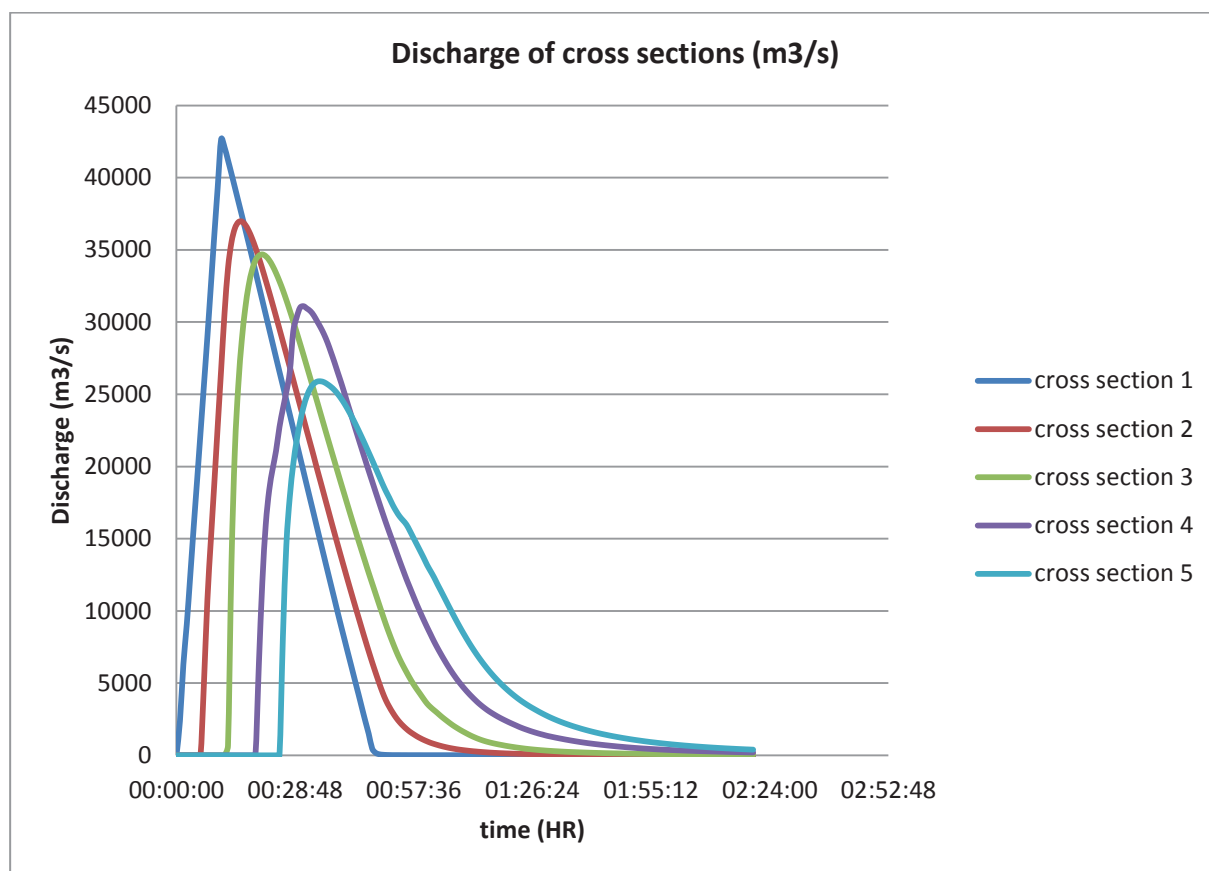
Figure 4: merged discharge of cross sections (m3)/s

Peak flood depths

In BLUE KENUE software we can also calculate the maximum flood depths in the project area. Figure 3 shows the results for the peak flood depths where the blue color indicates the safe area with maximum water depths less than 0.5 m and the red color indicates dangerous areas with minimum water depths of 4.5 m.
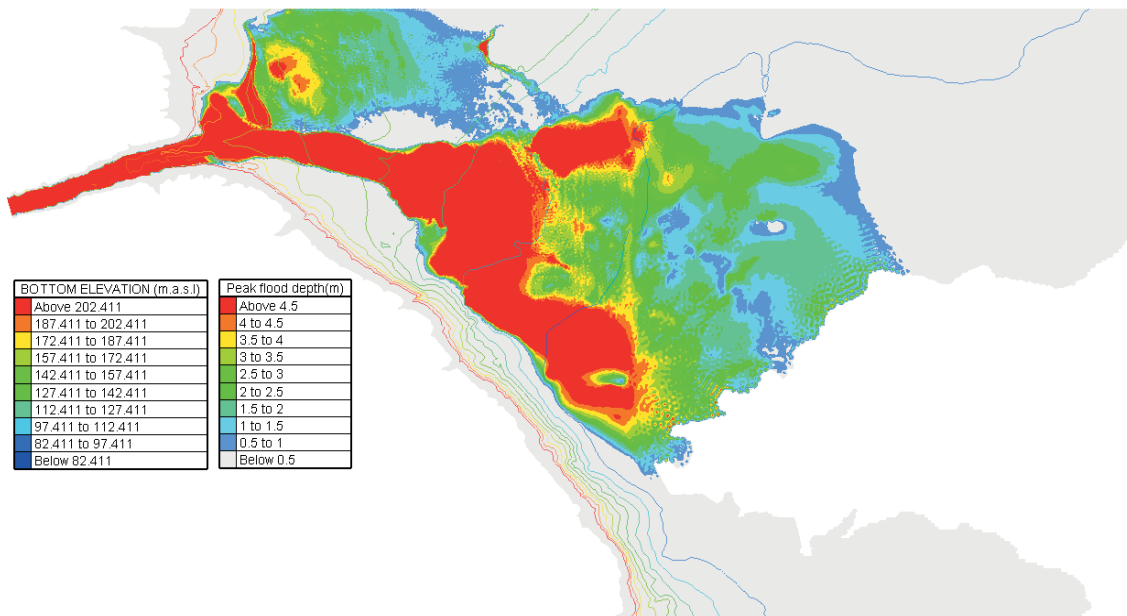
Figure 5: Peak flood depths (m)

Flood wave arrival time and water depths

In this part we calculated the arrival time of flood. This will help us to find out how long it takes for the flood to reach each part of downstream area. BlueKenue software visualizes the water depths separately for each chosen time interval. It means BlueKenue gives us one gridded dataset for each time intervall. Figures 4, 5 and 6 shows the water depths or flood wave arrival times for certain time intervals.
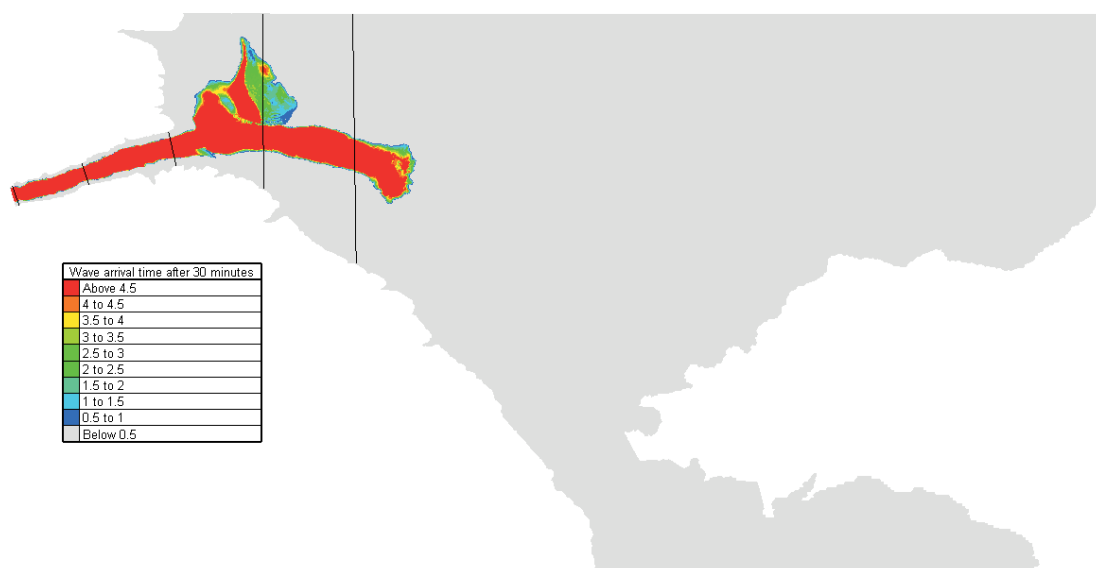
Figure 6: Water depths after 30 minutes
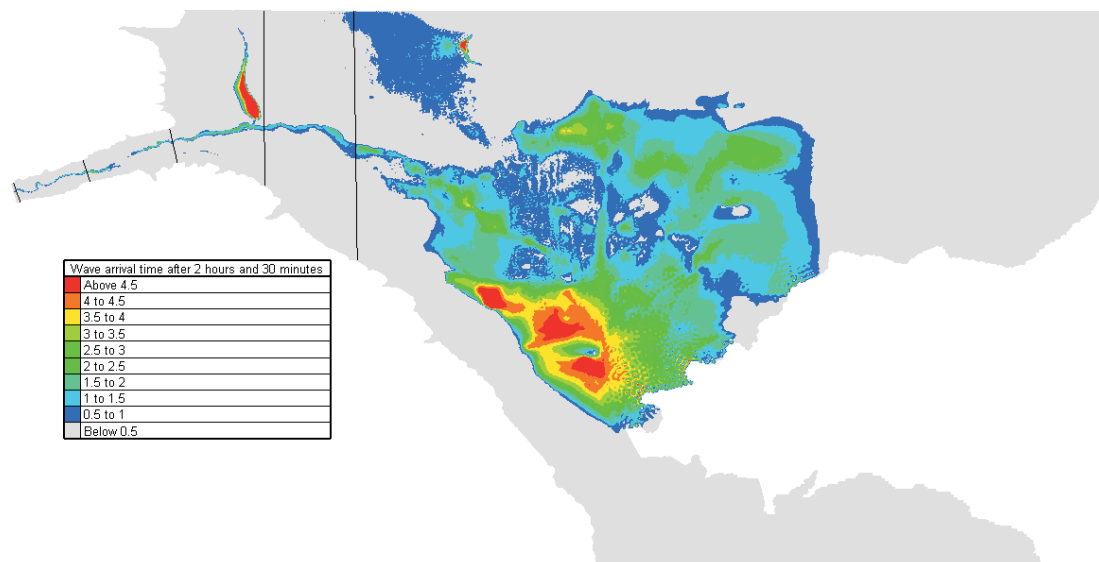
Figure 7: Water depths after 2 hours and 30 minutes

As we can see in Figure 4, 5 and 6 these visualizations are useful to analyze the flood wave arrival time and the locations of impact.

Peak unit flow rate

The unit flow rate is given in equation 6:

$$q = \sqrt{(U \times H)^2 + (V \times H)^2} \tag{6}$$

where q is the unit flow rate (m²/s), U and V are the water velocity components in x and y direction (m/s), and H is water depth (m).

The peak unit flow rate in every mesh node can be extracted from the time varying unit flow rate and is shown in Figure 7.
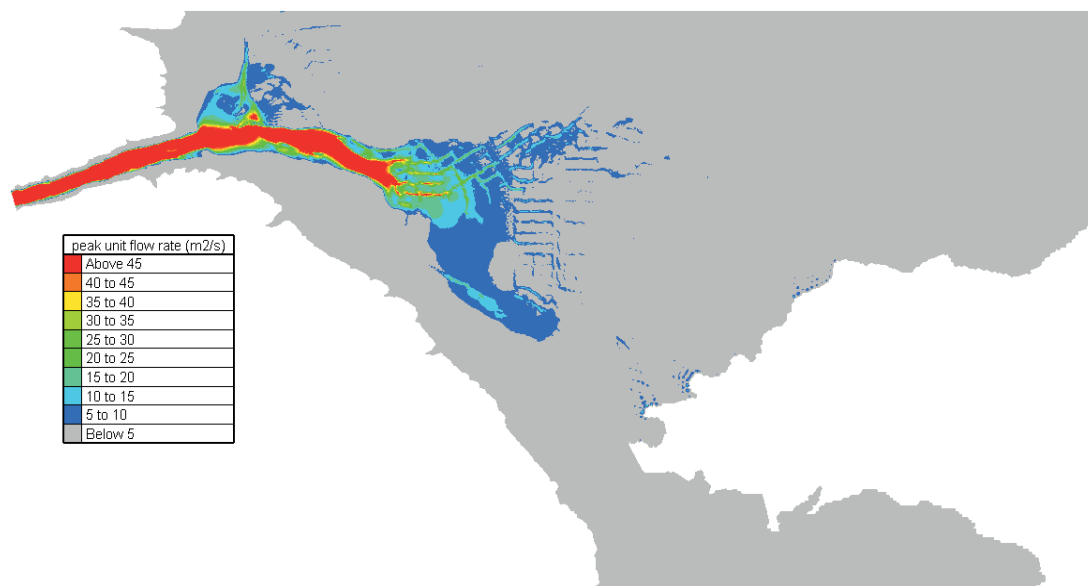
Figure 8: Peak unit flow rate (m²/s)

Flooded area

For calculating the flooded area we can define the total wet area by defining iso-lines. This option categorizes the flooded area for arbitrary water levels.

The total flooded area is given in Table 4 and the flooded areas for different water depths with interval of 0.5 m is given in Table 5.

Table 5: Total flooded area

Total flooded area (m²)	47626580

Table 6: Flooded areas, intervals 0.5 m

Water heights (m)	Flooded area (m²) *10^3
>8	4179
8	4290
7.5	4805
7	5565
6.5	6827
6	7910
5.5	9131
5	10269
4.5	11569
4	13349
3.5	15432
3	18145
2.5	22200
2	27109
1.5	32959
1	38433
0.5	41043

The results of these tables can be used in the risk management study for calculating the damage property and loss of life.

Conclusion

The first part of this study describes the BREACH model for predicting the breach hydrograph of a hypothetical embankment dam. The reason for the failure of dam is assumed to be overtopping. The following results can be deduced:

- The maximum outflow in this project is calculated as 41558 m³/s. The water flow is transferred into the downstream direction of the dam which can cause catastrophic consequences.

- The maximum discharge happens near the dam place at cross section number 1.

- One of the most important parameter in the risk management is the alarm time. In this study we have calculated the break initiation time as well as the formation time. Furthermore these data can help us to determination the Property damage and loss lives.

The above mentioned results used in the successive 2-D depth-averaged calculations with TELEMAC-2D. The following conclusions can be made based on the 2-D simulation results:

- The height of water and the maximum height of water which are important parameters in risk management fields are calculated to define inundation regions. These results also can be used to define warning zones according to the flooded areas.

- The wave arrival time is analysed for 15 minutes intervals. This time model shows us how long it takes for the flood to reach each part of the downstream area which is useful for reducing loss of human lives in risk management studies.

Acknowledgements

I would like to express my deepest appreciation to all those who provided me the possibility and help me to complete this report.

References

[1] Janice Sylvestre, Developer, 2010, BREACH GUI (BREACHJ) Version 1-0-0 08-01-2010
[2] TELEMAC modelling system, 2D hydrodynamics, TELEMAC-2D software Version 6.0, USER MANUAL
[3] A. S. Balasubramaniam, H. Cai, D. Zhu, C. Surarak and E. Y. N. Oh,Griffith School of Engineering Griffith University, Gold Coast, Australia, Settlements of Embankments in Soft Soils
[4] AFTA 2005 Conference Proceedings, Placement of Riparian Forest Buffers to Improve Water Quality
[5] Braja M.Das, 2008. Advance soil mechanic, third edition. This edition published 2008
[6] By Taylor & Francis 270 Madison Ave, New York, NY 10016, USA
[7] 12th International Benchmark Workshop on numerical analysis of dam, 2013, Austria, Graz
[8] Hydrodynamics of Free Surface Flows: Modelling with the Finite Element Method by Jean-Michel Hervouet(May 29, 2007)
[9] CHC - Canadian Hydraulics Centre, National Research Council, 2010. Blue Kenue, Reference Manual, August 2010.
[10] The NWS simplified dam-break flood forecasting model by Jonathan N.wetmore and Danny L.Fread (Reviesed 12/18/91) by Danny L.Fread, Janice M.Lewis, and Stephen M.Wiele

Risk Assessment Analysis of a Hypothetical Dam Breach Using Adaptive Finite Element Methods
Adaptive Hydraulic Model, ADH

D. McVan[1], J. Ellis[2], G. Savant[3] and M. Jourdan[1]

1Research Hydraulic Engineer, Engineer Research and Development Center, U.S. Army Corps of Engineers, Vicksburg, MS, 39180. E-mail: Darla.C.McVan@USACE.Army.mil
2Engineering Technician, Bowhead Science and Technology, LLC, and Onsite Contractor, Engineer Research and Development Center, U.S. Army Corps of Engineers, Vicksburg, MS 39180.

E-mail: Jeffrey.D.Ellis@usace.army.mil

3Research Water Resources Engineer, Dynamic Solutions LLC and Onsite Contractor, Engineer Research and Development Center, U.S. Army Corps of Engineers, Vicksburg, MS 39180.

E-mail: gaurav.savant@usace.army.mil

Abstract

A virtual computational test bed was developed by a committee sponsoring a session at the International Commission on Large Dam (ICOLD) 12th International Benchmark Workshop. The purpose of this virtual test bed was to serve as a platform for comparison of dam breach models and methodologies. This paper provides the results of one of the model comparisons.

The ADH model, developed by the U.S. Army Engineer Research and Development Center (ERDC) was used to simulate a catastrophic dam failure and gradual dam failure. The ADH Model is described, as well as the domain, setup, and boundary conditions for the specific simulations.

Results are provided as gridded and tabular data, as well as hydrographs. The gridded results include peak flood depths, flood wave arrival times, peak unit flow rates and total population at risk. Tabular results include flooded area and population as risk (including age demographics). Hydrographs are presented for both the dam failure discharge and at five down stream cross sections. Loss of life and economic impacts were not calculated.

Introduction

Computational capacity, along with multi-processors computing techniques, has grown resulting in development of new models for flooding and consequence/risk assessment. These new models which are computing flood wave propagation at higher spatial resolutions can be coupled with risk assessment models which allow for more detailed analyses of the effects of these flows.

This paper represents results of the numerical dam breach done using the virtual testbed developed for the International Commission on Large Dam (ICOLD) 12th International Benchmark Workshop.   This virtual testbed was developed as a tool for comparison of different numerical model results and the model capabilities.   The testbed includes a hypothetical dam above a hypothetical city named Hydropolis. The focus of this study was to estimate the consequences of failure of the dam. Demographics, infrastructure and dam

characteristics were provided so that comparison of these models could be made which will aid in the development of simulation frameworks that can support dam risk analysis. Two model scenarios were modeled; the first model represents a catastrophic event in which the entire dam is destroyed instantaneously. The second model represents a gradual breach using Froehlich (1995a) equations.

Methodology

Model Code Description
ADH is a state-of-the-art code developed by the U.S. Army Engineer Research and Development Center (ERDC) to simulate both saturated and unsaturated groundwater, overland flow, three-dimensional Navier-Stokes flow, and two and three-dimensional shallow water equations, including super-critical flows and shock capturing (Berger el.al. 2010). The ADH code is parallelized and is capable of running on high performance computing systems. ADH is also an implicit code meaning its time step size is not limited by the element size as with explicit codes. These features make ADH computationally efficient for large-scale applications. ADH has been utilized to study varied phenomena such as estuarine circulation (McAlpin et al. 2009; Tate et al. 2010; Martin et al. 2010, Martin et al. 2011), riverine flow (Stockstill and Vaughan 2009; Stockstill et al. 2010), and dam breach (Savant et al. 2011).

The two-dimensional shallow water (SW2) equations are used for the application presented here. This module solves the conservative form of the SW2 equations, allowing for local and global mass conservation. ADH is a temporally and spatially adaptive code. For temporal adaption, the code utilizes a variable time step such that failure to reach convergence at a given time step size does not end the simulation; rather, the time step size is reduced and the solve is attempted again (Savant et al. 2011). ADH also has the ability to allow continuous wetting and drying such that the flood front is computed and visualized accurately (Berger and Lee 2004; Savant and Berger 2011). For this model simulation, a maximum time step of 10 seconds was specified with smaller time steps being performed automatically as needed.

Model Setup
All hydrodynamic numerical models require certain basic input data to perform simulations. These data are bathymetric and topographic elevations for defining the model domain, inflow hydrographs or water elevations, as well as other boundary information such as rainfall and ocean water surface elevation (if the area of interest is in a tidal zone) for driving the model, as well as roughness characteristics and the ground surface and other parameterizations depending upon the objective of the modeling application. In the following sections, these domain construction data, driving data, and parameterization needs are addressed.

Model Domain
The bathymetric and topographic information for this workshop were provided from the ICOLD "Theme C" Formulation Team in the form of a DEM with 9.4 meter resolution. Two DEMs were provided, one representing the domain without the dam, and the other with the dam. The DEM covered an area that was approximately 250 km^2. The hypothetical dam was located at coordinate 4499.66 meters and 6681.57 meters and has a crest width of 24 meters and a crest length of 360 meters. The river bed elevation at the base of the dam is 211 meters and the crest elevation is 272 meters with 3H:1V embankment slopes. The maximum storage capacity of the reservoir is approximately 38 million cubic meters.

The ADH mesh was created using the Surface-water Modeling System (SMS) (Aquaveo 2009) meshing algorithms and consists of 13,790 triangular elements comprised of 7,138 nodes at the triangle corners. Both the catastrophic model and the gradual breach model used the same mesh. The dam was 'built' into the mesh at the provided coordinates specifying the width of the elements along the dam's crest and determining the upstream and downstream length of the embankment. Element areas range from approximately 250 m^2 to 25,000 m^2, with the finest resolution located at the dam and along the channel and the larger areas located downstream in the lake. After the mesh was constructed, the separate DEMs were interpolated to the mesh. The DEM without the dam was interpolated to the mesh for the catastrophic model and the DEM with the dam was for the gradual breach model. Figure 1 shows the mesh at the dam site, the model domain and bathymetry.

Model Boundary Conditions and Parameterization

Numerical modeling of any type requires the specification of driving boundary information. For the dam breach model, this driving force is maximum volume of the reservoir at the crest elevation, 272.0 meters. This is achieved by creating initial depth conditions at each node. For the nodes representing the reservoir, the water surface elevation was entered and the initial water depth was determined from the mesh bathymetry. The rest of the mesh was
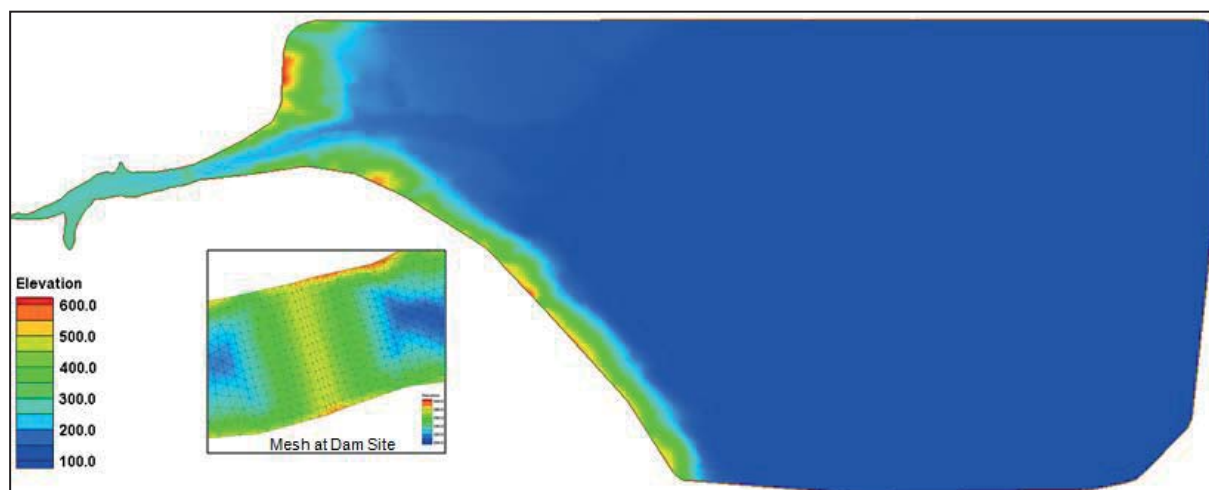
Figure 1: Model Domain.

given a -0.1 meter water depth in order to simulate a dry mesh. In an attempt to prevent back-up of the flow which may cause artificial inundation not created by the flooding, an evaporation boundary was applied to the downstream boundary that allows the water to be transported out of the domain. However, after the model was complete, it was observed that after the flood wave hits the boundary, the wave is reflected back into the model domain. This only occurred in the area of the lake and it was determined that it would not affected the area of interest.

Bed roughness was an additional user specified parameter that defines the frictional resistance. ICOLD's "Theme C" Formulation Team provided a gridded dataset representing the land use/land cover of the region. This data was used to identify areas of similarity and applied to the mesh as material types. Figure 2 shows the various material types used in the model. The elements and nodes associated with each material type will have the same material properties specified in the boundary conditions. Literature search describing the varying roughness coefficients for differing floodplains were used to determine the bed roughness for each material type (Arcement, G.J., Schneider, V.R., and Oregon Department

of Transportation, 2005). Table 1 shows the material types used in the model along with its roughness value.

Table 1: Bed Roughness

Material Type	Manning's n Value
Channel	0.018
Forest	0.100
Developed	0.020
Shrub/Cropland	0.050
Shrub/Forest	0.070
Lake	0.018
Reservoir	0.018
Dam Crest	0.018
Upstream Dam Face	0.018
Downstream Dam Face	0.018
Downstream Boundary	0.018

(Arcement, G.J., Schneider, V.R.,) (Oregon Department of Transportation, 2005)

In the ADH numerical code, the Manning's value is converted to an equivalent roughness height that depends on the instantaneous water depth at a particular node. The friction formulation is then derived from the logarithmic velocity profile based on open channel flow. Thus, while the user-specified frictional value (Manning's number) is constant over the specified material type, the actual applied resistance is spatially varying according to the water depth and velocity magnitude at each node in the mesh. This results in higher frictional values for locations of shallower depths as is experienced in nature and can be extremely important when estimating flood extents.
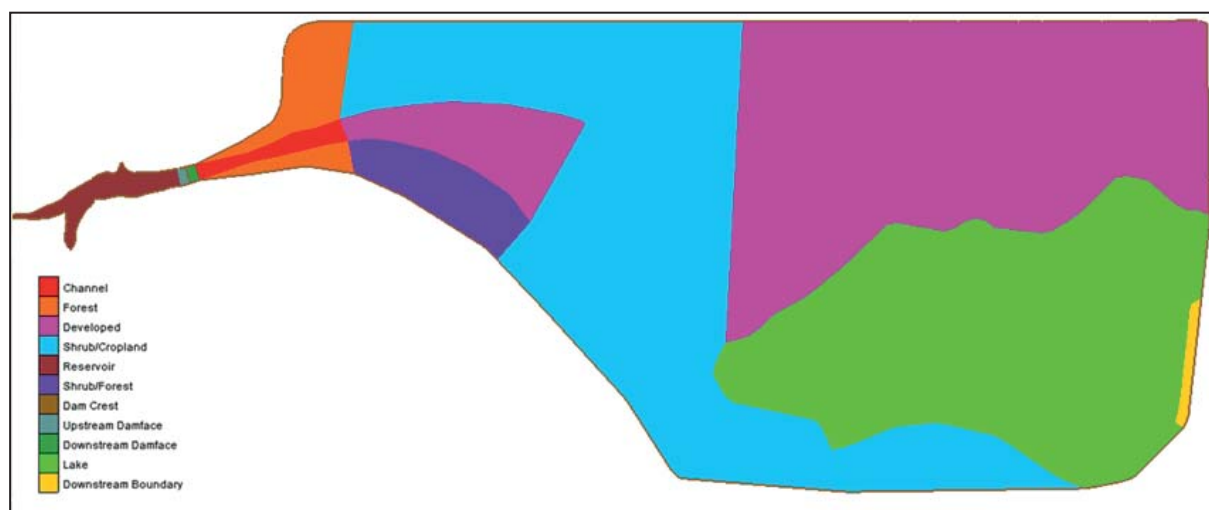
Figure 2: Material Types

For the catastrophic model, the dam does not exist in the mesh therefore the model's initial conditions at time 0.0 simulated a wall of water at a depth of 61 meters.

For the gradual breach, the dam does exist in the mesh. Equations developed by Froehlich (1995a) were used to determine the average breach width and the breach formation time and are shown below. Failure of the dam was assumed to be caused by overtopping resulting in 80-percent of the dam height removed or approximately 48.8 meters. Therefore, the maximum width of the breach was approximately 141 meters and the breach formation time was approximately 48 minutes (2940 seconds). (The height of the breach and the formation

time were rounded to 49 meters and 49 minutes). To achieve the gradual breach, elevations of the nodes representing the dam were gradually lowered at specified time intervals. At the end of the breach, the elevations of the nodes representing the breach were 223 meters.

$$B_{ave} = 0.183K_oV_w^{0.32}h_b^{0.19} \qquad\qquad (1)$$

$$t_f = 0.00254K_oV_w^{0.53}h_b^{-0.90} \qquad\qquad (2)$$

Where: B_{ave} = Average Breach Width (m)
K_o = Constant (1.4 for overtopping failures, 1.0 for piping)
V_w = Reservoir volume at time of failure (m^3)
h_b = Height of the final breach (m)
t_f = Breach formation time (hours)

Model Results

Model Simulations
The ADH model simulations for both the catastrophic and the gradual breach were performed on the SGI Altix Ice machine (Diamond) at the USACE ERDC (ERDC DSRC 2011). This machine uses an SLES (Linux) 11 operating system with a 2.8 GHz Intel Xeon Nehalem-EP Processor. The catastrophic model was run on 16 processors and simulated 6 hours 40 minutes (24,000 seconds) and required approximately 60 minutes to complete (wall time). The gradual breach was run on 12 processors and simulated 12 hours (43,200 seconds) and required approximately 2 hours to complete. Both models had output intervals of 100 seconds.

In accordance to ICOLD's "Theme C" Formulation Team, the information obtained for both the catastrophic event and the gradual breach were discharge hydrographs for the dam failure and along five cross-sections specified by the Formulation Team. The model also provided contours of the peak flood depths, peak unit flow rate, and the flood wave arrival times. Because ADH uses a mesh, the output results are also in the mesh format. In other words, each node in the mesh contains all the information for each time step. To determine the total population at risk including the age demographics as well as the flooded area, the ADH depth file were converted to a raster for each output time interval. The raster was then converted to a shapefile which contained the depth at 1 meter intervals. The Formulation Team specified 0.5 meter intervals, however due to the constraints of this methodology, only integer values could be used. The census block shapefile provided by the Formulation Team was clipped to the depth shapefile and the ratio of the clipped area compared to the entire area determined the total population potentially affected by the flood.

Catastrophic Model Results
As mentioned previously, the catastrophic model simulated the worst case scenario where the entire dam is removed instantaneously. The maximum discharge at the time of the breach was approximately 84,000 cms. At each cross section, the maximum discharge varied between approximately 61,000 cms and 81,000 cms. Figure 3 shows the discharge hydrographs for each location. The total volume at the reservoir was approximately 38.93 km^3 and at each of the cross sections, the volume varied between 39.4 km^3 and 40.9 km^3. Table 2 shows the maximum discharge with the associated times of occurrence at the dam and for each of the 5 cross-sections along with the total volume for each location.

Though ADH conserves fluid and constituent mass to machine precisions, for wet-dry problems this conservation is dependent on user specified tolerance parameters. These parameters control how accurately ADH solves the continuity and momentum equations using the Newton-Raphson iterative approach for solving a system of implicit equations. Very small tolerance parameters will drive the solution to conserve mass to machine precision but can significantly increase run time, large tolerances will significantly reduce run time but will not provide mass conservation or the correct results. A balance has to be achieved between the requirements of a particular project or simulation and whether exact mass conservation is required. For the simulations presented in this document the mass is conserved to 3-percent for catastrophic breach. ADH utilizes a diffusive wave type shock capturing scheme in wet-dry areas, this scheme, for extreme wet-dry scenarios, can hide fluid mass in dry cells and is an additional, though rare, source of mass errors. All elements/nodes are included in computations at all times and no minimum 'include in computation' depth is used by ADH. The error shown in Table 2 shows how well ADH conserved the mass at each cross-section.

Table 2: Maximum Discharge for Catastrophic Event

Location	Time of Maximum Discharge (seconds)	Maximum Discharge (cms)	Total Volume (km^3)	Error
At the Dam	1	83,828	38.93	-
X-Section 1	26	80,855	39.37	1.01
X-Section 2	207	66,027	39.47	1.01
X-Section 3	293	60,738	39.69	1.01
X-Section 4	385	62,089	39.65	1.00
X-Section 5	546	67,166	40.91	1.03
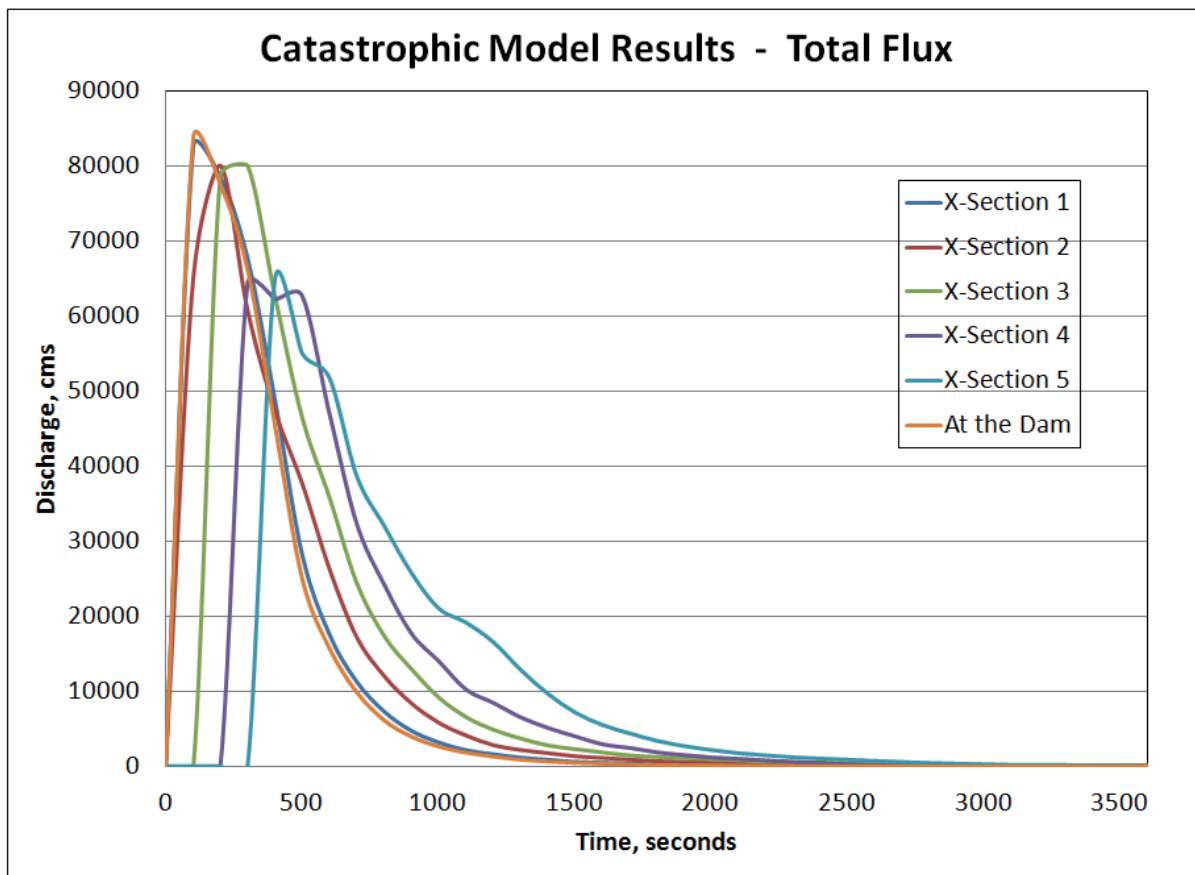
Figure 3 Maximum Discharges for Catastrophic Event.

The reservoir was completely emptied in approximately 50 minutes (3000 seconds). The flood wave was completely at the lake after 2.7 hours. As one would expect, the greatest depths occur within the channel. Maximum depths in the floodplain range between 2 and 12 meters. The unit discharge in the floodplain is less than 50 m^2/s. Figures 4 and 5 show the maximum peak depth for the catastrophic model and the peak unit flow rate, respectively. The flood wave reaches the floodplain about 5 minutes after the dam is breached and reaches the downstream boundary at approximately 1.67 hours (100 minutes). Figure 6 shows the arrival time in 15 minute intervals.
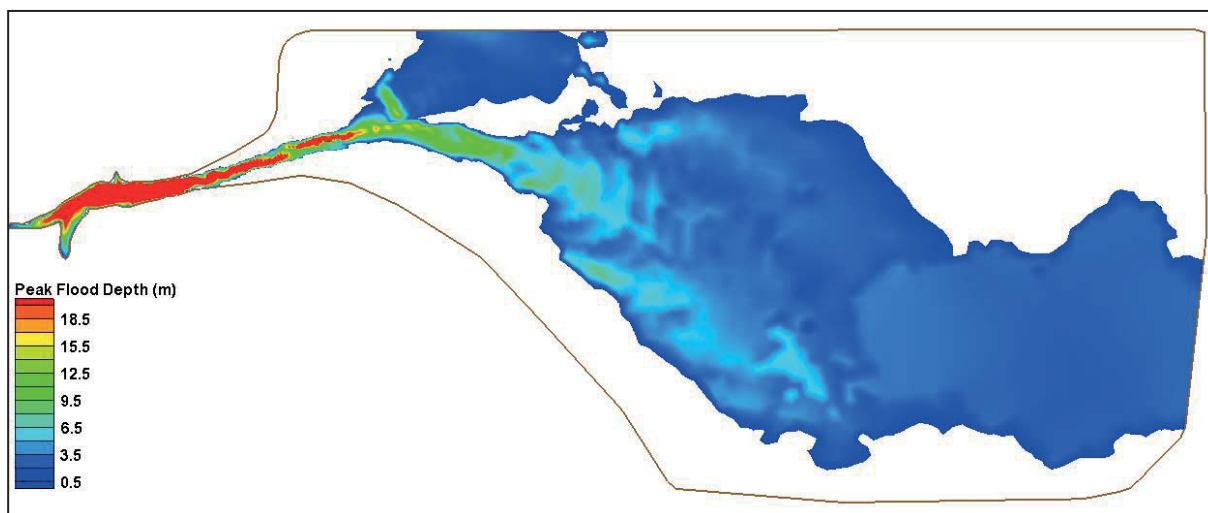
Figure 4 Peak Flood Depth in meters for Catastrophic Event
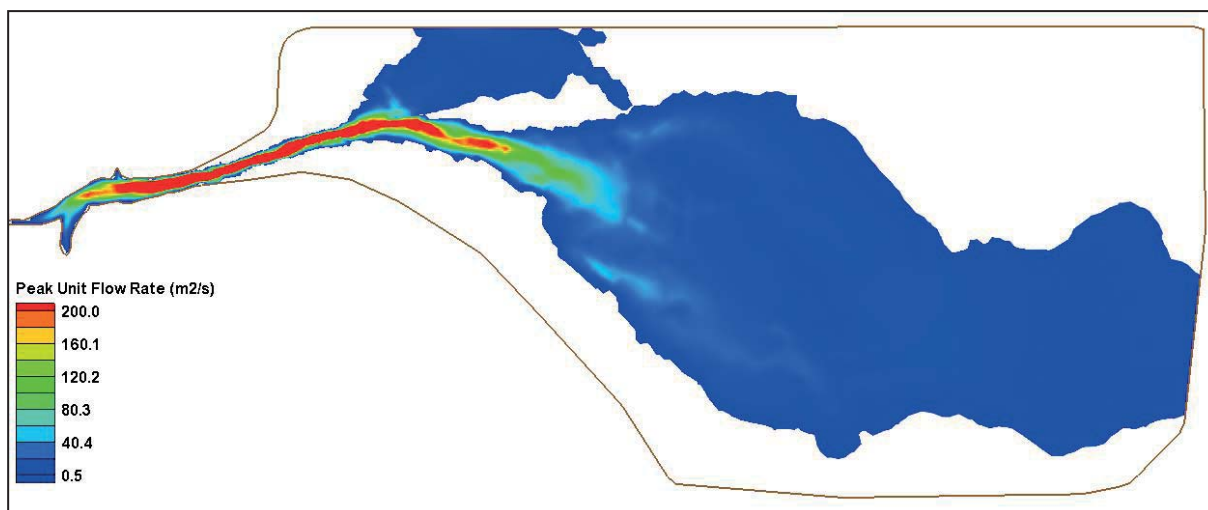
Figure 5 Peak Unit Flow Rate (m2/s) for Catastrophic Event
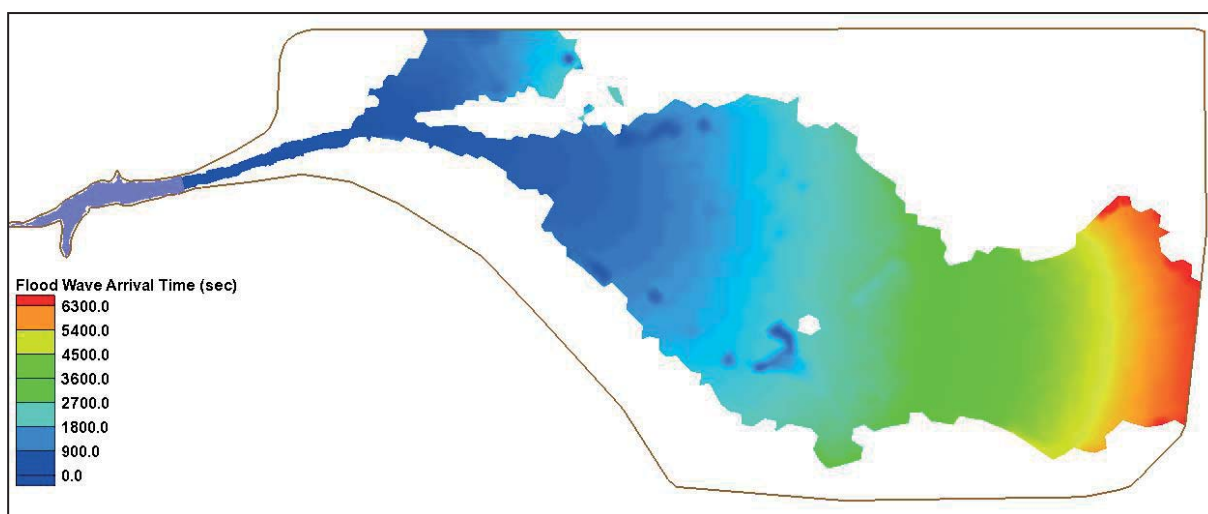
Figure 6 Flood Wave Arrival Times for Catastrophic Event

The total flooded area at peak depths, excluding the area of the lake, was approximately 41.1 km^2 and affected well over 28,000 people. The total population at risk after 180 minutes is over 26,000. These differences are the results of taking a single snap shot of the population in time. As the flood wave travels downstream, the inundated area covers a finite area. For the next time, the inundated area covers a completely different area. Sometimes these areas overlap which result in duplicating the population at risk and at other times there is a gap resulting in the population at risk not being accounted for. Therefore, when assessing loss of life and economic consequences, it is best to use the peak flood depth values. Figure 7 shows the clipped total population at risk for the peak depths. Table 3 shows the population at risk at 15 minute time intervals and includes age demographics and Table 4 shows the flooded areas at 1 meter intervals along with the total population at risk and the age demographics. For the 12-year and under age demographic, the total population at risk after 3 hours is over 4,300 and about 4,600 for the maximum flooded area. The 65-year and over age demographic has over 4,700 at risk after 3 hours and around 5,200 for the maximum flooded area. The total flooded area with depths greater than 8 meters is over 3.35 km^2 which affects a total population at risk of less than 2,000. For the 12-year and under demographics, the total population at risk affected by depths greater than 8 meters is slightly over 400 and over 130 for the 65-year and over demographics.

Table 3: Total Population at Risk for Catastrophic Event

Time Intervals (minutes	Total Population at Risk	12-yr and Under Population at Risk	65-yr and Over Population at Risk
15	3,179	815	225
30	12,516	1,936	2,487
45	9,807	1,449	1,910
60	629	97	132
75	33	7	1
90	19	4	1
105	13	2	0
120	12	2	0
135	12	2	0
150	11	2	0
165	11	2	0
180	11	2	0
Total	26,253	4,320	4,759

Table 4: Flooded Area Population at Risk for Catastrophic Event

Peak Flood Depth Range (meters)	Flooded Area excluding lake (km^2)	Total Population at Risk	12-yr and Under Population at Risk	65-yr and Over Population at Risk
>/= 1	41.09	28,802	4,641	5,208
>/= 2	32.37	21,273	3,429	3,994
>/= 3	17.55	6,274	1,207	1,044
>/= 4	9.73	3,494	835	327
>/= 5	5.94	2,886	710	220
>/= 6	4.56	2,598	635	202
>/= 7	3.82	2,201	535	167
>/= 8	3.35	1,710	413	136
Total	41.09	28,802	4,641	5,208
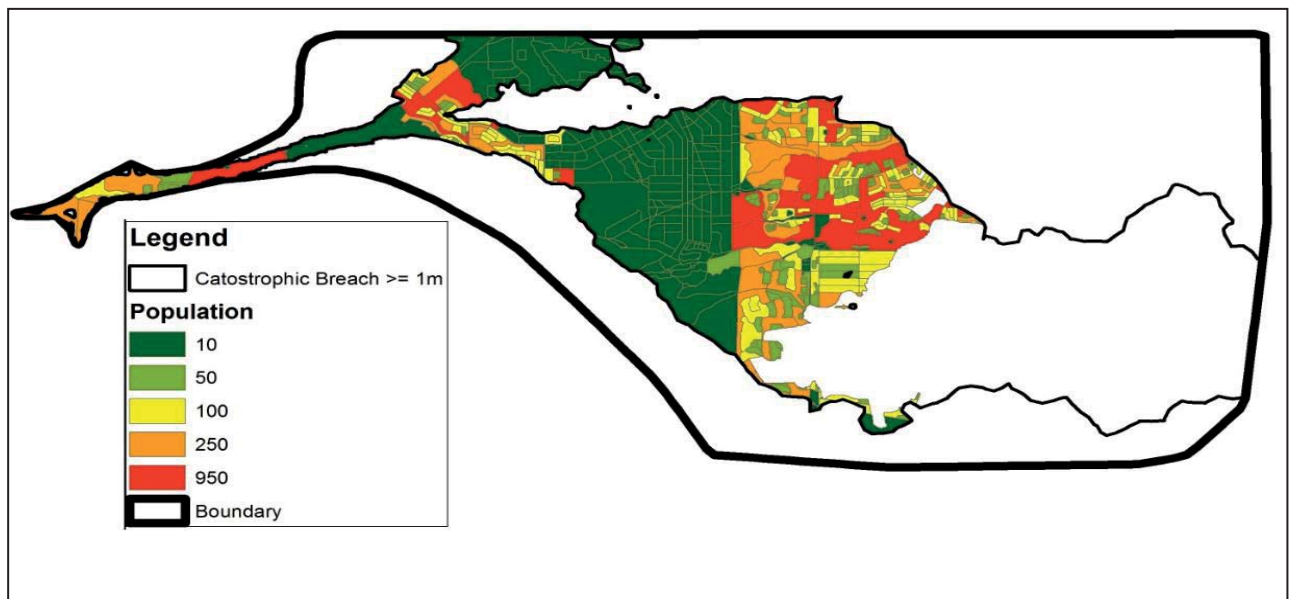
Figure 7 Total Populations at Risk for Catastrophic Event

Gradual Breach Model Results

Failure of the dam for the gradual breach scenario was assumed to be caused by overtopping resulting in 80-percent (49 meters) of the dam height removed. The maximum width of the breach was 141 meters and the breach formation time was 49 minutes (2940 seconds). Elevations of the nodes representing the dam were gradually lowered by 1 meter at 1 minute intervals. At the end of the breach, the elevations of the nodes representing the breach were 223 meters.

The maximum discharge at the dam location was over 17,000 cms and occurred 33.33 minutes (2000 seconds) after the initial time of breach. The maximum discharges for the 5 cross-sections ranged from between 16,400 cms and 20,500 cms. Table 5 shows the maximum discharges at the dam and the 5 cross sections along with the calculated volumes of each hydrograph. Figure 8 shows the discharge hydrographs for each location. Since the lowest elevation of the final breach is 223 meters, the reservoir is assumed to retain a volume of approximately 0.36 km^3. The volumes at the cross sections range from 38.5 km^2 to 42.2 km^2. As previously mentioned, for wet-dry problems, the conservation of mass is dependent on the tolerance parameters specified by the user which controls how accurately ADH solves the continuity and momentum equations. For the gradual breach simulation, the mass was conserved to 8-percent. The error in Table 5 shows how well ADH conserved the mass at each cross section.

The maximum peak depths for the gradual breach inundated area are over 20 meters and occur in the channel. The floodplain depths range from 0.5 meters to less than 6 meters, with a few scattered pockets of slightly higher depths. The peak unit flow rates in the floodplain are less than 10 m^2/s and in the channel, the peak unit flow rate is over 120 m^2/s. The flood wave arrives at the floodplain about 45 minutes after the initial breach and reaches the downstream boundary after a little over 140 minutes. The flood wave was completely in the lake after 3.3 hours. Peak flood depth, peak unit flow rate and the flood arrival times are shown in figures 9 through figure 11, respectively.

Table 5: Maximum Discharge for Gradual Breach Event

Location	Time of Maximum Discharge (seconds)	Maximum Discharge (cms)	Total Volume (km^3)	Error
At the Dam	2000	17,357	38.93	-
X-Section 1	1690	16,717	38.54	0.99
X-Section 2	2246	16,839	39.03	1.0
X-Section 3	1029	16,447	40.19	1.03
X-Section 4	1174	20,527	40.82	1.05
X-Section 5	1409	18,185	42.21	1.08
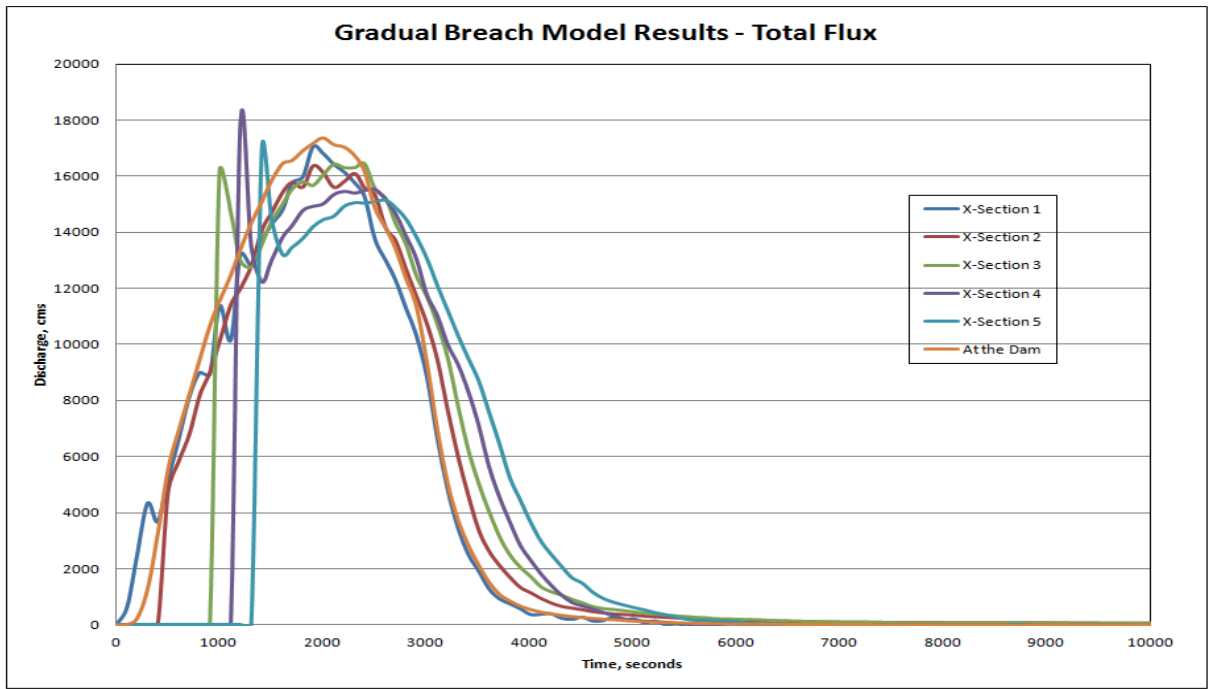
Figure 8 Maximum Discharges for Gradual Breach Event.
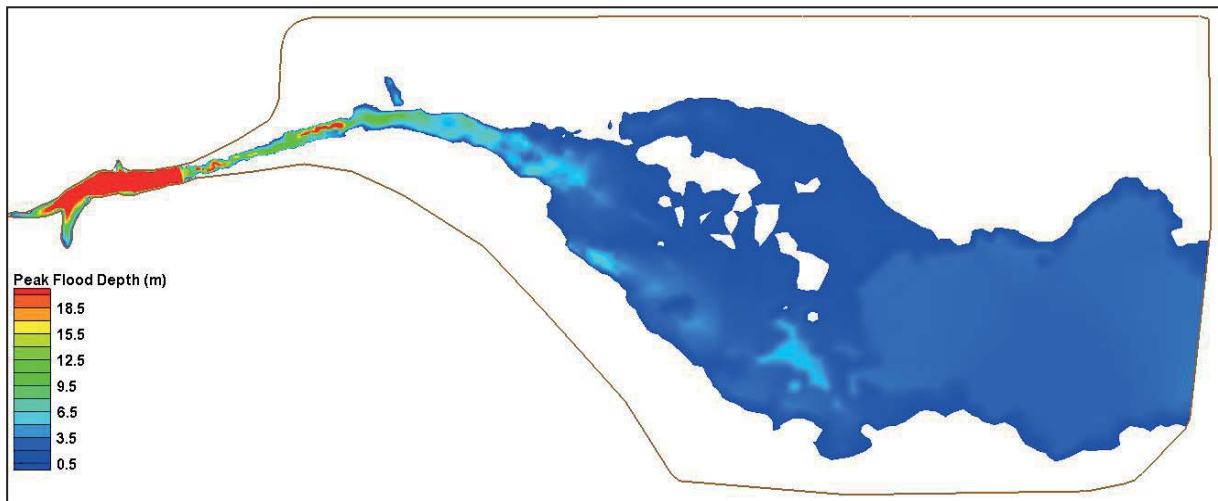
Figure 9 Peak Flood Depth in meters for Gradual Breach Event.
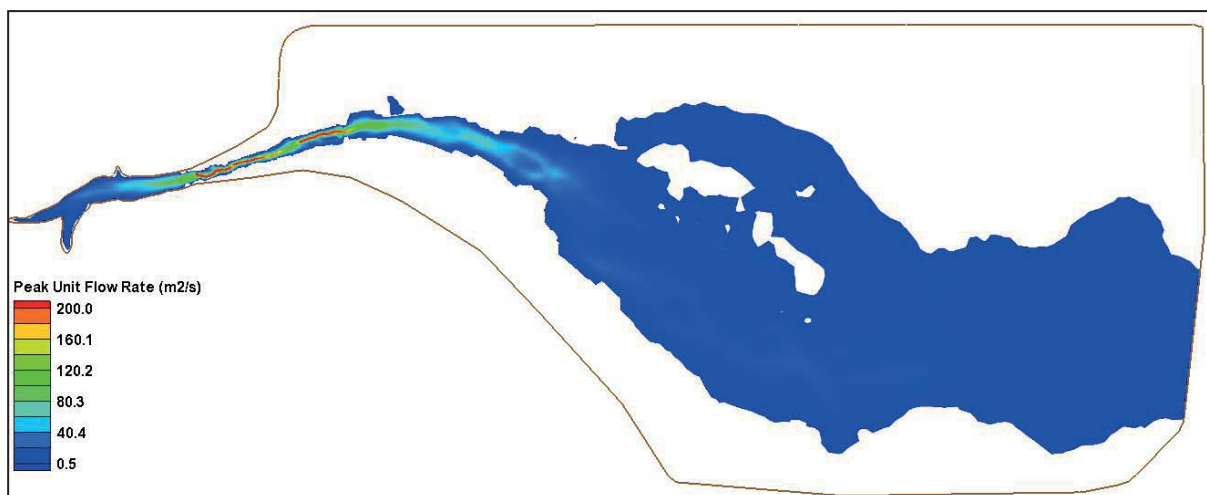
Figure 10 Peak Unit Flow Rate in square (m²/s) for Gradual Breach Event.
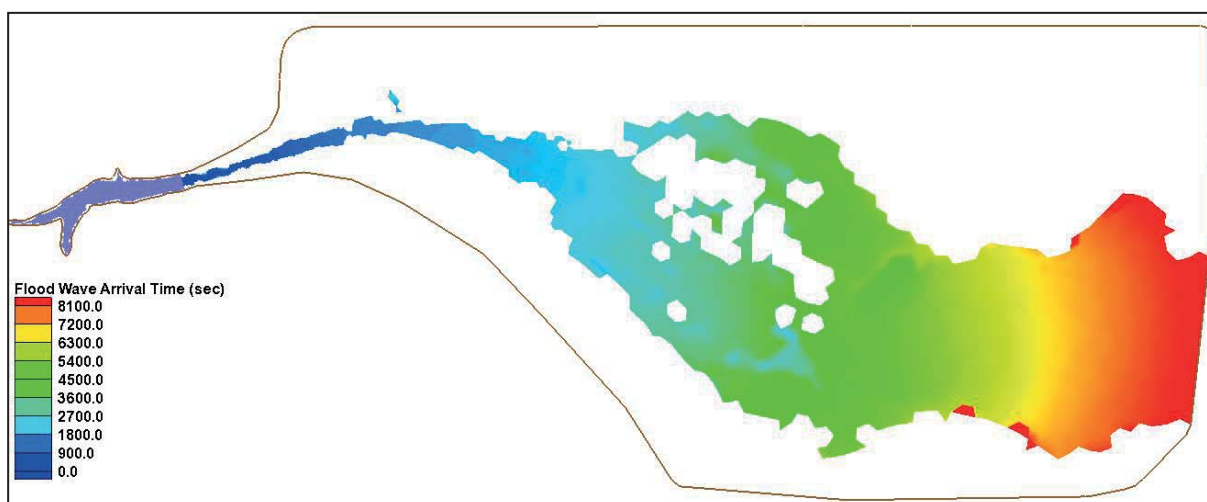
Figure 11 Flood Wave Arrival Times for Gradual Breach Event.

The total flooded area, excluding the lake, was slightly over 20 km². The total population at risk from this inundation is over 9,000 people. The highest population at risk occurs within the first 75 minutes of the breach and affects over 15,500 people. As mentioned previously, as the flood wave travels downstream, the single snap shots in time may over lap resulting in the duplication of the number of population at risk. This is the case for the gradual breach which results in the total population at risk at the end of 3 hours being double the total population at risk from the peak flooded area. Again, the more reasonable assessment of the total population at risk should be based on the peak depth flooded area. For the 12-year and under age demographic, the total population at risk after 3 hours is over 3,500 and half that, about 1,600 for the maximum flooded area. The 65-year and over age demographic has over 3,000 at risk after 3 hours and around 1,700 for the maximum flooded area. The maximum inundated area affected by depths greater than 8 meters is 1.99 km². The total population affected by these depths is less than 300, with the 12-year and under population at risk slightly over 50 and under 30 for the 65-year and over demographics.

Table 6: Total Population at Risk for Gradual Breach Event

Time Intervals (minutes)	Total Population at Risk	12-yr and Under Population at Risk	65-yr and Over Population at Risk

15	217	32	29
30	2,871	738	208
45	2,966	760	223
60	4,795	882	890
75	4,812	728	1,024
90	1,664	233	395
105	800	114	199
120	182	18	62
135	82	6	28
150	32	3	8
165	30	3	8
180	38	4	10
Total	18,489	3,523	3,084

Table 7: Flooded Area Population at Risk for Gradual Breach Event

Peak Flood Depth Range (meters)	Flooded Area excluding lake (km^2)	Total Population at Risk	12-yr and Under Population at Risk	65-yr and Over Population at Risk
>/= 1	20.02	9,226	1,600	1,699
>/= 2	10.00	4,107	892	541
>/= 3	5.85	2,768	699	220
>/= 4	3.99	2,121	531	166
>/= 5	3.05	1,302	321	101
>/= 6	2.49	326	142	48
>/= 7	2.21	401	86	34
>/= 8	1.99	272	52	27
Total	20.02	9,226	1,600	1,699
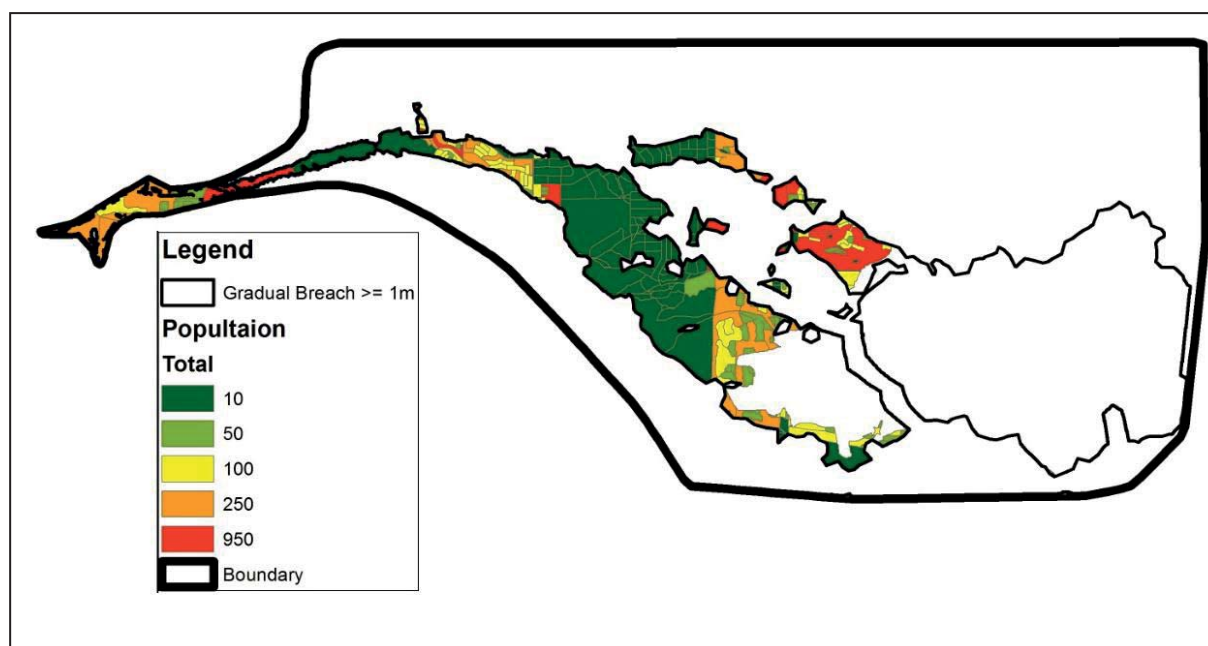
Figure 12 Total Populations at Risk for Gradual Breach Event

Conclusion

The results from the catastrophic breach event showed a total flooded area, excluding the lake, of 41.1 km^2 which affects over 28,800 people.   The total number of 12-year and under affected by the maximum inundated area is over 4.600 and the total number of 65-year and over is over 4,200. The flooded area with depths greater than 8 meters is 3.3 km^2 and affects about 1,700 individuals, over 400 are 12-year and under and over 130 are 65-year and over. The greatest number of the population at risk occurs within the first hour of the dam breach resulting in over 26,000 being affected. Three hours after the initial dam breach, the majority of the flood wave has reached the lake and no longer affects the city of Hydropolis.

The gradual breach scenario assumed breaching was caused by overtopping resulting in 80-percent of the dam being removed. The time to reach the maximum breach and the maximum width were determined using equations developed by Froehlich (1995a). The results showed a total flooded area excluding the lake of over 20 km^2 which affects over 9,200 people. The number of 12-year and under affected by the maximum flooded area is 1,600 and the number of 65-year and over is 1,699. The flooded area with depths greater than 8 meters is 1.99 km^2 affects less than 300 individuals with over 50 being 12-year and under and less than 30 being 65-year and over. The majority of the population at risk occurs within the first 90 minutes of the dam breach; however the total number is skewed because the inundated area for each time interval overlaps.

These results represent the impacts of a dam breach, whether that breach is catastrophic or gradual. Though loss of life was not calculated using the described model, the population at risk was significant. Additionally, economic impacts were not considered, as this is not part of the applied model. Even without these values available for comparison, there are many data elements that will be useful in comparing the ADH model to other models presented at this workshop. The use of the virtual test bed should prove to be a valuable tool, both now and in the future, for comparison of such models.

References

[1] Aquaveo (2009). "Surface-water Modeling System Version 11.0", Aquaveo. http://www.aquaveo.com/pdf/SMS_11.0.pdf.

[2] Arcement, G.J., Schneider, V.R. "Guide for Selecting Manning's Roughness Coefficients for Natural Channels and Flood Plains" U.S. Geological Survey Water-supply Paper 2339. http://www.fhwa.dot.gov/bridge/wsp2339.pdf

[3] Berger, R.C. and Lee, L.M. (2004) "Multidimensional Numerical Modeling of Surges Over Initially Dry Land." Coastal and Hydraulics Engineering Technical report, ERDC/CHL TR-04-10. Vicksburg, MS: U.S. Army Engineering Research and Development Center.

[4] Berger, R.C., Tate, J.N., Brown, G.L., and Savant, G. (2010). "Adaptive Hydraulics: User Manual." Vicksburg, MS: U.S. Army Engineering Research and Development Center. https://adh.usace.army.mil/.

[5] Engineer Research and Development Center (ERDC) DoD Supercomputing Resource Center (DSRC), http://www.erdc.hpc.mil/docs/diamondUserGuide.html, accessed December 5, 2011.

[6] Martin, S.K., Savant, G., and McVan, D.C. (2010). "Lake Borgne Surge Barrier Study." Coastal and Hydraulics Engineering Technical Report, ERDC/CHL TR-10-10. Vicksburg, MS: U.S. Army Engineering Research and Development Center.

[7] Martin, S.K., Savant, G. and McVan, D. (2011) "Two Dimensional Numerical Model of the Gulf Intracoastal Waterway Near New Orleans: Case Study", Journal of Waterway, Port, Coastal and Ocean Engineering, doi:10.1061/(ASCE)WW.1943-5460.0000119.

[8] McAlpin, T.O., Berger, R.C., and Henville, A.M. (2009). "Bush Canal Floodgate Study." Coastal and Hydraulics Engineering Technical Report, ERDC/CHL TR-09-09. Vicksburg, MS: U.S. Army Engineering Research and Development Center.

[9] Oregon Department of Transportation (2005). "Hydraulics Manual (Part 1); Chapter 8, Appendix A". Engineering and Asset Management Unit Geo-Environmental Section. ftp://ftp.odot.state.or.us/techserv/Geo-Environmental/Hydraulics/Hydraulics%20Manual/Chapter_08/Chapter_08_Appendix_A/Chapter_08_Appendix_A.pdf

[10] Savant, G., Berger, R.C., McAlpin, T.O., and Tate, J.N. (2011). "An Efficient Implicit Finite Element Hydrodynamic Model for Dam and Levee Breach." Journal of Hydraulic Engineering, ASCE. Vol. 137, No. 9, pp: 1005-1018.

[11] Savant, G and Berger, R.C. (2011) "Wetting and Drying Characteristics of Adaptive Hydraulics." USACE, ERDC Technical Note, USACE/ERDC-11-DRAFT, In Progress.

[12] Stockstill, R.L. and Vaughan, J.M. (2009). "Numerical Model Study of the Tuscarawas River below Dover Dam, Ohio." Coastal and Hydraulics Engineering Technical Report, ERDC/CHL TR-09-17. Vicksburg, MS: U.S. Army Engineering Research and Development Center.

[13] Stockstill, R.L., Vaughan, J.M., and Martin, S.K. (2010). "Numerical Model of the Hoosic River Flood-Control Channel, Adams, MA." Coastal and Hydraulics Engineering Technical Report, ERDC/CHL TR-10-01. Vicksburg, MS: U.S. Army Engineering Research and Development Center.

[14] Tate, J.N., Lackey, T.C., and McAlpin, T.O. (2010). "Seabrook Fish Larval Transport Study." Coastal and Hydraulics Engineering Technical Report, ERDC/CHL TR-10-12. Vicksburg, MS: U.S. Army Engineering Research and Development Center.

Assessment of ICOLD Benchmark Case Study using Flood2D-GPU and HEC-FIA

B. A. Thames [1] and A. J. Kalyanapu [2]

[1] US Army Corps of Engineers, 801 Broadway, Nashville, TN 37203, USA
[2] Department of Civil & Environmental Engineering, Tennessee Technological University, 1020 Stadium Drive, Prescott Hall 334 Box 5015, Cookeville, TN 38505, USA

E-mail: brantley.a.thames@usace.army.mil

Abstract

This paper presents a benchmark case study of a dam failure using Flood2D-Graphics Processing Unit (GPU), a two-dimensional hydraulic modeling software, coupled with the Hydrologic Engineering Center's Flood Impact Analysis (HEC-FIA) software, a flood consequence model, to evaluate flood risk in a hypothetical test bed environment. The defined objective of this study is to present the findings prescribed by the ICOLD Theme "C" Formulation Team, which include inundation mapping, population at risk, loss of life, and direct economic impacts. The increased computational capability afforded by Flood2D-GPU allows for a much deeper analysis of the hypothetical scenario. Many studies have been conducted to evaluate the uncertainty in the estimation of breach parameters (breach width and time of failure); however, how breach parameter estimation uncertainty affects the uncertainty in consequence estimation has been rarely evaluated. A secondary objective of this study is to determine the affects of breach parameter estimation uncertainty on consequence estimation uncertainty through a comparative analysis of four breach parameter estimation (BPE) methods and a sensitivity analysis of the main breach parameters such as breach depth, breach width, time of failure, and breach side slope. Through these analyses, breach depth, typically assumed using engineering judgment, is found to be the most sensitive breach parameter. Similar breach formation times are computed for three of the BPE methods, Froehlich (1995a), Froehlich (2008), and Von Thun and Gillette, evaluated while varying breach widths are computed; however, the consequence results are similar despite the varied breach width computations highlighting the importance of breach formation time.

Introduction

With the increased awareness of the infrastructure deficiencies within the United States and world-wide, dam safety and understanding the impacts of dam failures has become much more emphasized due to the large number of dams world-wide with population centers within the destructive path of dam failure discharges. Studies such as these strive to better define the hydraulics of a dam failure and the resulting flood impacts.

Many US federal agencies, such as the US Army Corps of Engineers (USACE), the Department of Homeland Security (DHS), and the Bureau of Reclamation (USBR), are working diligently through research and practical analysis to better understand the mechanics of a dam failure. This case study provides insight into hydraulic and consequence modeling tools available to simulate a dam failure and evaluate possible impacts from flooding.

Methodology

Various modeling software are used to obtain the risk assessment results prescribed by the ICOLD formulation team for Theme C, which consist of an array of hydraulic and consequence-based products. To evaluate the proposed problem, a dam breach discharge hydrograph is first developed using the unsteady flow component of the Hydrologic Engineering Center's River Analysis System (HEC-RAS) version 4.1. The dam breach discharge hydrograph is a necessary input into Flood2D-GPU, which leverages the computer's graphics card for much improved computational capabilities of the model input [8]. Output from Flood2D-GPU, which includes inundated areas, depth grids, and flood wave arrival time grids, serve as inputs into HEC-FIA, which provides the consequence assessment for the solution to the problem statement. HEC-FIA is a single event GIS-based software that determines impacts from flooding, such as population at risk (PAR), economic damages, and loss of life (LOL) on a structure-by-structure basis [9].

Ultimately, a dam failure within the proposed hypothetical test bed is evaluated using this combination of modeling software through a comparative analysis of the four suggested BPE techniques and a sensitivity analysis of four breach parameters to evaluate the range of possible PAR, LOL, and economic damage outcomes and the sensitivity of these outcomes to breach parameter estimations.

Development of Dam Failure Hydrograph (HEC-RAS)

HEC-RAS is utilized to generate dam failure discharge hydrographs for input into Flood2D-GPU. HEC-RAS is one-dimensional hydraulic model capable of performing unsteady flow dam failure simulations utilizing user-provided hydraulic inputs (cross-section and inline structure geometry, boundary conditions, Manning's n-values, etc.) and breach parameters (breach opening dimensions and location, breach weir coefficients, breach formation time, etc.) [13].

The HEC-RAS model developed for this evaluation uses the information provided by the formulation team including a digital elevation model (DEM), a land use layer, and information about the dam embankment and failure scenario. Because the only purpose of the HEC-RAS model is the generation of a dam failure discharge hydrograph, the extent of the model is limited to the reach just adjacent to the proposed dam.

The HEC-RAS model geometry is developed by processing the DEM using HEC-GeoRAS, a data pre- and post-processing software developed for HEC-RAS. The HEC-RAS model consists of a storage area to represent the reservoir above the dam, an inline structure representing the dam and the necessary bounding cross sections upstream and downstream of the dam. The stage-volume curve provided by the formulation team is utilized in the HEC-RAS model to represent the storage characteristics of the reservoir. The cross section geometry is developed directly from the DEM and imported into HEC-RAS using HEC-GeoRAS. The inline structure geometry is developed using a combination of information provided by the formulation team in the problem statement and the DEM.

The most critical input into the HEC-RAS model is the determination of the breach geometry and parameters that include the final breach bottom width (W_b), final breach invert elevation (El_b), breach side slopes (SS), and breach formation time (t_f). [16] conducted an uncertainty analysis of embankment dam breach parameters for all of the proposed BPE approaches provided by the formulation team with the exception of Froehlich (2008), which did not exist at the time of publication. This study focuses on four BPE methods: Froehlich 1995a [3],

Froehlich 2008 [5], the MacDonald and Langridge-Monopolis (MLM) [10], and the Von Thun and Gillette (VTG) [15] methods, and the calculated or assumed values are presented in Table 1. [16] shows through an uncertainty analysis, that in predicting breach width, breach failure time, and peak flow through the breach, the Froehlich (1995a) technique produced the lowest mean prediction error and the narrowest width of uncertainty band for all three estimations. The only exception to this is the width of the uncertainty band for the breach width estimation which is only slightly larger than the VTG technique. Based on these results, the Froehlich (1995a) BPE technique emerges as the best compromise; however, the current study compares the four methodologies across the range of sensitivity for all methods to highlight the range of possible outcomes in terms of hydraulic and consequence results. In addition, this evaluation provides a better understanding of how breach parameter sensitivity affects consequence estimation uncertainty through a sensitivity analysis of four breach parameters, SS, W_b, El_b, and t_f, for each BPE method. The sensitivity analysis approach involves computing these four breach parameters using each BPE method (Table 1) and adjusting these values to create a sensitivity range. SS, W_b, and t_f are increased and decreased by 25 and 50%. Because the initial assumption is that the breach height formation will extend to the toe of the dam for all BPE methods, the sensitivity range for El_b is developed by increasing the base assumption of 211m by 7.625m or one eighth of the total breach depth (h_b) until the value reaches half of the total breach depth.

Using the computed values from Table 1, a base condition breach failure hydrograph is developed for each BPE method using HEC-RAS serving as the basis for the comparative analysis. In addition, breach hydrographs are developed for the range of sensitivity values. Sixty eight simulations are computed to produce breach hydrographs for input into Flood2D-GPU. In interest of space, the resulting breach hydrographs for the four base condition simulations are presented in Figure 1.

Table 1: Computed Breach Parameter Estimates using the Four BPE Methods

Parameter	Froehlich (1995a)	Froehlich (2008)	MLM (1984)	VTG (1990)
SS	1.4	1.0	0.5	1.0
W_b	62 m	110 m	12 m	207 m
h_b	61 m	61 m	61 m	61 m
t_f	0.7 hrs	0.6 hrs	2.0 hrs	0.9 hrs
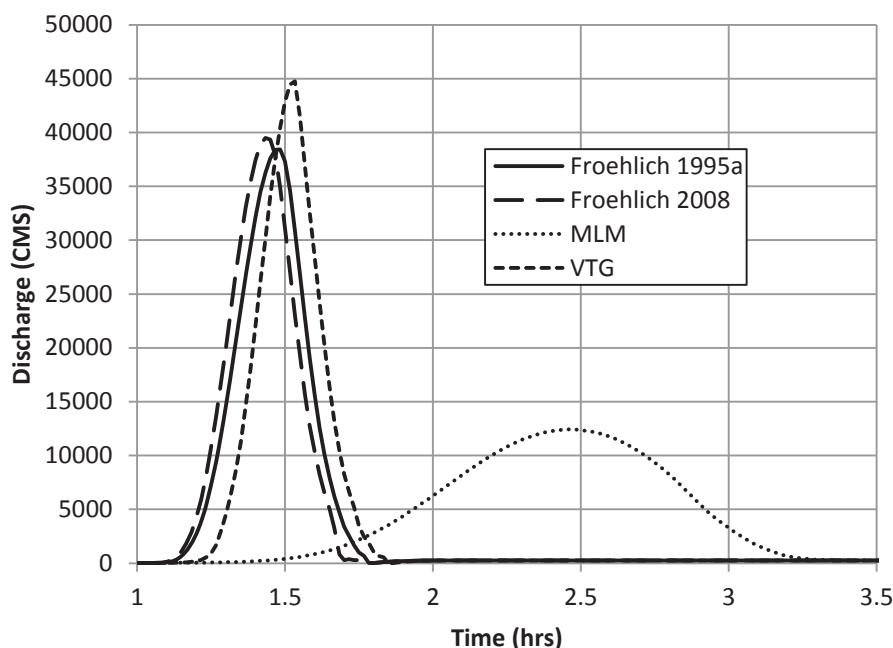
Figure 1: Computed Discharge Breach Failure Hydrographs from unsteady flow HEC-RAS Model for Base Simulations

Two-Dimensional Hydraulic Modeling (Flood2D-GPU)

In this study, a GPU flood model, named Flood2D-GPU, developed in NVIDIA's CUDA programming environment is used [8]. The modelling framework uses the 2D unsteady numerical flood model that solves the non-linear hyperbolic shallow water equations using a first-order accurate upwind difference scheme. These equations are developed from the Navier-Stokes equations by integrating the horizontal momentum and continuity equations over depth often referred to as the depth averaged or depth integrated shallow water equations (i.e., Saint Venant equations). The non-conservative form of the partial differential equations is [7;8;12]:

$$\frac{\partial h}{\partial t} + \frac{\partial uh}{\partial x} + \frac{\partial vh}{\partial y} = 0 \qquad \text{Continuity Equation} \quad (1)$$

$$\frac{\partial u}{\partial t} + u\frac{\partial u}{\partial x} + v\frac{\partial u}{\partial y} + g\frac{\partial H}{\partial x} + gS_{fx} = 0 \qquad \text{Momentum Equation in x-direction} \quad (2)$$

$$\frac{\partial v}{\partial t} + u\frac{\partial v}{\partial x} + v\frac{\partial v}{\partial y} + g\frac{\partial H}{\partial y} + gS_{fy} = 0 \qquad \text{Momentum Equation in y-direction} \quad (3)$$

where, h is the water depth, H is the water surface elevation, u is the velocity in the x-direction, v is the velocity in the y-direction, t is the time, g is the acceleration due to gravity, S_{fx} is the friction slope in the x-direction, and S_{fy} is the friction slope in the y-direction. The upwind finite difference numerical scheme is used to discretize governing equations (1-3), as it yields non-oscillatory solutions, through numerical diffusion [2;11]. A staggered grid computational stencil is used to define the computational domain with the water depth (h) in the centre of the cell and u and v velocities on the cell edges. The model requires a digital elevation model (DEM) to represent topography, Manning's n for surface roughness representation and a flow hydrograph. The CPU environment in this module consists of the

random number generator, and storage of input data and parameters and source code to calculate future time step using Courant condition, and implement hydrograph update. The GPU environment contains the computational engine that solves continuity and momentum equations, and boundary condition implementation. A 2D model is chosen because of its better representation of flood flow (especially in floodplains) simultaneous flood extent delineation and instantaneous flood velocities at all nodes in the computational domain. Flood2D-GPU is validated for accuracy and found to provide significantly reduced computational time (up to two orders of magnitude) compared to the same flood model implemented serially in a CPU-based environment [8].

Application of Flood2D-GPU in this study uses HEC-RAS dam breach hydrographs, Manning's n map generated from the land use/cover data provided along with the digital elevation model (with dam burnt into the topography). The methodology of dam breach hydrograph is explained in previous section. To develop spatially variable Manning's n surface map, the National Land Cover Dataset (NLCD) Land cover (LC) codes were used to estimate approximate Manning's n values based on recommendations from [6]. Table 2 provides the LC code and its assigned Manning's n value and Figure 2 depicts the resultant spatially variable Manning's n map.

Table 2: Estimated Manning's values for National Land Cover Dataset

NLCD LULC Class Name	LULC Code	Manning's n
Open Water	11	0.025
Developed, Open Space	21	0.016
Developed, Low Intensity	22	0.030
Developed, Medium Intensity	23	0.030
Developed, High Intensity	24	0.050
Barren Land (Rock/Sand/Clay)	31	0.025
Deciduous Forest	41	0.120
Evergreen Forest	42	0.200
Shrub/Scrub	52	0.070
Grassland/Herbaceous	71	0.050
Pasture/Hay	81	0.030
Cultivated Crops	82	0.035
Woody Wetlands	90	0.160
Emergent Herbaceous Wetlands	95	0.110
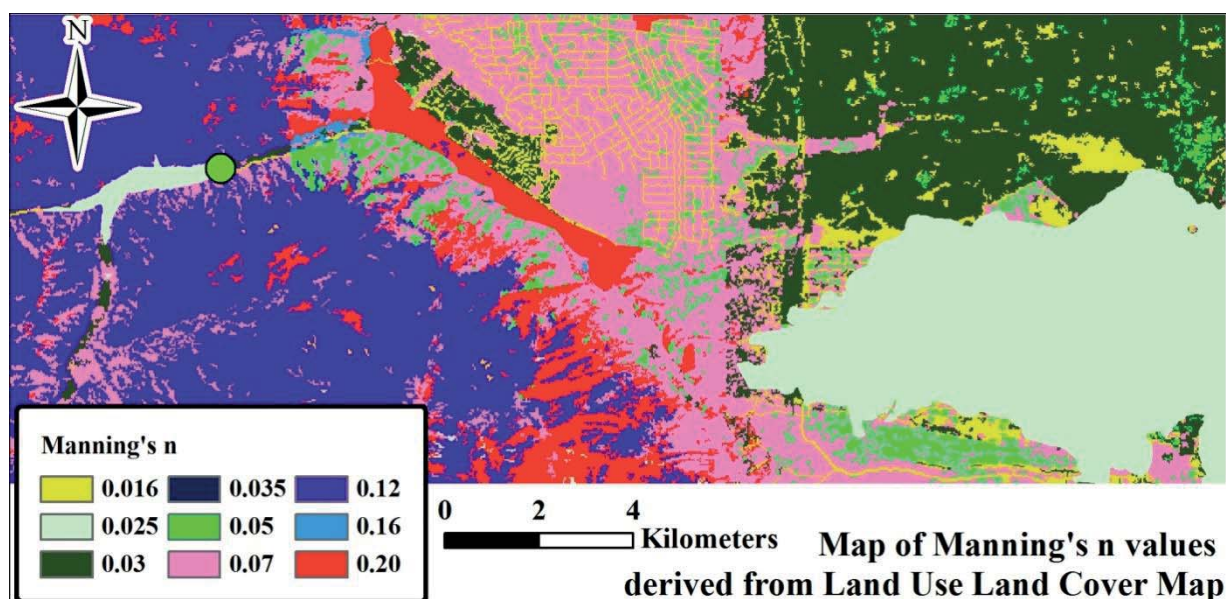
Figure 2: Land Use Land Cover Derived Manning's Map for the case study

Consequence Assessment (HEC-FIA)
HEC-FIA is used to determine the consequences, such as PAR, economic damages, and LOL, using the results of the Flood2D-GPU simulations. [9] presents that "HEC-FIA is a stand-alone, GIS enabled model for estimating flood impacts due to flooding…that generates required economic and population data…to compute urban and agricultural economic flood damage, area inundated, number of structures inundated, population at risk, and loss of life." Input requirements for HEC-FIA include a stream alignment, terrain grid, depth grid, arrival time grid, a structure inventory, and timing information for the purpose of evaluating a single event [9]. Based on the information provided by the formulation team, several assumptions and derivations from the provided data are made to develop the required inputs into HEC-FIA.

ArcHydro Tools, an extension of ArcGIS Desktop, is used to create a stream centerline by processing the DEM. The depth and arrival time grids for all simulations are derived from the results of the Flood2D-GPU simulation. The depth grid required for HEC-FIA is the max depth grid; however, additional depth grids for the specified time intervals were derived for the required PAR, LOL, and economic damage results. The arrival time grid is assumed to be the time after failure at which the flood depth will reach two feet of depth.

For this study, the structure inventory must include a structure name, occupancy type, damage category, structure value, and population information in order to derive the prescribed results. HEC-FIA utilizes two separate databases, a structure occupancy and global inventory table, to define the structure inventory against which all consequence estimations are made.

The structure occupancy table consists of general occupancy types, such as residential, commercial, and industrial, and, for this study, is populated using occupancy types using the database that comes with Federal Emergency Management Agency's (FEMA) HAZards United States – Multi-Hazard (HAZUS-MH) Tool [1]. The structure occupancy type table includes the content-to-structure value ratio for defining content values for each structure, links to depth-damage curves for structure and content values, and risk elevations for defining at what elevation an individual is at risk of fatality based on age. HEC-FIA only considers

two age groups, those under and over the age of 65; however, to ascertain consequence results for populations under the age of 14, a separate HEC-FIA model is created for each simulation. The assumption is that anyone under the age of 14 would be accompanied by an adult and either carried vertically to safety or is mobile enough to move vertically to safety.

The global inventory table consists of each structure, or parcel for this study, and specific parameters related to each structure such as depth-damage curves for the structure and contents, structure and content value, first floor elevations, and number of stories. This information is either user-defined or derived from other sources such as the DEM or through a relationship with the structure occupancy type table. For instance, the depth-damage curves for the structure and contents are adopted from the structure occupancy type table by way of the general occupancy type assigned to each structure by the user. The structure appraised values, population values for the various age groups, structure name, and number of stories is defined by the user in ArcGIS Desktop and imported into HEC-FIA. First floor elevations are derived from the DEM and increased by an assumed three feet to account for foundation height.

The most time intensive process is related to the development of the global inventory. Spatially joining the parcel dataset layer with the census block layer in ArcGIS Desktop to compute the number of parcels per census block provides the ability to uniformly distribute the necessary population values for the age groups of interest, under 14, between 14 and 65, and over 65 years of age, into each parcel. The uniformly distributed population values are spatially joined back to the parcel dataset to attain an age group specific population value for each parcel.

With no structure values and limited information regarding structure condition and square footage provided by the formulation team, the structure values are assumed for each occupancy type provided in the parcel dataset through collaboration with a US Army Corps of Engineers (USACE) economist to achieve reasonable values for each structure occupancy type (Table 3). Each structure is assigned a generic name based on the occupancy type. The structure name, population, structure values, and HAZUS occupancy type are compiled within ArcGIS Desktop and imported into HEC-FIA's global inventory.

Table 3: Estimated Structure Value Assumptions

Zone	Description	Estimated Value ($1000)
A-1	Rural Agriculture - 1-ac Minimum Zone	50
C-1	Neighborhood Commercial Zone	650
C-2	Community Commercial Zone	650
O-1	Office and Institutional Zone	1000
P	Parking Zone	750
R-1	Single Family Residential Zone	125
R-2	Residential Zone: Houses, Townhomes and Medium Density Apartments	1000
R-3	Residential Zone: Houses, Townhomes and High Density Apartments	2500
RA-1	Residential and Agricultural Zone, Semi-Urban Area	75
R-D	Residential and Related Uses Zone, Developing Area	100
R-LT	Residential Zone: Houses and Limited Townhomes	750
R-T	Residential Zone: Houses and Townhomes	500
SU-1	Special Use Zone	1500
SU-2	Special Neighborhood Zone, Redeveloping Area	125

A time window is needed for each HEC-FIA simulation, which defines a start, end, and warning issuance time for each simulation. The start time is based on the initiation of the breach. The assumption of no warning is made based on the scenario described of no cell phone service and no emergency action plan. [9] assert that warning time plays a critical role in preventing loss of life and property, and as such, is a very sensitive parameter in the HEC-FIA software. The sensitivity of warning time also emphasizes the importance of a robust warning system especially in situations of high risk dams just upstream of major population centers.

PAR, LOL, and economic damages at specific time intervals are required results for this study. Because of the manner in which HEC-FIA treats incremental changes in PAR, LOL, and economic damages, depth grids, derived from Flood2D-GPU results, for each of these time intervals are simulated individually through HEC-FIA to develop these consequence results and post-processed to determine the PAR, LOL, and economic damages incrementally for each time interval. Because this is a labor intensive task, this time interval analysis is only conducted for the four base BPE method simulations.

With all of the necessary information pre-processed and imported into HEC-FIA, two simulations, one for over and under the age of 65 and one for under the age of 14, are set up and run for each BPE method simulation, each sensitivity range, and for each required time interval totaling 184 HEC-FIA simulations. The results from these simulations are presented in the Results and Discussion section, and electronic copies of the required models, modeling outputs, GIS results, and spreadsheet results are provided supplemental to this document.

Results and Discussion

Two-Dimensional Hydraulic Modelling Results
In this report, the two-dimensional hydraulic modeling results using the base condition Froehlich 1995a BPE method are presented results and used in comparisons. Also, a sensitivity analysis of four breach parameters is evaluated and results are compiled and discussed. Additional results from these analyses and from other BPE methods are provided supplemental to this report.

The Froehlich 1995a base simulation resulted in flood depths ranging from 0.5 m to nearly 8 m in the downstream areas of the dam. Figure 3 presents the map of the standard deviation in the peak flood depths from the multiple breach hydrographs which were derived from the sensitivity analysis of the four breach parameters. A high variation in the peak flood depths is noticed along the canyon immediately downstream of the dam. In the downstream region away from the mountainous terrain, smaller standard deviation in simulated peak flood depths is noticed that indicates less sensitivity due to the breach parameters. Thus it is likely that variability in consequence estimates including direct flood damages, LOL, PAR in the downstream region may be smaller compared to the upstream region of the floodplain. A similar trend is also observed in the maximum flood velocities for these breach hydrographs.
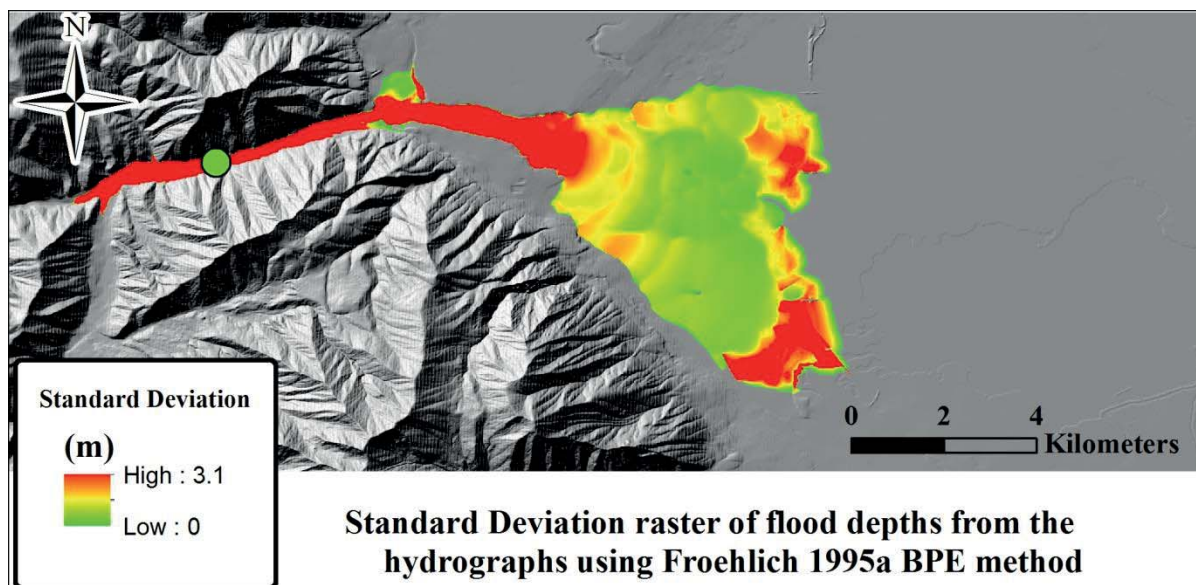
Figure 3: Standard deviation map of the peak flow depths from the dam breach hydrographs developed for the four breach parameters using Froehlich 1995a BPE method

Figure 4 presents the simulated flood discharge hydrographs at the five required cross-section locations. For the Froehlich 1995a BPE method, the variability of flood discharge from all the sensitivity runs are represented by the error bars. It is observed that a large variability in the magnitude of flood discharge is observed at the beginning of the dam breach. This is attributed to the influence of breach parameter sets used for generating the hydrographs. This is a clear indication that the consequence analysis, especially the LOL, PAR, direct economic damages during the initial 60 minutes of the breach, will be significantly affected by the choice of breach parameters used. With progression of time, the variability decreases at all cross-section locations.
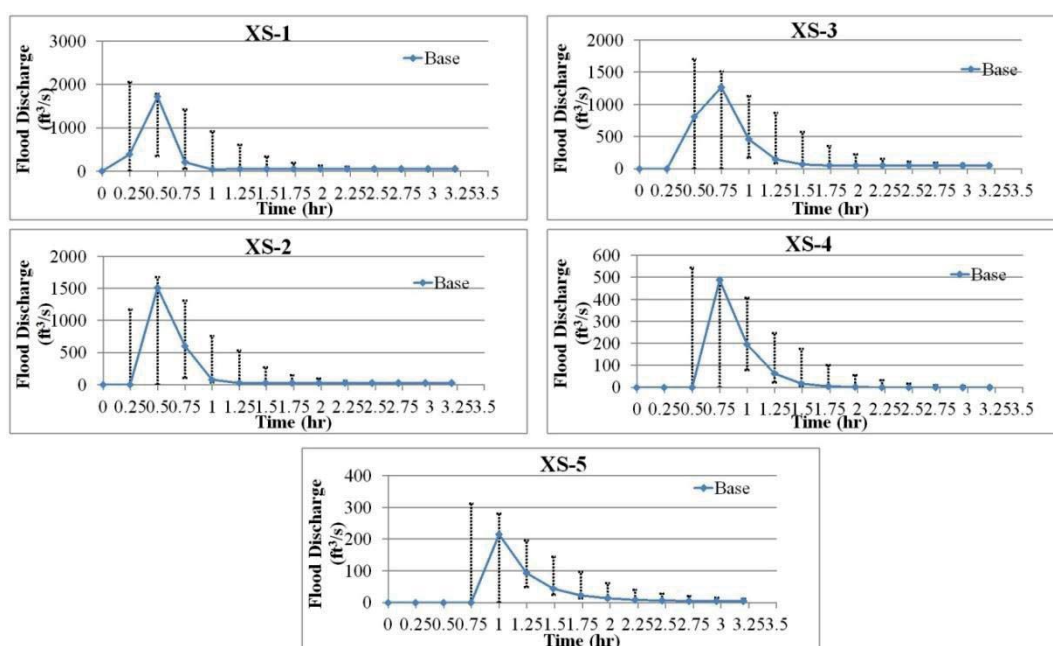
Figure 4: Simulated flood discharge plots at the five cross-section locations for the Froehlich 1995a BPE method. Error bars indicate the variability of discharges due to various breach parameter sets.

Consequence Assessment Results

For the purposes of presenting results and making comparisons, the consequence results using the base condition Froehlich 1995a BPE method is considered the basis of the comparative analysis. In addition to this comparative analysis, a sensitivity analysis of four breach parameters are evaluated for each BPE method and results are compiled and discussed in this report. Additional results from these analyses are provided supplemental to this report.

The Froehlich 1995a base simulation results in a PAR of 13976 persons with 2223 persons (about 16% of total PAR) under the age of 14 and 2695 persons (about 19% of total PAR) over the age of 65. HEC-FIA estimates a fatality total of 1914 persons under these simulation conditions, which is almost 14% of the total PAR. In reality, the total LOL seems to be inflated and is probably overestimated when considering the resilience and resourcefulness of a typical population. However, the assumption of no warning time appears to be the largest source of the elevated LOL totals, and a sensitivity of this assumption could provide a large range of possible outcomes for LOL. For instance, a warning just 15 minutes in advance of the breach reduces the total estimated LOL by 55% to 862 persons. A warning 1 hour in advance of the breach results in an estimated LOL of 511 persons or a 73% reduction.

Direct economic damages are estimated using HEC-FIA using a depth of flooding derived from the depth grid and a first floor elevation for each structure in combination with a depth-damage curve. The total economic damages estimated by HEC-FIA are approximately $361 million dollars; however, this value is based strongly on the structure value assumptions made based on occupancy type and the content-to-structure value ratio derived from the FEMA HAZUS-MH Tool [1].

For the Froehlich 1995a base simulation, Table 4 shows incremental PAR, LOL, and direct economic impacts for specified time intervals. The PAR does not become affected by flooding until 30 minutes after the initiation of the dam breach based on flood wave propagation estimated by Flood2D-GPU and the population provided by the census block dataset. However, during the 30-60 minute time interval following the breach a large percentage of the PAR becomes affected and the greatest LOL occurs during this period. The greatest percentage of the PAR actually becomes affected in the 120-180 minute time interval due to an area of low population in the center of the damage reach. Interestingly, the LOL during the 120-180 minute time interval is not substantial even with the larger PAR due to lower flood depths allowing individuals to retreat vertically to safety within each structure. The decreased flood depths also explain why the direct economic damages are also greatest in the 30-60 minute time interval as opposed to the 120-180 minute time interval.

Table 4: Incremental Time Interval Results for the Froehlich
1995a Base Simulation

Time Interval (min)	Total PAR	14-yr and Under PAR	65-yr and Over PAR	LOL	Direct Economic Impact ($US)
0-15	0	0	0	0	$0.00
15-30	0	0	0	0	$0.00
30-60	2915	755	210	1549	$128,971,979.93
60-90	512	122	31	329	$77,632,731.34
90-120	1410	168	347	5	$42,877,015.97
120-180	7638	956	1835	7	$85,161,297.09
> 180	1501	222	273	24	$26,714,802.91
Total	**13976**	**2223**	**2695**	**1914**	**$361,357,827.24**

The majority of the flooding by area occurs at the lower depths of flooding (0 to 1.5m) with a majority of the PAR contained within these same lower depths of flooding. Table 5 illustrates the distribution of PAR and flooded area across the various depth ranges.

Table 5: Incremental Depth Range Results of PAR
and Flooded Area

Peak Flood Depth Range (m)	Flooded Area (m²)	Total PAR	14-yr and Under PAR	65-yr and Over PAR
0 - 0.5	3498463	2786	447	464
0.5 - 1	6433454	4993	664	1079
1 - 1.5	5310192	2056	267	488
1.5 - 2	3706161	887	89	286
2 - 2.5	2874378	424	49	126
2.5 - 3	2379332	262	35	71
3 - 3.5	1600888	107	29	8
3.5 - 4	756803	68	20	4
4 - 4.5	427789	69	19	5
4.5 - 5	337724	115	32	8
5 - 5.5	372655	217	59	15
5.5 - 6	378761	249	71	17
6 - 6.5	252956	155	43	11
6.5 - 7	247030	282	78	22
7 - 7.5	200874	228	61	16
7.5 - 8	198091	245	61	12
>8	2305519	827	199	62
Total	**31281068**	**13976**	**2223**	**2695**

Supplemental results for the various simulations are provided electronically.

When initially choosing a BPE method, the question of which technique provides the most accurate results is raised driving the need for a comparative and sensitivity analysis. The goal of this evaluation is to understand how the uncertainty of these methods and the sensitivity of the critical breach parameters affect the results of a consequence analysis. Table 6 summarizes the consequence results of both the comparative and sensitivity analysis.

For the comparative analysis, the results from the Froehlich 1995a, Froehlich 2008, and VTG base simulations are extremely similar while the results of the MLM base simulation are much lower than the other three simulations, which is expected based on the dam failure hydrographs computed using HEC-RAS.

The mean results for all parameters is typically only slightly less than the base simulation results. In addition, the base simulation results are typically much closer to the higher end of the range of values from the sensitivity analysis. A closer look at the results of the breach

invert sensitivity analysis shows that consequence results are very sensitive to the breach invert assumption. These breach invert simulations are skewing the range of consequence results on the lower end of the range while also lowering the mean of the sensitivity simulations.   The large values for standard deviation for all consequence results can also be attributed to the breach invert simulation runs. For the Froehlich 1995a sensitivity analysis, removing the breach invert sensitivity simulations from the statistical calculations produces a much tighter range for all consequence results with a 66% reduction in total PAR standard deviation, a 68% reduction in LOL standard deviation and an 80% reduction in direct economic impacts standard deviation, which indicates that these reductions in standard deviation are also due to the sensitivity of the breach invert parameter.

In terms of sensitivity, breach invert is, above all, the most sensitive breach parameter; however, when comparing the breach hydrograph and consequence results of the various BPE methods, time of formation also drives the shape and peak of the breach hydrograph, which is directly related to flood consequence results. In fact, the difference in breach hydrograph peak and shape between the MLM and other three BPE methods, which is quite significant, is primarily due to the longer time of formation computed for MLM.

In interest of space, many of the results discussed are not presented in this document; however, the results are provided supplemental to this report electronically.

Result		Froehlich 1995	Froehlich 2008	MLM	VTG
Total PAR		**13976**	**14190**	**4857**	**14072**
	Range	7614 - 14934	7710 - 15117	2598 - 10261	10261 - 14838
	Mean	13240	13380	5041	13459
	Standard Deviation	1770	1875	1796	1098
14 and Under PAR		**2223**	**2256**	**961**	**2240**
	Range	1271 - 2374	1282 - 2408	681 - 1616	1618 - 2357
	Mean	2095	2125	978	2138
	Standard Deviation	286	291	217	181
65 and Over PAR		**2695**	**2726**	**737**	**2710**
	Range	1396 - 2830	1419 - 2858	185 - 2039	2033 - 2817
	Mean	2553	2582	783	2608
	Standard Deviation	355	358	430	184
LOL		**1914**	**1810**	**988**	**2055**
	Range	1006 - 2016	1069 - 2008	503 - 1606	1437 - 2055
	Mean	1822	1801	930	1916
	Standard Deviation	245	221	282	157
Direct Economic Damages		**$361,357,827**	**$363,241,142**	**$233,781,020**	**$371,676,978**
	Range	$241,584,42 0 - $381,108,48 0	$242,015,26 0 - $367,496,61 0	$169,234,85 0 - $324,048,42 0	$276,986,72 0 - $380,023,87 0
	Mean	$350,512,327	$351,424,195	$230,385,592	$355,470,456
	Standard Deviation	$32,123,272	$32,438,404	$36,026,006	$23,441,647
Total Flooded Area (sq m)		**31,281,068**	**31,489,575**	**20,609,051**	**31,369,428**
	Range	22,487,230 - 33,959,242	22,603,157 - 34,037,724	13,478,150 - 27,580,205	25,127,420 - 35,073,793
	Mean	30,413,441	30,705,369	20,413,671	30,777,639
	Standard Deviation	2,862,370	2,828,314	3,201,852	2,385,027

Table 6: HEC-FIA Base Simulation Results for Comparison and Sensitivity Simulation Statistics

Conclusions

This paper presents a solution to the problem statement using Flood2D-GPU coupled with HEC-FIA offering possible hydraulic and consequence outcomes under the hypothetical scenario provided. The comparative analysis of various BPE methods provides recognition of the similarities and differences between the methods. The sensitivity analysis of the breach parameters demonstrates the importance of specific parameters by illustrating the effects of these parameters on not only the hydraulic outputs but also the consequence results. These analyses combined begin the conversation into utilizing the most appropriate BPE method and focusing in on which breach parameters are the most critical to approximate the most accurate hydraulic and consequence results in a study of this nature.

The results of the comparative analysis suggests that similar consequence results can be expected when using the Froehlich 1995a, Froehlich 2008, and VTG breach parameter estimation methods but, without additional case studies using this same approach, relative replication of these results is not substantiated. However, all of these approaches are based on straightforward regression relationships and should produce similar results. The MLM BPE method is similar in many aspects to the other three BPE methods with the exception of the inclusion of a volume of material eroded term. Additional case studies could provide insight into the differences of results experienced during this study.

In general, the results of the sensitivity analysis follow the expected trends. As breach depth, width, and side slopes increase and the time of breach formation decreases, the breach discharge hydrograph shape becomes more compressed resulting in higher peak discharges, which ultimately results in more significant flood impacts and consequences. Several conclusions can be drawn from these analyses.

Final breach invert is very difficult to estimate and is an assumed value not calculated by any of the BPE methods. Unfortunately, the results of this analysis show that the breach hydrograph and consequence results are extremely sensitive to the breach invert assumption. When conducting a risk-based assessment of a dam failure, special care should be taken to ensure that the best estimation of breach invert is assumed based on the sensitivity of breach hydrograph and consequence outcomes to the estimation of this parameter. Ultimately, additional research could provide a better approach to estimating this parameter drastically reducing the uncertainty in these types of analyses.

When comparing the breach parameter estimations of SS, El_B, W_b, and t_f, using the three BPE methods that produced similar consequence results, with the results of the sensitivity simulations, the breach formation time proves to be a critical parameter in the development of breach discharge hydrographs. Even with a W_b varying between 49 and 146 m, the resulting breach hydrograph shape and peaks are similar due to the similarity in formation time, which ranges from 0.6 to 0.9 hours.

References (arranged in alphabetical order)

[1] Department of Homeland Security, Federal Emergency Management Agency (2007), Multi-Hazard Loss Estimation Methodology Flood Model HAZUS-MH MR3 Technical Manual, Washington, D. C.
[2] Ferziger, J.H., and Peric, M. (2002). "Computational methods for fluid dynamics, 3rd edition" Springer, New York.

[3] Froehlich, D. C. (1995a). "Embankment dam breach parameters revisited." Water Resources Engineering, Proceedings of the 1995 American Society of Civil Engineers Conference on Water Resources Engineering, New York, 887–891.

[4] Froehlich, D. C. (1995b). "Peak outflow from breached embankment dam." Journal of Water Resources Planning and Management, American Society of Civil Engineers, 121(1), 90–97.

[5] Froehlich, D. (2008). "Embankment Dam Breach Parameters and Their Uncertainties." Journal of Hydraulic Engineering, 134(12), 1708–1721.

[6] Hossain, AKM Azad, Yafei Jia, and Xiabo Chao. (2009). "Estimation of Manning's roughness coefficient distribution for hydrodynamic model using remotely sensed land cover features." Geoinformatics, 2009 17th International Conference.

[7] Judi, D. R., Burian, S. J., and McPherson, T. N. (2010). "Two-dimensional fast-response flood modeling: Desktop parallel computing and domain tracking." Journal of Computing in Civil Engineering, in press.

[8] Kalyanapu A. J., Shankar S., Stephens A., Judi D. R., Burian S. (2011). "Assessment of GPU computational enhancement to a 2D flood model" Journal of Environmental Modeling and Software, 26, 1009-1016.

[9] Lehman, W. and, Needham, J. (2009). "Consequence estimation for dam failures." Hydrologic Engineering Center, US Army Corps of Engineers.

[10] MacDonald, T. C., and Langridge-Monopolis, J. (1984). "Breaching characteristics of dam failures." Journal of Hydraulic Engineering, 110(5), 567–586.

[11] Patankar, S.V. (1980). Numerical heat transfer and fluid flow, Taylor and Francis.

[12] Tingsanchali, T. and Rattanapitikon, W. (1999). "2-D modeling of dambreak wave propagation on initially dry bed." International Journal of Science and Technology, 4(3), 28-37.

[13] United States Army Corps of Engineers. (2010). HEC-RAS River Analysis System - Users Manual, Hydrologic Engineering Center, US Army Corps of Engineers.

[14] United States Army Corps of Engineers. (2012). HEC-FIA Flood Impact Analysis - Users Manual, Hydrologic Engineering Center, US Army Corps of Engineers.

[15] Von Thun, J. L., and Gillette, D. R. (1990). "Guidance on breach parameters." Internal Memorandum, U.S. Dept. of the Interior, Bureau of Reclamation, Denver, 17.

[16] Wahl, T. L. (2004). "Uncertainty of Predictions of Embankment Dam Breach Parameters." Journal of Hydraulic Engineering, 130(5), 389-397.

Dam Failure and Consequence Assessment with Standardized USACE MMC Procedures

International Commission on Large Dams 12th International Benchmark Workshop on Numerical Analysis of Dams (Theme C: Computational Challenges in Consequence Estimation for Risk Assessment)

D. Williams[1] and K. Buchanan[2]

[1] U.S. Army Corps of Engineers, Tulsa, Oklahoma, USA
[2] U.S. Army Corps of Engineers, Huntington, West Virginia, USA

Email: david.j.williams@usace.army.mil

Abstract

The U.S. Army Corps of Engineers' (USACE) Modeling, Mapping and Consequences (MMC) Production Center has submitted an entry for the International Commission on Large Dams (ICOLD) 12th International Benchmark Workshop on Numerical Analysis of Dams (Theme C: Computational Challenges in Consequence Estimation for Risk Assessment). As part of this exercise, standard MMC processes were used to develop hydraulic modeling of a dam break inundation as well as the associated consequences. Modeling techniques included one- and two- dimensional numerical models, use of geographic information systems, and economic and life loss estimation. Breach parameters were developed from standard regression equations. Based on the rules and regulations that USACE has established for the estimation of risk, economic consequences and life loss modeling results from this breach analysis corresponded to a high hazard dam. This analysis demonstrates the standardized MMC process for consistently evaluating all USACE dams while providing the flexibility to analyze projects that range from small and simple to large and extremely complex.

Introduction

The Modeling, Mapping and Consequences (MMC) Production Center supports the U.S. Army Corps of Engineers (USACE) Institute for Water Resources (IWR) Risk Management Center (RMC) and the HQ USACE Office of Homeland Security, Critical Infrastructure Protection and Resilience (CIPR) program by analyzing the potential consequences of dam and levee infrastructure failures. The mission of the MMC includes production of hydraulic models, consequences estimates, and inundation maps for USACE dams and levees in support of these programs. All products are developed in accordance with MMC standard operating procedures. The intent of MMC products is to support a risk-based assessment, prioritization, and management framework for USACE CIPR, Dam Safety, and Levee Safety programs. Analysis of the risk associated with dam and levee failure events allows decision makers to prioritize investments to reduce the risk to life and property.

MMC dam safety analysis is typically based on five failure and five non-failure dam breach scenarios needed for CIPR and Dam Safety program evaluations. Breach parameters for earthen dams (e.g. average breach width, breach formation time, and side slopes) are calculated using the following empirical equations: MacDonald and Langridge – Monopolis (1984) [1], Von Thun and Gillette (1990) [2], Froehlich (1995) [3], and Froehlich (2008) [4]. Results from all of these methods are compared, and results from a single empirical equation

is selected for the analysis. Parameters from multiple equations are not considered to be interchangeable.

Hydraulic modeling is performed using either HEC-RAS [5] (one-dimensional) or FLO-2D [6] (two-dimensional) unsteady flow analysis. The use of FLO-2D in the MMC process is generally restricted to areas where the one dimensional flow assumption utilized in HEC-RAS is not appropriate; such as coastal plains, alluvial fans, flat dense urban areas, and other large flat unconfined floodplains. Both models provide unsteady flow simulation. Steady flow models are not permitted within the MMC process.

Following the development of the hydraulic model, the output from the dam failure analysis is processed using ArcGIS [7]. Inundation depth grids and inundation boundary shapefiles are generated, and these files are used in conjunction with structure and population data from tax parcels, point shapefiles, or the Federal Emergency Management Agency (FEMA) HAZUS [8] dataset to develop a HEC-FIA (Flood Impact Analysis) [9] model. The structure information is compared with the extent and timing of the flooding to estimate damages and life loss. This information (in the form of a consequence assessment report), along with an atlas of the downstream inundation, is provided by the MMC to USACE district offices for emergency action planning.

Project Description

The MMC is participating in the International Commission on Large Dams (ICOLD) 12th International Benchmark Workshop on Numerical Analysis of Dams (Theme C: Computational Challenges in Consequence Estimation for Risk Assessment). Participants in Theme C are free to select the type and sophistication of modeling used to develop flood inundation areas and consequences estimates. When possible, the standard MMC process [10] was followed in the development of the dam break modeling and consequence estimation for this project.

The numerical problem proposed for the workshop consists of estimating the consequences of failure of a dam in a mountain valley above the fictitious city of Hydropolis. The hypothetical dam, which was constructed for flood control, is 3.5 kilometers upstream from the city. Sandy clays and clayey sands are the predominant material within the rolled earth fill dam. With a 61-meter vertical distance from toe to crest, the structure has a high head differential when the reservoir is completely filled. The corresponding volume of the reservoir at the dam crest elevation is 38,276,000 cubic meters [11] (Figure 1).
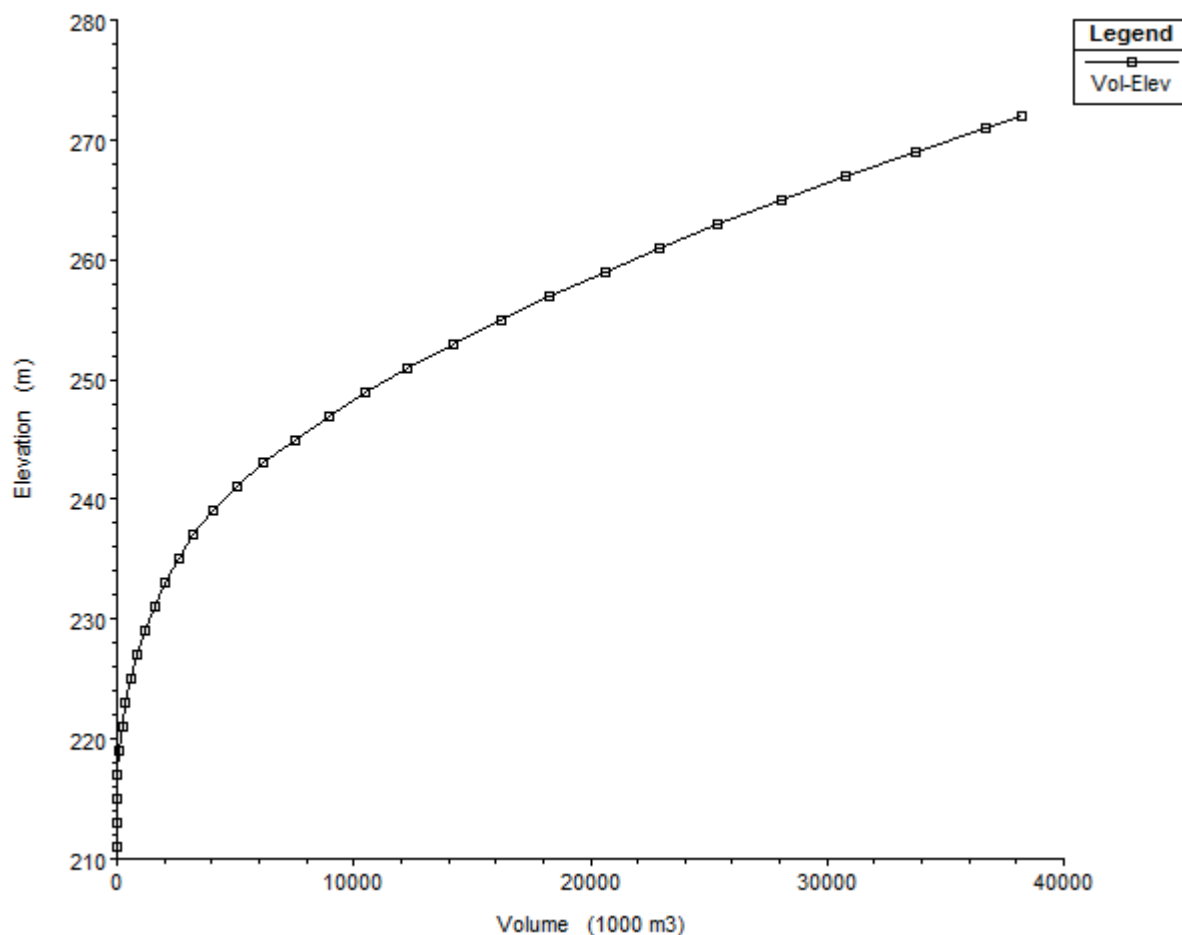
Figure 1: Storage-elevation curve for the reservoir.

This exercise examines the downstream consequences of a catastrophic failure of the dam resulting from overtopping. Expected outcomes from this study include gridded data (peak flood depth, flood wave arrival time, peak unit flow rate, population at risk, loss of life, flood severity, direct economic impact), tabular data (flooded area, population at risk, loss of life, direct economic impact), and hydrographs (dam failure discharge, cross-sectional hydrographs). All of these products except for the peak unit flow rate are standard deliverables in a MMC dam breach analysis.

Model Development

Modeling for this exercise was developed using both one- and two-dimensional techniques that are consistent with MMC standard operating procedures. Initially, only a HEC-RAS hydraulic model was planned for this study. This model computes flood wave parameters at cross-sectional nodes along a one-dimensional channel. Inspection of the terrain grid provided for this study revealed that the use of HEC-RAS for the entire downstream reach would be inappropriate since Hydropolis is located within a relatively flat plain below the base of the mountain range. In this reach, it was determined that a two-dimensional model would be more appropriate; therefore, FLO-2D was also used.

Existing terrain downstream from the dam was provided by the Theme C formulation team. This dataset was provided in a gridded format with a cell width of 9.476 meters. No projection was assigned to the terrain dataset, but all geospatial data provided by the formulation team was in the same unknown coordinate system.

The terrain dataset was used to extract cross sections in ArcGIS 10 (HEC-GeoRAS [12]) for use in a HEC-RAS model. The spatial extent of this model was restricted to 200 meters below the dam (modeled as an inline structure) as it was used to generate a dam breach hydrograph for a FLO-2D inflow boundary condition (Figure 2). The HEC-RAS model was run as an unsteady flow simulation with a computation interval of 5 seconds. A breach hydrograph was written to file with a 1-minute output interval, which was sufficient for defining the dam breach hydrograph.
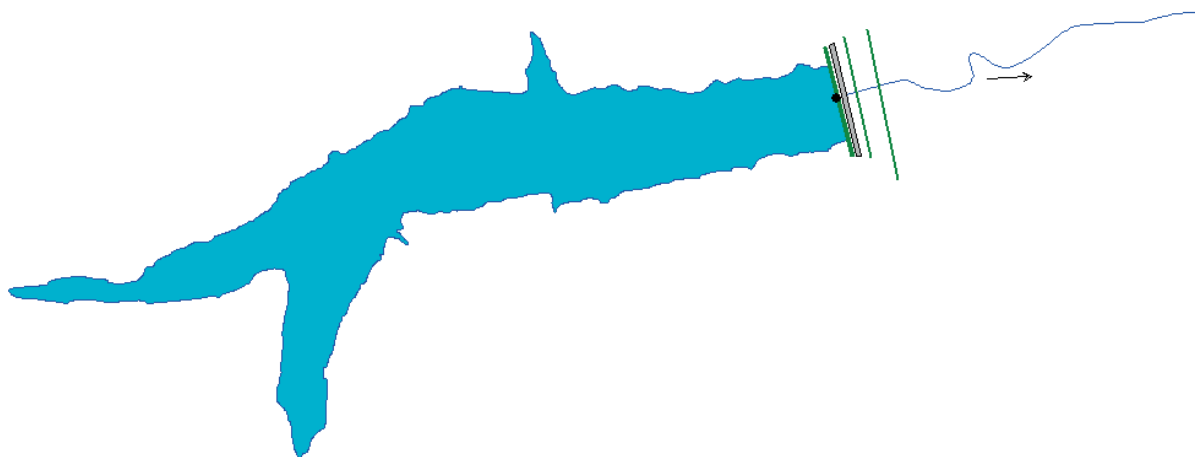
Figure 2: HEC-RAS model geometry for breach hydrograph determination.

Parameters from the MacDonald and Langridge – Monopolis empirical breach equation were not specifically considered in this analysis since it is considered to be an envelope equation, although parameters from the other equations were checked to ensure that they fell within the envelope range. The Froehlich (1995), Froehlich (2008), and Von Thun and Gillette equations were carried forward as unique scenarios in the HEC-RAS model. Since each of the three methods estimated a short breach formation time, a computational time step of 5 seconds was used in the HEC-RAS model in order to capture the peak discharge.

Following the initial model development with the Froehlich (1995), Froehlich (2008), and Von Thun and Gillette breach parameters, the Froehlich (1995) equation was carried forward as the preferred method. Froehlich (1995) analyzed 63 earthen, zoned earthen, earthen with a core wall, and rockfill dam failures [3]. Data from these events was used to develop regression equations for average breach width $\bar{B}$ (meters) and breach formation time t_f (hours):

$$\bar{B} = 0.1803 K_0 V_w^{0.32} h_b^{0.19} \qquad (1)$$

$$t_f = 0.00254 V_w^{0.53} h_b^{-0.90} \qquad (2)$$

For this exercise, K_0 = 1.4 (overtopping failure). The reservoir volume V_w (38,276,344 m^3) and breach height h_b (61 meters) were provided by the organizers of the benchmark workshop. This method provided a short breach development time coupled with a relatively wide breach width (Table 1):

Table 1: Breach parameters for hypothetical dam

Breach Equation	Formation Time (hours)	Bottom Width (m)

MacDonald and Langridge-Monopolis	1.8	5
Froehlich (1995)	0.7	62
Froehlich (2008)	0.6	39
Von Thun and Gillette	1.5	177

A breach hydrograph generated in HEC-RAS was then used as the inflow boundary condition in a FLO-2D model (Figure 3). The model assumed a static pool elevation of 272 meters with no inflow. Overtopping of the dam crest was the prescribed mode of failure. Unlike the one-dimensional flow model (HEC-RAS), FLO-2D computes flow across a network of grid cells with eight possible directions of flow into or out of each cell. This type of flow distribution makes FLO-2D well-suited for analysis of the flood wave downstream from the dam.
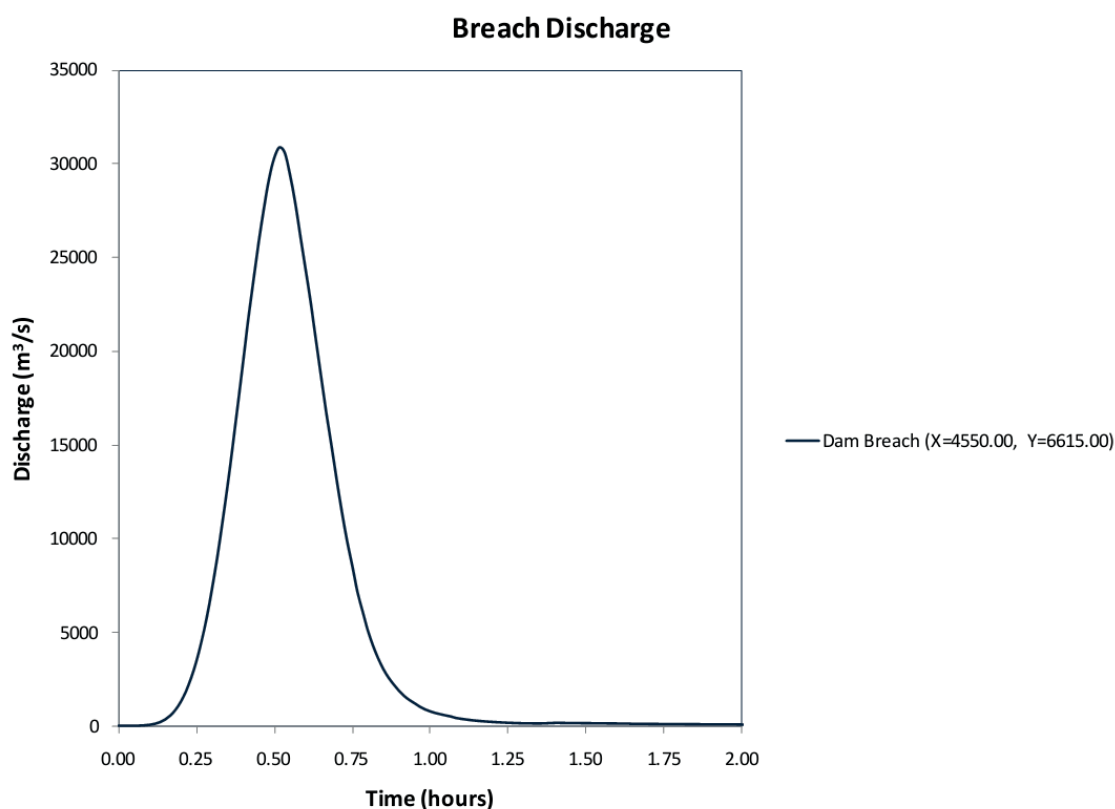
Figure 3: Breach hydrograph resulting from Froehlich (1995) parameters

Faster computation time of the FLO-2D model required a grid-cell width larger than 9.476 meters. By choosing an integer multiple of the terrain grid-cell size, conversion between the two could be simplified when resampling. Therefore, a computational grid-cell dimension of 94.76 meters (square) was selected. Elevation values were interpolated for the larger computational grid dimensions when imported into FLO-2D.

Surface roughness values were developed by converting a National Land Cover Database (NLCD) shapefile [13] to corresponding Manning's 'n' values [14]. The NLCD shapefile was provided by the Theme C formulation team. Once a new surface roughness shapefile was created, the values were interpolated for the computational grid dimensions when imported into FLO-2D.

The FLO-2D model was run with a simulation time of 12 hours and an output interval of 5 minutes. Since the downstream reach is both short and steep, the simulation time was more than sufficient for routing of the breach hydrograph through the entire study area. An output

interval of 5 minutes was necessary to capture the peak of the flood wave at downstream locations.

A depth grid, flood wave arrival time grid, and flood severity grid were generated by using MAPPER [6], a post-processing tool for FLO-2D models. Peak unit flow rate is not a FLO-2D output. This variable was therefore determined by taking the maximum flow rate for each grid cell and dividing by the computational grid-cell width. Cross-sectional hydrographs, which were required at five locations downstream from the dam, were developed by setting those locations as outflow nodes in sequential FLO-2D model runs. The time-series discharge for each cross-sectional outflow grid cell was then summed to construct a representative hydrograph for each key location. This was necessary because FLO-2D does not generate time-series discharge for grid cells within the computational domain if no channel element is used; it does write this output to file for outflow nodes, however. Hydraulic modeling results were then used for the determination of consequences based on a structure inventory.

A structure inventory was developed using three datasets provided for the workshop [15]. These included a parcel shapefile with zoning information, a census block shapefile with population and employment information, and a land use grid. Typically, the economic and life loss analysis in a MMC study includes the utilization of a FEMA HAZUS dataset supplemented by imagery, land use, or parcels. Since this was not provided for the benchmark exercise, non-standard methods were used to estimate consequences. The following assumptions were required for the creation of a structure inventory with population values in HEC-FIA:

- Since the dam fails at 11:00pm on a Saturday, all residential populations are in their homes.
- Due to the day and time, only 10% of the workers in certain job types are working. These included the following jobs: Mining, Quarrying, and Oil and Gas Extraction; Utilities; Manufacturing; Transportation and Warehousing; Administrative and Support and Waste Management; Health Care and Social Assistance; Arts, Entertainment, and Recreation; and Accommodation and Food Services.
- All workers come from census blocks outside the inundation area (not enough data to model movements from one census block to another).
- All workers are under the age of 65.
- All data was up to date and accurate (parcels, blocks, and land use).

Once the structure inventory and hydraulic data for the dam breach had been developed, they were used to develop the HEC-FIA model. Depth grids and arrival time grids were developed from FLO-2D output and imported into the model. The arrival time grids represented the time at which the water depth at each cell reached 0.6 meters (approx. 2 feet).

Impact areas were created by reclassifying the arrival time grid into arrival time zones required for reporting results (0-15min, 15-30min, etc.). A polygon was created from that file. Some features had to be manually merged to create a unified impact area polygon for the HEC-FIA model. The structure inventory was created from the parcel file with populations and values developed in the pre-modeling phase. Structure placement was at the centroid of each parcel and was done within HEC-FIA.

For estimates of necessary evacuation time for each structure, a hazard boundary shapefile was created representing the boundary where the inundation becomes 0.6 meters (2 feet) or less, which is considered a safe zone. Evacuation was modeled as a path from the structure to the nearest point on this boundary at an average speed of 16 kilometers per hour.

The warning time used for the loss of life calculation was set at 30 minutes after the breach initiation. The problem statement specified that the failure was sudden and unexpected, and that witnesses within the canyon had no mobile phone service. A warning would not be issued until after the water reached the urban area at the end of the canyon, approximately 20 minutes after the failure. The warning curve used was the HEC-FIA default curve for the United States Emergency Alert System, and the mobilization curve was the default HEC-FIA curve included in the program.

The HEC-FIA program evaluates damages with depth-damage curves based on occupancy type. Population distribution is also performed by occupancy type. To determine occupancy types, a cross walk table was created that assigned each parcel zone description to a specific occupancy type typically used in a HEC-FIA structure inventory.

Populations and jobs were provided for each census block and broken down by category. To facilitate the distribution to individual parcels, the populations were combined into the following categories by census blocks:

- Resident Population under age 14
- Resident Population under age 65
- Resident Population over age 65
- Working Population (10% of the workers from industries potentially in operation at 11pm on a Saturday)

In order to determine the amount of population for each structure, each occupancy type was assigned a number of residential households or working households. Then for each census block, the residential populations were divided by the total number of residential households in the block and the working populations were divided by the total number of working households in the block. The resulting residential and working household sizes per census block were then used to create the populations for each parcel based on the number and type of households assigned to the occupancy type of the parcel. For example, if the residential household size in a census block was 2.5, then a single family residential structure in that block would get 2.5 people while a five to nine unit multiple family dwelling in the same census block would get 7 households, or 17.5 people.

Table 2 shows the final occupancy types used and the number of assigned households. In the beginning there were more occupancy types included, but the ones listed below represent all of the types included in the final inventory after being clipped to the inundation boundary. The methodology, including the number of households assigned to each occupancy type, is representative of a typical HAZUS based structure inventory used by the MMC.

Table 2: Population distribution by occupancy type

Occupancy Type	Occupancy Type Description	Residential Households	Working Households
COM1	Average Retail	-	1
COM4	Average Prof/Tech Services	-	1
GOV1	Average government services	-	-
RES1-1SNB	Single Family, 1 Story no Basement	1	-
RES1-2SNB	Single Family, 2 Story no Basement	1	-
RES1-3SNB	Single Family, 3 Story no Basement	1	-

RES3AI	Multi Family Dwelling, Duplex	2	-
RES3CI	Multi Family Dwelling, 5-9 Units	7	-
RES3DI	Multi Family Dwelling, 10-19 Units	14.5	-

No data was provided on structure values in the parcel dataset. A standard USACE dam failure consequence estimate will often use the National Structure Inventory (NSI) developed by the USACE Hydrologic Engineering Center and based on HAZUS and Census data. The team decided to use average values from the NSI for each occupancy type to determine structure values. The NSI data is broken down by county, so a national average would have required significant effort. Instead of using a national average, the team reviewed data on housing values from the 2011 American Community Survey and determined that the state of Maine had the closest housing value to the national average. Data from the NSI for each county in Maine was combined and average values for each occupancy type were calculated. Vehicle and content values were also assigned (Table 3).

Table 3: Average values by occupancy type

Occupancy Type	Occupancy Type Description	Average Structure Value	Average Content Value	Average Vehicle Value
COM1	Average Retail	$545,888	$545,888	$21,819
COM4	Average Prof/Tech Services	$550,027	$550,027	$22,707
GOV1	Average government services	$481,998	$481,998	$27,020
RES1-1SNB	Single Family, 1 Story no Basement	$122,061	$61,030	$14,825
RES1-2SNB	Single Family, 2 Story no Basement	$121,957	$60,528	$14,766
RES1-3SNB	Single Family, 3 Story no Basement	$127,135	$63,568	$15,175
RES3AI	Multi Family Dwelling, Duplex	$206,625	$103,312	$19,795
RES3CI	Multi Family Dwelling, 5-9 Units	$753,610	$376,805	$26,195
RES3DI	Multi Family Dwelling, 10-19 Units	$1,288,765	$644,383	$29,931

Since the parcel shapefile appeared only to have information about zoning and not specific information about structures, the team assumed that not every parcel had a structure on it. Also, some parcels had "unknown" zone information so those parcels were removed from the final inventory. Information in the census blocks and the land use file also needed to be evaluated to inform the structure inventory development.

One particular issue involved a large number of parcels in the middle section of the study area. These parcels appeared to be subdivided into mostly single family home lots. However, the census block data showed no residential population in those areas. Figure 4 shows census blocks labeled with total residential population with the parcels overlain on top in blue. The red census blocks have zero population.
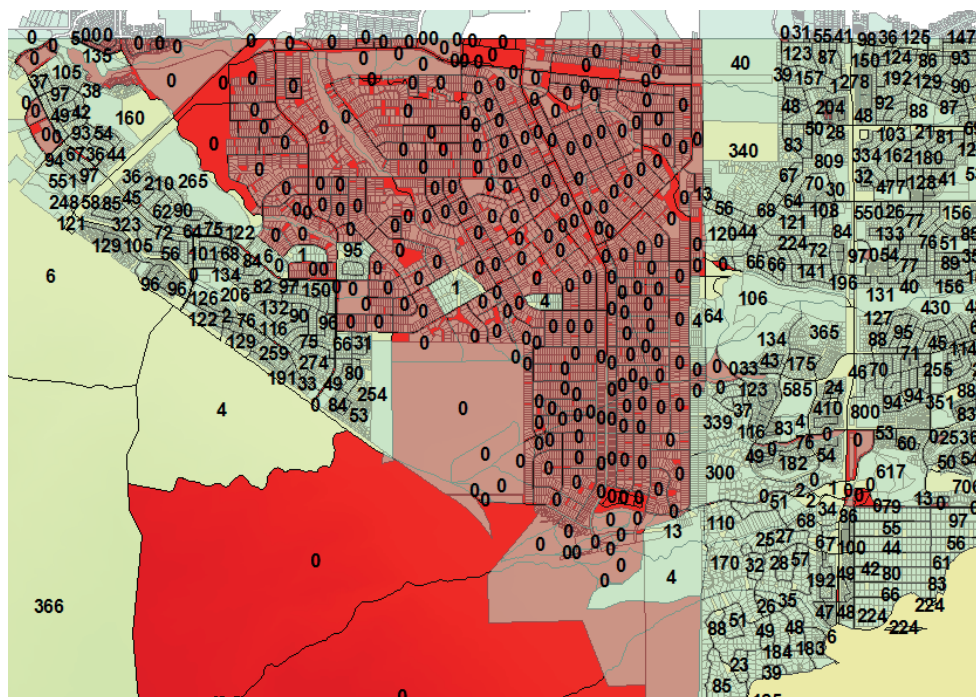
Figure 4: Comparison of parcels and census block populations

The land cover file showed no development in the area in question except for the roads themselves; no development is shown to indicate structures. Figure 5 shows development as red or pink. The roads in the center area are listed as Developed-Open Space and everything other than roads is listed mostly as grassland or shrub (brown and pale green colors).
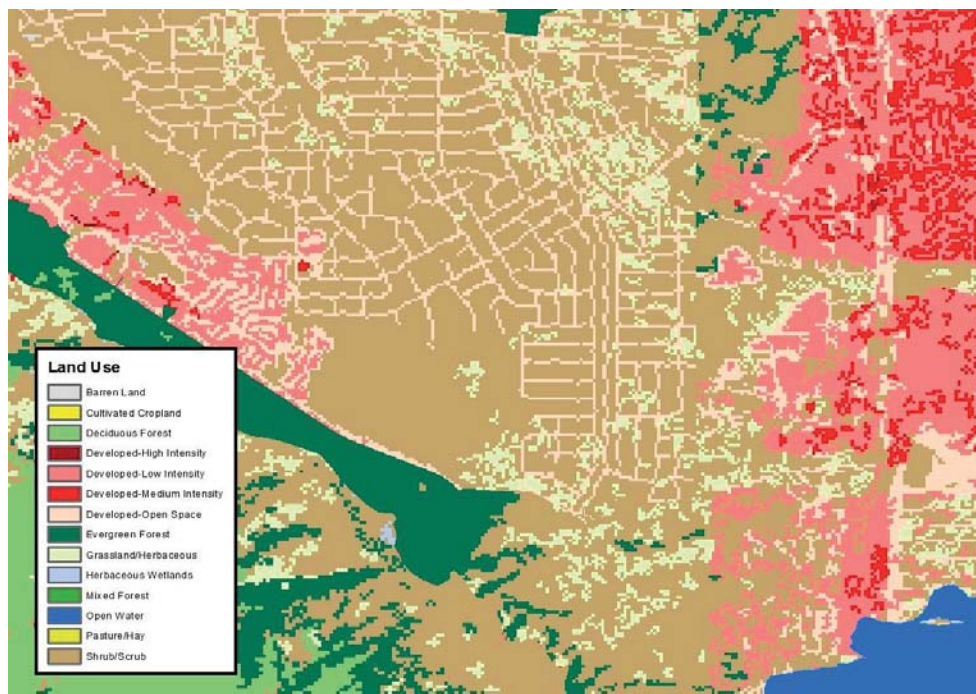
Figure 5: Land use downstream of the dam

This data can be interpreted in several ways. For example, it may be a situation where a subdivision has been planned for future development, and the land has been parceled off and a

road system developed but no houses have been built and occupied. Alternatively, it could be a scenario where the parcel data was recently updated while the land cover and census data are several years old and do not reflect the recent development. With no way to ground truth the data through aerial imagery or site visits the team chose to adopt the first interpretation, assuming that all data was current and structures had not yet been built in that area. The large group of central parcels was removed from the final inventory by deleting all residential parcels in census blocks with no residential population.

In addition, all parcels more than 100 meters outside the dam failure inundation area were deleted. This minimized the parcels to only those necessary for the HEC-FIA structure inventory.

Results and Discussion

The hydrograph that was computed from Froehlich (1995) breach parameters had a peak discharge of 30,917 m^3/sec at the dam site. The time to peak discharge occurred 31 minutes after breach initiation began. Nearly all of the reservoir volume was evacuated within 90 minutes of the breach initiation.

Discharge immediately downstream from the dam remained confined to the mountain valley. This part of the reach, in which the flood wave was limited to a maximum width of 400 meters, continues downstream for approximately 3,000 meters. Minimal attenuation of the flood wave occurred through the valley, which was verified by developing cross sections downstream to the base of the higher terrain (Figure 6). At the lower end of the valley, the peak discharge of the cross-sectional hydrograph had only decreased to 26,474 m^3/sec.

Cross-Section Discharge
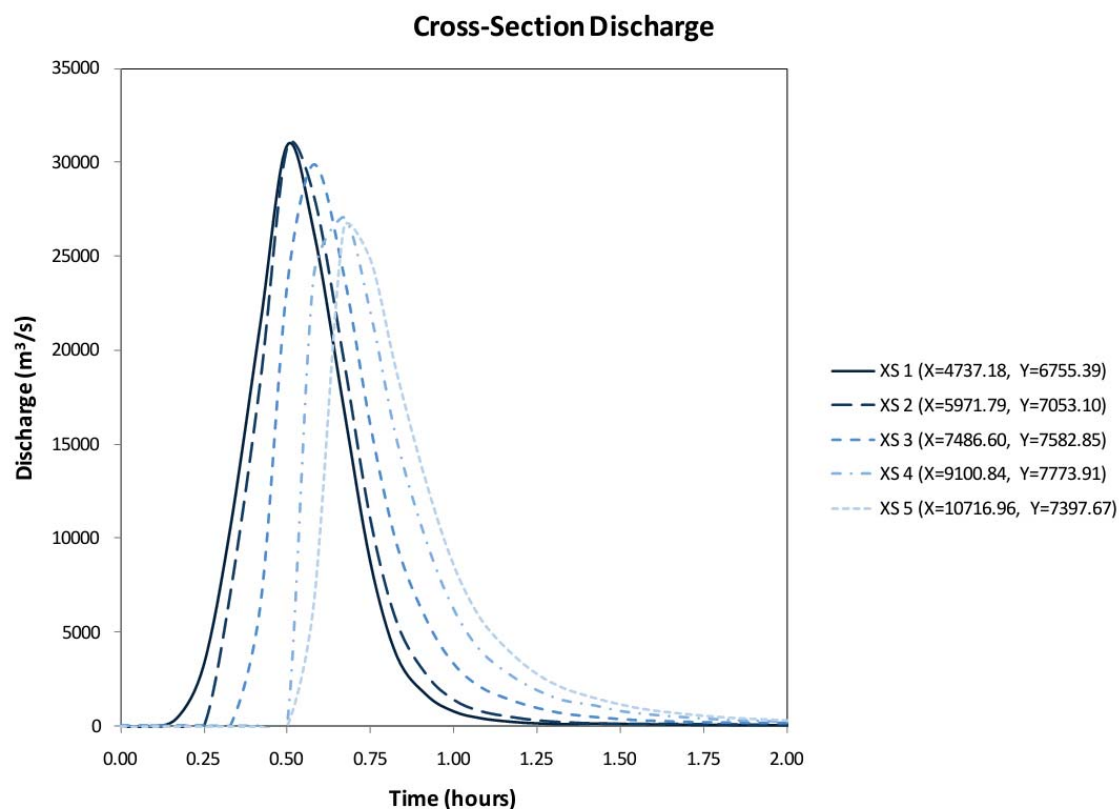
Figure 6: Breach hydrographs at selected locations downstream from the dam

When the flood wave reached the more highly populated area below the base of the mountain, a change in the slope and layout of the surrounding terrain resulted in a more pronounced attenuation and lateral dispersion of the inundated area. This behavior of the flood wave is consistent with the transition from a steep mountain valley to a relatively flat, unconfined plain such as an alluvial fan or coastal area. This attenuation was highlighted by peak unit flow rates, which ranged from 300 m^2/sec immediately downstream from the dam to less than 1 m^2/sec for most of the area in the broader flood plain.

Peak depths of the flood wave ranged from 24.5 meters immediately downstream from the dam to less than 1 meter at the downstream computational boundary (Figure 7). Much of the populated area fell within the 1- to 3- meter range, although some structures in the lower part of the mountain valley were inundated by depths as high as 12 meters. Arrival times for the flood wave were only 30 minutes for the lower part of the mountain valley. The population residing within the broader flood plain below the valley fell within an arrival time zone of 1 to 1.5 hours. The most distant reach of the modeled area coincided with an arrival time of 4 hours.

reservoir_outline

High : 24.5085

Low : 0.01
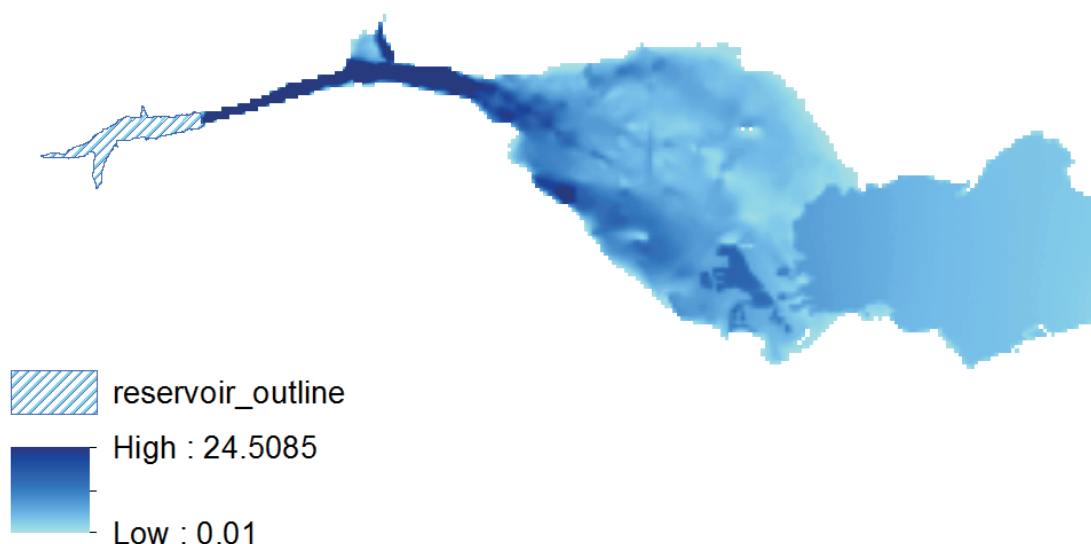
Figure 7: Peak inundation depths (meters) below the dam

Initial results from the HEC-FIA model are displayed below in Tables 5 and 6 (by arrival time and by depth of flooding) as required by the benchmark reporting requirements.

Table 4: Consequences by arrival time

Time Interval (min)	Total Population At Risk	14-yr and Under Population at Risk	65-yr and Over Population at Risk	Loss of Life	Direct Economic Impact ($US)
0-15	-	-	-	-	-
15-30	3,951	1,002	282	1,844	$142,504,368
30-60	7,612	933	1,855	34	$266,968,912
60-90	12,672	1,952	2,166	11	$248,115,360
90-120	-	-	-	-	-
120-180	-	-	-	-	-
> 180	-	-	-	-	-
Total	24,235	3,887	4,303	1,889	$657,588,640

Table 5: Consequences by depth

Peak Flood Depth Range (m)	Flooded Area (m²)	Total Population At Risk	14-yr and Under Population at Risk	65-yr and Over Population at Risk
0 - 0.5	3,699,606	2,749	399	511
0.5 - 1	11,646,576	4,249	660	687
1 - 1.5	23,248,253	9,162	1,401	1,626
1.5 - 2	12,625,355	3,183	446	716
2 - 2.5	6,151,044	1,353	160	373
2.5 - 3	2,990,216	540	85	122
3 - 3.5	2,128,172	153	13	55
3.5 - 4	1,670,211	129	28	19
4 - 4.5	1,068,576	173	49	15
4.5 - 5	511,839	133	32	9
5 - 5.5	377,144	259	71	17
5.5 - 6	448,981	299	78	27
6 - 6.5	233,470	250	67	15
6.5 - 7	152,654	136	33	9
7 - 7.5	287,348	286	69	19
7.5 - 8	296,328	502	131	43
> 8	1,562,455	679	167	43
Total	69,098,227	24,235	3,887	4,303

Conclusion

This exercise demonstrates the practices and procedures that the MMC uses to analyze the large inventory of dams that are owned and operated by USACE. Most of these dams are larger and more complex than the hypothetical dam that was analyzed in this project. Some include complex reaches that extend for hundreds of miles downstream with travel times that last for days or weeks. Elements of each of these dams and their downstream reaches are unique, and it is important to emphasize that the sophistication of MMC models, while incorporating a standardized process, varies by project.

Since the reach in this exercise was both steep and short, flood wave travel times to the downstream boundary of the model were very quick. As a result of these conditions, comparisons of the inundation areas resulting from the Froehlich (1995), Froehlich (2008), and Von Thun and Gillette equations were very similar. Modeling with dam breach parameters from all three equations resulted in a flood wave with a steep peak and fast travel time through the confined mountain valley below the dam followed by lateral attenuation of the flood wave in the broad plain below the base of the mountain range.

Breach parameters from Froehlich (1995) were carried forward in the modeling used for consequences analysis. Estimation of economic damages and life loss was challenging because FEMA HAZUS data, a standard input for MMC HEC-FIA models, was not available for the benchmark exercise. Therefore, average values were used, which may or may not be representative of Hydropolis. Total damages of $657M and a life loss of nearly 2,000 persons were estimated for this dam breach.

Based on the rules and regulations that USACE has established for the estimation of risk, these results correspond to a high hazard dam. The procedures that were used in developing the hydraulic modeling and consequences estimation for the benchmark exercise were consistent with USACE MMC processes. These guidelines, while providing consistency in the analysis of all USACE owned and operated dams, also provide enough flexibility to analyze projects that range from small and simple to large and extremely complex.

Acknowledgments

References

[1] MacDonald, T.C., and Langridge-Monopolis, J. (1984). Breaching characteristics of dam failures. *Journal of Hydraulic Engineering*, 110(5): 567-586.

[2] Von Thun, J.L. and Gillette, D.R. (1990). Guidance on breach parameters. Unpublished internal memorandum, U.S. Bureau of Reclamation, Denver, CO, March 13, 1990.

[3] Froehlich, D.C. (1995). Peak outflow from breached embankment dam. Journal *of Water Resources Planning and Management*, 121(1): 90-97.

[4] Froehlich, D.C. (2008). Embankment dam breach parameters and their uncertainties. *Journal of Hydraulic Engineering*, 134(12): 1708-1721.

[5] U.S. Army Corps of Engineers (2010). HEC-RAS River Analysis System (Version 4.1) [Computer software]. Davis, CA: Hydrologic Engineering Center.

[6] O'Brien, J.D. (2009). FLO-2D (Version 2009) [Computer software]. Nutrioso, AZ: FLO Engineering.

[7] ESRI (2011). ArcGIS Desktop (Release 10) [Computer software]. Redlands, CA: Environmental Systems Research Institute.

[8] Federal Emergency Management Agency (2012). HAZUS-MH (Version 2.1) [DVD]. Washington, DC: FEMA.

[9] U.S. Army Corps of Engineers (2012). HEC-FIA Flood Impact Analysis (Version 2.2) [Computer software]. Davis, CA: Hydrologic Engineering Center.

[10] U.S. Army Corps of Engineers (2013). MMC standard operating procedures for dams. Vicksburg, MS: Modeling, Mapping and Consequences Production Center.

[11] International Commission on Large Dams (2013). Part 1 – Hydraulic Modelling and Simulation. Graz, Austria: 12th International Benchmark Workshop on Numerical Analysis of Dams (Theme C).

[12] U.S. Army Corps of Engineers (2011). HEC-GeoRAS Extension for ArcGIS 10 (Version 10.0) [Computer software]. Davis, CA: Hydrologic Engineering Center.

[13] Homer, C.G., Huang, C.C., Yang, L., Wylie, B., and Coan, M (2004). Development of a 2001 national landcover database for the United States. *Photogrammetric Engineering and Remote Sensing*, 70(7): 829-840.

[14] Mattocks, C., and Forbes, C. (2008). A real-time, event-triggered storm surge forecasting system for the state of North Carolina. *Ocean Modelling*, 25: 95-119.

[15] International Commission on Large Dams (2013). Part 2 – Consequence Estimation. Graz, Austria: 12th International Benchmark Workshop on Numerical Analysis of Dams (Theme C).

OPEN THEME

OPEN THEME

Behavior of an arch dam under the influence of creep, AAR and opening of the dam/foundation contact

E. Robbe[1]

[1] Hydro Engineering Center of EDF,Savoie-technolac, 73373 Le Bourget du Lac, FRANCE

E-mail: emmanuel.robbe@edf.fr

Abstract

This paper summarizes the behavior analysis of a thin, 37m high, arch dam built in 1956. At first, the behavior of this dam was quite difficult to understand: irreversible displacements occur during the years following the first filling, and then, from 1960 until now, others displacements were observed and difficult to read considering usual behavior of arch dam. In order to understand it and to evaluate the stress level of the concrete, finite-element analyzes are leading. First linear, then non-linear analysis taking increasingly into account dam/foundation contact opening, swelling, creep and damage are used to answer the problem and understand the historic behavior of this dam

Introduction

The subject of this paper is an arch dam with a particularly complex behavior observed. The purpose of the study is to understand this behavior and to evaluate the level of stress of the dam. Increasingly complex finite-element analyzes are used (from linear to non-linear) and calibrated on the observed displacements of the dam. Stress levels are also compared to crack patterns observed on the structure.

In this presentation, geological conditions and safety evaluation of the gravity abutment will not be discussed.

Presentation of the dam
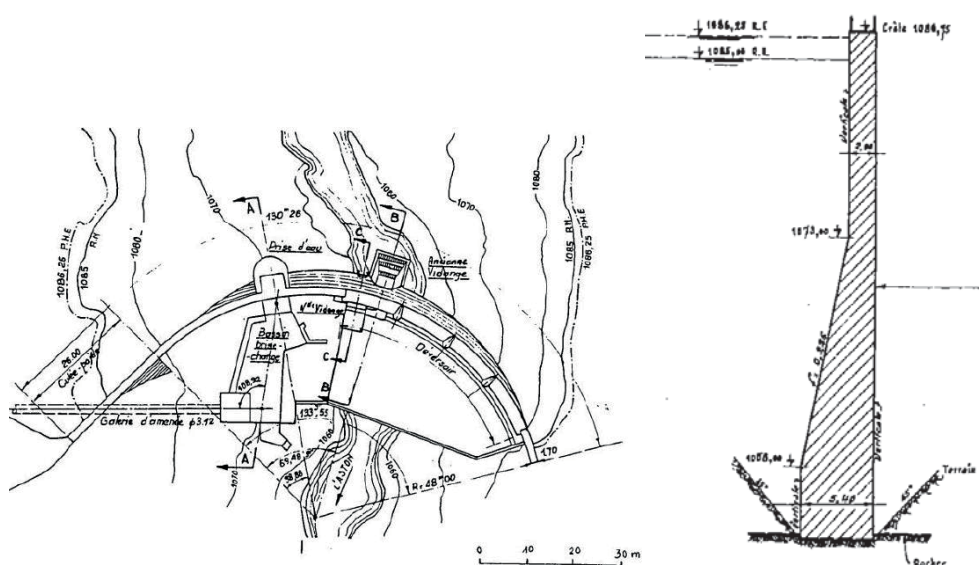
Figure 1: view of the dam

The studied dam is a thin arch, with a gravity abutment on the right side. 37 m high above its foundation made of gneiss, the dam is divided into 6 cantilevers (about 17m wide) for the arch part and 2 cantilevers for the right abutment. Figure 1 shows the design of the dam: the thickness goes from 2 m on the crest to 5.4 m at the bottom, with a sloping upstream face in the lower part only. The valley is quite wide (L/H about 3) and clearly asymmetrical.

The dam has been built from 1954 to 1956. In 1961, works has been done in order to grout 2 parallels faults discovered on the left abutment and to build an apron to protect the foundation in case of overflowing.

Observed behavior

This part describes the behavior of the dam monitored with points on the downstream face of the dam from the first filling in 1956 until 2001. These points are represented on Figure 2. From 2001 until now, pendulums are used in order to follow the dam's behavior.

A statistic analysis of the monitoring data is used in order to evaluate the part of the hydrostatic and the seasonal effects on the dam's displacements. Once theses reversible effects evaluate, the irreversible effects can be estimate. Regarding these data, the behavior can be separated in 2 phases:

- During the 5 years after the first filling of the dam (1956-1960)
- 40 years from 1961 until 2001

Behavior after first filling

The analysis of the radial displacements of the dam shows the following behavior:

- At the crest, the central part moves downstream while the top of the sides cantilevers move upstream,
- All the points at the central cantilever records downstream displacements.

Long-term behavior

The radial displacements of the monitored points located on the downstream face of the dam are represented on the Figure 2 for approximately 40 years.

Theses displacements can be described the following way:

- The crest of the dam moves upstream continuously (0.3 mm/year for the central cantilever)
- The lower part of the arch goes first downstream during 10 years then upstream after 10 years of stabilization. The velocity of the downstream displacement is close to the one observed on the crest.

A first global interpretation of these observations is that the concrete is under the influence of swelling, which can explains the upstream displacements of the crest. For the lower part, creep is more important during the first 10 years, that explains the first downstream displacements, and decreases gradually and therefore swelling become leading.
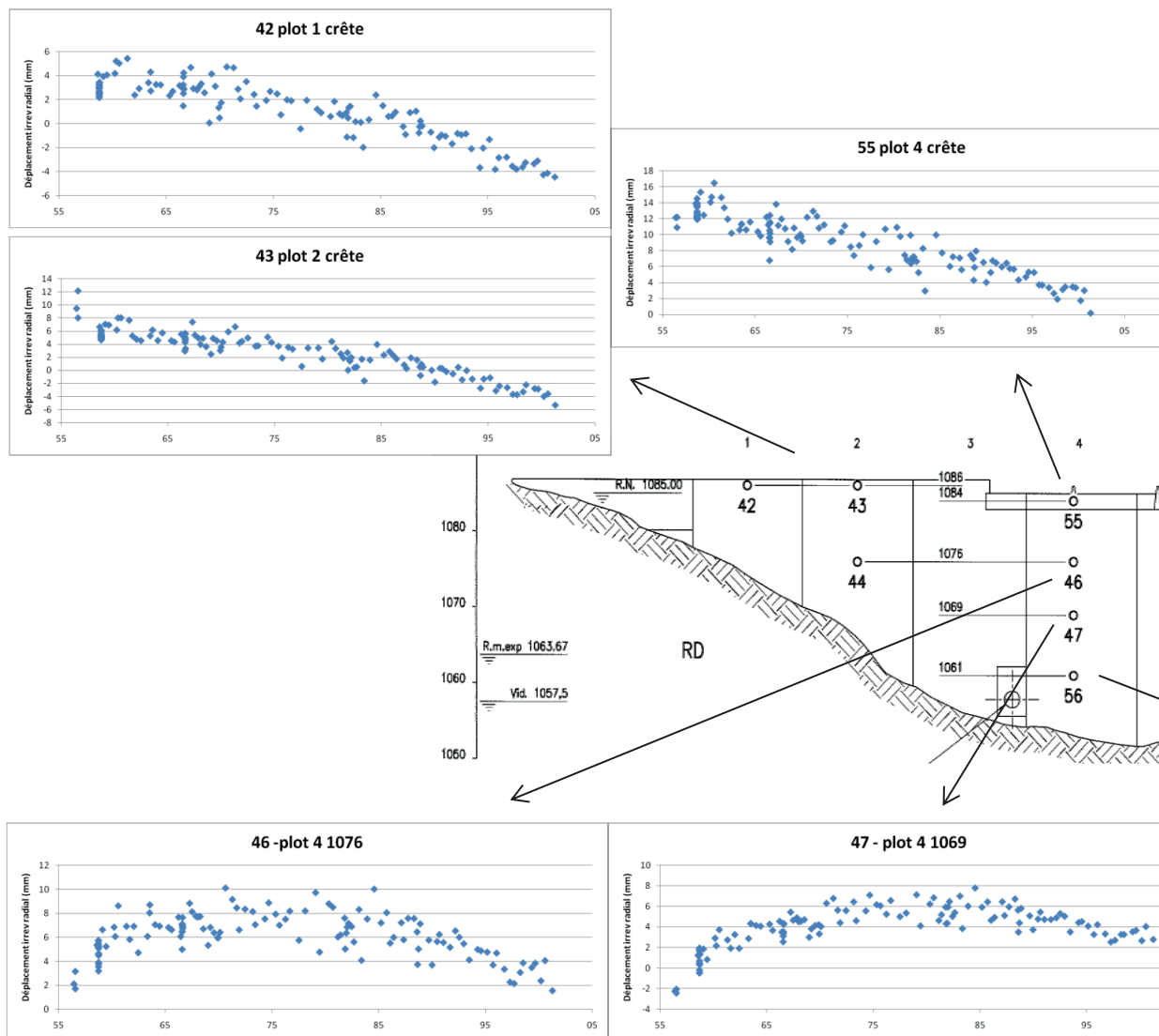
Figure 2: irreversible radial displacements (from 1956 to 2001)

Linear analysis

A finite-element linear analysis of the dam is realized with Code_Aster [1]. The physical properties for concrete and rock are chosen by comparison between the monitored data and the results of the FE analysis. The calibration is done considering hydrostatic load and thermal load in order to represent correctly the behavior of the dam in winter and summer for example.
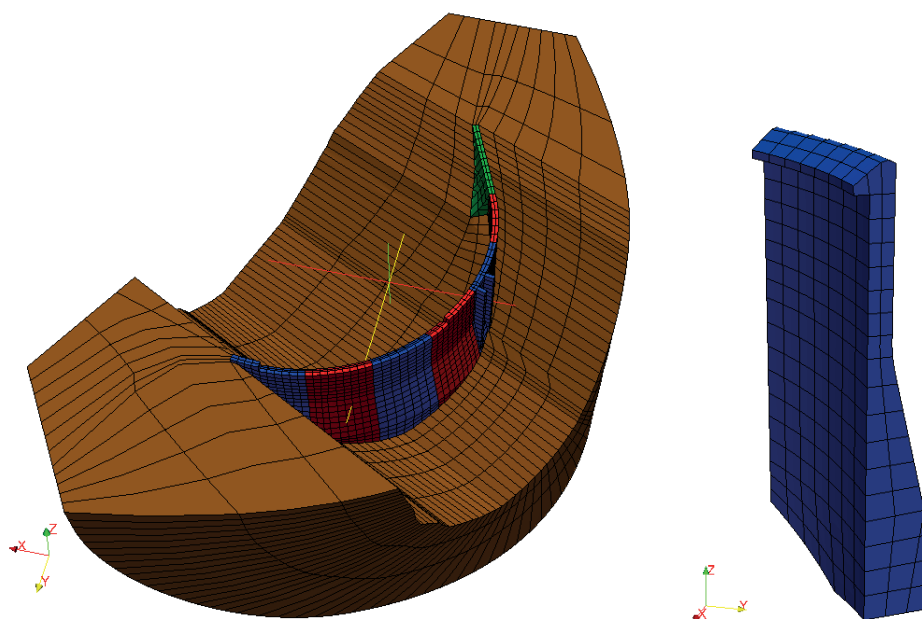
Figure 3: Mesh of the dam and foundation

The linear analysis shows that the particular design leads to an unconventional behavior of the dam: the lower part works as cantilever while arch-effects appear in the upper part. That leads to high vertical tensile stress at the heel of the dam (close to 8 MPa in winter) and in the middle of the downstream face where seepage are already observed on a lift joint. Because of theses high tensile stresses, the FE is upgraded in order to take into account the opening of the dam/foundation contact and the lift joint, and to evaluate their consequences.

Non-linear analysis including dam/foundation contact

The Figure 4 presents the joint elements introduced in the mesh in order to simulate the non-linear behavior:
- dam/foundation contact under the 6 cantilevers,
- dam/foundation contact under the right gravity abutment,
- horizontal lift joint at the change of inertia of the dam,
- contraction joints.

Joint elements open under normal tensile stress but share behavior is still elastic-linear whatever the opening-state of the joint. Except for vertical contraction joints, uplift is taking into account. In particular, spread of the uplift under the dam with joint opening is used.
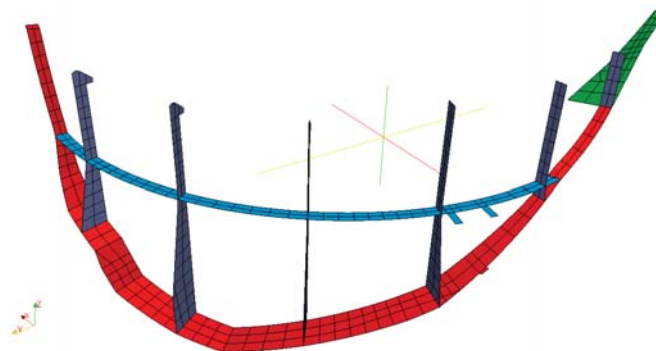
Figure 4: mesh of the joint elements
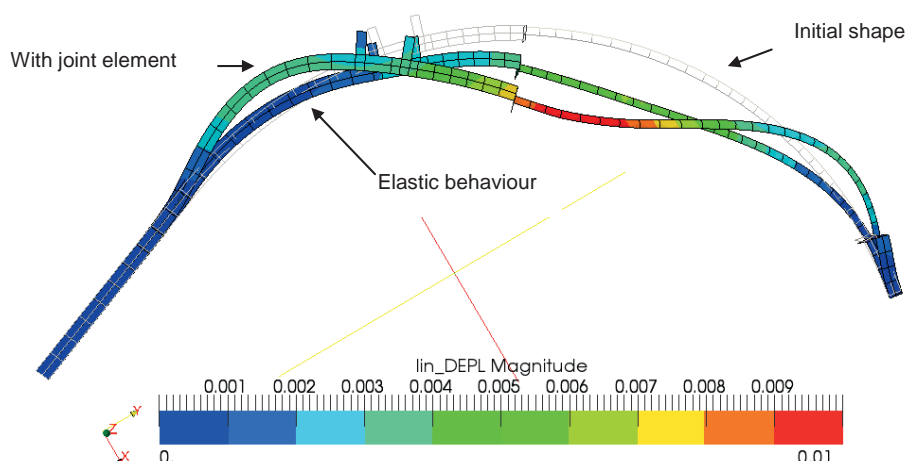
Figure 5: comparison of the deformed shapes at the crest (elastic, with joint elements)

The introduction of the joint elements modifies the deformation at the crest of the dam (Figure 5) Theses irreversible displacements are equivalent to the ones observed during the first years after the first filling of the dam and presented earlier. The analysis shows that the dam/foundation contact is open at the heel of the dam, particularly in winter (5 mm). That leads to an increase of the uplift under the central cantilever. This is confirmed by a recently installed piezometer which records the almost full uplift during winter.

Non-linear analysis including AAR and creep

If the previous section evaluates the behavior of the dam after few years, the recorded displacements during the following 40th years need to be taken in account in order to estimate correctly the stress state of the dam. Considering the displacements recorded, the behavior of the dam is under the influence of swelling and creep and therefore, the model used have to be able to represent correctly these phenomena. In this purpose, the model developed by Grimal [2] for AAR on concrete dam is particularly adequate. This visco-elasto-plastic orthotropic damage model includes chemical pressure induced by AAR and takes into account the influence of creep on the behavior. It has been used to evaluate the behavior of Chambon's dam [2] and showed the model's capability to reproduce displacements with acceptable accuracy. The main developments brought by this model concern interactions between AAR pressure and long term strain (creep) on the one hand, and the swelling anisotropy induced by oriented cracking on the other hand.

Here, this model is coupled to the joint elements presented earlier. The calibration of the model is realized the following way:

- first, the kinetic of the chemical pressure induced by AAR and the volume of AAR gel are chosen in order to fit the displacement monitored on the crest of the dam
- then, the parameters for creep are chosen in order to fit displacements of the lower part of the dam

The result of this calibration is presented on Figure 6.
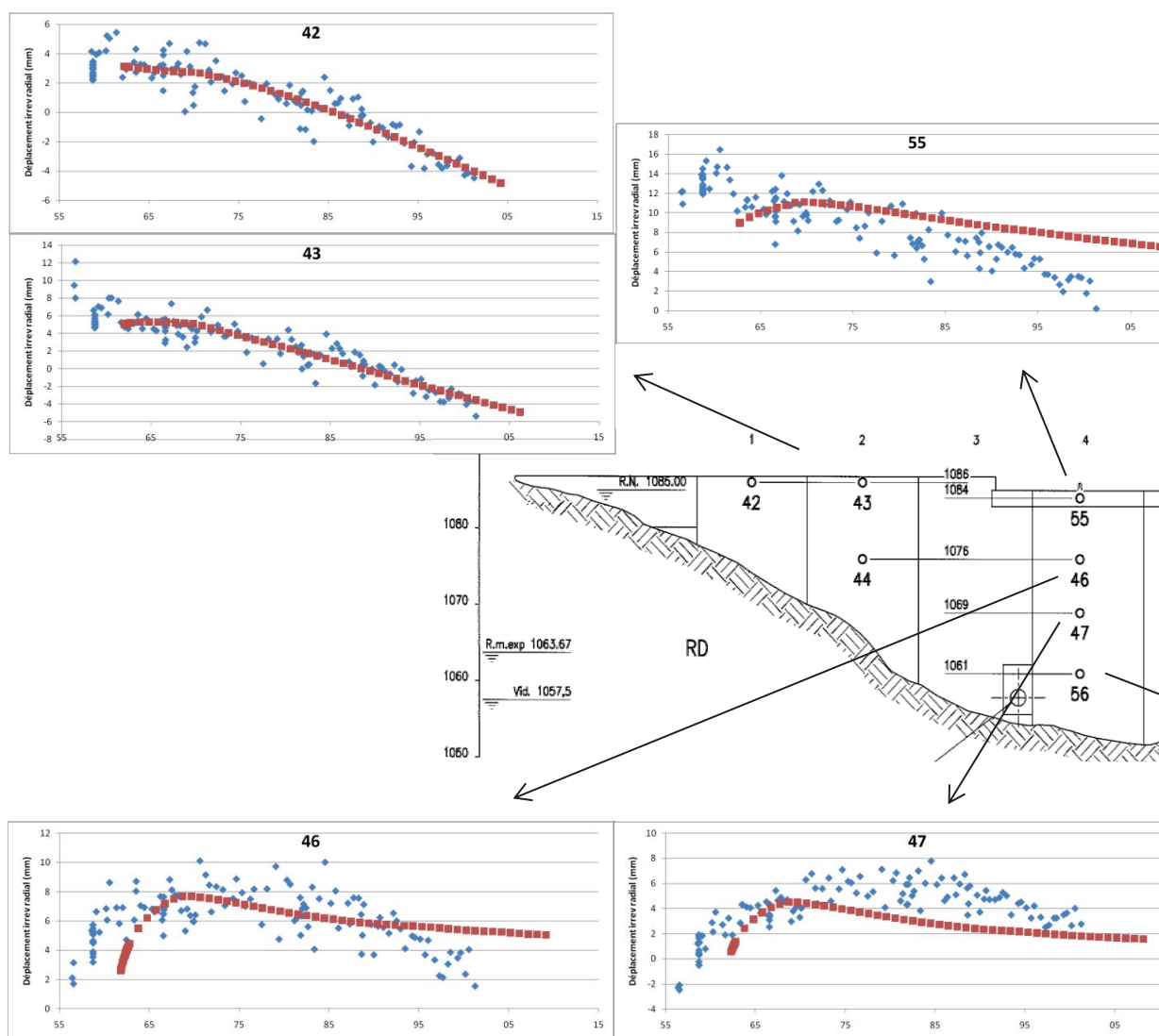
Figure 6: irreversible radial displacement estimated and calculated

Considering the complexity of the dam's behavior, the calibration is considered acceptable despite the fact that the central cantilever's behavior isn't perfectly represented. However, the model is able to represent the change of direction of the lower part of the dam (displacements downstream then upstream) while the crest is moving continuously upstream.

The influence of the long term behavior of the dam is analyzed regarding the evolution of the dam/foundation contact opening (Table 1) and of the stress state of the concrete (Figure 7). For the first point, the model shows a closure of the dam/foundation contact, particularly in summer while an opening is still likely possible (3.3 mm). That can explain why the full uplift is recorded only in winter under the dam. The analysis of the stress state of the dam shows an important increase of the compression stress close to the left abutment: from 5 to 10 MPa between 1960 and today. On the right side, the gravity abutment brings more flexibility, which leads to lower stress values. In-situ stress measurements with flat jack are under consideration in order to confirm the stress values calculated.

Table 1: evolution of the opening of the dam/foundation contact with swelling

	Opening of the dam/foundation contact (mm) 1961	Opening of the dam/foundation contact (mm) 2010
Hydrostatic load + Summer	2.8	1
Hydrostatic load + Winter	4.8	3.3
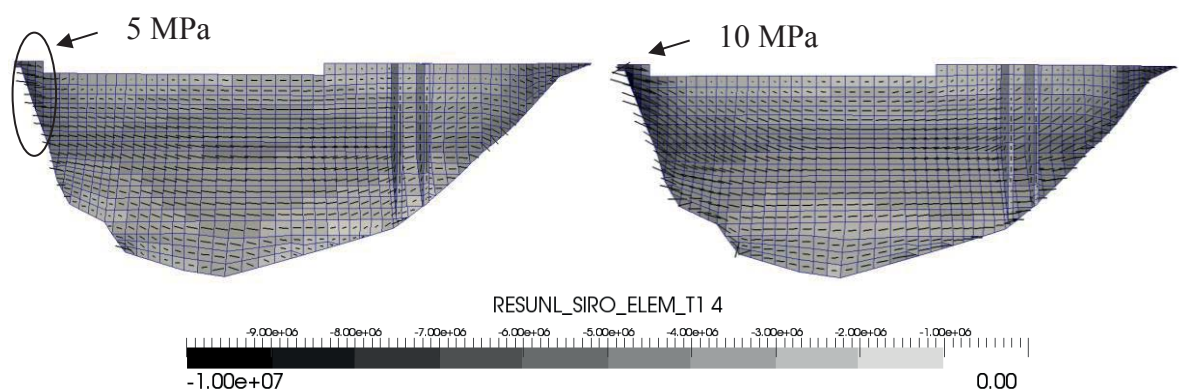
Figure 7: main arch stress on the upstream face in summer: without (1961) and with swelling (2011)

Conclusion

At the beginning of this study, the dam's behavior was difficult to understand: multiple mechanisms were involved and therefore, the problem could not be solved with basic interpretations. As often, model increasingly complex allow to separate each phenomena (opening of the dam/foundation contact, swelling, creep) and to understand their influences on the general behavior of the dam. The last model is used to evaluate the impact of the long-term behavior on the stress state of the dam and to decide what need to be done to assure the safety of the structure.

References

[1] Code_Aster software, www.code-aster.org
[2] Grimal E., Bourdarot E (2013). Modeling AAR on concrete dam. ICOLD 81th Annual Meeting Symposium, Seattle, 2013, pp. 99-109.

Need for transient thermal models, with daily inputs, to explain the displacements of arch gravity dams

I. Escuder-Bueno[1], D. Galán[2] and A. Serrano[3]

[1]Instituto de Ingeniería del Agua y Medio Ambiente. Universitat Politècnica de València

(Spain) http://www.ipresas.upv.es

[2]División de Seguridad de Presas. Canal de Isabel II Gestión (Spain)

http://www.gestioncanal.es

[3]iPresas, SPIN-OFF UPV. web: http://www.ipresas.com

E-mail: iescuder@hma.upv.es

Abstract

La Aceña Dam, with 66 meters of maximum height, belongs to the typology of concrete gravity dams, and is operated as part of the water supply infrastructures of a Spanish major city. Many instrumentation records were available but among them, the ones provided by four direct pendulums outstood by its quality and consistency. The range of the values of the movements registered by those pendulums, of almost 4 cm and of totally elastic nature (showing no irreversible movements), set some interpretation challenges. The apparent incapacity of the models to reproduce the observed behaviour was used as a starting point for the diagnosis of the main sources of uncertainty: the nature of the foundations and the state of the joints, among others. These aspects have constituted the developmental axis of a series of works that have led to a number of effective and efficient actions on the dam during the last years. However, an updated transient thermal model with daily inputs on external and internal measured temperatures, coupled with a mechanical model has shown an spectacular improvement in the explanation of the displacements recorded by the instrumentation.

Software and constitutive models

The first numerical model of global simulation of the stress-deformation behaviour of the dam of la Aceña was done as part of the works "First review and general safety analysis", carried out by the consultancy firm OFITECO in 2005 for CANAL DE ISABEL II, owner of the dam. The model was done with SAP2000NL and intended, among others, to capture some existing radial movements that have been registered by the four direct pendulums and that were higher that expected.

Based on the results of these works, Francisco Blazquez Prieto and Ignacio Escuder presented the case as one of the problems to be tackled by independent calculation teams during the "Ninth International Benchmark Workshop on Numerical Analysis of Dams", organized by the Dam Calculation Committee of the International Commission on Large Dams (ICOLD) in Saint Petersburg, Russia, in June 2007.

According to Escuder and Blazquez (2007), despite the great diversity of software (SAP 2000NL, CANT-SD, COQ-EF, SOFiSTiK, MERLIN, DIANA y ANSYS) and thermal models (three of which were transient), none of the seven teams that worked on the records of the radial movements tracked by the pendulums from January 1999 till September 2001, was able to predict the magnitude of the recorded displacements when using realistic values of stiffness of the dam body and foundations.

In 2012, a re-evaluation of the model was done, which is presented in the present paper. The distinctive feature and more promising fact of this re-evaluation when adopting different software and a new behaviour model, was the fact having a much longer list of data (now running until 2011) that included daily temperature measurements (whereas at the time of the Benchmark Workshop, the experts had to work on monthly measurements given that daily measurements were missing in 1999 and an important part of 2000).

With regard to thermal modelling, it is worth mentioning that the 2005 model, though done with a SAP 2000NL Licence, a very appropriate code for structures in general, could not guarantee to make the most of the data, mainly due to the limitations of the thermal module of the package (stationary nature).

Upon consideration of this aspect, it was decided to develop the numerical models with a different software package, FLAC (Itasca, 2004), which would allow a transient analysis of temperature transmission and thus provide the best-adjusted results realistically attainable.

FLAC (Itasca, 1994) is a finite differences code (explicit scheme) that allows the simulation of the behaviour of soils, rocks, concrete structures, etc. as well the interaction among these elements. The program is based on a scheme of Lagrangian calculation in which each element behaves accordingly to a specifically prescribed stress-displacement relation, as a response to the applied forces and the existing constrains in its boundaries.

FLAC is doted with an internal programming language (FISH) that allows the definition of each calculation organization (i.e., complex construction sequences) and calculations of very different nature (i.e., for each constitutive relation). The main potential of the base code is the capacity of the software to model tensional states through the use of pre-set constitutive models and others purposely defined by the user. For la Aceña case, a mechanical elastic and linear model was adopted and coupled with a transient thermal model.

The stiffness parameters that define the mechanic model are Young's Modulus (E) and Poisson's Ratio (v), which are somehow equivalent and that can express the strain-displacement relations accordingly to the Volumetric Deformation Coefficient (K) and Shear Deformation Coefficient (G).

With regard to the thermal module of FLAC 3D, it must be noticed it incorporates diffusion models as well as advection ones. The simulation of the first type of model, used for the case of la Aceña, allows the analysis of heat transmission through the materials along time and the development of thermally induced stresses and displacements.

The process of heat diffusion that the program solves through the optional thermal module is defined by the following differential equation:

$$\rho \cdot C \cdot \frac{\partial T}{\partial t} - k \cdot \left(\frac{\partial^2 T}{\partial x^2} + \frac{\partial^2 T}{\partial y^2} + \frac{\partial^2 T}{\partial z^2} \right) = q_v \tag{1}$$

Where ρ is the density of the medium, C the specific heat, k is the conductivity and q_v is the source of hydration heat.

In the development of the model, all involved parameters (density, conductivity and specific heat) have been assumed as being constant and independent of the temperature. Indeed, since the variations of concrete properties with temperature are very small, they can be neglected without concern. With respect to the boundary conditions, the external parameters of the dam are considered as convective surfaces, that is, as behaving accordingly to the following relation:

$$q_n = h \cdot (T - T_e)$$

(2)

Where q_n is the component of normal flux pointing towards the outside of the considered boundary expressed in W/m^2, h is the convective heat transfer coefficient expressed in W/m^2°C, T is the temperature of the boundary surface and T_e is the temperature of the surrounding fluid, with both temperatures expressed in °C.

In the coupled thermal-mechanical model, the solution of the thermal stresses requires a reformulation of the incremental relations of stress-displacements that FLAC 3D achieves through a subtraction of the part of movement due to the change of temperature from the total incremental deformation.

Finally, the laws of movement defined in a continuous medium are transformed through the former approximation into a system of equations that are applied to the nodes that represent the structure. These equations correspond to the laws of Newton applied to these discretized nodes and result in a system of ordinary differential equations that can be solved numerically from the explicit method of finite differences with respect to time.

Summing up, it can be stated that the code FLAC gathers the necessary conditions to tackle successfully the study of La Aceña dam behaviour, taking advantage of the existence of thermal and movements records of a level of detail and quality very unusual in such structures.

Simulation methodology

The present analysis simulates the stress-deformation behaviour of the dam of La Aceña in the period of 1999-2011, which is the one for which movement data were available through pendulum readings. In particular, two radial measurements were available (crest and horizontal gallery) from 4 pendulums (pendulums from 1 to 4).

The mechanical properties used in the model are the same employed in former studies of the dam and are shown hereafter (Table 1):

Table 1: Dam and concrete mechanical properties

Young's Modulus (dam)	$20 \cdot 10^9$ Pa
Poisson's Ratio (dam)	0.2
Density (dam)	2405.7 kg/m³
Young's Modulus ((foundation)	$10 \cdot 10^9$ Pa
Poisson's Ratio (foundation)	0.2
Density (foundation)	2242.6 kg/m³

The main difference between the current analysis and those carried out in the past is that better data are now available. In particular:
1. Daily records of the external temperatures in the dam since October 2000. Before, only average monthly temperatures were available.
2. Daily data from the three thermometers located in the concrete since January 2008. Prior to this date there was no data about dam concrete temperatures.
3. Data on the reservoir water temperature (year 2011, monthly periodicity).

Higher periodicity (daily) of pendulums readings since July 2004 thanks to the installation of automatic readers.

In order to understand the effect the different hypotheses have on the results, several models of the dam have been done, through the combination of the following options:
- Geometry: 2d and 3d
- Foundation: With and without foundation
- Temperatures: simplified hypothesis and improved hypothesis

Since 2008 there exists a register of the temperatures measured in three points inside the concrete that have helped to improve the original thermal hypothesis in the terms indicated hereafter, and that correspond to what has been named "improved hypothesis":
- The temperature of the concrete in contact with the air is equal to the ambiance temperature plus the effect of solar radiation ($\Delta T = 10$ °C).
- The temperature of concrete in contact with the water has been assumed to be constant and equal to 5° C except for the superior layer that acts as a transition element between the ambiance temperature and water.
- Specific heat: 3.5 W/m K, thermal conductivity: 650 J/kg K, convection coefficient: 16 W/m² K and linear thermal expansion coefficient: 10^{-5}

Figure 1 shows the global geometry of the model and Figure 2 the location of the pendulums whose movements, measured in the crest, were used to check the goodness of the adjustment. Figure 3 represents the whole of the external variables (water level and external average temperature) as well as the pendulums measurements.

Rotation:
X: 40.000
Y: 0.000
Z: 30.000
Mag.: 1
Ang.: 22.500

shown
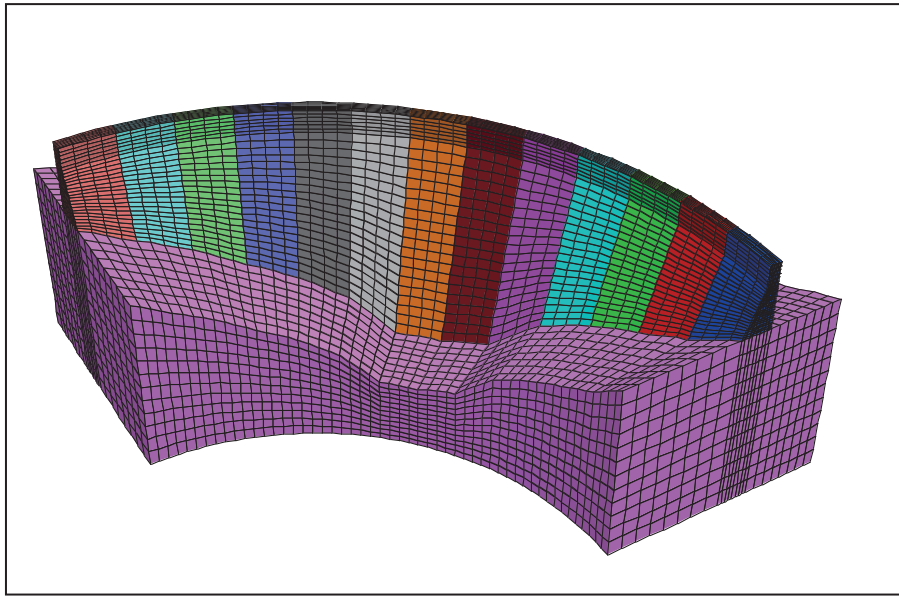
Figure 1: Complete geometrical model
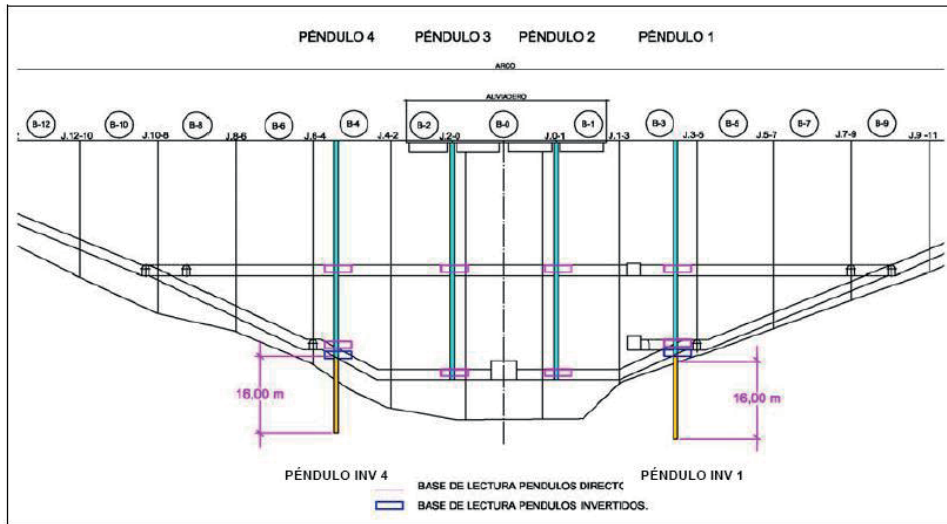
Figure 2: Location of the four direct pendulums
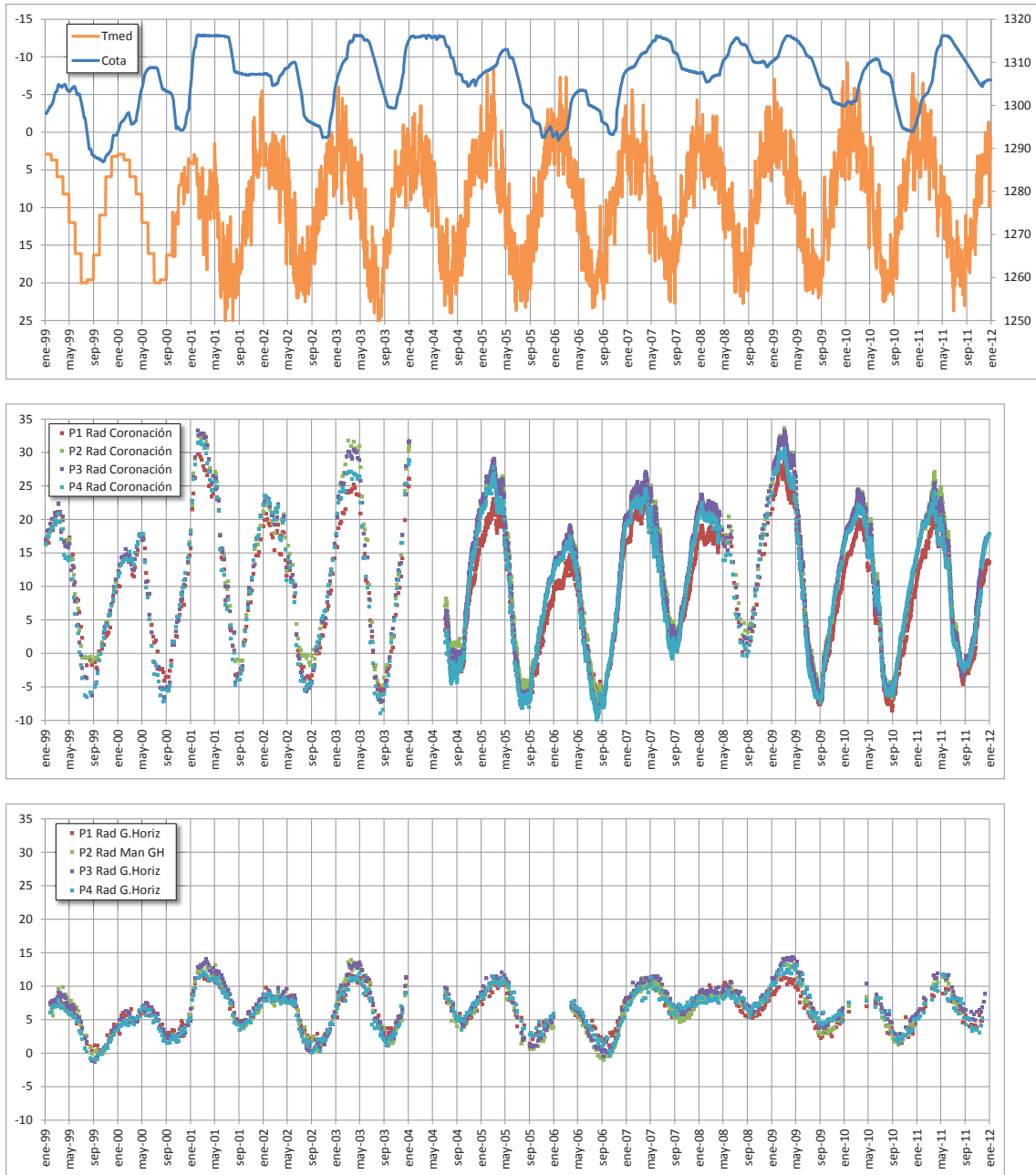
Figure 3: External variables (level in the reservoir and average ambiance temperature) and movements measured by the pendulums

Summary of the results and conclusions

The main conclusions that can be extracted from the current analysis of the stress-deformation behaviour of the dam of La Aceña through the simulation methodology described along the former sections, established in order to make the most of the whole set of records of thermal monitoring and movements, are:

- The elaborated models reproduce in a reasonably satisfactory way the thermal behavior of the structure as well as the movements observed in the dam.
- The fact of having carried out a transient thermal simulation for each day, capturing the impact of the direct sun exposure on the downstream side of the dam and estimating with accuracy the water temperature have been key elements to the goodness of the obtained numerical model.

Figure 4 shows a summary of the average errors incurred by the different models. As it can be observed, the best model is the so called "reference one" (3D, with foundation and the hypothesis of improved temperature).
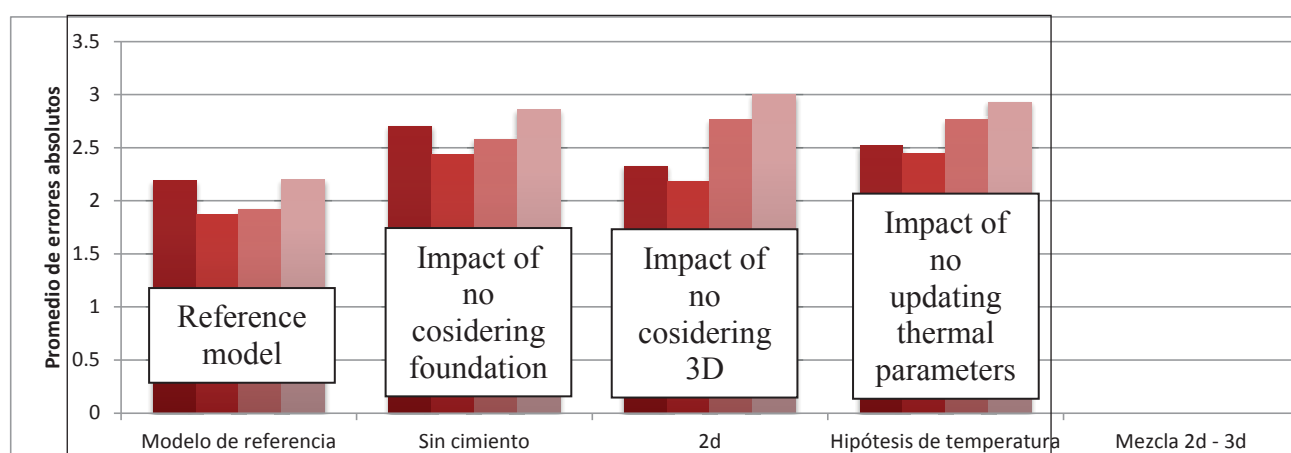
Figure 4: Average errors in mm for each model (shown for each pendulum, from P1 in darker red to P4, in a lighter grade.)

It can be stated that thanks to the recently developed numerical models a new tool is at hand to interpret the strain-deformation behaviour of the dam of La Aceña. This tool can complement the auscultations that are currently being done on the dam and that have provided an excellent level of information about both the thermal and movement behaviour. Also, the numerical tool has permitted the satisfactory and consistent reproduction of the stress-deformation behaviour auscultated until the end of 2011 and can act in the future as a way of contrasting the impact of new actions planned on the dam as well as a form of detecting potential behaviour change trends.

Figure 5 shows the comparison between the reference model (with the hypothesis of improved temperature) and the model with the original hypothesis of temperature.
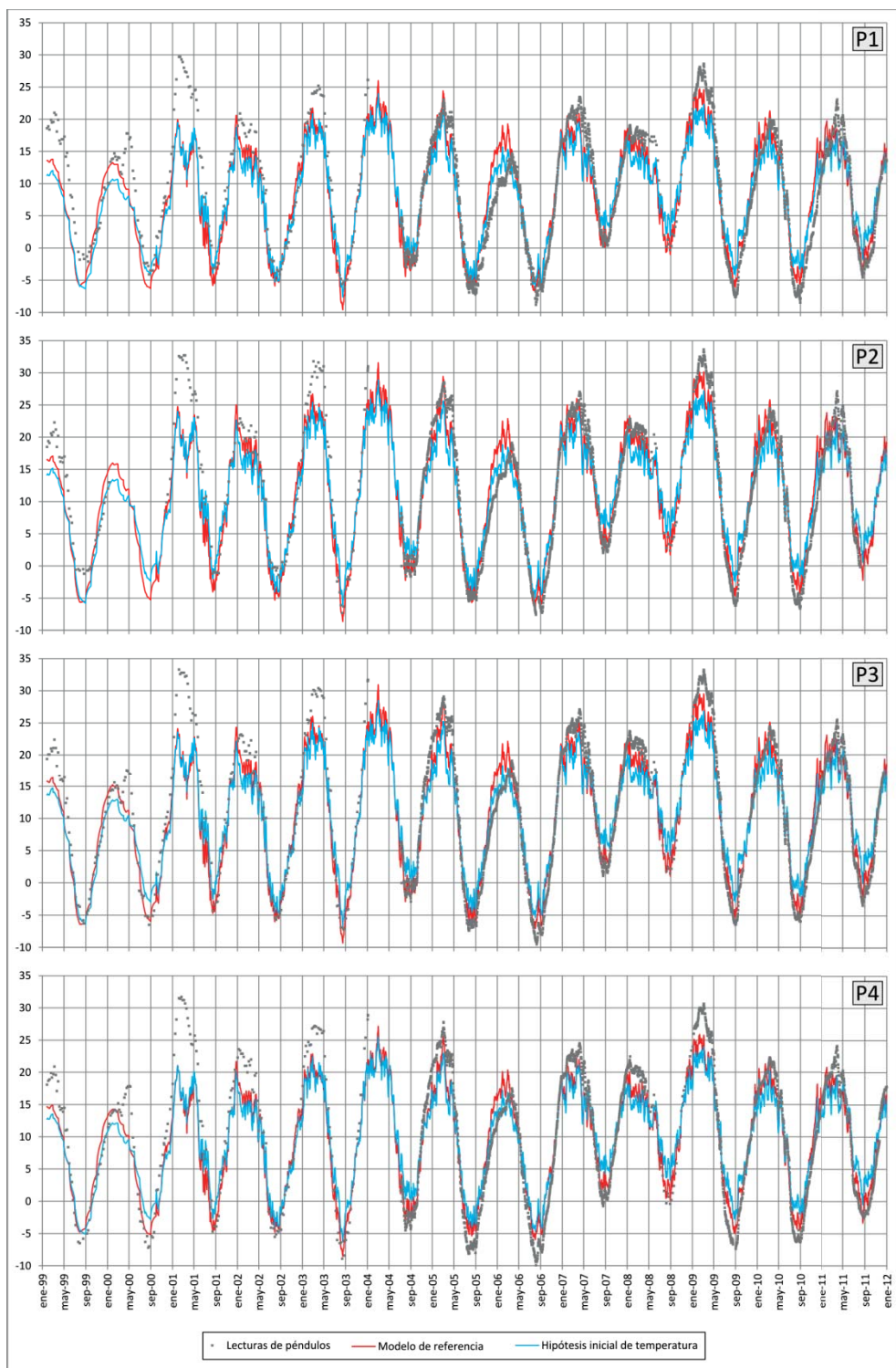
Figure 5: Extent of the improvement of the thermal model (reference model in red, non-updated thermal model in blue)

Acknowledgements

References

[1] I. Escuder and F.Blazquez, Analysis of the Elastic Behaviour of an Arch Dam, Hydropower and Dams, Issue 5, (2007)

The rehabilitation of Beauregard Dam: the contribution of the numerical modeling

A. Frigerio[1] and G. Mazzà[1]

[1] Ricerca sul Sistema Energetico – RSE S.p.A., via R. Rubattino 54, Milan, ITALY

antonella.frigerio@rse-web.it

Abstract

The paper describes the case-history of the Beauregard dam (Italy), a concrete arch-gravity structure 132 m high built between 1951 and 1960 on the Dora di Valgrisenche River. The design reservoir volume was about 70 mil. m^3. The geological and geotechnical investigations carried out since the dam construction and deepened in the last decade have underlined that a Deep-Seated Gravitational Slope Deformation (DSGSD) is located on the left slope. Since the first fillings of the reservoir, the interaction between the DSGSD and the dam was recognized to have relevant implications on the dam structural safety. For that reason, the Italian Dam Authorities in 1969 prescribed a limitation of the reservoir level with a corresponding reduction of the its volume to 6.8 million m^3, about 1/10 of the initial design volume.

The studies, which include a detailed analysis and thorough interpretation of the monitoring data over a time span of more than 50 years, have allowed to gain insights into the understanding of the DSGSD behavior and its interaction with the dam.

To interpret the already experienced effects of the bank movements against the dam and to forecast the future possible trends, the numerical modeling activities have played a key role. The solution chosen to guarantee a long-term safety operation foresees the demolition of the upper part of the dam in order to drastically reduce the cracking pattern of the dam body caused by the compression of the vault for the DSGSD movement.

Introduction

The Beauregard dam, located in the Aosta Valley, Italy (Figure 1) was completed in 1958. Operated by the Italian Electric Energy Company (ENEL) up to July 2001, the entire scheme was then acquired by CVA (Compagnia Valdostana delle Acque).

Figure 1: Location of the Beauregard dam on the Italian territory and aerial view of the dam

The 132m high arch-gravity dam has a crest length of 408m, it is 45.6m thick at the foundation level and 5m thick at the crest level. With a maximum operating design level of 1770m asl, the total reservoir volume was estimated in 70 mill. m³. The filling of the reservoir was undertaken in stages between 1958 and 1968.

Since the dam construction, the monitoring system installed on the left slope abutment showed the presence of a clear relationship between the reservoir level and the rate of movement of the Deep Seated Gravitational Slope Deformation (DSGSD) located on this left slope (Figures 2, 3, and 4).
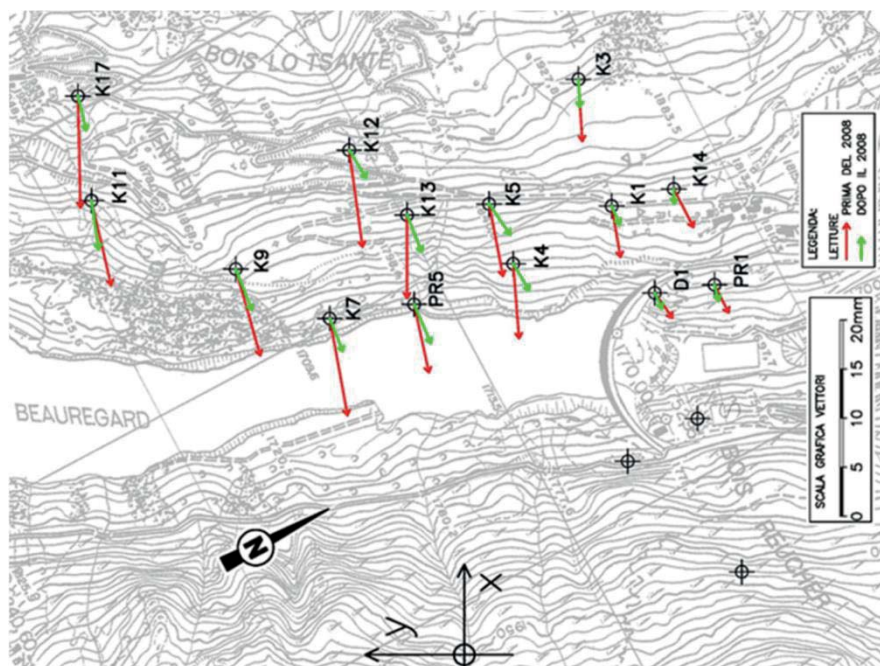
Figure 2: Displacement vectors measured from surface targets
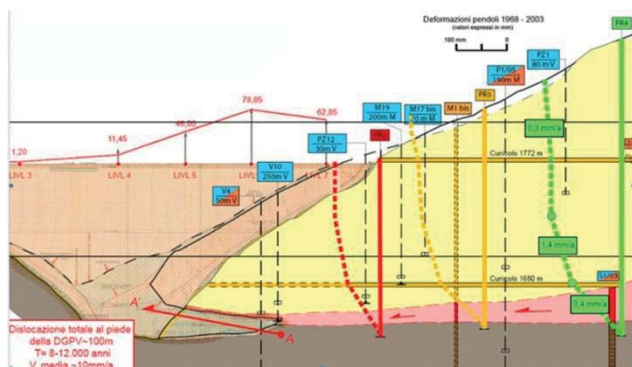
Figure 3: Horizontal displacement distribution along the plumb-lines installed in the lower portion of the slope close to the dam
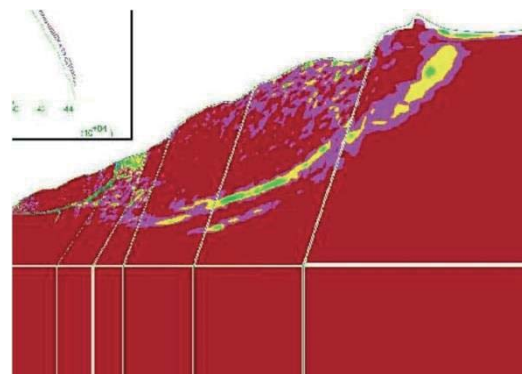
Figure 4: Zones of maximum shear strain rate: overall slope (safety factor = 1.40-1.45)

Coherently with the left bank movement, the dam was observed to deflect upstream, due to the trust of the slope against the vault, having as a consequence the appearance of cracks on the downstream face (Figure 5). As a consequence, in 1969 the operational reservoir level was lowered down to 1710m asl, corresponding to a reservoir volume of 6.8 mill. m3, as enforced by the Italian Dam Authorities.

Figure 5: The dam was observed to deflect upstream with cracks appearing on the downstream face and openings of some upstream vertical joints

The continuous monitoring of the DSGSD and of the dam, carried out by ENEL, first, and by CVA, in recent years, has allowed to operate the hydroelectric power scheme under closely controlled conditions. Moreover, some works carried out to control the superficial water flows due to melting snow and rain, in order to limit their filtration into the sliding body, have allowed to reduce the yearly speed of the slope from 1-2 cm to few mm. However, the interaction between the DSGSD and the dam has been recognized to have relevant effects on the long-term dam behavior as the cracking pattern was continuously progressing in time. Figure 6 shows the results of an on-site investigation carried out with a tomographic system that put into evidence the areas of the dam where cracking is particularly important, i.e. along the peripheral joint and close to the downstream dam toe.
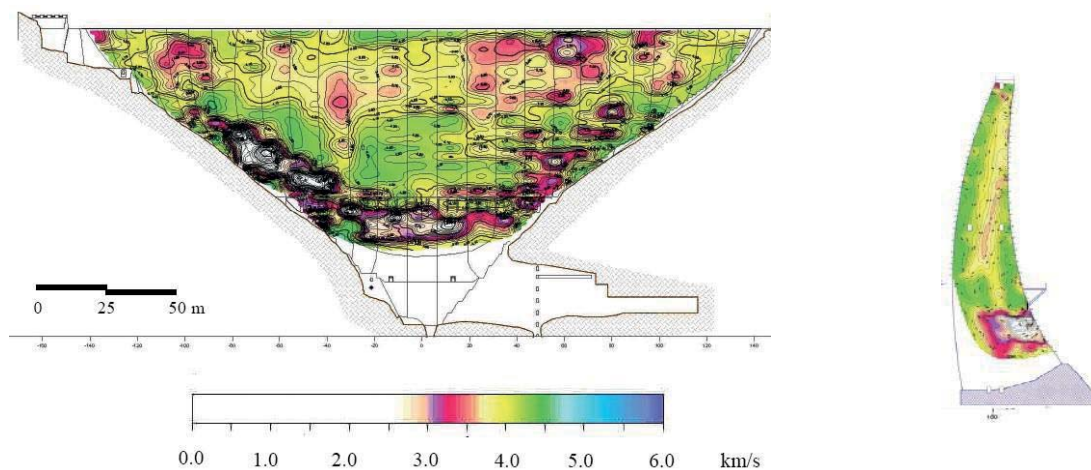
Figure 6: P-wave velocity tomogram: (left) downstream face; (right) main cross section

The strong interaction between the DSGSD and the dam has been recognized to have relevant possible implications from the civil protection as well as energy production points of view, and posed important territorial and environmental issues. For this reason the Owner decided to start a further study, making also reference to the support offered by numerical modeling, with the aim to find the most suitable and long-term solution of the problem.

The contribution of the numerical modelling

Synthetically, the main aims of the numerical model were:
- The interpretation of the dam behavior experienced since its first fillings,
- The calibration of the mechanical parameters of the dam-rock system in terms of comparison between the observed dam behavior and model results,
- The forecast of the future dam behavior at short-middle term adopting the calibrated model,
- The support to the designer for the analysis of possible technical solutions to guarantee the long term operation of the dam.

The numerical simulations of the dam were carried out using the FEM code ABAQUS/Standard [1]. A three-dimensional finite element model of the concrete arch dam including a proper portion of the surrounding rock mass foundation was generated in order to carry out numerical analyses (Figure 7).

In the rock mass foundation the active portion of the DSGSD has been taken into account as well as the shear surface, modeled in terms of an interface whose behavior is described by a frictional law. The nodes where the DSGSD movements were imposed are outlined with a red point in Figure 7.
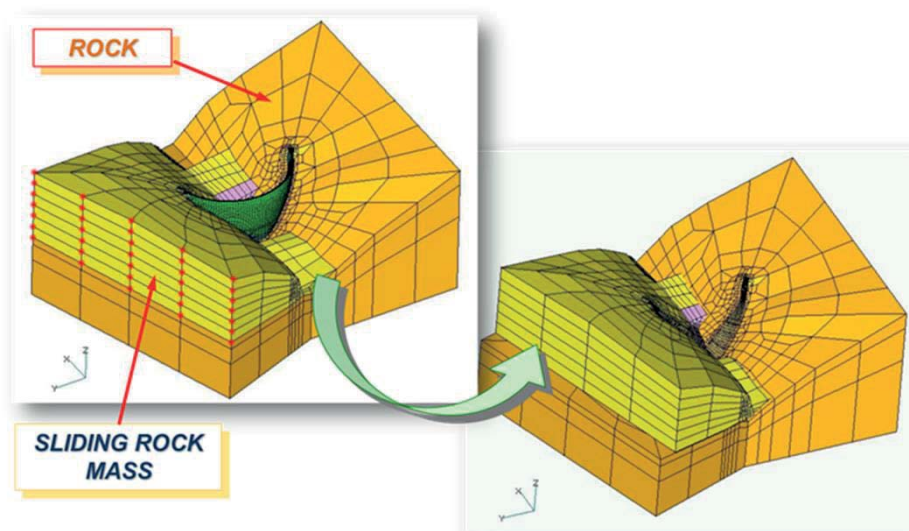
Figure 7: Finite Element mesh of the dam and the surrounding rock mass

A linear elastic isotropic constitutive law was assumed for the rock mass foundation whose mechanical parameters were defined on the basis of the results provided by the more recent geotechnical studies.

The Concrete Damaged Plasticity (CDP) constitutive law, available in ABAQUS library, was adopted to describe the concrete behavior (Figure 8). The model assumes that the uniaxial tensile and compressive responses of concrete are characterized by damaged plasticity. Under uniaxial tension the stress-strain response is linear-elastic until the failure value is attained; beyond this value a strain softening relationship follows. In compression the softening behavior occurs after an initial stress hardening. On the basis of the results of the indirect tensile tests, two different sets of material parameters were assigned to the concrete of the dam body and the "pulvino".
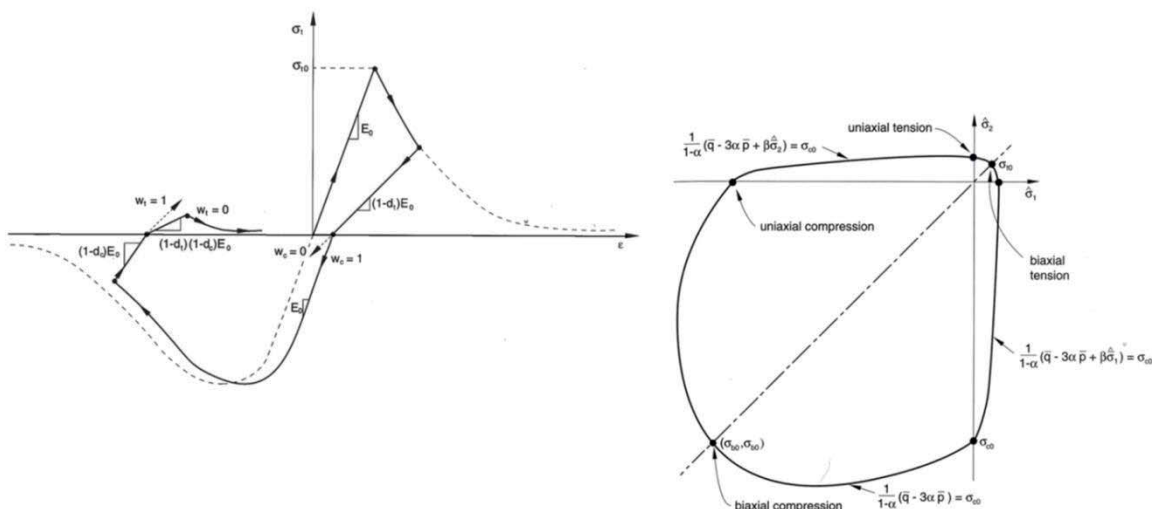
Figure 8: The Concrete Damage Plasticity constitutive law (Fenves, 1998) has been assumed for concrete and pulvino of the dam

Several preliminary analyses were carried out to identify the numerical model (calibration phase) in order to reproduce the real dam behavior dealing with the interaction between the structure and the slope sliding.

The movement of the left slope abutment was imposed by appropriate displacement boundary conditions applied at the nodes marked in red (as explained above, Figure 7) and the hydrostatic load was firstly considered taking into account the variation relevant to the first fillings; later, a constant reservoir level at 1710 m asl was assumed, according to the present operational conditions.

The identification process was mainly based on:

- The measured displacements along the dam crest (Figure 9);
- The monitoring points of two plumb lines, located inside the dam body in the main cross section and in the fourth block towards the left abutment respectively;
- The crack pattern of the structure as determined by tomographic investigations (Figure 10, to be compared with Figures 5 and 6).

As shown in Figures 14-15, the identified numerical model exhibits a good agreement with the deformation of the dam crest as well as the.
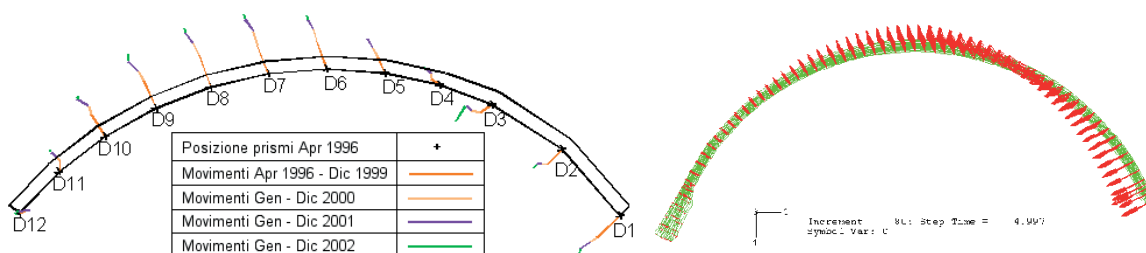
Figure 9: Deformation of the dam crest: (left) based on monitoring; (right) based on computations
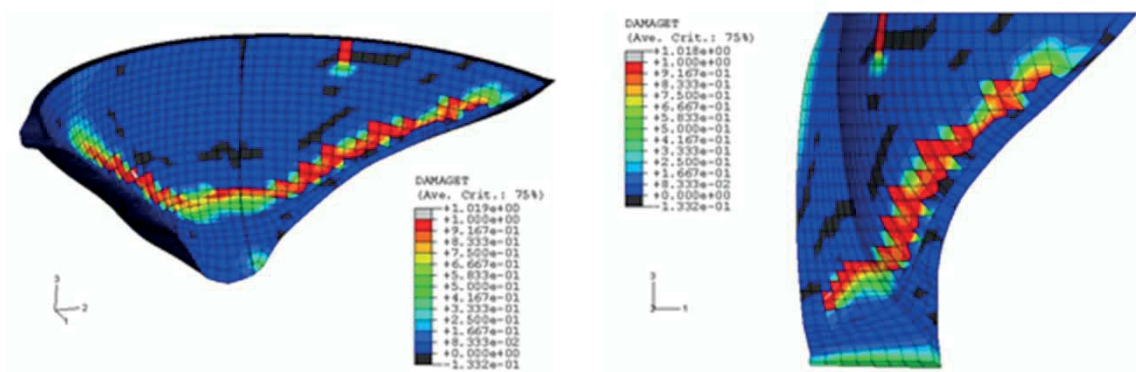
Figure 10: Localisation of damage computed with the 3D numerical model: (left) on the dowstream face of the dam; (right) on the main cross section

Afterwards, the identified numerical model was used to predict the future behavior of the structure considering a continuous increase of the landslide movement according to the trend foreseen from the past behavior.

The main purpose of the analyses was to assess if the dam might undergo to local or global instability phenomena such as snap-back.

The curve nr. 1 in Figure 11 allows to exclude snap-back instability for the overall structure because beyond the peak value the reaction force on the main cross section of the dam decreases gradually as the landslide movement increases.

Although the measured displacement towards the upstream direction of the middle point of the dam crest (about 0.21 m) is close to the peak value of the reaction force curve, it has to be bear in mind that the structure is subjected to an imposed deformation rate due to the landslide movement. For this reason the structure will be able to follow the softening branch of the reaction force curve avoiding sudden failure when the peak value will be attained.
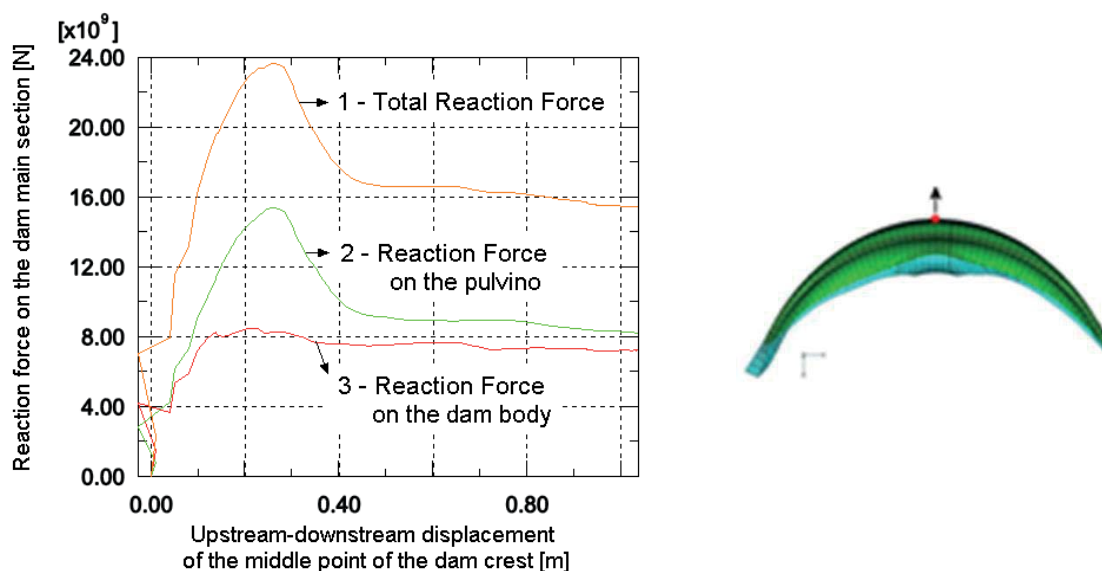
Figure 11: Reaction force on the main cross section of the dam vs the upstream-downstream displacement of the middle point of the crest dam

The dam rehabilitation

Different possible long-term solutions were considered by the designer (Studio Marcello, Milan) who was in charge of the rehabilitation program.

Numerical modeling was widely adopted in order to analyze the different solutions which main aim was the reduction of the trust effect of rock sliding against the dam.

Among the different solutions, the two more widely analyzed were those shown in Fig. 12.
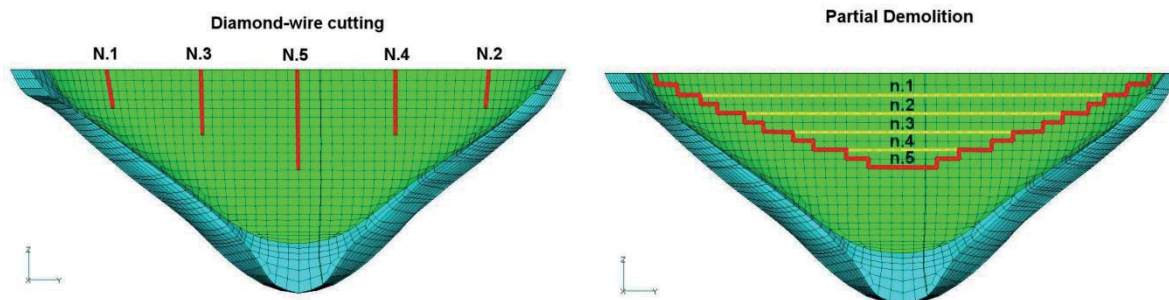
Figure 12: Two of the possible long-term solutions adopted for the rehabilitation of Beauregard dam

The partial demolition solution (right picture of Figure 12) was the one finally decided by the rehabilitation designer. The demolition of the upper part of the dam will lower the crest elevation from 1772m to 1720m asl.

The estimated volume of the demolished concrete will be about 150,000 m^3. The demolished material will be used to fill the two volumes located at the upstream and downstream dam toes (Figure 13).

Additional works have been carried out in the frame of the rehabilitation interventions, among which the improvement of the hydraulic scheme with the construction of a gated spillway and a discharge tunnel.
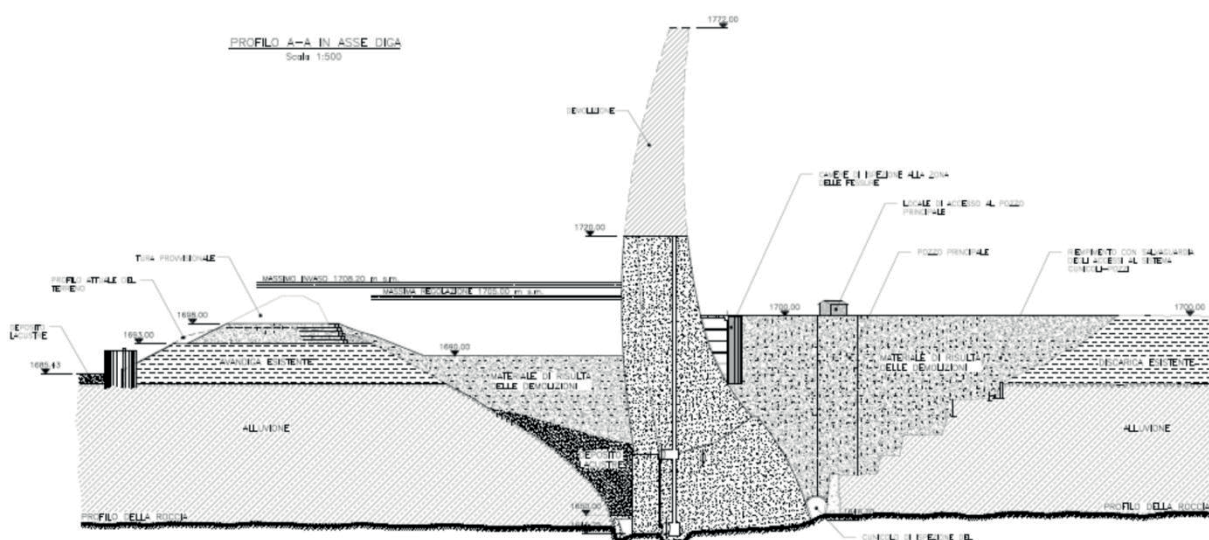
Figure 13: Cross section of the dam: final configuration after the demolition

The methodology chosen for the demolition is blasting. The demolition started in the Spring of 2013 and will end in 2014.

Figures 14 and Figure 15 show some phases of the dam demolition that is in progress.

Just to give some figures about each demolition step, the case shown in Figure 15 is relevant to an explosion carried out with about 850 ton of explosive located in 120 boreholes with a diameter of about 8 cm and a length of 6m.

The demolished concrete shown in the picture regards a volume of about 6m high x 7m thick x 50m wide.

Figure 14: Different sequences of the dam demolition: the dam before the starting of works (up-rigth); the preparation of one explosion step (up-left and down)

Figure 15: Different sequences of the dam demolition

Conclusion

The case history of Beauregard dam is an emblematic case that has posed to the engineers in charge of operation and safety very critical choices, considering that the construction of new dams, and structures in general, represents their main mission.

In the Beauregard case it has been deemed necessary to proceed, as sometimes happen for the human life, with a sort of a limb amputation in order the save the dam life.

The decision has been difficult and it has been necessary to investigate very deeply and for long time before all possible aspects affecting the system, deciding which could have been the most reasonable solution from the engineering point of view.

The choice has been taken considering the different facets of the problem: safety, mainly, environmental protection, energy production.

Environmental as well as economic and financial aspects are not in the aim of the present paper and could be widely shown in a future paper. Analogously, also some other technical aspects relevant to the civil works that are under construction at the downstream toe and facing to check the presence of possible leakages, will be discussed in further papers.

The present paper has the aim to put into evidence the support that numerical modeling can give to decision makers in a very complex problem like the one proposed by Beauregard dam.

Acknowledgements

References

[1] Hibbitt, et al, ABAQUS/Standard Theory Manual, Release 6.6, 2005.
[2] G. Barla et al., The Beauregard dam (Italy) and the deep-seated gravitational deformation on the left slope. Hydropower 2006, Kunming, China, October 2006.

Earthquake Assessment of Slab and Buttress Dams

H. B. Smith[1,2] and L. Lia[2]

[1] Norplan AS, Oslo, Norway
[2] Department of hydraulic and environmental engineering, NTNU, Trondheim, Norway

E-mail: herman.bjorn.smith@norplan.com

Abstract

This paper outlines work on the examination of the dynamic properties and seismic safety of slab and buttress dams [1]. The work has been carried out with a linear elastic numerical model established in the Finite Element Method program Abaqus.

One single dam section in a typical Norwegian slab and buttress dam with heights of 12 and 25 meters has been modeled in regards to varying reservoir water level and lateral bracing. Abaqus has been used for the frequency analysis and the dynamic time-history analysis.

The natural vibration modes of the dam represent movements in separate directions. Through a seismic event the greatest response will be represented by the buttress deflection in direction along the dam axis (axial direction). The resistance towards earthquakes will depend significantly on individual stability of elements rather than the global stability. In particular, the tensile stresses occurring in the buttress when deflecting in the axial direction are found to be a potential failure mechanism.

Providing lateral bracing by struts positively influences the response of the slab and buttress dam in seismic events. When lateral bracing is provided, the ability of the dam to transfer the inertial forces to the abutment is important.

Introduction

The American-Norwegian engineer Nils Ambursen developed the slab and buttress dam, the Ambursen dam, in the early 20th century. Several of these dams were built until the 1970s, especially in North America and Norway. Figure 1 presents the Håen Dam, a typical Norwegian slab and buttress dam with a structural height of 12 meters. [2] [3]

Figure 1: The Håen Dam, view of downstream side with insulating wall

The reinforced concrete structure consists of the buttresses and an upstream inclined slab. The typical section and dimensions of Norwegian slab and buttress dams are presented in Figure 2. Insulating walls and lateral bracing, such as struts, are not always present. The upstream

slab is often constructed as continuous over two or three sections, with joints where the moment is zero. The resulting moment diagrams are as presented in Figure 3.

Earthquake safety regulations were introduced for Norwegian dams in 2010. Due to the recently updated regulations and the low number of slab and buttress dams in earthquake prone regions, there is uncertainty regarding the dynamic assessment of existing slab and buttress dams in Norway.

Figure 2: Typical cross section [4]

The slab and buttress dam is proven to be highly efficient for static loading. Based on the experiences from registered dam breaches, earthquake incidents and upgrades, the slab and buttress dam needs to be checked for earthquake loads in both horizontal directions. Structural slenderness of buttresses and slabs makes the structure particularly vulnerable to axial loading. Load distribution and interaction between the various elements could cause the strength and stability of individual elements to be more critical than the global stability. When dynamic loads are considered, several possible failure mechanisms are identified.

Figure 3: Moment distribution in continuous slabs [4]

Finite Element Model

Based on a literature review, existing computational methods and site inspections of slab and buttress dams, a linear elastic numerical model was established in the Finite Element Method (FEM) program Abaqus. The importance of various structural details in a seismic context has been analysed and utilised for the modeling of a single dam section in typical Norwegian slab and buttress dams with heights of 12 and 25 meters. Two models have been used for the analysis regarding height variation, reservoir water level and presence of lateral bracing. Dynamic properties, global response and impact on the structural elements have been analysed through eigenfrequency analysis and dynamic response-history analysis. For convenience the results presented in this paper focus on the base case of a 25 meters high dam section.

The dam section was modeled, as presented in Figure 4, as a single buttress and continuous slab with symmetrical
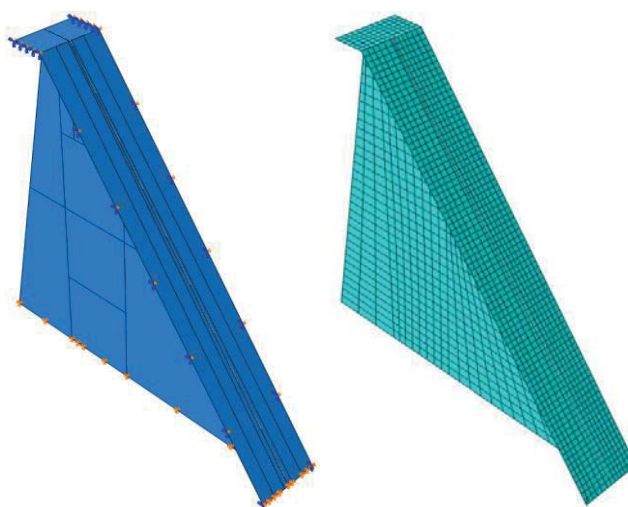
Figure 4: Illustration of the model and generated

boundary conditions in the slab's axial direction at the mid-span.
The dimensions of the modeled section are:

- 5 meters c/c between buttresses
- Crest width of 2.5 meters
- 5V:4H inclination of the upstream slab
- 5V:1H downstream inclination of the buttress
- Both the slab and buttress thickness increases 20 mm per meter from *t = 300 mm*, at the dam crest

The model was partitioned in order to provide nodes in the locations of all lateral bracing. The generated mesh gave a total of 2676 shell elements and 2863 nodes.

The foundation rock is expected to be of good quality and is therefore idealised with no mass and with great stiffness compared to the slender slab and buttresses. The slab and buttress dams are normally designed without transmission of reinforcement to the foundation or between the structural elements. The joint between slab and buttress is designed with a shear key to avoid displacement in the axial direction. As these joints will allow some rotation, all connections are modeled as hinged.

Lateral Bracing

When present, struts and insulating walls will provide lateral bracing for the buttresses in addition to the upstream slab. Insulation walls are introduced to reduce the temperature gradient through the slab. With typical thickness of *t = 120 mm* lightly reinforced, low concrete quality, the actual contribution of the insulation wall in a seismic event is not included. Only the effect of lateral bracing on the dynamic properties of the slab and buttress dams' by struts is therefore investigated.

Struts are normally simply supported between the buttresses, i.e. only compression forces are transferred through the struts. The struts are modeled by massless elastic springs that ensure the stiffening effect in the axial

Figure 5: Selected placement of struts

direction. Working both in compression and tension, the springs were modeled only on one side of the buttress in the chosen locations presented on Figure 5.

Loads

The applied static loading includes gravity and hydrostatic water pressure. Uplift, sediment loads and downstream water pressure are neglected, in addition to temperature loads.

Seismic loads are applied according to Eurocode 8 [5] regulations. This gave a maximum peak ground acceleration for mainland Norway of 1.6 m/s^2 horizontally and 1.0 m/s^2 vertically. The applied acceleration time histories, presented in Figure 6, are developed for ground type A and adjusted for Norwegian geological and seismic conditions.

The acceleration time histories are applied along the foundation in all three directions simultaneously. The acceleration time history in the axial direction is also applied along the edges of the slab.

Because of the upstream inclination, the horizontal hydrodynamic pressure is simulated according to Zangar's theory of added mass [7]. The overlaying masses of water are assumed to be directly accelerated by the dams' vertical accelerations [8]. The applied hydrodynamic added mass was decomposed from the horizontal and vertical contributions to work perpendicular to the upstream slab, and applied as inertia point masses at different levels, according to the presented distribution from Figure 7. Because of the flat slab, no hydrodynamic interaction was taken into account in the axial direction.

a) Applied in the upstream-downstream direction

b) Applied in the axial direction

c) Applied in the vertical direction
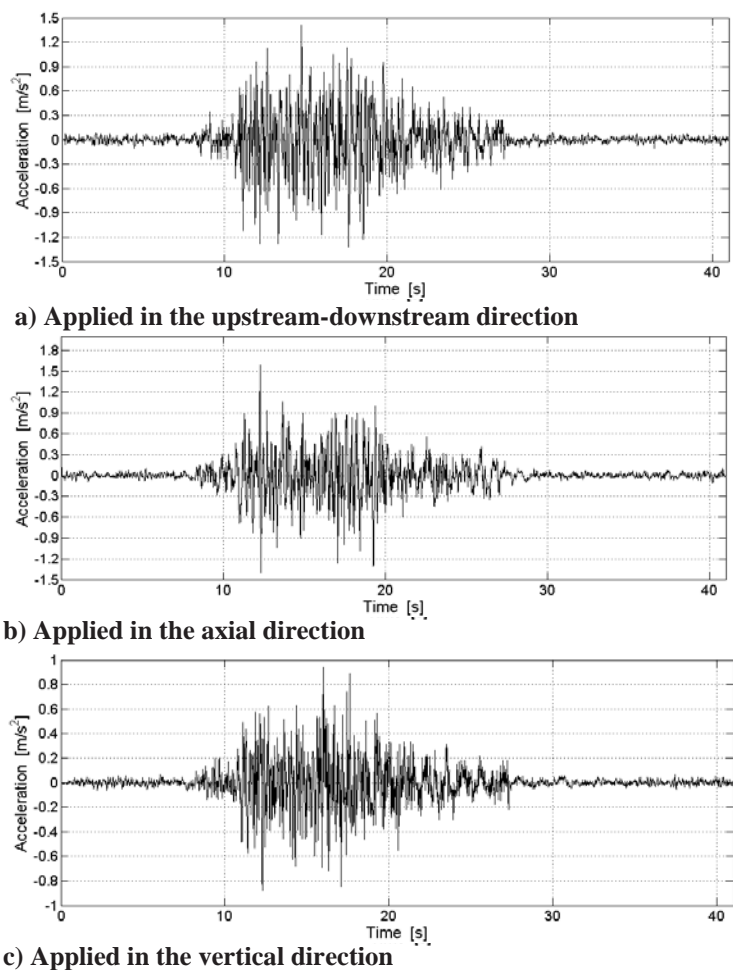
Figure 6: Utilized acceleration time histories [6]
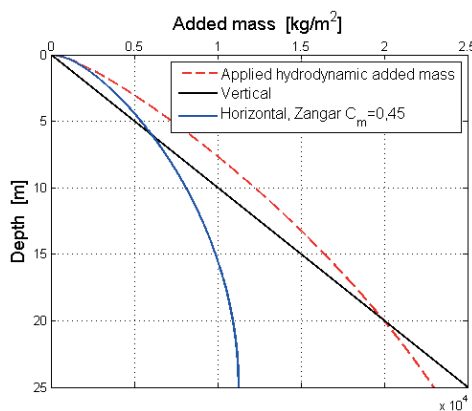
Figure 7: Distribution of applied hydrodynamic added mass

Material Properties, Strengths and Prescribed Damping

The concrete is modeled with elastic properties corresponding to a B25 concrete, described in Eurocode 2 [9]. The struts are modeled as elastic springs, with corresponding stiffness $k = EA/L$, acting both in tension and compression.

The concrete strength was determined in accordance with Eurocode 2 [9] regulations, adjusted for a 50 % increased dynamic tensile strength, according to Raphael [10]. The struts' capacity was determined by calculations of buckling and compression capacity.

Viscous Rayleigh damping, embedded in the concrete material properties and the hydrodynamic point masses, are used to model all damping in the system, including dam-water-foundation interaction and frictional dissipation. The additional stiffness proportional damping from the struts was not taken into account. Because the model represents the structure's elastic behaviour, a damping ratio of two percent was considered appropriate. It should be noted that an increased damping ratio would reduce the systems response.

Results

Frequency Analysis

The frequency analysis described the structures' natural vibration modes with movements in separate directions. In all analysed cases, the first mode is governing for the axial direction. Figure 8 describes the vibration mode shape and variation of period for oscillations in the slab and buttress dam section with water at crest level for different section heights and with or without lateral bracing.
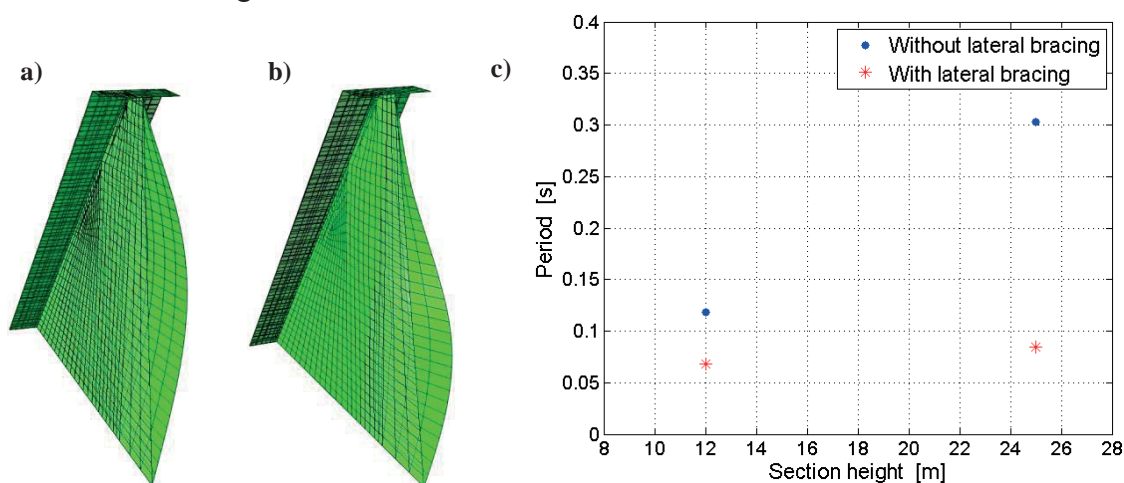
Figure 8: The first vibration mode a) Mode shape without lateral bracing b) Mode shape with struts present c) Variation of the vibration period

The first mode describing movement in the upstream-downstream and vertical direction was also governing in these directions for all cases. Figure 9 describes the mode shape and variation of period for the slab and buttress dam section with or without presence of water at crest level, for different section heights without lateral bracing.
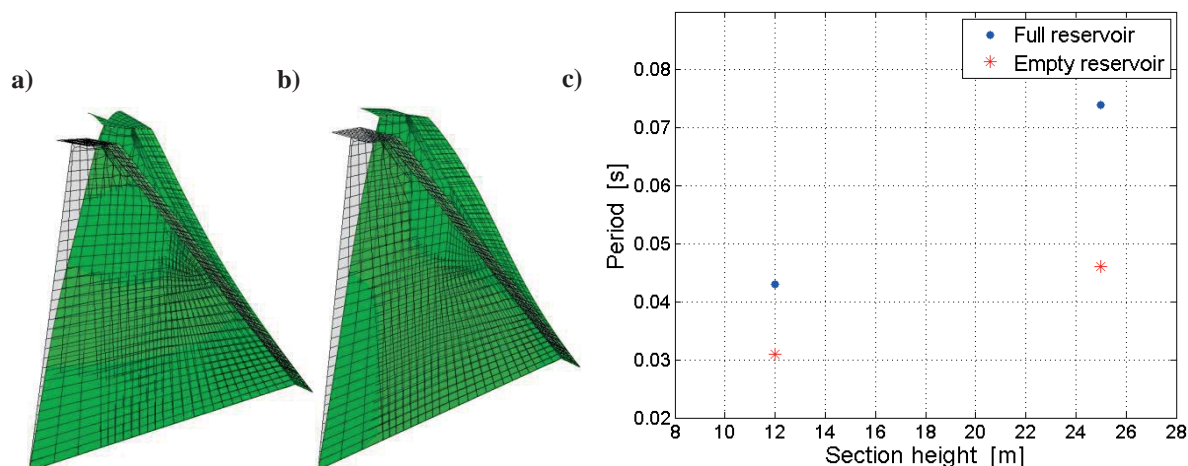
Figure 9: The first vibration mode describing movement in the upstream-downstream direction a) Mode shape without water b) Mode shape with water at crest level c) Variation of the vibration period

Dynamic Response-History Analysis

Through the seismic event, the models were never exposed to compressive stresses close to the concrete design capacity. The maximum principal stresses are therefore presented. It is assumed that cracking of concrete will occur when the design dynamic tensile strength $f_{ctd,dyn} = 1,5\ MPa$, is exceeded, marked by gray in the graphic presentations.

The typical deflected shape and maximum principal stress state during a seismic event are presented in Figure 10, for the 25 meters high dam section with water at crest level and with or without lateral bracing in the form of struts.
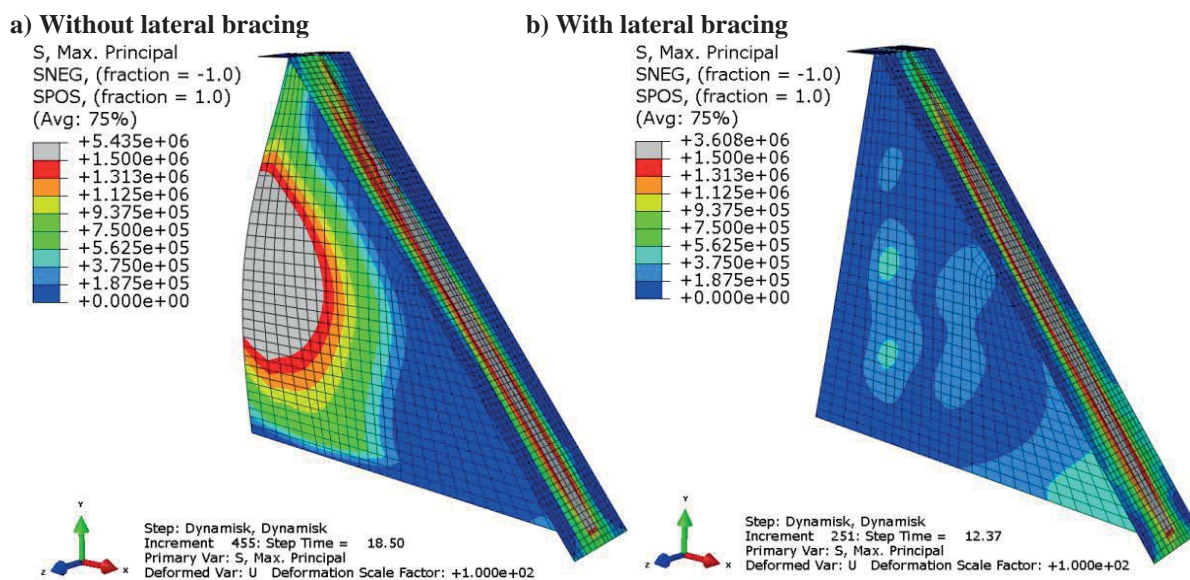
Figure 10: Typical deflected shape during seismic event, deformation scale factor of 100

The maximum principal stresses on each side of the buttress with water at crest level, are presented on Figure 11 without lateral bracing and on Figure 12 with struts.
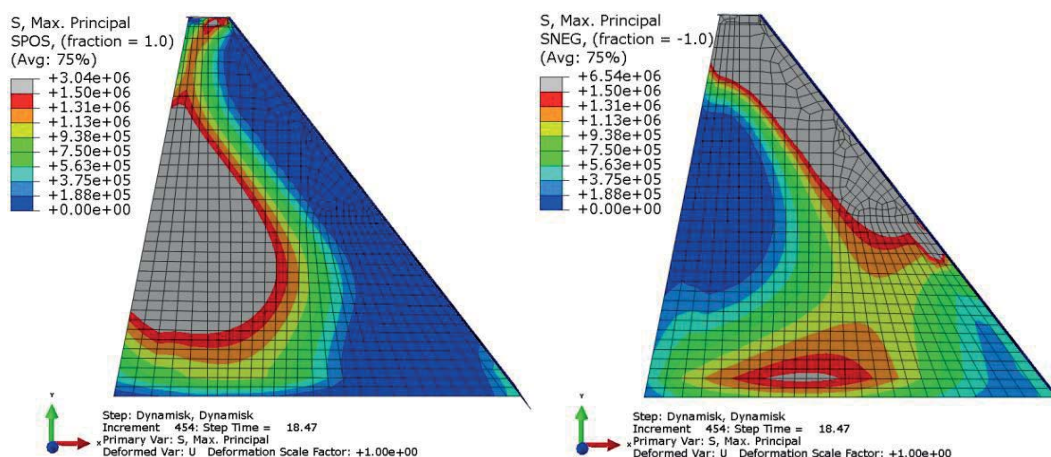
Figure 11: Maximal principal stresses on both sides of the buttress without lateral bracing during a seismic event
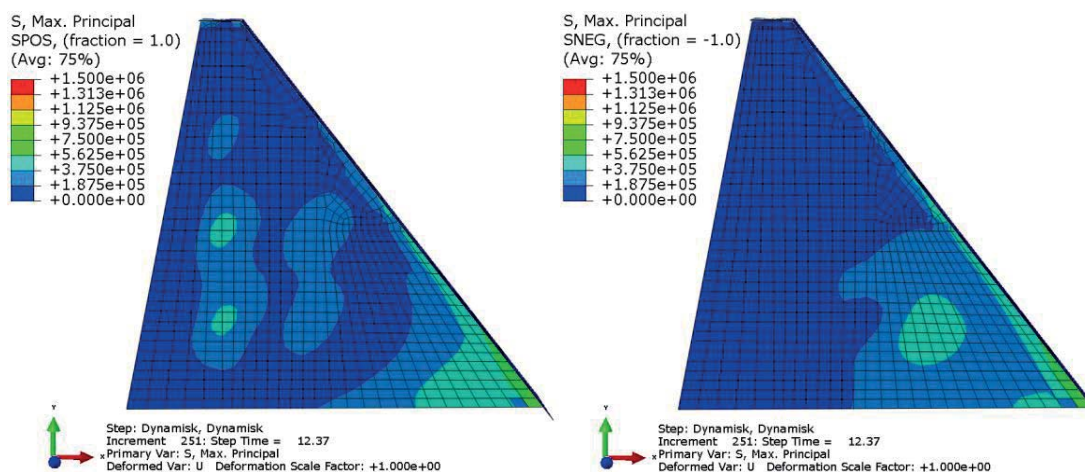
Figure 12: Maximal principal stresses on both side of the buttress with lateral bracing during a seismic event.

The time-history plot of transferred inertia forces to the highest loaded strut in the dam section of 25 meters height is presented in Figure 13. Representing both the struts on each side of the buttress, the plot describes the absolute value of the forces through the given elastic spring.
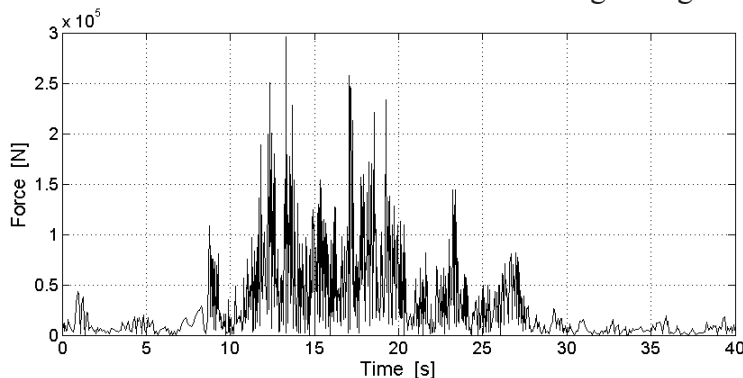
Figure 13: Time-history plot of the highest loaded strut in the 25 meters high dam section.

Discussion

Dynamic Properties

The distinct differences in the structures vibration modes in different directions, combined with the variation of the vibration period, leads to the following observations:

Dam height	An increase in the section height results in a greater mass while the dam stiffness decreases both in the axial and the upstream-downstream direction. Thus, a greater vibration period in all directions is obtained.
Water level	At higher water levels, the additional hydrodynamic mass increases the vibration period in the upstream-downstream direction.
Lateral bracing	Increased stiffness in the axial direction due to lateral bracing reduces the vibration period in the same direction.

Seismic Safety

Dam safety requirements for slab and buttress dams include overturning and sliding stability in addition to the required structural strength for all cross sections.

The dam safety should be considered in a seismic event and retain its integrity during the earthquake. The seismic safety has been evaluated based on global stability and occurring stress levels in the buttress. The struts are additionally considered. As the upstream slab is designed for tensile stresses, it is not further considered.

Global Stability

The maximum fluctuations of the reaction forces acting in different directions on the dam's sections would, in combination with one another, constitute a danger to the system's global stability. Nevertheless, the maximum fluctuations occur at various times throughout the event and are only applicable in very short time periods. The system will not have time to react, and there will be no danger of collapse even if the theoretical factor of safety against sliding or overturning in a given time goes below 1.0. The consequences may be minor deformations if exceedance of capacity is repeated.

The theoretical safety factor against sliding through the seismic event for the 25 meters high dam section with water at crest level is presented in Figure 14.
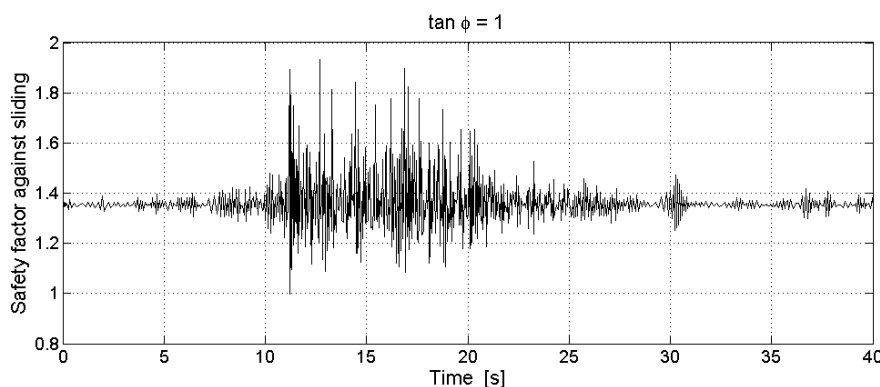
Figure 14: Variation in theoretical safety factor against sliding for a 25 meters high dam section with water at crest level.

Also considering the rest capacity when assuming a frictional factor of *tanϕ = 1*, the risk of sliding is not the critical case. Nevertheless, the theoretical safety factor against sliding for slab and buttress dams is reduced as the dam height increases.

The upstream inclination keeps the dam stable against overturning throughout the seismic event, as tensile stresses never occur along the buttress foundation.

Stresses in the Buttresses
A lower section height reduces both the response and stress level of the buttress. The presence of lateral bracing prevents the buttress deflection out of its own plane, and largely reduces the stresses. When struts are present, the buttress is bent around its connection points, and the maximum stresses are found in those locations.

The occurring tensile stresses in the numerical model have to be seen in relation with the presence of reinforcement. Before 1955 it was common to construct the slab and buttress dams without reinforcement in the buttresses [11]. In addition to tensile stresses, construction joints would endanger the buttress stability in such a case.

For dams constructed later than 1955, a minimum amount of reinforcement will always be present. Even though tensile stresses can cause cracking of the concrete, the strength and ductile nature of reinforcement will nevertheless increase the safety level compared to an unreinforced buttress.

Struts
The impact on the struts from a single section must be seen in relation to the struts compression capacity, found to be dimensioning over the buckling capacity. The transferred inertia forces are accumulated towards the abutments through the struts from neighbouring sections. When beams are not continuous over the dam length, unfavourable moments can be introduced into the buttresses.

Other Potential Failure Mechanisms
The following potential failure mechanisms should also be taken into consideration; the connections between elements, shear capacity and punching shear capacity of the buttresses, stress accumulation around cutouts, strength of the foundation and bearing capacity of the struts.

Uncertainties – Sources of Error
Because only one single dam section has been modeled, several assumptions have been required. Among others, the influence of adjacent sections, especially of different heights, is of importance.

As the results show a non-linear response and because reinforcement is not taken into account, the response and maximum occurring tensile stresses in the numerical model can only be indicative.

Conclusions

The results demonstrate how the dam vibration modes represent movements in separate directions. An increased dam section height results in an increased response because of the greater oscillating mass. Meanwhile, a raised water level in the reservoir increases the period for oscillation in the upstream-downstream direction.

Through a seismic event, the greatest response will be represented by the buttress deflection in the axial direction. The resistance towards earthquakes will be mainly dependent on the individual stability of elements rather than the global stability. In particular, the tensile stresses occurring in the buttress, as a result of deflection in the axial direction, is found to be a potential failure mechanism.

Providing lateral bracing by struts positively influences the response of the slab and buttress dam in seismic events. For the Norwegian slab and buttress dams in particular, the contribution of the existing insulating walls is considered to be small but positive. When lateral bracing is provided, the ability to transfer the inertial forces to the abutment is important.

In addition to the assessment of simplified analytical methods, it is recommended that further numerical studies should focus on the slab and buttress dams' nonlinear response, on the importance of global dam geometry, and verification of the numerical input parameters by physical vibration tests of an existing slab and buttress dam.

References

[1] Smith. Earthquake Assessment of Slab and Buttress Dams, Master thesis at the Department of Hydraulic and Environmental Engineering, NTNU, Trondheim, Norway, 2013.

[2] Various authors. Ambursen dams - Selected articles from the Ambursen Hydraulic Construction Company. R. M. Rudolph, Approximate Date 1912.

[3] NORUT Narvik AS. Innovativ forvaltning av betongdammer, 2009. In Norwegian.

[4] Guttormsen. TVM4165 - Vannkraftverk og vassdragsteknikk. Tapir akademiske forlag, 2006. Compendium of the Department of hydraulic and environmental engineering, NTNU. In Norwegian.

[5] Standards Norway. Eurocode 8: Design of structures for earthquake resistance - Part 1: General rules, seismic actions and rules for buildings, 2004. NS-EN 1998-1:2004+NA:2008.

[6] Kaynia. Communicated by. NTNU and NGI, Oslo, Norway.

[7] Zangar. Hydrodynamic pressures on dams due to horizontal earthquake effects. Engineering monographs, No. 11, 1952.

[8] Scott et al. Dam Safety Risk Analysis, Best Practices Training Manual. U.S. Department of the Interior, Bureau of Reclamation in cooperation with the U.S. Army Corps of Engineers, 2011. Version 2.2.

[9] Standards Norway. Eurocode 2: Concrete structure - Part 1-1: General rules and rules for buildings, 2004. NS-EN 1992-1-1:2004+NA:2008.

[10] Raphael. Tensile strength of concrete. Journal of the American Concrete Institute, 2:158 – 165, 1984.

[11] Kleivan, Kummeneje and Lyngra. Concrete in Hydropower Structures. Hydropower Development. Norwegian Institute of Technology, Division of Hydraulic Engineering, 1994.

Solution of dam-fluid interaction using ADAD-IZIIS software

V. Mircevska[1], M. Garevski[1], I. Bulajic[2] and S. Schnabl[3]

[1] Institute of Earthquake Engineering and Engineering Seismology,
univ. "Ss. Cyril and Methodius", Box 101, 1000 Skopje, R.Macedonia
[2] Mining institute, Batajnicki put 2, 11000 Belgrade, Serbia
[3]Faculty of Civil and Geodetic Engineering, University of Ljubljana,
1000 Ljubljana, Slovenia

E-mail: violeta@pluto.iziis.ukim.edu.mk

Abstract

Fluid dam interaction has a remarkable impact on the dynamic response of dams and could play an important role in assessment of their dynamic stability. This is particularly emphasized when dams are subjected to strong seismic excitations. The phenomenon has been for the first time physically explained and mathematically solved by Westargaard. The very first dynamic analysis based on application of "Added Mass Concept"; underestimated the random earthquake nature in assessment of the hydrodynamic effects. In the recent years, various BEM-FEM and FEM-FEM techniques have been developed to account for many significant parameters that influence the accuracy of calculated hydrodynamic effects. This paper presents a BEM-FEM orientated solution based on the use of the matrix of hydrodynamic influence as a very effective tool for analyses of extensive domains of fluid-dam-foundation rock systems for two major reasons: the computation time is far more effective than that in direct or iterative coupling methods and stability of the solution. The presented analyses are based on the use of genuine software originally written for static and dynamic analysis and design of arch dams.

Introduction

The ADAD-ver.3 computer program [1], originally written for static and dynamic analysis and design of arch dams, is under development for the last several years. It implements an analytical procedure for the three-dimensional dynamic analysis of arch dams including the effects of dam-water interaction (water incompressibility), soil-structure interaction and the nonlinear behavior of the of contraction joint manifested by partial joint opening and closing as well as tangential displacement. The process of generation of mathematical model runs parallel and interactively with the process of design of the particular dam. The program gives an option for computer design of the dam body [2,3], whose embedment is in accordance with topology of the terrain. Program offers automatic pre-processing for generation of finite element mesh of dam and part of the foundation mass to account for the dam-foundation interaction phenomenon, as well as effective way of generation of boundary element mesh, sufficiently accurate in following the topology of the terrain to account for the fluid structure interaction.

The program use sensitivity search analysis to detect the "most adequate" location of the truncation surface [4], where non-reflecting truncation boundary conditions should be imposed. The truncation surface should be located in a way to define the required completeness of the wave field where expansion of P compressive and dilatational waves takes place followed by scattering and radiational effects. Its further displacement away from

the dam should have a negligible impact on the calculated magnitude of the hydrodynamic effects.

The conducted analyses are based on an original and simple FEM–BEM fluid–structure interaction solution embedded in the ADAD–IZIIS software. This solution eliminates the difficulties of "direct" and "iterative" coupling methods by analyzing independently the two physically coupled sub-domains. The interaction effect is obtained in an uncoupled way computing the matrix of hydrodynamic influence by applying the concept of virtual work of "unit accelerations". The suggested method does not belong to direct coupling or to iterative coupling methods, yet with its computational steps it offers a two-way coupling by transferring the fluid forces to the structure and the structural accelerations back to the fluid.

The paper presents BEM-FEM oriented solution of the fluid-dam interaction along with the boundary element discretization of the reservoir domain. The dam was subjected to El Centro earthquake excitation with duration of 7 sec., scaled to the pick acceleration of 0.3g. The dam properties are the following: Dam height H=130m; Young's modulus E = 31.5 GPa; mass density ρ = 2450 kg/m^3; Poisson's ratio ν = 0.2; the acoustic wave velocity in water c = 1440 m/s.

Numerical Model of Arch Dam and Fluid Domain

The process of generation of the discrete mathematical model of the arch dam and the fluid domain runs parallel with the process of design of the dam body. This process starts by digitization of topographic data of the terrain and the shape of the main central cantilever, Figure 1. The developed pre-processing within the ADAD–IZIIS software enables each topographic isoline to be mathematically presented by a set of equations of a second order, i.e., curves passing through three neighboring digitalized points on it. Each isoline is stored in the computer by means of a certain number of polynomials. The program gives an option for computer design of the dam body [2,3], whose embedment is in accordance with topology of the terrain. Arch dam body can be modeled in a form of few circular segments as well as in the form of a parabola. During modeling, it is possible to observe the shape of the arches at all elevations along with the corresponding tables containing their geometrical parameters and to observe their mutual position in order to control overlapping. Figure 2, presents the mathematical model of the dam generated automatically, using adopted shapes of the arcs at all selected elevations in accordance with the topology of terrain. The model is formed by 199 substructures. The substructures are automatically digitized into a certain number of finite elements that are not presented in the figure. The model contains 6294 finite elements and 11170 external nodes. The bend of the system is 3111. The model posses 2013 contact elements that are involved at the connections between substructure's blocks. The contact elements are generated automatically and the contact element mesh refinement is in accordance of the model analyst request.

ADAD-IZIIS software offers a very efficient and accurate modeling of the 3D fluid boundaries according to the downstream topology of the canyon terrain. The boundary elements at the extrados of the arch dam are directly extracted from the general FE model while the boundary element mesh that represents the boundaries of the reservoir, i.e., both banks, the reservoir bottom, the water mirror and the reservoir end, very accurately follows the shape of the topographic isolines. Generation is simply by giving the number of planes that intersect the terrain along with their distances from the uppermost point of the crown cantilever. In case of highly irregular and twisted terrain, more section planes and a more refined mesh should be used in order to model the complexity of the terrain in the most accurate way, which is undoubtedly easily feasible and with shorter computational time if BEM technique is engaged. However, for the concrete configuration of the terrain and detected "most adequate" location of the truncation surface situated at the downstream

distance of 210m from the dam, the number of boundary elements used in the model for accurate modeling of the 3D fluid boundaries is 1600, figure 3.
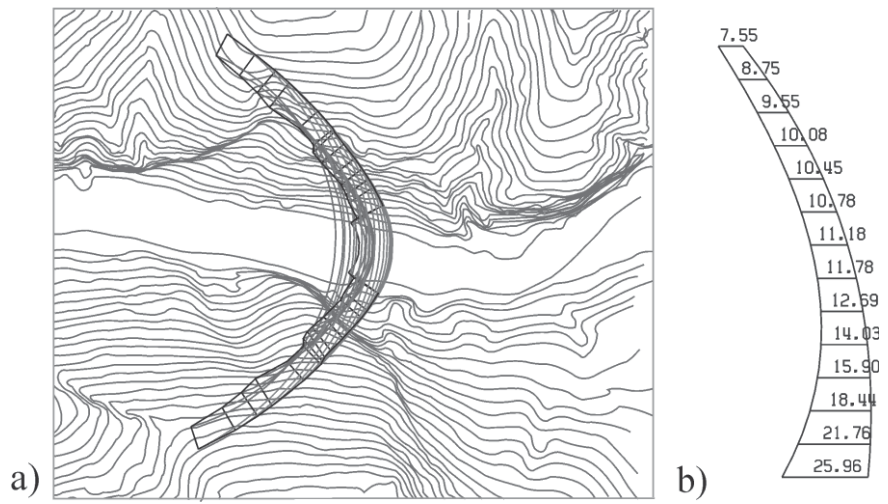
Figure 1: a) Topology of the terrain b) Shape of the central cantilever
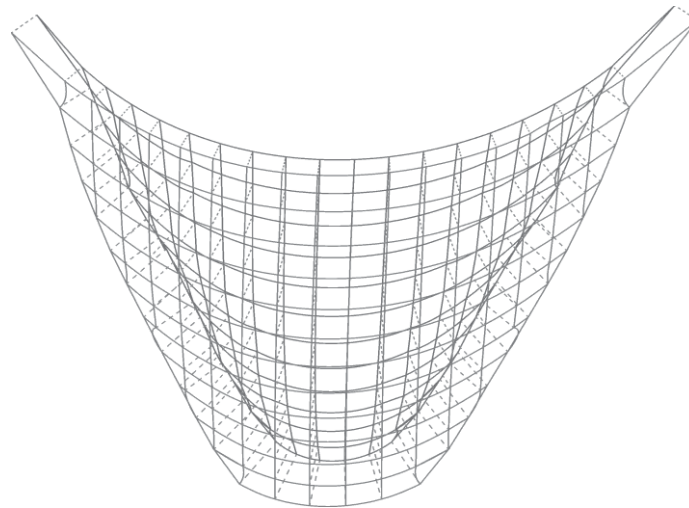
Figure 2: Mathematical model of a dam (substructures and construction joints)
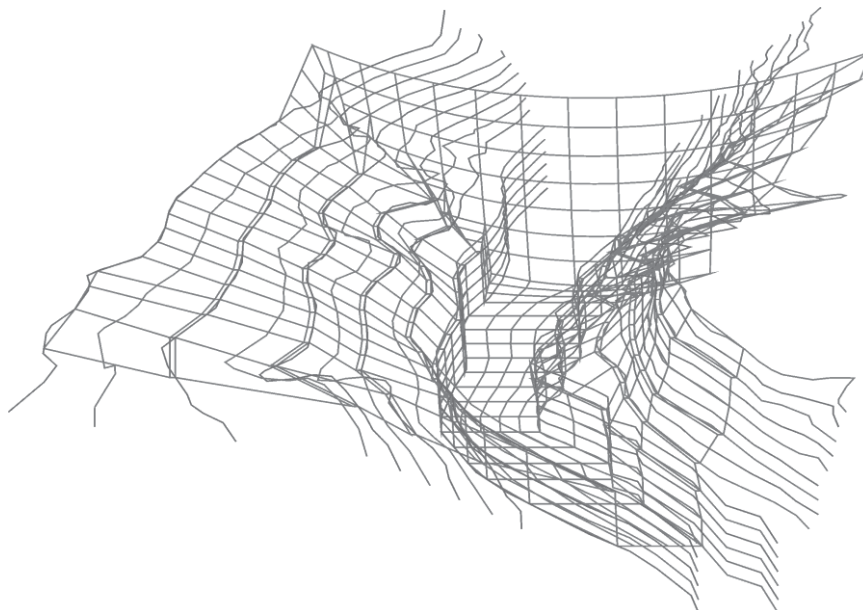
Figure 3: Boundary element mesh of the fluid domain

Fluid-structure interaction is affected by the irregularity of the terrain in the near surrounding of the dam-fluid interface. The topology of the terrain dictates the "most adequate" location of the truncation surface where non-reflecting truncation boundary conditions should be imposed. The detection of the "most adequate" location of the truncation surface is an important task in development of a reservoir model due to the fact that the HDP intensities on the dam-fluid interface are sensitive to the extent and type of waves generated by the boundaries. The truncation surface should be located in a way that its further displacement away from the dam has a negligible impact on the calculated HDP intensities.

The program offers sensitivity search analysis to detect the most adequate location of the truncation surface. For the presented BE model in figure 3., the elapsed CPU time for performing such analysis is approximately 15 min. The numerical procedure is based on the conventional BEM. Laplace differential equation that governs the incompressible and inviscid fluid motion is used. The procedure is conducted over a rigid dam-canyon-walls assemble. It follows a horizontal acceleration of 1g applied in downstream direction. The acoustic elastic P waves were generated as a result of the vibration of the considered upstream dam face and the rigid canyon's walls. The expansion of generated waves and the way of their propagation as compressive or dilatation waves depends not only on the specified boundary conditions but on the shape of the reservoir boundaries in respect to the direction of the seismic excitation. Three different types of truncation boundary conditions were considered: a) stationary type of truncated boundary conditions, i.e., perpendicular acceleration at all the points on the truncation surface is set to zero; b) hydrodynamic pressure at all points on the truncation surface set to zero; and c) non-reflecting boundary condition. Sixteen different location of the truncation surface were considered and analyzed. The curve associated with the TBC that allows dissipation of the outgoing waves shows mostly decreasing trend until reaching the meeting point of the curves of TBC type (a) and TBC type (b), at distance of L=180 m (L=1.6-1.7Hw) away from the dam. Further on, this curve remains almost horizontal, indicating unaltered value of HDP. This means that it is irrelevant whether TS is positioned at a greater distance than L=180m, since the effect of the amount and type of generated waves is negligible with further increase of the model length. However, this effect is remarkable along length L<180m, wherefore placing TS closer to the dam means overestimation of the HDP. In accordance with the applied direction of ground acceleration and due to the irregular configuration of the terrain in the vicinity of the dam, the right bank generates mostly dilatation waves while the left bank generates compressive waves. For the concrete topological conditions, the considered depth of impounded water, according the results presented in [4], the "most adequate" location of the truncation is selected at a distance of L=1.9Hw=210m.
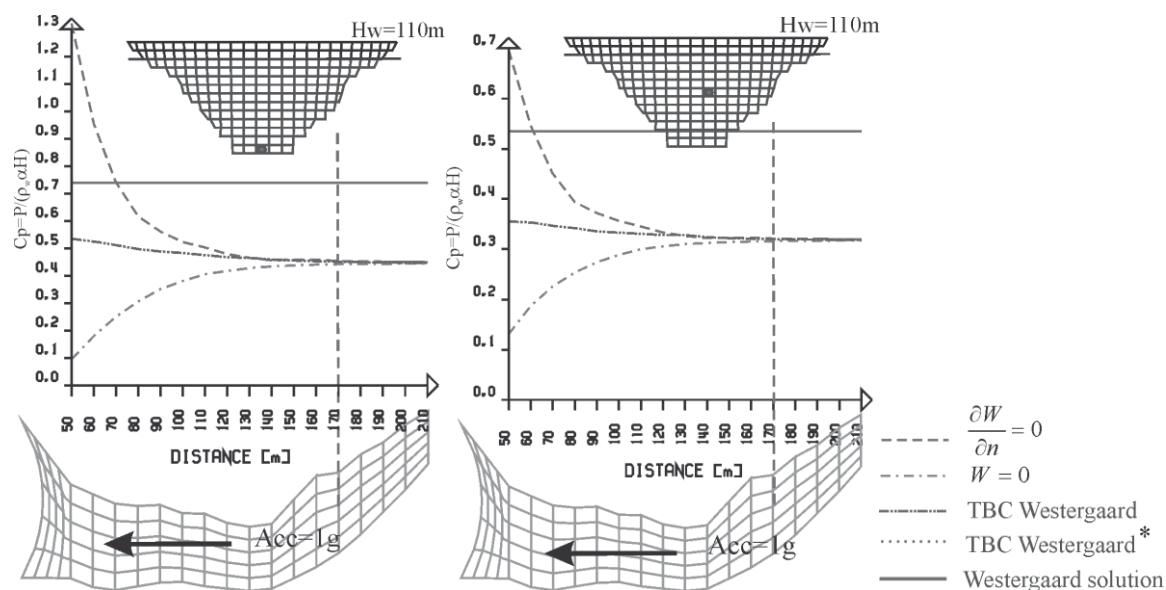
Figure 4: Variation of the normalized hydrodynamic pressure magnitudes as a function of the considered 16 locations of the truncated surface and different truncation boundary conditions (selected node at the bottom and at the middle of the crown cantilever)

BEM-FEM Solution of Fluid-Dam Interaction

Fluid–structure interaction is the interaction of a moveable and/or deformable structure that is immersed in a fluid and/or contains a fluid. A model that captures such an interaction must use two-way coupling model, where the fluid motion affects the structure's motion and the structure's motion affects the fluid's motion. Coupling should provide compatible link of both media which means equilibrium and correct transition of the physical variables at the interface. There exist various algorithms for coupling the merits of both BEM and FEM numerical methods, direct [5-8] and iterative coupling methods [9-12]. ADAD-IZIIS software [1] is based on BEM-FEM oriented solution of the coupled structure and the incompressible and inviscid fluid. The solution of the coupled system is accomplished by calculating in advance the matrix of hydrodynamic influence utilizing the concept of virtual work of "unit accelerations". This matrix is stored in the system and recalled in any time step of the dynamic response of the dam. Hence the solution of the coupled systems is actually separated and mutually independent. Hydrodynamic forces are obtained as a product of the matrix of hydrodynamic influence and the vector of manifested total accelerations along the normal at any interface node. The interaction effect at the fluid–solid interface is enforced by adding the matrix of hydrodynamic forces to the classic equation of dynamic motion of the dam, eq. (3). The governing equation for solving the small amplitude irrotational motion of the impounded incompressible and inviscid fluid is governed by the three-dimensional Laplace's equation as follows:

$$\frac{\partial^2 W}{\partial x^2} + \frac{\partial^2 W}{\partial y^2} + \frac{\partial^2 W}{\partial z^2} = 0 \qquad (1)$$

where W(x,y,z) is a function of the potential in the fluid domain. The equation (1) has to be amended by the specified "essential" and "natural" type of boundary conditions that exists at the boundaries of the analyzed fluid domain. Applying BEM technique, Brebbia [13], the discretization of boundary surfaces is by an assemble of eight nodded quadratic "Serendipity" type of boundary elements as follows:

$$\frac{1}{2}W_i + \sum_{nel=1}^{NEL} \int_{\Gamma 1} (\frac{\partial W}{\partial n}p - \overline{W}\frac{\partial p}{\partial n})d\Gamma_1 + \sum_{nel=1}^{NEL} \int_{\Gamma 2} (\frac{\partial \overline{W}}{\partial n}p - W\frac{\partial p}{\partial n})d\Gamma_2 = 0 \qquad (2)$$

where: i=1,NBE; NBE is a number of nodes in the boundary ele ment model.
The differential equation of motion of a discrete system written in an incremental form for the "i"-th time increment is the following:

$$M_i\hat{\Delta}\ddot{u} + C_i\hat{\Delta}\dot{u} + K_i\hat{\Delta}u = \hat{\Delta}P_i + \hat{\Delta}F_{HD_i} \qquad (3)$$

where: $\hat{\Delta}F_{HD_i}$ is a vector of hydrodynamic force increment and $\hat{\Delta}P_i$ is a vector of seismic force increment.
In eq. (3), the vector of hydrodynamic force increment eq, 4 is calculated by use of previously defined matrix of hydrodynamic influence and directly added to the vector of seismic force increment.

$$\hat{\Delta}F_{HD_i} = \left[W_{ij}\right]\Delta a_{nj}^{tot} \qquad i,j=1,NPT \qquad (4)$$

where: $\left[W_{ij}\right]$ is a matrix of hydrodynamic influence; Δa_{nj}^{tot} is the absolute acceleration along the boundary element normal; NPT is the total number of nodes at dam-fluid, bottom-fluid and banks-fluid interfaces, where the natural type of boundary condition exists

Figure 5, presents the time history response of relative displacement velocity and acceleration for the selected node at the dam crest, top of the crown cantilever, where the extremes of the response occurred. Obviously, fluid structure interaction based on BEM-FEM numerical solution modifies the extreme of the response acceleration at the dam crest by 38% in respect to the dam responce with empty reservoir. Additionally calculated are hydrodunamic effects by use Westergaard added mass concept. It gives lower modification of the dam responce, i.e, the exterem of the relative responce acceleration at the dam crest is modified by 31% Nothe that, the time of extreme occurance is not coinside. Westergaard added mass concept do not give recogition to the impact of the dam flexibility on the amount of generated energy in the fluid domain and therefore on the intensity of the manifested FSI effects. The flexibility property of the dam and the influence of the reservoir domain alter the behavior of the fluid significantly and consequently the coupled system has a stronger response.

The figure 6 shows the izolines of distribution of the principal stress G3 that acts along the arches with and without included hydrodynamic effects, whereat hydrodynamic effects are calculated according to added mass method and coupled BE-FE method. The stress extreme is increased by 15% if added mass method is used and 49% if coupled BE-FE method is used.

Despite the influence of the terrain irregularities on the amount of energy transferred to the fluid domain, this effect so far, has not been analyzed in detail by exsisting software regardless whether boundary element method (BEM) or finite element method (FEM) is used for fluid discretization. ADAD-IZZIS software gives an opption for taking into account the influence of terrain irregularities on the magnitide of calculated hydrodymanic effecs.

Figure 7., presents a snapshot of hydrodynamic pressure distribution over the interface, at time T=4.95sec. It is obtained under the assumptions that the topology of the canyon has a regular shape as indicated in the drawing.
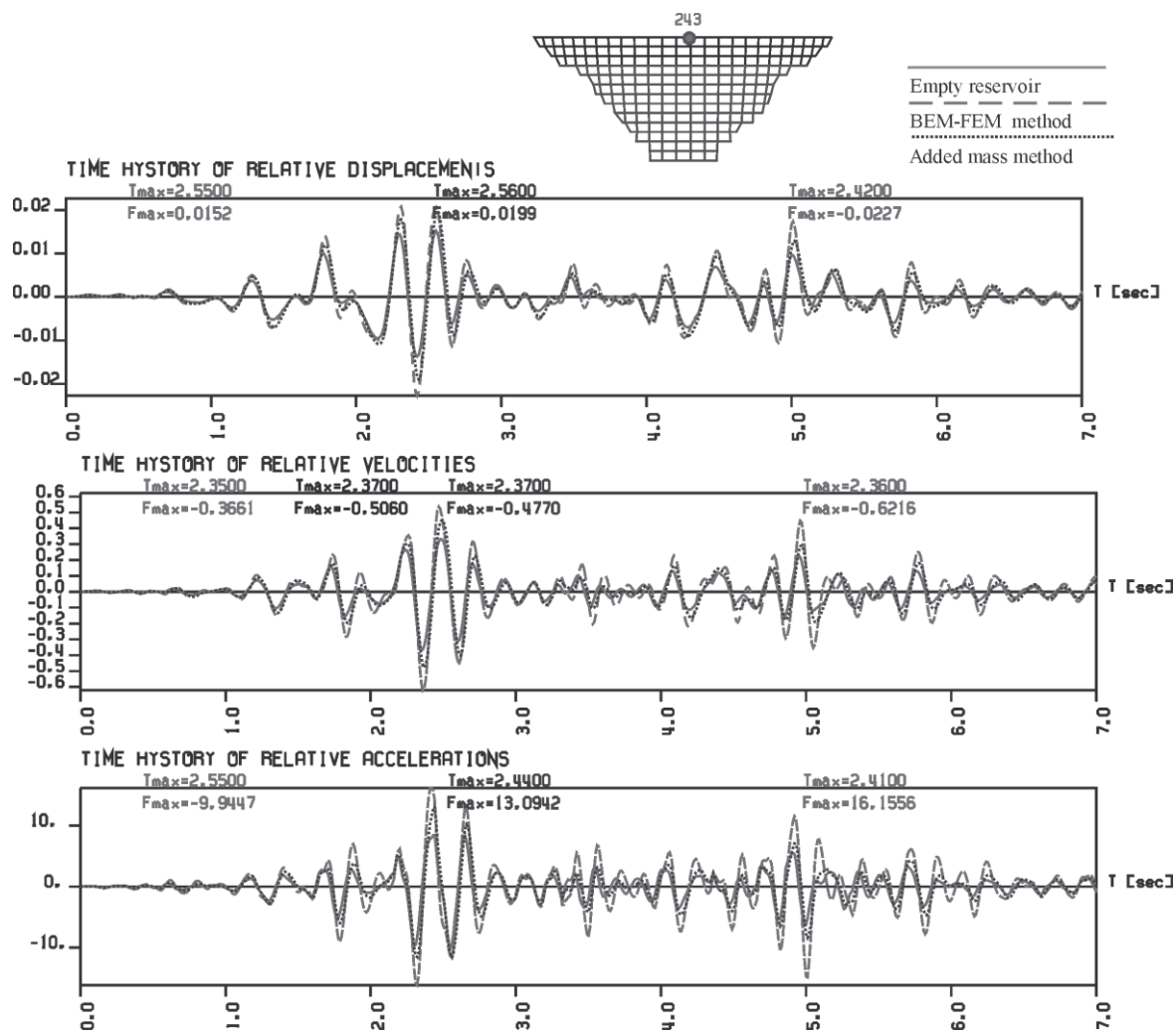
Figure 5. Modification of the dam response at the dam crest, relative displacement in (m) ; relative velocity in (m/sec) and relative acceleration in (m/sec^2). FSI effects defined by use of BEM-FEM solution and Westergaard added mass method

a)
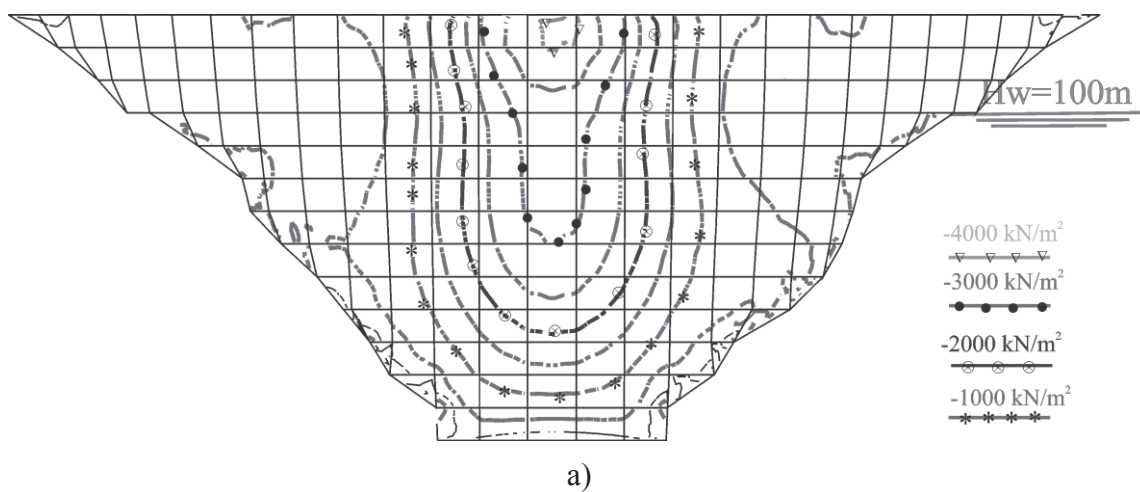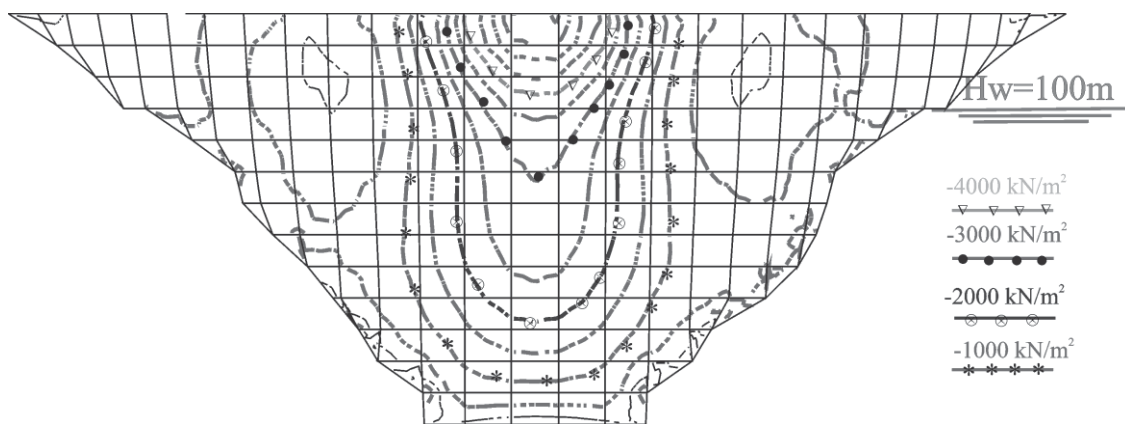
b)
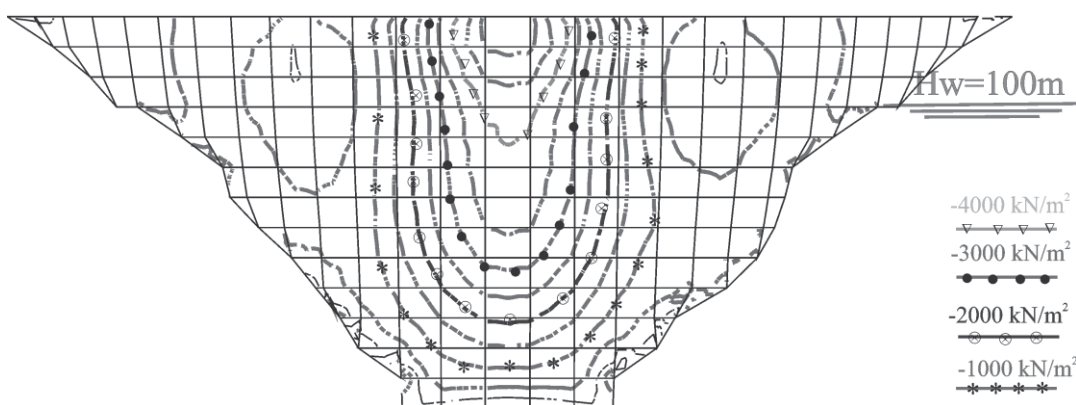
c)

Figure 6: Distribution of principal stress G3 at the extrados face at t=2.42 s

a) empty reservoir   b) FSI using BEM-FEM regular terrain

c) FSI using added mass method
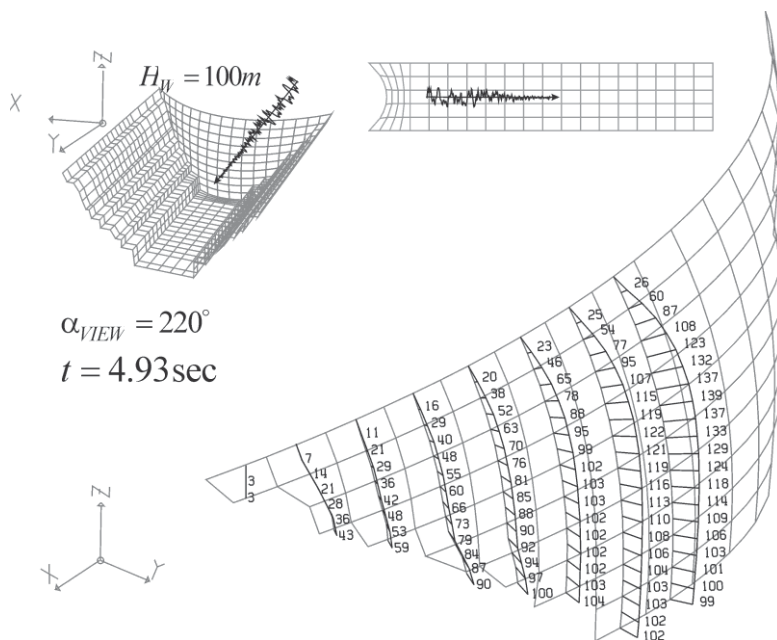
Figure 7: Snapshot of hydrodynamic pressure distribution at time T=4.95 sec

Conclusion

ADAD-IZIIS software is based on BEM-FEM oriented solution of the coupled structure and incompressible and inviscid fluid domain. The software offers process of generation of the mathematical model that runs parallel and interactively with the process of design of the arch dam body. Automatically are generated the finite element mesh of the dam and part of the foundation mass for accounting the phenomena of dam-foundation interaction, and boundary element mesh that presents the boundaries of the fluid domain for accounting the fluid structure interaction. The solution of the coupled system is accomplished by use of matrix of hydrodynamic influence utilizing the concept of virtual work of "unit accelerations". Comparison of the calculated hydrodynamic effects using both BEM-FEM solution and added mass method is made. The added mass method provides acceptable results only in the range of Westergaard restricted hypothesis. Since it neglects the dam flexibility and water compressibility and does not require any discretization of the reservoir domain wherever these features have an impact on the magnitude of hydrodynamic effects there will be discrepancy of the obtained resultants.

References

[1] Mircevska V., Bickovski V. (2008). ADAD-IZIIS software: Analysis and Design of Arch Dams, IZIIS- univ. "Ss. Cyril and Methodius", User's Manual.

[2] Houard L., Boogs (1997). Guide for Design of Arch Dams. A Water Resources, Technical Publication, Engineering Monograph No 36., 1-17.

[3] Wiliam, P., Greager, and Joel D., Justin (1984). Engineering for Dams, John Wiley & Sons

[4] Mircevska V., Bickovski V., Aleksov I., and Hristovski V. (2013). Influence of irregular canyon shape on location of truncation surface. Engineering Analysis with Boundary Elements, Vol. 37, pp. 624–636.

[5] Estorff von O., Prabucki M.J. (1880). Dynamic response in the time domain by coupled boundary and finite elements. Computational Mechanics Vol. 6, pp. 35–46.

[6] Pavlatos G.D. Beskos D.E. (1994). Dynamic elastoplastic analysis by BEM/FEM. Engineering Analysis with Boundary Elements Vol. 14, pp. 51–63

[7] Czygan O., Estorff von O. (2002). Fluid–structure interaction by coupling BEM and nonlinear FEM. Engineering Analysis with Boundary Elements Vol. 26, pp. 773–779.

[8] Yu G. Mansur, W.J., Carrer J.A.M., Lie S.T. (2001). A more stable scheme for BEM/FEM coupling applied to two-dimensional elastodynamics. Computers & Structures Vol. 79, pp. 811–823.

[9] Lin C-C, Lawton EC, Caliendo JA, Anderson LR.(1996). An iterative finite element-boundary element algorithm. Computers & Structures Vol. 39(5), pp. 899–909.

[10] Feng YT, Owen DRJ. (1996). Iterative solution of coupled FE/BE discretization for plate-foundation interaction problems. International Journal for Numerical Methods in Engineering Vol. 39(11), pp. 889–901.

[11] Soares Jr D, von Estorff O, Mansur WJ. (2004). Iterative coupling of BEM and FEM for nonlinear dynamic analyses. Computational Mechanics Vol. 34, pp. 67–73.

[12] Estorff von O., Hagen C. (2006). Iterative coupling of FEM and BEM in 3D transient elastodynamics. Engineering Analysis with Boundary Elements Vol. 30, pp. 611–622

[13] Brebbia C.A. (1978).The boundary element method for engineers, Pentech Press

Influence of Surface Roughness on Sliding Stability
Tests and numerical modeling

Ø. Eltervaag[1], G. Sas[2] and L. Lia[3]

[1]Department of Structural Engineering, Faculty of Engineering Science and Technology, Trondheim, Norway
[2]Northern Research Institute, Narvik, Norway
[3]Department of Hydraulic and Environmental Engineering, Faculty of Engineering Science and Technology, Trondheim, Norway

E-mail: oystein.eltervaag@sweco.no

Abstract

Lightweight concrete dams slide when the shear capacity of one or more sliding planes in the dam's structure or foundation is exceeded. Several laboratory shear tests were carried out on concrete rock samples. The two materials were mated trough teeth-sawed interfaces with different inclination profile. This paper presents the results of the numerical modeling of those tests.

The results of the shear tests were compared to the predictions of the model used in the Norwegian guidelines. It has been found that the model used in the guidelines do not predict the shear capacity accurately. Through finite element analyses a better representation of the tests has been achieved, especially regarding the influence of roughness.

Introduction

In Norway, the stability of a dam is reconsidered every 15 to 20 years, depending on the consequence class for the given dam. In the past 40 - 50 years, since the large hydropower development époque in Norway, the level for required safety has increased. Consequently some dams constructed during that period no longer are considered to have the sufficient safety and expensive upgrading is needed.
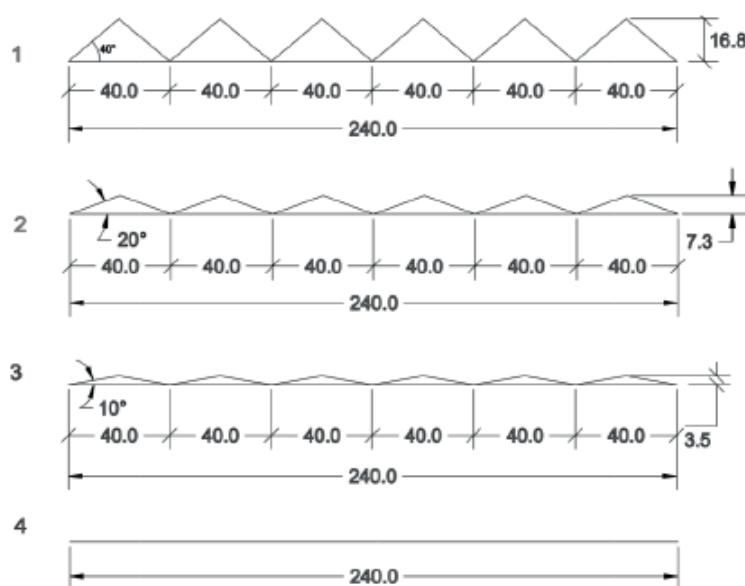
Figure 1: Profiles of test samples [1]

Two of the samples with geometry 1 and 4 were casted with bond between the rock and concrete. The remaining ten samples had no bond. During casting of concrete a plastic film was attached on the rock surface of those ten samples to prevent bonding.

Theory

According to the Norwegian regulations [2] the sliding stability is assessed using the shear friction method, and is expressed by a factor of safety (FS). For a horizontal sliding plane this factor is found from the following equation.

$$FS = \frac{c \cdot A + \sum V \cdot \tan \phi}{\sum H}$$ (1)

In equation (1) c is the cohesive parameter, A is the shearing plane area, V and H are the vertical and horizontal forces acting on the plane respectively. The frictional factor of the plane surfaces is expressed by $\tan (\phi)$. Thus, the factor of safety is calculated from the averaged normal stress and friction factor of the sliding plane. The shear friction method is based on the Mohr-Coulomb criterion [3] for describing the shear capacity of the sliding plane. This criterion states that the shear capacity, τ, is linearly dependent on the applied normal stress, σ, trough a material specific frictional parameter $\tan(\phi)$ plus a cohesive parameter, c. This can be expressed as follows:

$$\tau = c + \sigma \cdot \tan \phi$$ (2)

In the 1960's it was recognized that the failure envelope for rock mass (rocks with joints and faults) was curved. One of the major contributions to this understanding was when Patton [4] derived a bi-linear failure criterion from experiments with "saw-toothed" rock specimens shown in Figure 2. Patton observed that sliding occurred at lower levels of normal stress than what was needed to cut off the saw-toothed geometry. This failure mechanism can be described on the form:

$$\tau = \sigma \cdot \tan(\phi_b + i)$$ (3)

Were ϕ_b is the material specific friction angle, simply denoted ϕ in the Mohr-Coulomb relation, equation (2), and i is the angle of the asperities, called the asperity inclination or dilation angle. When the normal stress exceeded a certain value the saw teeth were cut off at their base. Patton [4] explained this as a change of governing failure mode, from a sliding failure along the material interface, to a failure in the material itself. The shear capacity regarding this material failure is described by:

$$\tau = c_x + \sigma \cdot \tan(\phi_r)$$ (4)

Where c_x is the bond of the failing material, and ϕ_r is the residual friction angle of the failure plane. The shear envelope obtained from these expressions is shown in Figure 2 .
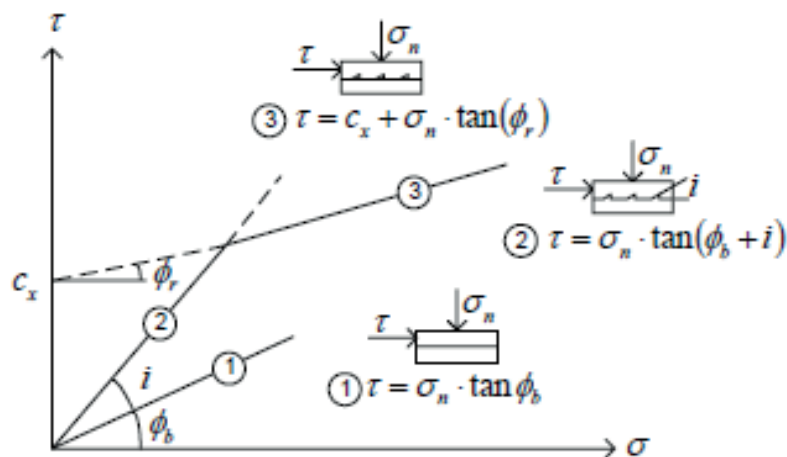
Figure 2: Patton's bi-linear failure criterion [4]

According to Patton [4] the bi-linear failure envelope illustrates that there are two possible failure mechanisms for the rock specimens studied. The first mechanism is sliding over the asperities (saw-teeth) and occurs at low normal stresses. The second mechanism is shearing through the asperities and occurs at relatively high normal stresses.

These different failure modes have been further described by Johansson [5]. Johansson [5] developed a conceptual model to describe sliding failure of one idealized quadratic asperity. Three failure modes were identified; sliding along the side of the asperity facing the load, shear-failure along the base of the asperity, and tensile failure in the rock-base of the asperity. A sketch of an idealized asperity is shown in Figure 3.
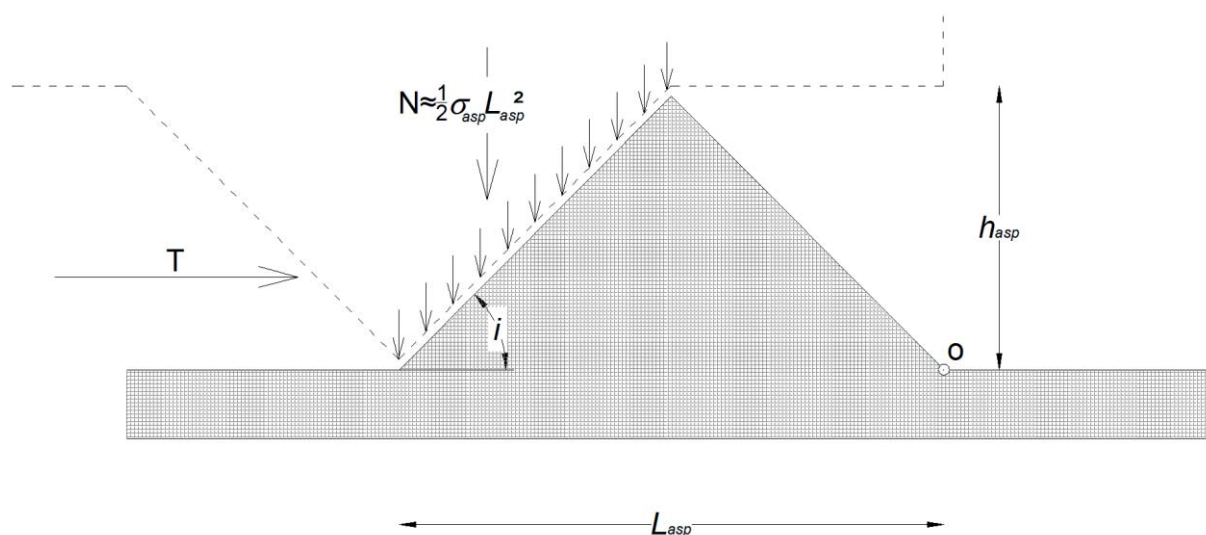
Figure 3: Principle sketch of an idealized 2D asperity [5]

To describe sliding along the loaded face of the asperity (the left side in Figure 3) Johansson [5] uses Patton's formulation, eq. (4), for shear capacity for low normal stresses (transformed from stresses to forces).

$$T = N \cdot \tan(\phi_b + i) \tag{5}$$

The equation for shear failure along the base of the material is derived based on the Mohr-Coulomb criteria, eq. (2) and Patton's equation for high normal stress, eq. (4).

$$T = c_i \cdot L_{sp}^{\ 2} + N \cdot \tan(\phi_i)$$ (6)

For a tensile failure to occur in the rock-base, the vertical tensile stresses must exceed the tensile capacity of the rock. To calculate the average tensile stress in the rock Johansson [5] assesses the moment-equilibrium about point O in Figure 3.

$$T = \frac{(3 \cdot \sigma_{ci} + 4\sigma_{ti}) \cdot L_{asp}^{\ 2}}{2 \cdot \tan(i)}$$ (7)

Where σ_{ti} is the tensile strength and σ_{ci} is the compressive strength of the rock.

Method

For this work the finite element software ATENA-Science developed by Cervenka Consulting has been used [6]. The geometry of tested samples is modeled as a 2D plane stress problem, left side of Figure 5. To avoid numerical instability when applying the loads directly on concrete, the surrounding steel shear box was modeled also, right side and medallion in Figure 4. In Atena the boundary conditions were applied as fixed lines along the outside of the lower steel frame, the loading was introduced by a vertical line load along the top of the steel frame, and horizontal displacement along the left edge of the upper steel frame. Monitoring points were added at the left edge of the upper steel frame and at the right edge of the concrete material to enable load/displacement curves.
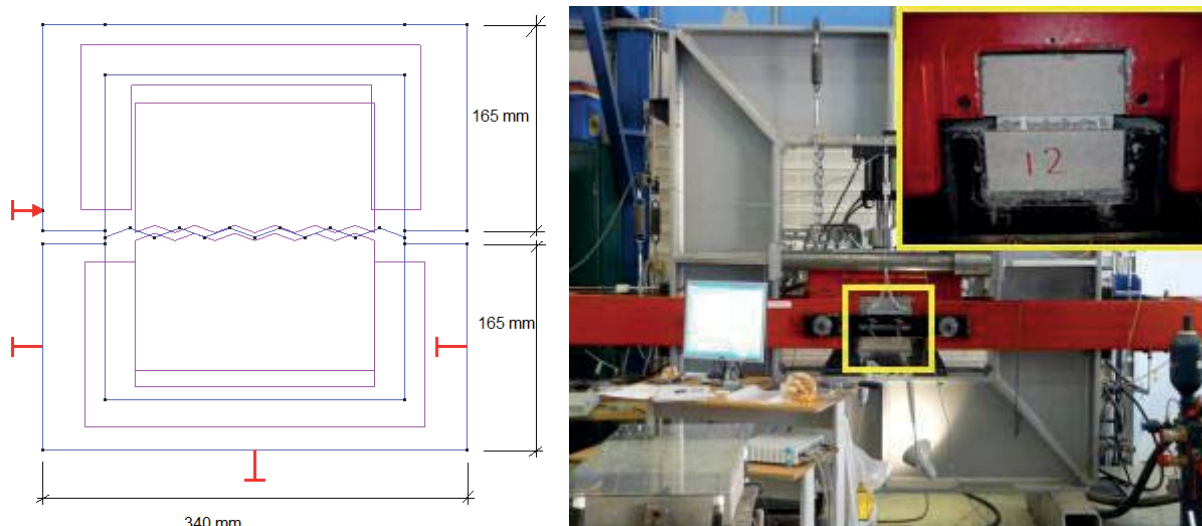
Figure 4: 2D geometrical model of a test sample with ten degree asperity angle

ATENA uses interface elements to model contact between two parts of a model. To model the behavior of the interface elements ATENA uses the Penalty Method [6]. The physical properties of these interface elements are governed trough the Mohr-Coulomb criterion presented in eq. (1). To obtain input values of the interface properties the results from the tests are compared to the failure criteria described above. However, these classic formulations present large errors compared to the test results. Reliable input parameters were obtained by applying a hybrid formulation where the shear capacity is determined from the actual failure

mechanism for the tests; sliding over or shearing off the asperities, eqs. (5) or (6). This hybrid formulation for shear capacity of the samples can be expressed as follows,

$$V = \frac{c \cdot A}{\cos i (1 - \tan i \cdot \tan \phi_b)} + N \cdot \tan(\phi_b + i) \tag{8}$$

where i is the residual inclination angle of the asperities, which may differ from the original inclination angle if the asperities are sheared off. The basic friction angle is material constant and therefore equal for all the samples. Thus, the basic friction angle can be found from a sample without asperities, and is determined to be 34.4˚. The cohesive parameter is found by inserting the known values from the results of each of the tests into eq. (8). These values are listed in Table 1. The physical explanation of this parameter is believed to be wear of the interface as cut-off of micro asperities (micro roughness) as shown in eq. (6). The cut-off shows a decreasing effect as the samples slide against each other. To account for this a softening behavior of the cohesive parameter is introduced. In ATENA the effect of the asperities (macro roughness) is included trough the geometry of the interface.

In ATENA the loading is applied incrementally. First the normal pressure was applied as a vertical line-load. The line-load for the different tests has been found by distributing the applied experimental vertical force presented in [1] over the length of the samples (240mm). The applied line-loads are presented in Table 1.

Table 1: Interface and loading input parameters

Test results [1]				Input used in ATENA			
Sample	i [˚]	δ_{Hmax} [mm]	N [kN]	i [˚]	δ_H [mm]	"Cohesion" [kPa]	Q [kN/m]
1.1	40	15.23	27.52	0	20	1245	114
1.2	40	15.44	46.91	0	20	1720	195
1.4	40	26.34	68.49	0	20	2371	285
2.1	20	24.99	27.57	20	20	282	115
2.2	20	21.98	47.77	20	20	781	199
2.3	20	20.07	68.36	20	20	1552	285
3.1	10	33.16	24.82	10	20	309	103
3.2	10	32.94	45.98	10	20	382	192
3.3	10	33.23	67.65	10	20	536	282
4.2	0	33.23	67.23	0	20	62	280

Then the horizontal force is applied trough prescribed deformation of ten millimeter at the left edge of the upper steel frame, see Figure 4. To achieve plane horizontal displacement (avoid rotation) of the upper part master-slave boundary conditions are introduced along the upper edge in this interval. Interval three and four are identical to interval two, except that the master-slave boundary conditions are removed. The standard incremental and iterative Newton–Raphson method for material nonlinear structural analysis was used in the numerical simulations, based on the finite element method. The specimens were modeled with a mesh of 8-node serendipity plane stress finite elements. A Gaussian integration scheme with 2 x 2 integration points was used for all the concrete elements, [6,7].The mesh is shown in Figure 5.
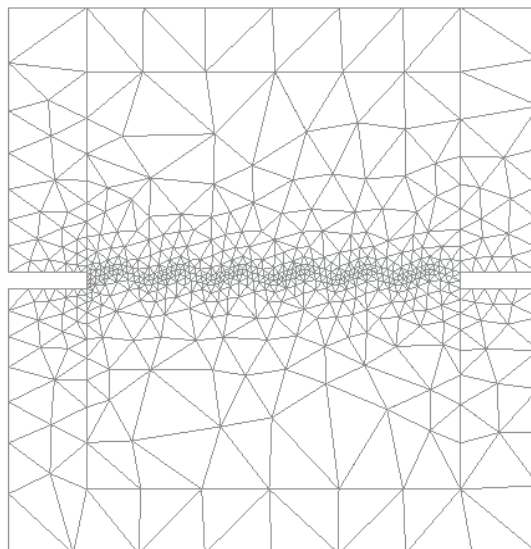
Figure 5: Mesh of test 2.2

Both the concrete and rock materials are modeled using a fracture-plastic model that combines constitutive sub-models for tensile and compressive behavior, as presented in the ATENA user manual [6], see Figure 6. This fracture model employs the Rankine failure criterion and exponential softening, with the hardening/ softening plasticity component based on the Menétrey– William failure surface [6]. The concrete post-cracking tensile behavior was simulated by a softening function in combination with the crack band theory [6].
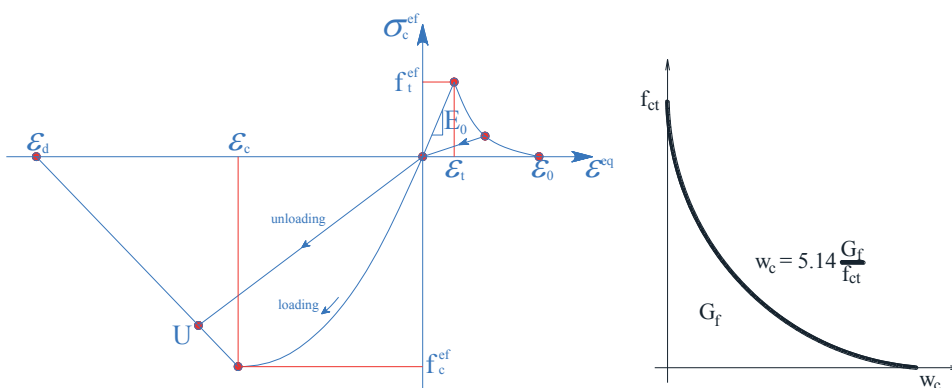
Figure 6: Constitutive model for concrete (left) and softening function (right) [6]

The decision for modeling the rock as concrete is based on the behavior of the actual rock samples during compressive standardized tests. It was observed that this behavior is more in line with the available material models for concrete than rock. The steel shear box was modeled as a linear elastic material. Theoretical background of the above mentioned constitutive models are given in the ATENA Theory manual [7]. Input parameters for the rock and concrete material are given in Table 2.

Table 2: Material parameters for concrete material models

Material	Concrete	Rock
Young's Modulus [GPa]	37	100
Poisson's Ratio	0.2	0.2
Tensile strength [MPa]	4.1	2.317
Compressive Failure Stress [MPa]	58	280
Fracture Energy [MN/m]	1.03×10^{-4}	1.05×10^{-5}
Plastic strain	-0.00147	-0.000296
Onset of crushing [MPa]	-8.61	-1.54
Critical compressive displ. [m]	-0.0005	-0.0005
Density [kN/m³]	23	23

In Table 1 it is seen that the geometry of tests 1.1 to 1.4 is modeled with zero inclination angle. The reason for this is that these tests showed a shearing failure mode, where the asperities were cut off, therefore there were no sliding between asperities but material failure. A total shearing failure mode has been hard to obtain from the numerical models. The main reason for this is that the analyses crash after the material starts to crack due to instability problems with zero or negative Jacobian for the stiffness matrix. This error message is an indication of an ill-conditioned system of equations [8]. Perhaps a more refined mesh with more integration points could have been used. Due to low computational capacities this was not possible at the time when this work was carried out. In Figure 7 the concrete material failure is shown. The blue field in the left part indicates that the tensile strength of the material is reached.
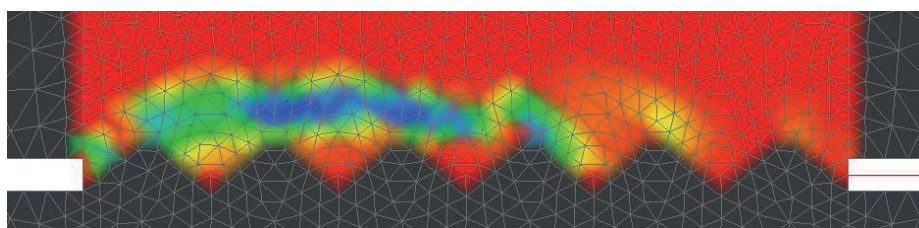
Figure 7: Material failure for test 1.4.

Due to the numerical instability problems only the peak shear capacity was obtained from these analyses. However, this capacity is governed by the concrete material parameters alone, not by the interface parameters. In the test report [1] only the compressive strength was given for the rock and concrete materials. Thus, the tensile strength and onset of crushing have been generated automatically by ATENA. To overcome these problems the tests in series 1 have been modeled using the residual inclination angle of the asperities (zero) according to eq. (8).

Results

The results from the numerical analyses have been monitored by recording the horizontal displacement and reaction-force along the loaded edge of the model. The load-displacement curves from the analyses (labeled ATENA) are presented in the same diagrams as the curves from the actual tests (labeled LTU after the lab where the tests were conducted). In total, eleven of the twelve shear tests were analyzed. Due to space limitation in Figure 8 below, the graphical results are shown for selected analyses only. Full description of all results are presented in [9].
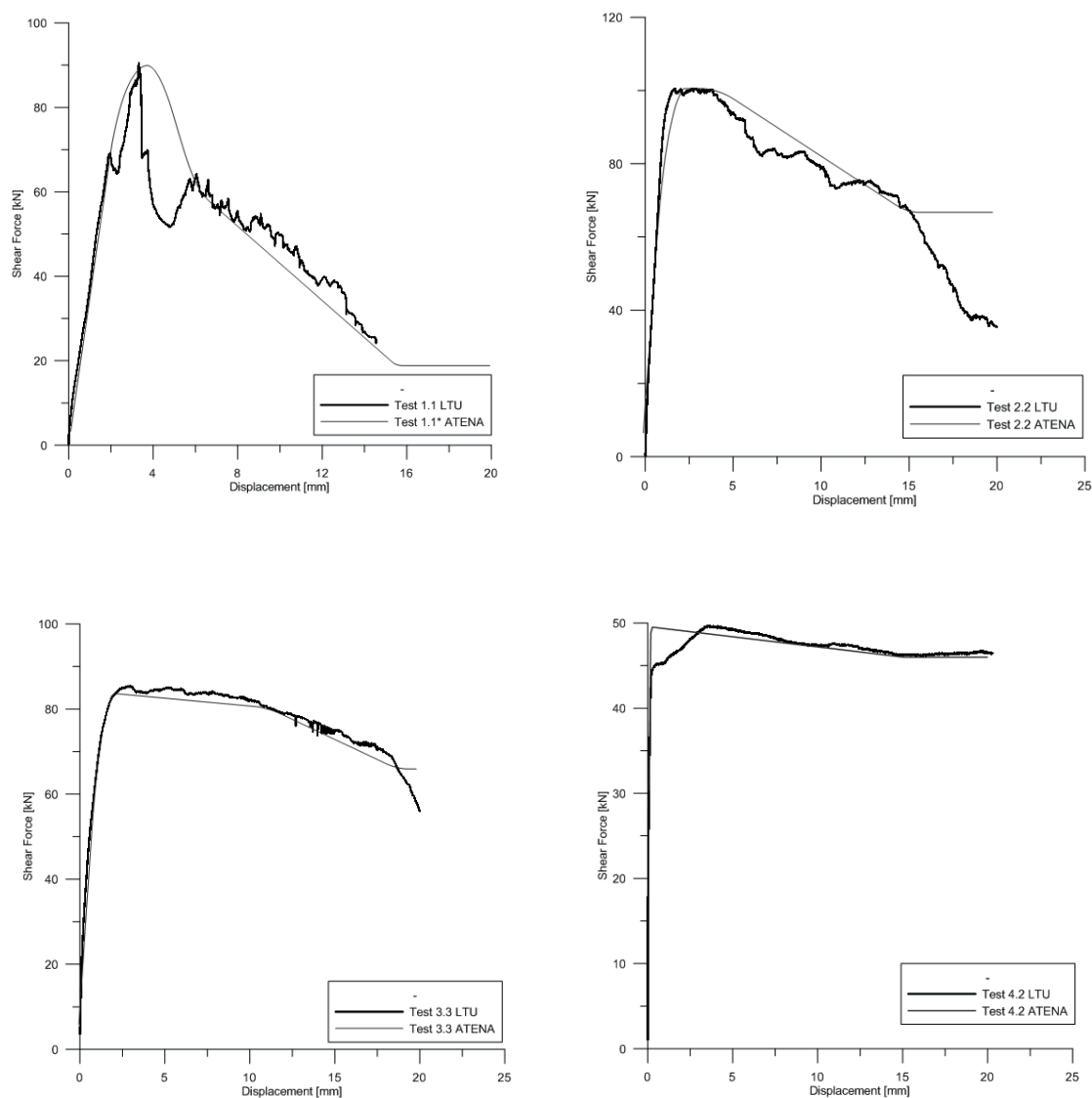
Figure 8 Load displacement diagrams showing tests and numerical results

In general the procedure of assuming cut-off of micro roughness as cohesion gives a good representation of the peak shear capacity of the actual tests. When coupled with a softening behavior of the cohesive parameter, the capacity along the failure development and the residual shear capacity are represented sufficiently accurate. Since the input parameters are found from each specific test the finite element models should produce results that match both the peak and residual shear capacity from the tests exact. However, studying the results, it becomes evident that some errors still occur. The difference between the peak shear capacity from the laboratory tests and the numerical analyses are listed in Table 3.

Table 3: Error in peak shear capacity from the numerical models.

Sample	V_{max}[kN] test	V_{peak} [kN] ATENA	Error	
			[kN]	[%]
1.1	90.53	89.91	0.62	1
1.2	131.19	125.80	5.39	4
1.4	183.42	173.21	10.41	6
2.1	50.74	50.81	0.07	0.1
2.2	100.59	100.57	0.02	0.02
2.3	162.83	162.08	0.75	0.5
3.1	35.38	34.65	0.73	2.
3.2	58.70	57.56	1.14	2
3.3	85.43	83.65	1.78	2
4.1H	240.00	225.75	14.25	6
4.2	49.56	49.52	0.04	0.1

The error-% is calculated with respect to the actual value from the tests [1]. The average error is approximately 2% with a maximum of 6% for two analyses. Compared to the results from the Mohr-Coulomb and Patton criteria in Table 4 this is a significant improvement.

Table 4: Error in peak shear capacity from hand calculations.

From tests [1]				Mohr-Coulomb		Patton	
Sample	I [°]	N [kN]	V [kN	V [kN]	Error [%]	V [kN]	Error [%]
1.1	40	27.52	90.53	361.60	332	113.73	26
1.2	40	46.91	131.19	380.99	190	193.86	48
1.3	40	68.49	183.42	402.57	119	283.04	54
2.1	20	27.57	50.74	20.32	59	41.19	18
2.2	20	47.77	100.59	35.21	65	71.89	28
2.3	20	68.36	162.83	50.39	69	102.88	37
3.1	10	24.82	35.38	18.29	48	26.06	26
3.2	10	45.98	58.70	33.89	42	48.28	18
3.3	10	67.65	85.43	49.86	42	71.04	17

Although the errors in Table 3 are not large, their cause needs to be addressed. One possible source is the inaccurate recording of the residual capacity in the tests. Due to the fact that when concrete was cracking the analysis was not always stable, the residual capacity only describes the capacity as long as the interface asperities are intact. This explains why the residual capacity is not well represented for test series 2 where some deformation of the asperities was registered in the tests. For test series 1 this source of error is avoided as the interface is modeled with the inclination of the residual sliding plane from the actual tests.
It is hard to determine why stable results after material failure in the concrete was not obtained, but it is believed that a fine mesh and more refined material models would improve this. Not all the required input parameters for the material models were obtained from the physical tests, thus some default values were used in the modeling. With lacking parameters, a full parametrical study would be needed to refine the materials.
The results from the analyses show that the actual shear capacity of the tests are better represented through numerical modeling than the formulations available for hand calculations. Especially the opportunity to represent the softening behavior after the peak shear capacity is reached, is a large benefit.

Conclusion

Through finite element modeling, more sophisticated analyses regarding stability towards sliding might be obtained. This allows more sustainable design of structures subjected to sliding instability. However, it must be noted that due to the limited amount of samples analyzed and the scale effects encumbered with shear capacity, further work is needed to utilize the potential of finite element modeling of stability towards sliding for full scale dams. A full parametric study is needed to improve the method.

Acknowledgements

References

[1] Liahagen, S., (2012) Stabilitet av betongdammer - Ruhetens påvirkning på skjærkapasiteten mellom betong og berg. Master's Thesis. NTNU,IVM, Trondheim, unpuplished.

[2] NVE, Norwegian Water Resources and Energy Directorate, (2005), Retningslinje for betongdammer.

[3] Coulomb, C. A. (1776). Essai sur une application des regles des maximis et minimis a quelquels problemesde statique relatifs, a la architecture. Mem. Acad. Roy. Div. Sav., vol. 7, pp. 343–387.

[4] Patton, F.D (1966). Multiple modes of shear failure in rock. 1st ISRM Congress, September 25 – October 1, 1966, Lisbon, Portugal. LNEC

[5] Johansson, F., (2009). Shear Strength of Unfilled and Rough Rock Joints in Sliding Stability Analyses of Concrete Dams. Ph.D. Thesis. Royal Institute of Technology (KTH), Stockholm.

[6] Cervenka, V. Cervenka, J. Zednek, J. Pryl, D. (2013) ATENA program Documentation, Part 8: User's Manual for ATENA_GiD Interface. http://www.cervenka.cz/assets/files/atena-pdf/ATENA-Science-GiD_Users_Manual.pdf

[7] Cervenka, V., Jendele, L., Cervenka. J., (2012) ATENA Program Documentation, Part 1: Theory. http://www.cervenka.cz/assets/files/atena-pdf/ATENA_Theory.pdf

[8] Pryl, D., Cervenka, V. (2013) ATENA Program Documentation, Part 11: Troubleshooting manual. http://www.cervenka.cz/assets/files/atena-pdf/ATENA-Troubleshooting.pdf

[9] Eltervaag, Ø. (2013) Sliding stability of Lightweight Concrete Dams – Development of numerical models. Master's Thesis. NTNU, IKT, Trondheim. Unpublished.

Seismic Analysis of a Concrete Arch Dam
Considering Concrete Heat Generation Damage Effects

P. Dakoulas[1]

[1] University of Thessaly, Volos, GREECE

E-Mail: dakoulas@uth.gr

Abstract

This study evaluates the seismic performance and safety of Tavropos arch dam (Greece) considering the dynamic canyon-dam-water interaction. Tavropos dam has a height of 83 m and crest length of 220 m. The numerical model of the arch consists of 17 concrete cantilevers separated by vertical joints, whereas the foundation-abutment model represents a large region of the canyon. The interface behavior at the vertical joints and the horizontal base joint is modeled in three different ways: as bonded surfaces, as surfaces in contact with frictional strength, and as a combination of bonded and contact surfaces. To account for possible prior damage, the study simulated the thermo-mechanical phenomena that took place during dam construction, related to heat generation due to concrete hydration. The seismic analysis is performed against a MCE having a magnitude of 7.5 and peak ground acceleration of 0.47g. The seismic evaluation is based on an extensive parametric investigation of the effects of various key factors, including concrete strength, joint interface behavior, water level, hydrodynamic pressures, ambient temperature, canyon rock flexibility, spillway geometry, earthquake excitation characteristics, etc. It is concluded that the expected overall stability and performance of Tavropos concrete arch dam is satisfactory.

Introduction

Lake Plastiras was created after construction of an arch dam (Fig. 1) in Tavropos river, a tributary of Acheloos river in Northern Greece [4]. The double-curvature Tavropos arch dam has a height of 83 m and crest length of 220 m. Construction started in 1955 and was completed in 1959, during which the dam was impounded. Today, Lake Plastiras provides drinking water to the city of Karditsa and nearby villages, and irrigation to the region near Larissa. Its electric power is 130 MW, whereas the lake is an attractive tourist destination with more than 120,000 tourists annually.

Figure 1: Tavropos Arch Dam in Lake Plastiras, Greece

The objective of this work is to conduct a seismic performance and safety evaluation of the data, considering the dynamic canyon-dam-water interaction and current data about the local seismicity based on recent research [11][3][8][9][10].
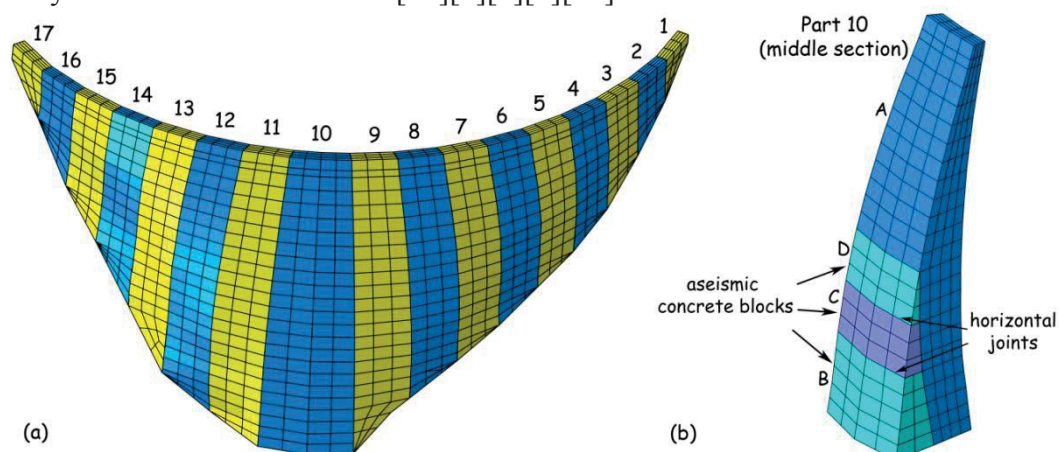
Figure 2: Finite element discretization of (a) concrete arch dam geometry consisting of 17 parts and (b) Part No.10 geometry at the middle section
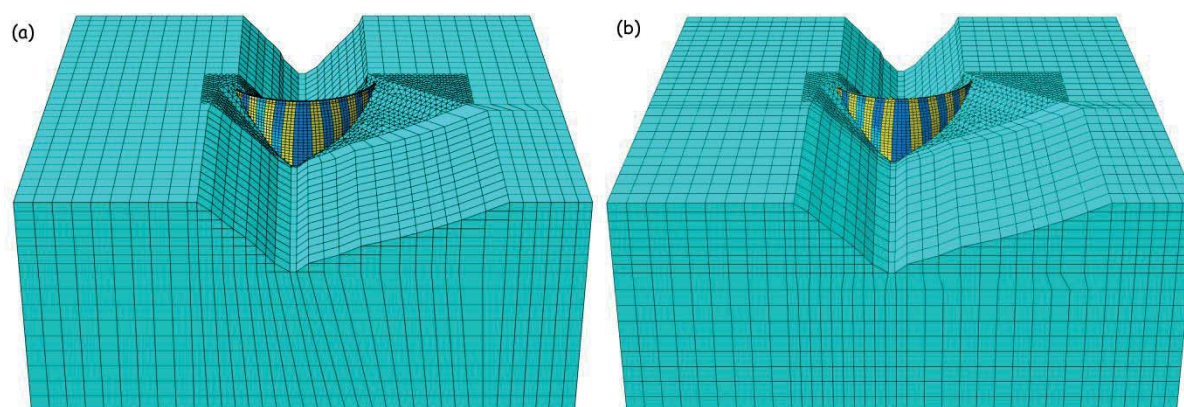
Figure 3: Finite element discretization of the canyon geometry (a) model A and (b) model B consisting of full quadratic finite elements for the entire canyon region.

Numerical Model

Dam geometry

The study is based on a detailed numerical model of the dam and canyon using the code ABAQUS [1]. Fig. 2a illustrates the numerical discretization of the arch dam body. The dam body consists of 17 parts, having a width equal to 12 m, except of the central part, which has width equal to 16 m. The 17 parts are connected with vertical joints. Fig. 2b shows Part 10, located at the mid-section of the dam. As all parts near the central region of the arch, Part 10 consists of 4 concrete blocks: A, B, C and D. Blocks B, C and D at the lower upstream side were designed as to increase the stability of the dam in the case of a potential strong earthquake during the phase of construction. They are all attached to main block A, but there are horizontal joints between blocks B and C, as well as between blocks C and D to reduce seismic tensile stresses. To improve numerical efficiency, only 2 out of the 4 actual horizontal joints of each part were discretized, without any loss of accuracy. All dam parts are

discretized using solid hexahedral elements C3D8, having 8 nodes and 8 integration points. A total number of about 4400 elements were used for the modeling of the arch dam geometry.

Canyon geometry

The discretized canyon geometry has length of 600 m, width of 600 m and depth of 250 m. It consists of two parts: (a) the first part discretizes the irregular geometry near the foundation of the dam. It is discretized by using quadratic, reduced integration hexahedral elements C3D20R, each having 20 nodes, whereas the irregular rock surface and dam foundation excavation, are discretized using quadratic modified tetrahedral elements C3D10M, which are robust, accurate and suitable for frictional contact behavior; (b) for the rest of the canyon, two different models have been utilized:

(1) model A (Fig. 3a) consists of hexahedral solid elements C3D8, having 8 nodes
(2) model B (Fig. 3b) consists of quadratic hexahedral elements C3D20R, having 20 nodes.
About 30500 and 27000 elements were used for canyon models A and B, respectively.

Damage plasticity model for concrete

The plastic-damage constitutive model for cyclic loading by Lee and Fenves [6] is used here for modeling the behavior of concrete. The model takes into account the effects of strain softening, distinguishing between the damage variables for tension and compression. It incorporates a degradation mechanism that represents the effects of damage on the elastic stiffness and the recovery of stiffness after crack closure. Three values of compressive strength have been adopted, based on large cubic specimens (20cm x 20cm x 20cm) obtained during construction and tested after 365 days. The use of large size specimens is important to avoid the negative effect that the large diameter aggregates may have on strength prediction. The three values of compressive strength are: (A) the mean value $f_c = \mu = 46$ MPa (B) the mean value minus three standard deviations, $f_c = \mu - 3\sigma \approx 42$ MPa and (C) $f_c = 32$ MPa, i.e. an unlikely, much lower value to account for possible additional uncertainties. For $f_c = 46$ MPa, the stress-strain behavior during uniaxial loading-unloading-reloading of a cube of concrete, subjected separately to compression and tension tests is given in Figure 4. For the cyclic tension tests, the softening behavior and the effect of the accumulated damage are taken into account, whereas for the cyclic compression, these effects are ignored in the present study.

Table 1: Concrete Properties

Property	Case A	Case B	Case C
Density, ρ [kg/m^3]	2350	2350	2350
Compressive strength, f_c [MPa]	46	42	32
Dynamic tensile strength, f_{td} [MPa]	6.4	6.0	5.3
Static Young's modulus, E [GPa]	31	31	31
Dynamic Young's modulus E_d, [GPa]	42	42	42
Poisson's ratio, ν	0.15	0.15	0.15
Coefficient of thermal expansion, a [°C^{-1}]	10^{-5}	10^{-5}	10^{-5}
Specific heat, c [J/(kg °C)]	879	879	879
Conductivity, k [W/(m °C)]	2.5	2.5	2.5
Heat transfer coefficient [W/(m^2 °C)]	16	16	16
Hydration heat, q(t) [kcal/kg$_{cement}$] (t : in days)	$q(t) = t/(0.0653 + 0.0175t)$		

Joint behaviour

The behavior at the vertical joints and the horizontal joint at the dam base is modeled in three different ways: as bonded surfaces, as surfaces in contact with frictional strength, and as a

combination of bonded and frictional surfaces. The bonded joints are considered to have the tensile strength of concrete of the adjacent blocks. The surfaces with only frictional strength, have a coefficient of friction equal to 0.5 for vertical joints and 0.8 for the horizontal joints.
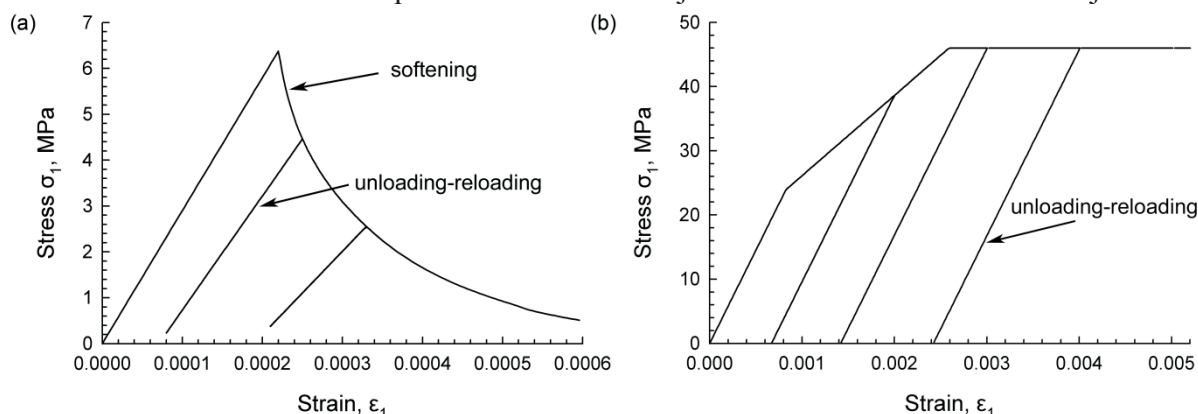
Figure 4: Damage plasticity concrete model: stress-strain relation during loading and unloading in uniaxial (a) tension and (b) compression.

Canyon rock properties

The canyon rock material is fine-layered limestone containing sparse intermediate layers of radiolarites. During the static and dynamic analyses of the dam-canyon system, the canyon rock is considered to behave as a linearly elastic material. Table 2 summarizes the canyon rock properties. Two scenarios are examined for the dynamic analyses, namely, case R1 and case R2, having shear wave velocities equal to $V_s = 2800$ and 2000 m/s, respectively.

Table 2: Canyon Rock Properties

Property	Case R1	Case R2
Density, ρ [kg/m^3]	2450	2450
Static Young's modulus, E [GPa]	16	16
Dynamic Young's modulus, E_d [GPa]	48	25
Poisson's ratio, ν	0.25	0.25
Shear wave velocity, V_s [m/s]	2800	2000
Hysteretic damping, ξ_r	0.03	0.03

Effect of heat generation during construction

It is of interest to examine concrete behavior immediately after construction, especially for high performance concrete, as cracking may develop due to deformation caused by heat that is generated during cement hydration reactions [7][2]. Potential cracking generated during or immediately after construction of various dam segments might have developed weak areas, which could affect its seismic performance during earthquakes. To examine the effects of premature cracking, a numerical simulation of the dam construction process is conducted, modeling the cement-hydration heat generation, radiation, convection, conduction and ambient temperature variation for a period of about 24 months. Fig. 5 plots the distribution of the temperature in a section of the dam after 200 days, whereas Fig. 6 plots the temperature variation with time at points A, B, C, D and E, as well as the ambient temperature. The maximum temperature occurs in the middle point (C) of the dam wall and has a value of 50.5 °C at 200 days from the construction start. Examination of the major principal plastic strain caused by the transient temperature differences within the dam showed that the concrete-hydration heat did not cause any significant cracking within the main body of the dam. Any

such cracking within the dam body is practically either zero or negligible. Some thermal cracking may have developed within the upstream aseismic concrete blocks (see Fig. 2b), but it has absolutely no effect on the performance and stability of the dam in its current state.
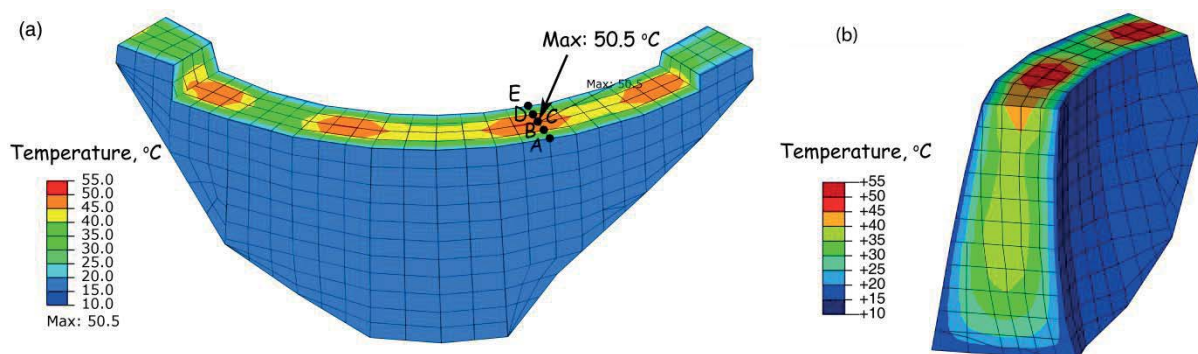
Figure 5: Distribution of temperature within the dam body at 200 days since construction start
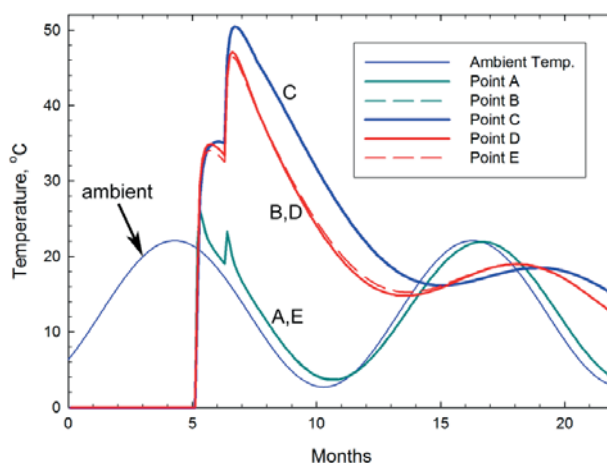
Figure 6: Variation of temperature at points A, B, C, D and E during construction versus time

Seismic analysis

Dynamic characteristics of the dam

The fundamental natural frequency of the dam for full reservoir and canyon rock with shear wave V_s=2800 m/s is 3.97 Hz, whereas for V_s=2000 m/s, it reduces to 3.81 Hz.

Earthquake excitation

The seismicity of the region has been studied by Panagiotopoulos and Papazachos [10]. For the present study, a Maximum Credible Earthquake of magnitude $M \approx 7.5$, with an epicentral distance from the dam site about $R = 15$ km, is considered. The Maximum Probable Earthquake is based on a magnitude of $M \approx 7.0$ and minimum distance $R = 15$ km. The seismic excitation considered consists of three different acceleration records. The first two have been recorded at rock sites (Lucerne and Pacoima Dam records). The third record is synthetic and has response spectra that match the Eurocode 8 design spectra for rock sites. All records have been base-line corrected and scaled to a peak horizontal outcrop-rock acceleration equal to 0.47g and peak vertical outcrop-rock acceleration equal to 0.30g. Fig. 7 plots the horizontal and vertical acceleration time histories of the synthetic record. Fig. 8 plots the acceleration response spectra for the horizontal component and the Eurocode spectra for rock site. The input excitation at the canyon base is computed through de-convolution of the selected

motions. To be able to account for the radiated seismic energy, appropriate dashpots are placed at the canyon boundary and the excitation is imposed in terms of seismic stresses.
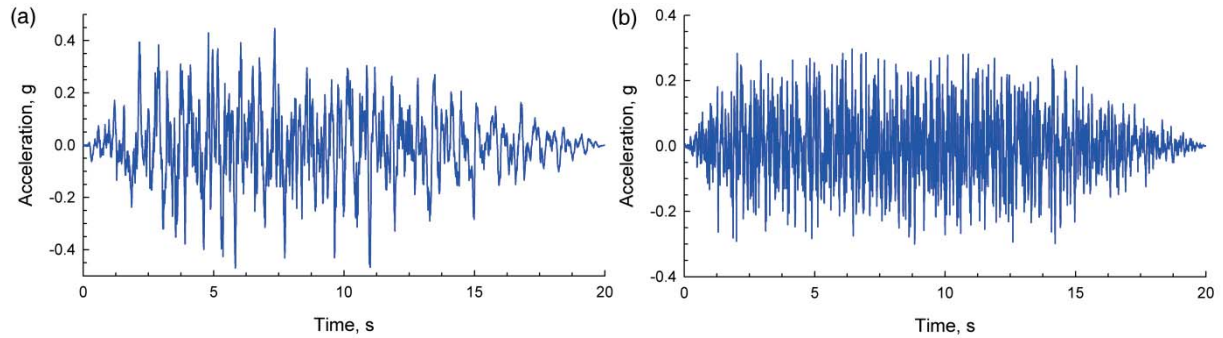
Figure 7: Synthetic excitation at outcrop rock (a) horiz. acceleration (b) vertical acceleration
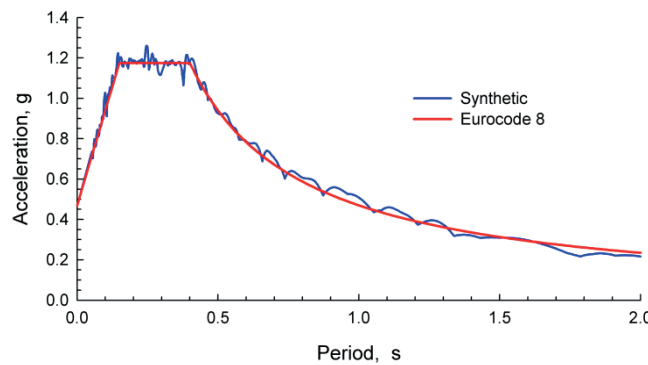
Figure 8: Synthetic horizontal acceleration spectra and Eurocode spectra for rock sites

Hydrodynamic pressures

The hydrodynamic pressures acting on the upstream side of the dam have a significant effect on the earthquake behavior of the dam. They are considered here by using the added-mass formulation proposed by Zangar [11], which was implemented in code ABAQUS [1]. The amount of mass b at a node is equal to:

$$b = \frac{1}{2} h \, C_m \left[\frac{z}{h}(2 - \frac{z}{h}) + \sqrt{\frac{z}{h}(2 - \frac{z}{h})} \right] \rho_w A \qquad (1)$$

where h = depth of the reservoir, C_m = coefficient based on the angle θ of upstream surface to the vertical, z = depth of node below water surface, ρ_w = water density and A = area around node contributing to hydrodynamic forces.

Results and discussion

The objective of the parametric analysis is to investigate the effect of various factors on the seismic performance of the Tavropos Arch Dam. More specifically, the parametric study examines effect of concrete strength variation, seasonal temperature variation, reservoir water level, canyon rock flexibility, joint behavior, hydrodynamic pressures, spillway geometry, and earthquake excitation characteristics. Due to lack of space, only representative results of the most likely scenario are presented in this article, whereas additional results will be published elsewhere. The results presented below are based on a concrete compressive strength of 46

MPa, dynamic tensile strength of 6.4 MPa, critical summer temperature variation, maximum reservoir water level (792 m), and canyon rock S-wave velocity 2800 m/s. Both models A and B (shown in Fig. 3) are utilized for the analysis. First, the overall response and the stability of the dam are considered.

Relative displacements

Results from two scenarios are presented here for the evaluation of the response and stability of the dam. The first scenario assumes that the vertical joints and the base joint behave as bonded surfaces. Figs. 9a and 9b plot the relative u/d displacement at mid-crest of the dam subjected to the synthetic record for bonded joints, using the two canyon models A and B, respectively (Fig. 3). The computed relative displacement by the two models is rather similar, with the peak value about 4.5 cm. There is no residual relative displacement at the end of shaking. The peak relative displacement for the other two excitations (not shown here) are about 4 cm. Fig. 10a plots the distribution of the u/d relative displacement for bonded joints using model A at a moment of peak response (t = 6 s). The second scenario is quite conservative as it assumes that the joints have zero tensile strength and behave as surfaces in contact having only frictional strength. Fig. 10b plots the residual relative u/d displacement for the case of un-bonded frictional joints, allowing opening and sliding during shaking. The maximum relative displacement in this case is less than 5 cm, which is considered as safe with regard to the stability of the dam for this very conservative scenario.
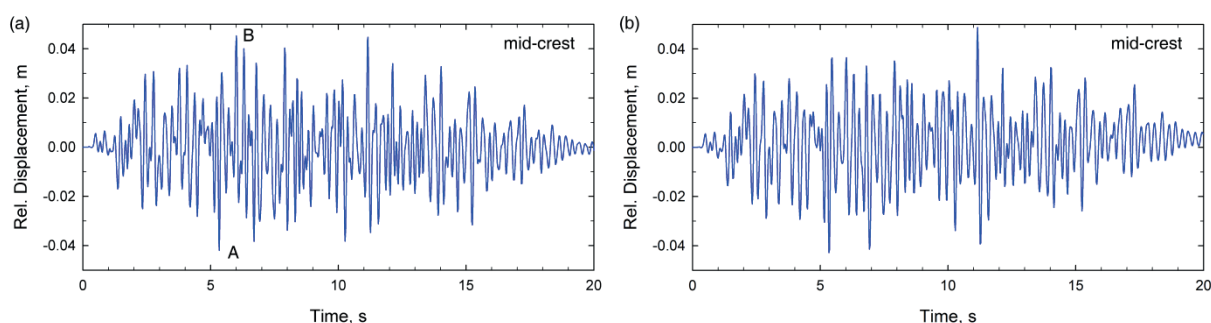
Figure 9: Time history of relative u/d displacement at mid-crest assuming bonded joints obtained from (a) model A and (b) model B
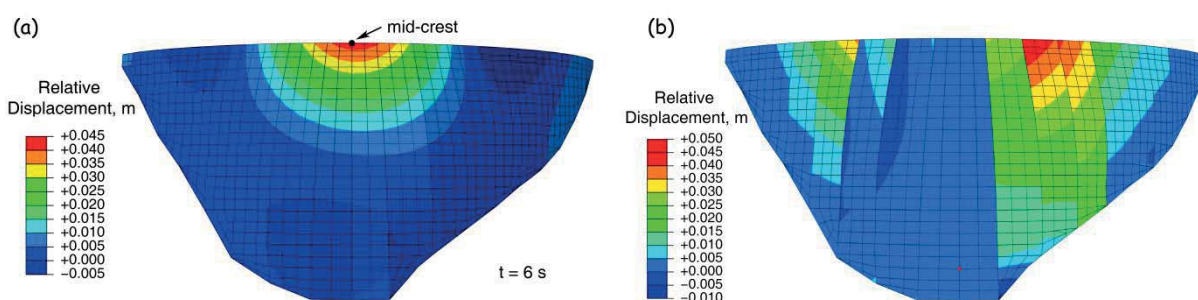
Figure 10: (a) Peak relative u/d displacement at t = 6 s assuming bonded joints and (b) Residual relative u/d displacement at the end of shaking assuming un-bonded frictional joints.

Stresses and strains

Fig. 11 shows the distribution of major principal stress, σ_1, at the moment of maximum response of the dam subjected to the Synthetic record based on Model A (Fig. 3). As shown in the figure, high tensile stresses develop at the upper middle part of the arch dam, reaching in some elements the concrete tensile strength for a very small time increment (e.g. 0.01s) and causing some limited plastic tensile strain. These tensile stresses occur when the upper part of the dam has a relative displacement towards upstream with respect to its base. In this case, the

combined effect of dam and water inertia (negative hydrodynamic pressure) cause the upper part of the dam to deform towards upstream. This upstream relative displacement becomes maximum at t=5.32 s for the Synthetic record (see point A in Figure 9a). Such deformation causes an extension of the arch dam along its length, which is maximum at the upper-middle area of the arch, resulting to relatively high, short-duration tensile hoop stresses. It is noted that the tensile stresses become maximum at the upstream surface of the central crest area of the arch, whereas they are quite smaller on the downstream side. Figs. 12a and 12b plot the major principal stress time history at mid-crest, evaluated at the upstream surface element using the two models A and B, respectively. The results show that σ_1 reaches the tensile strength momentarily in Fig. 12a, but it remains below the tensile strength in Fig. 12b.
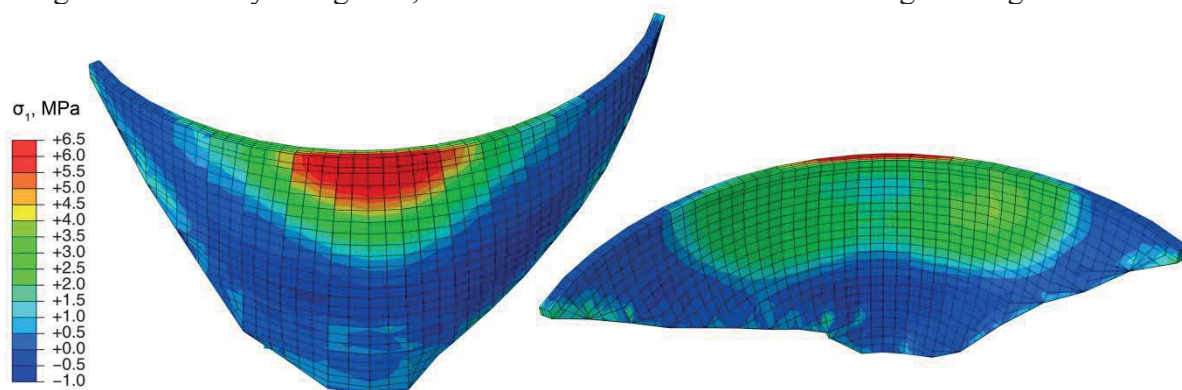
Figure 11: Distribution of major principal stress σ_1 at a moment of maximum tension of the dam subjected to the Synthetic record excitation (time t = 5.32 s)
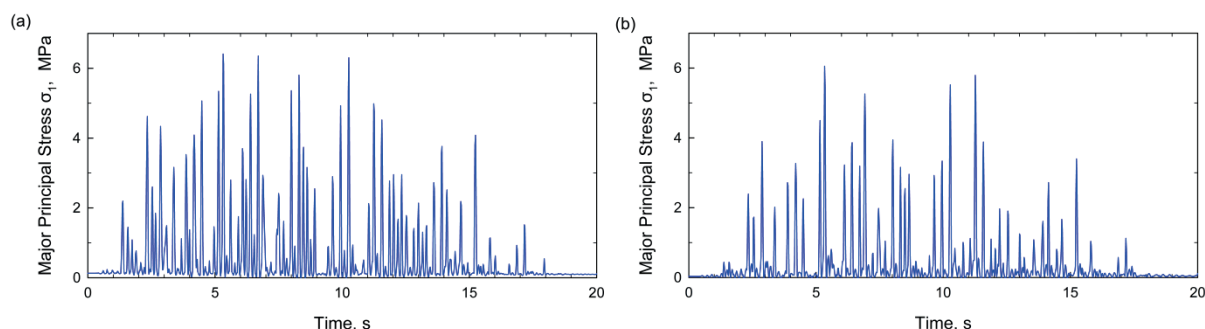
Figure 12: (a) Major principal stress and (b) minor principal stress time histories at mid-crest (upstream surface element)
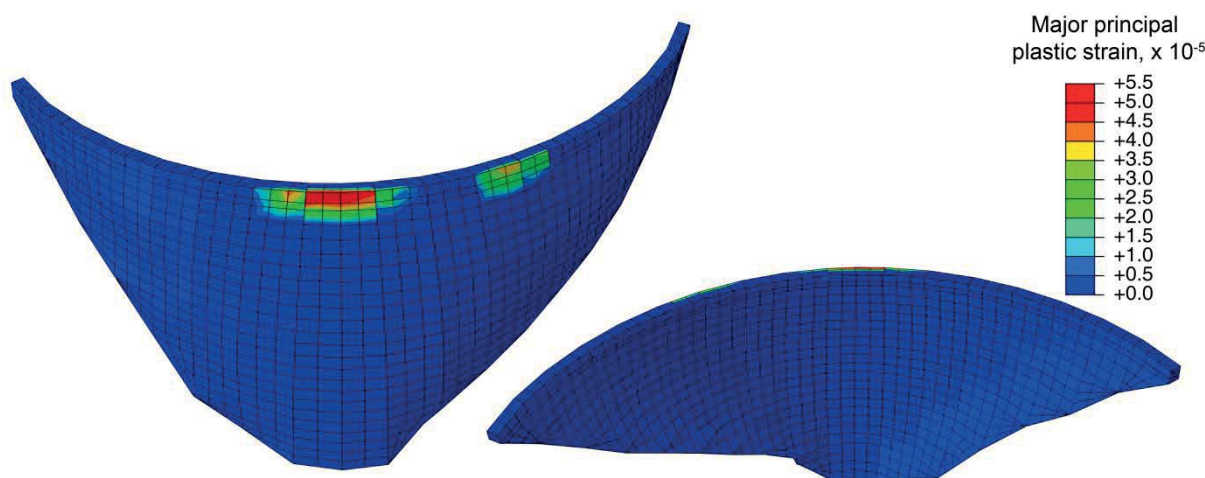
Figure 13: Accumulated major principal plastic strains at the end of shaking

Despite the large tensile stresses that may develop momentarily during shaking, the accumulated major principal plastic strain ε_1^p at the end of shaking is very limited. Fig. 13 plots the distribution of ε_1^p at the end of shaking for the Synthetic record based on model A. Its maximum value is only about 5 10^{-5}, located at the upstream face of the mid-crest (concrete part 10). In reality, it is expected that the value of the tensile plastic strain ε_1^p will be even smaller than the values shown in Fig. 13. This is because the actual tensile strength at the joints is expected to be about 0.7 f_t, where f_t is the tensile strength of the dam concrete. Thus, in areas of higher tensile stress concentration, as at the mid-crest area, any cracks most likely will occur at the weakest points, i.e. the vertical joints. As shown in other analyses not presented here, if the entire vertical joints rupture before shaking (i.e. the joint tensile strength is zero), the tensile stresses developing within the mid-crest area of the arch dam are significantly reduced, due to the instantaneous, local opening of the vertical joints. Therefore, the accumulated major principal plastic strains near the mid-crest area are much smaller.

Note that the results in Figs. 11, 12a and 13 are based on model A. By using the more refined model B, it is shown that the tensile stresses developing in the mid-crest area are slightly smaller and do not exceed the tensile strength. Thus, no plastic strains develop in the dam body for the presented case of concrete with compressive strength equal to the mean value f_c =46 MPa.

Figure 14 plots the distribution of the minor principal stress σ_3 (maximum compression) at a moment of maximum response, corresponding to time t = 6 s (point B in Figure 9a). This occurs when the dam base and canyon moves upstream, while the dam is pushed by the concrete and water inertia (positive hydrodynamic stresses) towards downstream, thereby increasing the compressive stresses in the mid-crest area of the arch. The maximum value of the compressive stresses at the mid-crest area during shaking is less than 12 MPa, i.e. the compressive stresses are very small compared to the compressive strength of concrete in uniaxial load (f_c =46 MPa). In this case, the minimum available factor of safety against compressive failure $FS_c = f_c /(\sigma_1 - \sigma_3)$ during shaking is larger than 2.5. Thus, no plastic deformations occur due to compressive stresses. The compressive stresses for the other two records are smaller than those obtained for the Synthetic record.
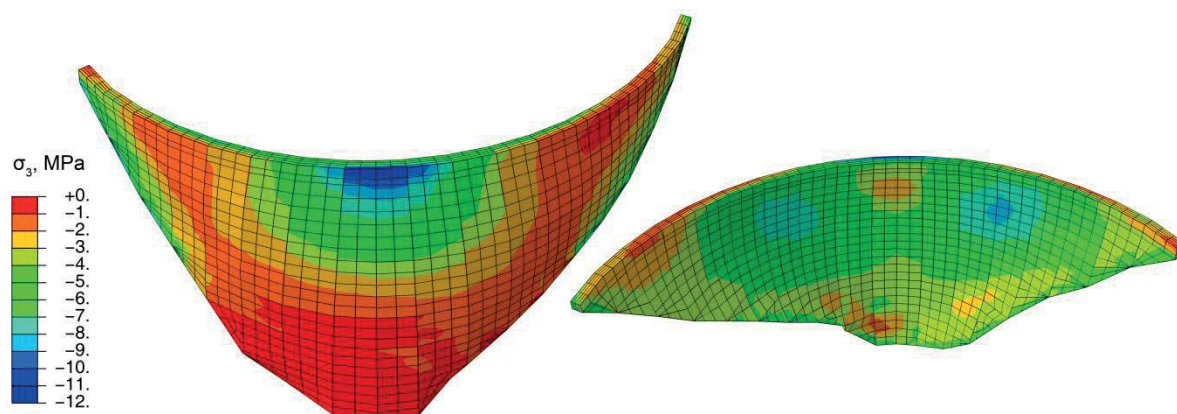
Figure 14: Distribution of minor principal stress σ_3 at a moment of maximum compression of the dam subjected to the Synthetic record excitation (time t = 6.00 s)

Conclusions

Evaluation of the results of all parametric studies leads to the general conclusion that, for the maximum earthquake intensity anticipated, the dam is safe against any instability and its overall performance is satisfactory. More specifically, the main conclusions are the following:

1. The concrete-hydration heat generated during construction did not cause any significant cracking within the main body of Tavropos dam.
2. The maximum seismic relative displacement of the dam for the case of grout-bonded joints is small (about 3 to 4.5 cm). There are no permanent relative displacements at the end of shaking.
3. For the extreme scenario in which the vertical joints and the joint at the base are already ruptured before the earthquake, the relative displacement of the dam at the end of shaking is limited to values less than 5 cm. Thus, even for this extreme scenario, the stability of the 17 cantilever dam parts is fully assured.
4. Based on the results of all analyses, the maximum compressive stresses developing during seismic shaking range between -10 MPa to -16 MPa and do not cause any plastic strains.
5. The magnitude of tensile stresses within the concrete parts depends on the behavior of the vertical joints. The results of the parametric analysis show that the tensile plastic strains (or cracking) developing within the dam body are very small. Therefore, the performance of the dam with respect to the development of tensile cracking during shaking is satisfactory.
6. The summer environmental temperature condition is the most critical one, as it results to higher tensile plastic strains within the dam body.
7. Among the four reservoir water elevations investigated, the most critical one is the maximum water level (792 m), which results to relatively higher tensile plastic strains within the dam body.
8. The stiffer rock, having a wave velocity v_s=2800 m/s, yielded consistently larger values of tensile plastic strains compared to those obtained for v_s=2000 m/s.

Acknowledgment

References

[1] ABAQUS (2012). Users' Manual, Simulia, Pawtucket, Rhode Island.
[2] Azenha, M., Faria, R., Ferreira, D. (2009), Identification of early-age concrete temperatures and strains: Monitoring and numerical simulation, Cement & Concrete Composites, 31, 369–378.
[3] Chopra, A. (2008). Earthquake analysis of Arch Dams: Factors to be considered, 14th World Conference on Earthquake Engineering, October, 2008, Beijing, China.
[4] Dakoulas, P. Seismic analysis of Tavropos Arch Dam, Research Report to Public Power Corporation, University of Thessaly, Volos, Greece
[5] Escuder, I.B. and Blazquez, F.P. (2007). Lessons learned in the analysis of the elastic behavior of an arch-gravity dam performed by seven independent engineering teams, 9th Bench. Work. Num. Analysis of Dams, ICOLD, St. Petersburg, Russia, June 22-24.
[6] Lee J., and Fenves, G.L (1998). A plastic-damage concrete model for earthquake analysis of dams, Journal of Earthq. Eng. & Struct. Dynamics, 27: 937-596.
[7] Meghella, M. and Frigerio, A. (2009). Theme A: Initial strain and stress development in a thin arch dam considering realistic construction sequence, 10th Benchmark Workshop on the Numerical Analysis of Dams, ICOLD, Paris, France, Sept. 16-19.
[8] Mills-Bria, B., Nush, L., and Chopra, A. (2008). Current Methodology at the Bureau of Reclamation for the Nonlinear Analysis of Arch Dams Using Explicit FE Techniques, 14th World Conference on Earthquake Engineering, October, 2008, Beijing, China.

[9] Mojtahedi, S. and Fenves, G. (2000). Effect of contraction joint opening on Pacoima Dam in the 1994 Northridge earthquake, California Strong-Motion Instrumentation Program Data Utilization Report, CSMIP/00-05 (OSMS 00-07), Sacramento, Calif.

[10] Panagiotopoulos, D. and Papazachos, K.B. (2008). Active tectonics of Thessaly and seismicity of Karditsa, 1st Conference on Development, Karditsa, Greece.

[11] US Bureau of Reclamation (2006). State-of-Practice for the Nonlinear Analysis of Concrete Dams at the Bureau of Reclamation, USBR Report, Colorado, USA.

Earthquake safety assessment of arch dams based on nonlinear dynamic analyses

S. Malla[1]

[1] Axpo Power AG, Parkstrasse 23, CH-5401 Baden, SWITZERLAND

E-mail: sujan.malla@axpo.com

Abstract

For the earthquake safety assessment of two major arch dams in Switzerland, various linear and nonlinear dynamic analyses were performed. For these analyses, a safety evaluation earthquake (SEE) with a return period of 10,000 years was considered in each case. Even though the input motion has a PGA of less than 0.2 g, the crest region would be subjected to amplified accelerations significantly larger than 1.0 g. Moreover, high tensile stresses occurring in the crest region are likely to exceed the tensile strength of the vertical contraction joints and the horizontal lift joints. Consequently, these joints could open during the earthquake shaking, possibly resulting in an upper portion of a dam block becoming fully detached from the rest of the dam. The dynamic analysis of possibly detached portions in the crest region showed that they could undergo some sliding and rocking motions. However, they would remain stable during and after the earthquake. Based on the results of the nonlinear dynamic analyses, it is concluded that the earthquake loading could cause some limited damages, but an uncontrolled release of reservoir water is unlikely to occur. Therefore, the investigated dams satisfy the safety requirements for the SEE.

Introduction

A program of systematic assessment of earthquake safety of all significant dams in Switzerland is scheduled to be completed by the end of the current year 2013. A document containing state-of-the-practice guidelines for this investigation program was issued by the Swiss Federal Office of Energy in 2003. The primary goal of this program is to ensure the safety of the downstream population against loss of life and property damage (Panduri et al., 2012). For this purpose, it must be shown that the safety evaluation earthquake (SEE) would not cause a dam failure resulting in an uncontrolled release of reservoir water. Depending on the height and the reservoir volume, a dam is categorized as class 1, 2 or 3 and it has to be checked for the SEE ground motion with a return period of 10,000, 5,000 or 1,000 years, respectively.

At the time of the design of most of the existing dams, the earthquake action was usually considered as a pseudo-static loading and typically a horizontal seismic coefficient of 0.1 g was assumed. This is clearly inadequate even in regions with relatively low seismicity. In practically all major arch dams, the crest region would experience horizontal accelerations significantly exceeding 1.0 g in the event of the SEE, even when the ground motion at the rock level has a horizontal peak ground acceleration (PGA) of the order of 0.20 g only.

In a linear elastic analysis, the earthquake shaking would typically cause high horizontal stresses in the arch direction in the crest region of the dam. As the tensile strength of the vertical contraction joints is usually quite low, these joints are likely to open during the earthquake shaking. Once the vertical joints are open, the dam blocks would behave as vertical cantilevers, leading to high vertical tensile stresses. Since the tensile strength of

horizontal lift joints is usually substantially lower than that of monolithic mass concrete, a horizontal crack may form, causing the upper portion of a dam block to become fully detached from the rest of the dam. Such a detached portion would be subjected to rather high accelerations and it could thus undergo sliding and rocking motions during the earthquake shaking. As long as a possibly detached portion remains stable during and after the earthquake, an uncontrolled release of reservoir water could be ruled out and the safety requirements for the SEE would be satisfied.

To investigate the dynamic stability of possibly detached upper portions in the crest region and to analyze the behavior of vertical contraction joints in an arch dam during an earthquake, nonlinear dynamic analyses have to be carried out. In this paper, two illustrative examples are presented to show how earthquake safety of arch dams can be assessed on the basis of results of 2D and 3D nonlinear dynamic analyses.

Methodology for simplified dynamic stability analysis

A simplified analysis of the seismic stability of possibly detached concrete blocks in the central upper portion of an arch dam can be performed in the following steps (Malla and Wieland, 2006; Wieland and Malla, 2012):

(i)   Linear elastic dynamic time history analysis of a three-dimensional (3D) finite element (FE) model of dam-reservoir-foundation system;

(ii)   Selection of detached concrete blocks for dynamic stability analysis based on envelopes of principal dynamic tensile stresses and absolute accelerations;

(iii)   Obtaining time histories of radial and vertical components of absolute acceleration at the base of each detached concrete block from the results of analysis step (i);

(iv)   Setting up 2D FE model of each detached concrete block using contact elements to simulate the cracked lift joint (gap elements may be employed to prevent the concrete block from moving beyond the downstream face of the dam in view of the geometrical constraints in an arch dam);

(v)   Nonlinear dynamic analysis of rocking-sliding response of each detached concrete block subjected to input base acceleration obtained in step (iii);

(vi)   Evaluation of the maximum sliding movement and the maximum crack opening displacements at the upstream and downstream edges of the base of each detached concrete block for at least three different earthquake ground motions; and

(vii)   Assessment of the dynamic stability of detached concrete blocks based on results of step (vi).

The seismic safety of the Roggiasca and Gigerwald arch dams in Switzerland was checked by employing this simplified procedure. The main results of this analysis are presented and discussed in the following sections. Furthermore, nonlinear 3D FE analysis of the Gigerwald arch dam was performed to investigate contraction joint openings during the earthquake.

All the dynamic calculations were performed with the help of the general-purpose FE software ADINA (ADINA R & D, 2008). For the dynamic analyses, the three components of earthquake excitation were simulated by artificially-generated spectrum-compatible acceleration time histories. The hydrodynamic pressure was modeled as added masses acting perpendicular to the upstream face of the dam.

Earthquake safety assessment of Roggiasca arch dam

The 68 m high Roggiasca arch dam was completed and first impounded in 1965. With a crest thickness of 2.5 m and a maximum thickness at the base of 7.5 m only, the dam has a relatively high Lombardi slenderness coefficient of 21. At the location of this dam, the 10,000-year SEE has a horizontal PGA of 0.17 g.

The linear seismic response of the Roggiasca dam was analyzed using a 3D FE model, which comprised the dam, the foundation rock, the sediment deposit on the upstream side and the soil fill on the downstream side. The main results of this 3D analysis performed for 3 different ground excitations (designated as earthquakes 1, 2 and 3) are listed in Table 1. The largest accelerations and dynamic stresses were obtained at the middle and also at the two quarter points of the dam crest. The results showed that the upstream sediment deposit and the downstream soil fill would not play a significant role in the dynamic behavior of the dam.

Table 1: Main results of 3D linear elastic earthquake analysis of Roggiasca dam subjected to SEE ground motion under full reservoir condition

Dynamic response (envelope)	Earthquake 1	Earthquake 2	Earthquake 3
Relative crest displacement (mm)			
• Along-stream direction	16.2	15.9	18.7
• Across-stream (left-right) direction	8.4	7.9	8.2
• Vertical direction	2.0	2.1	2.1
Absolute crest acceleration (g)			
• Along-stream direction	1.45	1.34	1.27
• Across-stream (left-right) direction	0.62	0.64	0.72
• Vertical direction	0.41	0.39	0.35
Principal tensile stress (MPa)	6.1	5.6	6.6
Principal compressive stress (MPa)	-6.3	-6.0	-6.2

The magnitude of the largest dynamic tensile and compressive stresses in the crest region of the dam is about 6 MPa (see Table 1 and Figure 1). Even higher elastic stresses are computed at the upstream and downstream edges of the dam-rock interface due to the stress singularities at these reentrant corners.
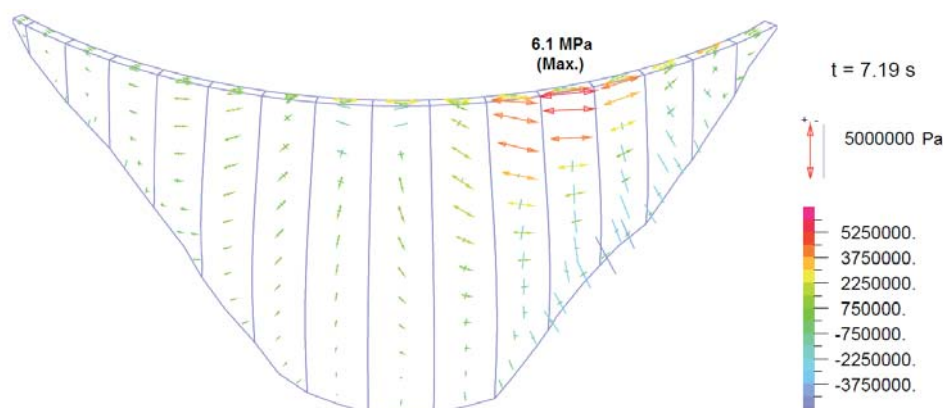
Figure 1: Principal stress vectors due to earthquake 1 (without static loads) at time t = 7.19 s when the highest tensile stress occurs under full reservoir condition

The largest compressive stress in the dam body under the combination of the static and dynamic loads is about -10 MPa, which is not a problem for the dam concrete with a static compressive strength of 46 MPa. In spite of the compressive stresses due to the static loads (self-weight and hydrostatic pressure), relatively high horizontal tensile stresses of up to about 4 MPa oriented in the arch direction still occur in the crest region during the earthquake shaking. If the thermal stresses in winter and the effect of the ongoing chemical expansion of the dam concrete would also be considered, the tensile stresses would be even higher.

In order to investigate the stability of possibly detached concrete blocks during the earthquake excitation, simplified 2D FE models shown in Figure 2 were employed. As the Roggiasca arch dam is rather thin, any detached block in the crest region would be quite slender.
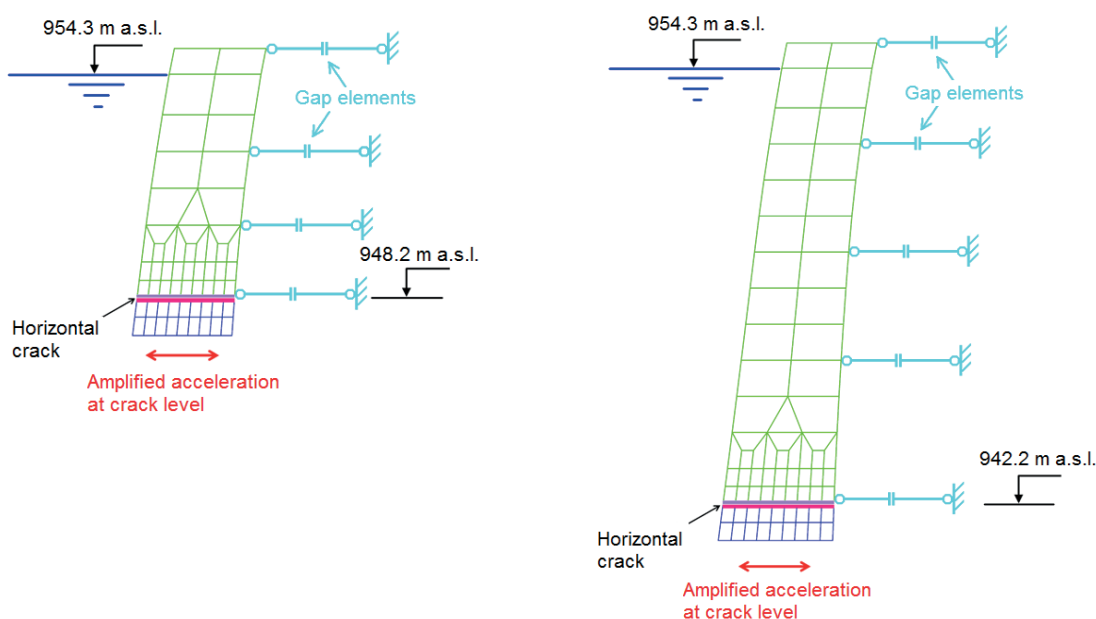
Figure 2: 2D FE models of 7 m and 13 m high detached blocks in crest region of Roggiasca arch dam (gap elements prevent any movement beyond the downstream face)

In a dynamic analysis involving rigid body motions, it is considered prudent to use only the stiffness-proportional part of the Rayleigh damping model, as the mass-proportional part corresponds to external viscous dampers connected to the nodes of the model (Hall, 2006). Three different Rayleigh damping models were considered in the stability analysis (see Table 2). Model A corresponds to that used in the 3D linear dynamic analysis. In model B, only the stiffness-proportional part is kept. In model C, the stiffness-proportional part is further substantially reduced, which is very conservative.

Table 2: Rayleigh damping models used for 2D dynamic stability analysis of detached cantilever blocks in crest region of Roggiasca dam

Rayleigh damping model	Parameter α (s^{-1})	Parameter β (s)
A	2.20	0.00124
B	0.00	0.00124
C	0.00	0.00020

The results of the dynamic stability analysis listed in Table 3 show that the detached portions in the crest region have a tendency to undergo only rocking with virtually no sliding, a behavior explained by the slender form. Even the rocking motion is quite small and causes dynamic crack openings of only a few millimeters at the base of the detached portion.

Table 3: Main results of 2D dynamic stability analysis of detached portions in crest region of Roggiasca dam subjected to SEE ground motion under full reservoir condition

Rayleigh damping model	Earthquake	Max. horiz. crest displace- ment (mm)	Max. sliding displace- ment (mm)	Max. crack opening, u/s face (mm)	Max. crack opening, d/s face (mm)
(a) 13 m high detached block above crack at level 942 m a.s.l.					
A	1	-4	0.0	0.0	0.7
B	1	-5	0.0	0.0	0.8
C	1	-6	0.0	0.0	1.1
B	2	-11	0.0	0.0	2.2
C	2	-14	0.0	0.0	3.0
B	3	-11	0.0	0.0	2.2
C	3	-17	-0.2	0.0	3.8
(b) 7 m high detached block above crack at level 948 m a.s.l.					
A	1	-15	-0.1	0.0	5.6
B	1	-16	-0.1	0.0	6.1
C	1	-79	-0.2	0.1	30.7
B	2	-22	-0.1	0.0	8.5
C	2	-128	-0.4	0.0	49.8
B	3	-25	-0.1	0.0	9.7
C	3	-171	-0.7	0.1	66.7

The results of the dynamic stability analysis show that the detached portions remain dynamically stable even when subjected to peak horizontal accelerations about twice as large as the pseudo-static overturning acceleration. This behavior can be explained by the fact that acceleration spikes would have a relatively high frequency of about 5 Hz corresponding to the dominant natural frequency of the dam. Hence, such a spike would exceed the pseudo-static overturning acceleration only for a very short duration of less than one-tenth of a second, which is too short to produce any significant block rotation. A review of literature on dynamic overturning of rigid blocks also confirms that acceleration peaks would have to be many times larger than the pseudo-static overturning acceleration for a block with dimensions of the order of a few meters to be toppled by a dynamic base excitation at such a frequency, as illustrated in Figure 3 (Shi et al., 1996; Zhang and Makris, 2001).
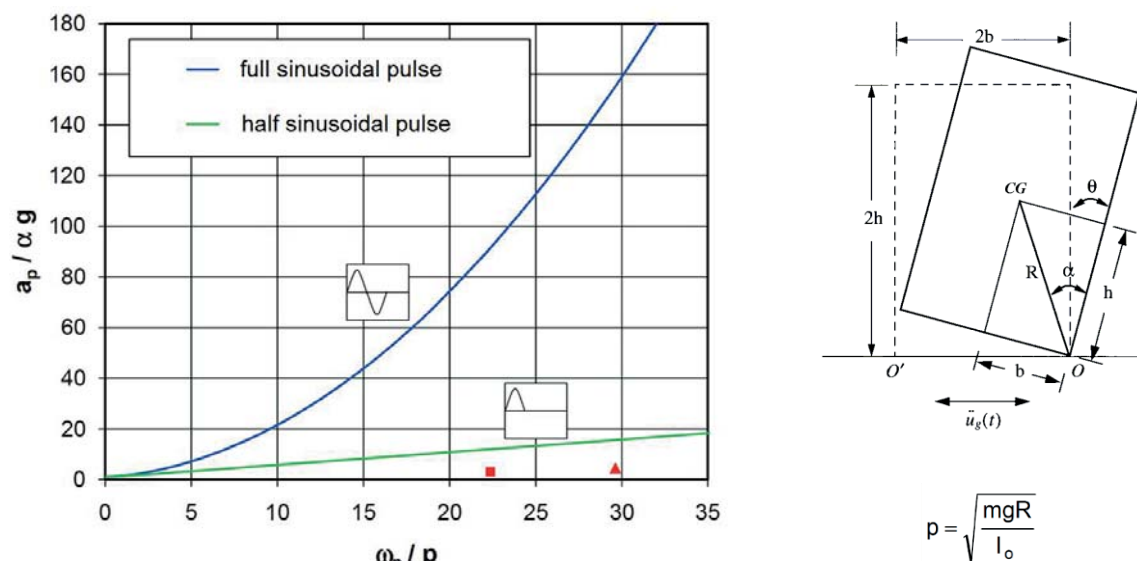
Figure 3: Boundaries between stable and unstable regions of dynamic rocking motion based on analytical solutions for half and full sinusoidal base excitations (Shi et al., 1996, Zhang und Makris, 2001)

Note: A ground excitation with an amplitude of 1.5 g and a frequency of 5 Hz corresponds to the red square (ω_p/p = 22.4 und $a_p/\alpha g$ = 3.2) and the red triangle (ω_p/p = 29.6 und $a_p/\alpha g$ = 4.5) in the case of, respectively, the 7 m and 13 m high detached portions.

Earthquake safety assessment of Gigerwald arch dam

The 147 m high Gigerwald dam was completed and first impounded in 1976. The dam thickness varies from 7 m at the crest to about 22 m at the base.

The main results of the linear elastic dynamic analysis of a 3D FE model of this double-curvature arch dam for 3 different earthquakes are listed in Table 4. The crest region would be subjected to amplified horizontal accelerations as high as about 2.0 g during the 10,000-year SEE with a horizontal PGA of 0.19 g.

Table 4:Main results of 3D linear elastic earthquake analysis of Gigerwald dam subjected to SEE ground motion under full reservoir condition

Dynamic response (envelope)	Earthquake 1	Earthquake 2	Earthquake 3
Relative crest displacement (mm) • Along-stream direction • Across-stream (left-right) direction • Vertical direction	48.0 15.3 6.6	45.6 16.0 7.4	44.5 18.0 6.9
Absolute crest acceleration (g) • Along-stream direction • Across-stream (left-right) direction • Vertical direction	1.83 0.84 0.75	2.04 0.86 0.78	1.98 0.80 0.71
Principal tensile stress (MPa)	8.7	9.8	8.7
Principal compressive stress (MPa)	-10.3	-9.5	-9.6

The earthquake shaking produces dynamic tensile stresses of nearly 10 MPa in the central crest region of the dam. Even after the combination with the compressive stresses due to the hydrostatic water load, high horizontal tensile stresses of up to about 6 MPa would still remain in the arch direction. In reality, such tensile stresses cannot develop due to the presence of the vertical contraction joints, whose tensile strength is normally quite low.

The next step was to perform the dynamic analysis of a 3D FE model in which all 23 vertical contraction joints were simulated as frictional contact surfaces and the dam concrete was assumed to be linear elastic (uncracked). This analysis was performed for 3 different input motions. Figures 4 to 6 depict some results obtained for earthquake 2. This analysis showed that the seismic shaking would cause relative sliding displacements of nearly 1 cm between the adjacent blocks and the contraction joints would open by maximum about 4 mm.

The largest compressive stress in the dam obtained in the nonlinear analysis approaches nearly -19 MPa (excluding the corner singularity at the dam-rock interface), which is not a problem for the dam concrete. In comparison, the maximum compressive stress in the case of the linear analysis is about -16 MPa. In spite of the joint displacements, the dynamic displacements and accelerations of the dam computed in the nonlinear analysis do not deviate significantly from those in the corresponding linear analysis. The main difference lies in the absence of any significant horizontal tensile stresses in the arch direction in the central crest region in the case of the nonlinear analysis owing to the presence of the contraction joints. During the brief openings of the contraction joints, the upper portion of a dam block acts temporarily as a cantilever, due to which relatively high transitory vertical tensile stresses exceeding 6 MPa appear on the downstream face of the dam, as depicted in Figure 6. Hence, horizontal cracks are likely to form, especially at the lift joints, possibly resulting in the detachment of the uppermost portion of a central block from the rest of the dam body.
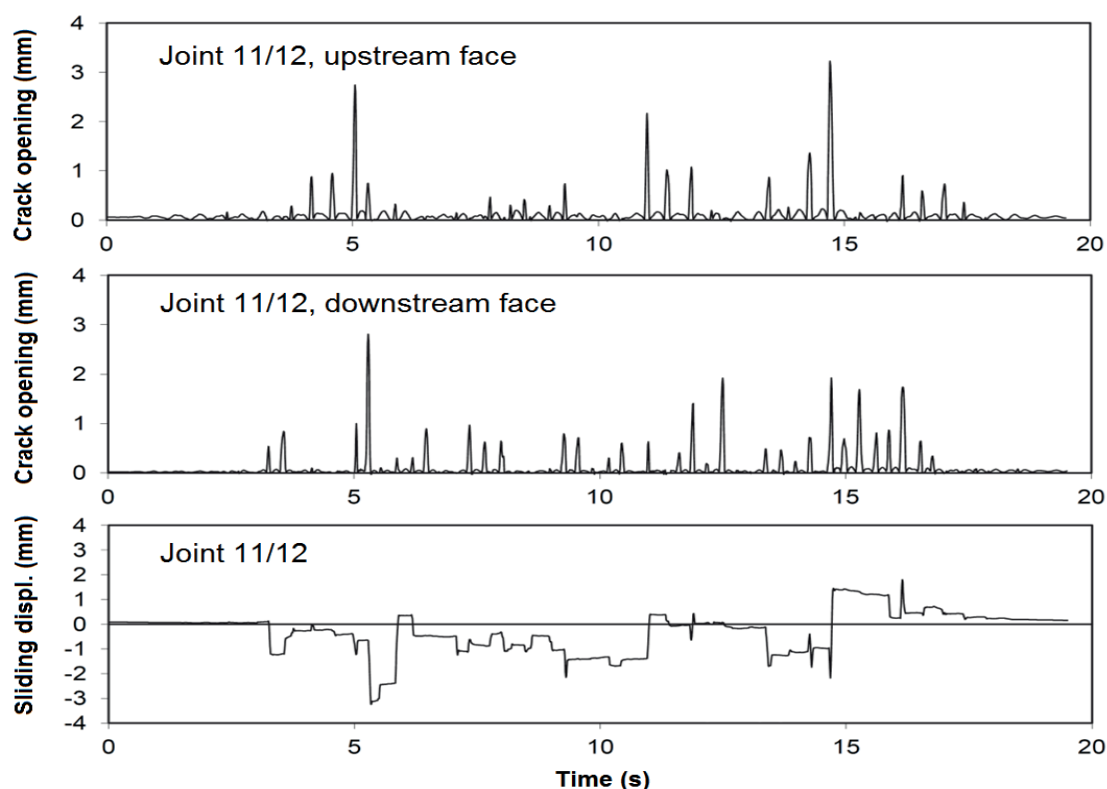
Figure 4: Time histories of opening and sliding displacements of vertical contraction joint 11/12 at crest level due to earthquake 2 under full reservoir condition
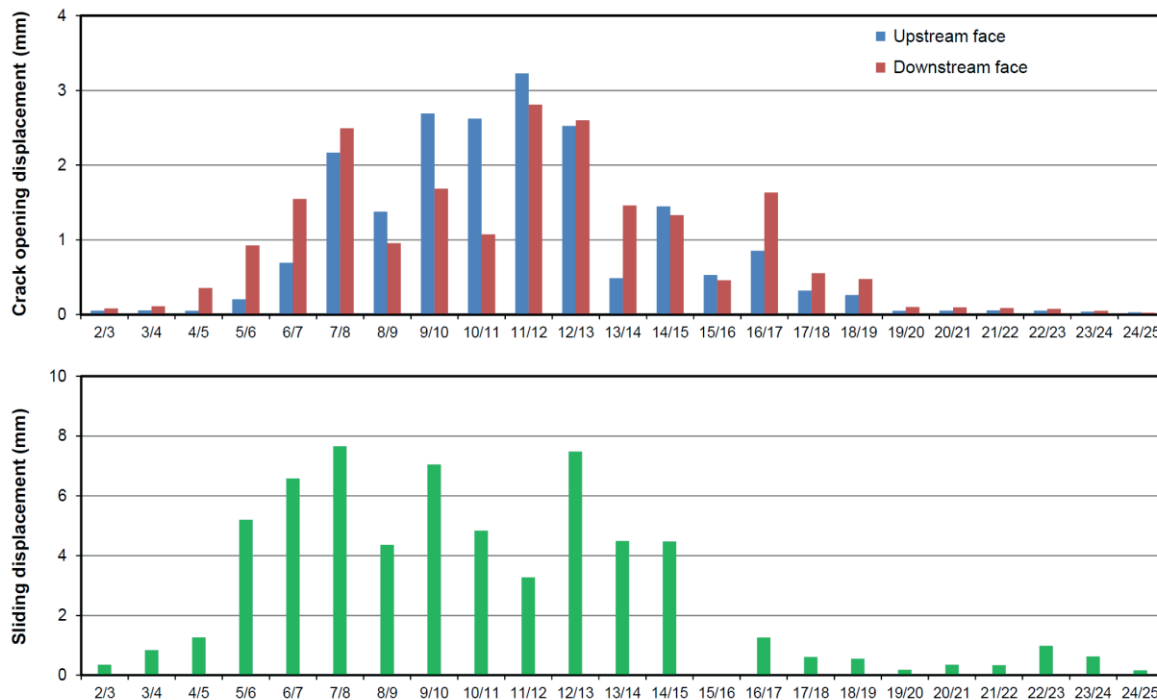
Figure 5:Maximum opening and sliding displacements of vertical contraction joints at crest level due to earthquake 2 under full reservoir condition
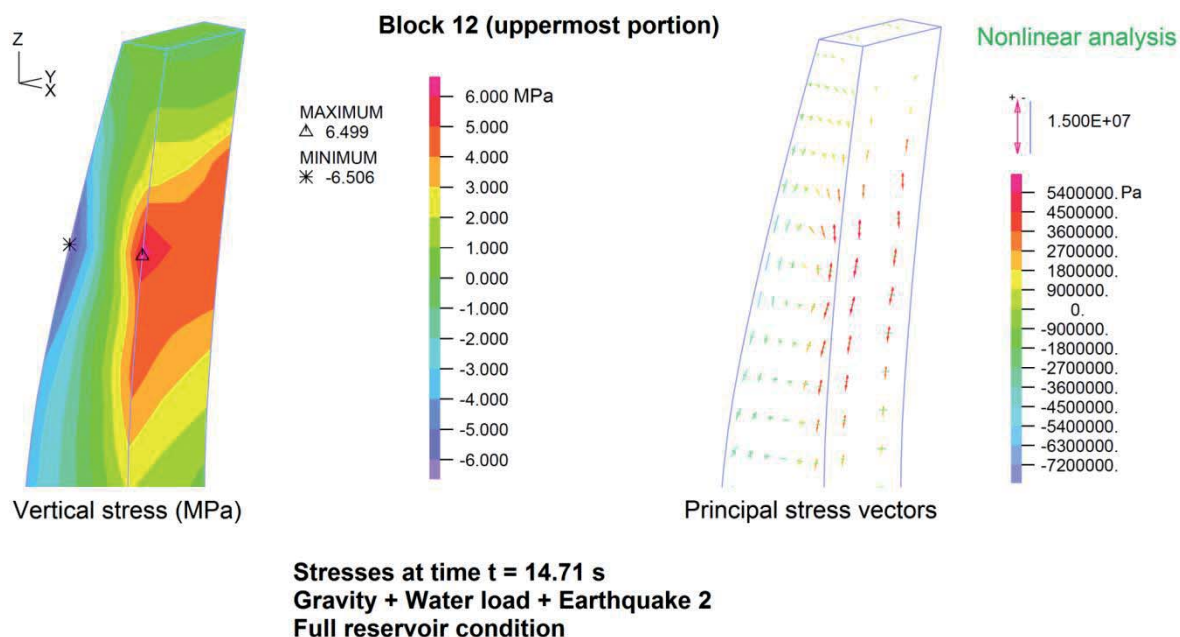
Figure 6: Stresses due to cantilever behavior during opening of vertical contraction joints

The safety of possibly detached portions in a central dam block subjected to the SEE shaking was assessed using simplified 2D models (see Figure 7). This analysis showed that an 8 m high detached portion could slide by up to about 50 cm towards the reservoir during the SEE and the rocking motion would result in crack opening displacements of up to about 7 cm. However, the detached block would remain stable during and after the earthquake and the earthquake damage would not lead to an uncontrolled release of water.
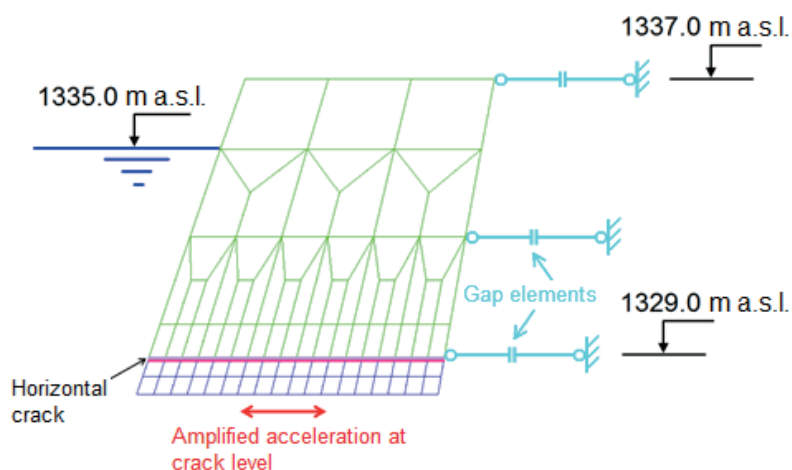
Figure 7: 2D FE model of 8 m high detached portion of a central block of Gigerwald arch dam (gap elements prevent any movement beyond the downstream face)

For a less conservative dynamic stability assessment, a nonlinear analysis was also performed using a 3D model in which the uppermost 8 m of the central dam block was assumed to be detached from the rest of the dam along the vertical contraction joints at the sides and an assumed horizontal crack along a lift joint. As shown in Figure 8, the 3D analysis showed that such a detached block would slide by up to 16 cm towards the reservoir, which is only about one-third of the result obtained in the corresponding more conservative 2D analysis. The substantially smaller sliding displacement in the 3D analysis can be attributed mainly to the additional frictional resistance at the vertical contraction joint on each side, an effect that could not be taken into account in the simplified 2D approach. The maximum crack opening also decreased to about 3 cm in the 3D analysis.
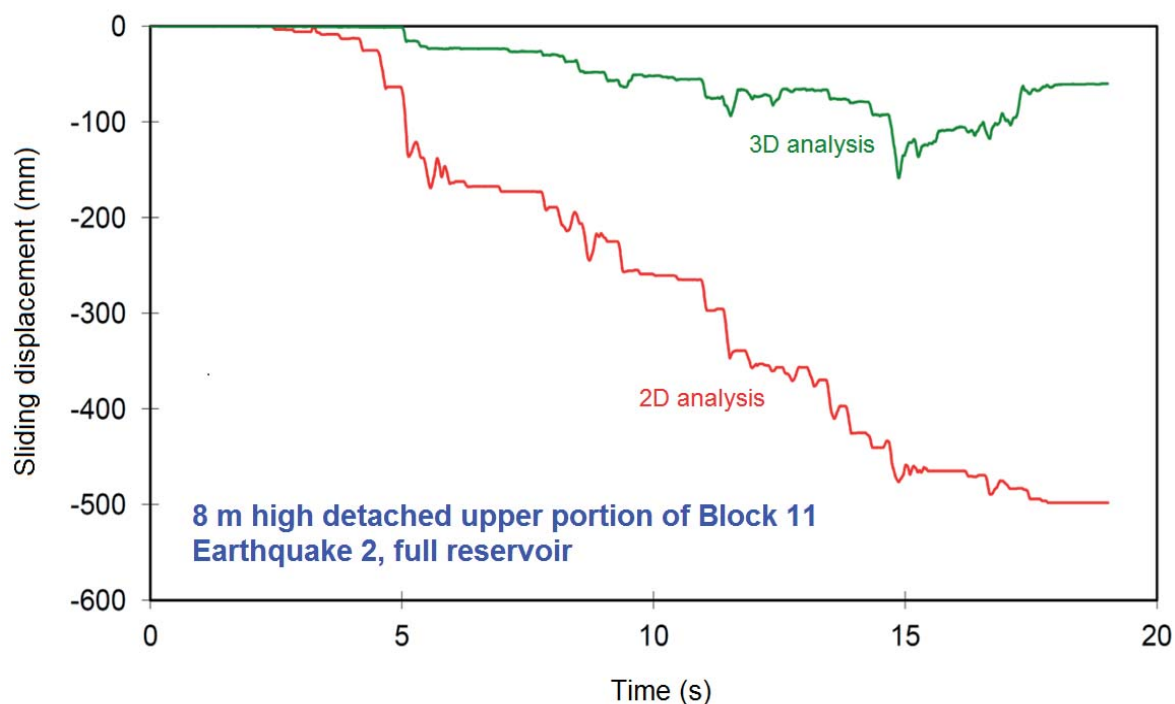
Figure 8: Sliding displacement of 8 m high detached concrete block in central cantilever of Gigerwald arch dam subjected to earthquake 2 under full reservoir condition

Conclusions

The results of the earthquake safety assessment of the Roggiasca and Gigerwald arch dams can be summed up as follows:

1. The ground excitation during the 10,000-year SEE produces relatively high accelerations and tensile stresses in the central upper portion of a large arch dam.
2. The tensile strength of the vertical contraction joints and the horizontal lift joints is usually significantly lower than that of the monolithic concrete. Thus, these joints may open during the earthquake shaking, possibly resulting in the upper portion of a dam block becoming fully detached from the rest of the dam.
3. Any detached uppermost part of a dam block in the investigated dams may be subjected to some sliding and rocking motions, but it will remain stable during and after the earthquake.
4. The earthquake loading could cause limited damages in the analyzed dams, but it will not lead to an uncontrolled release of reservoir water. Hence, the investigated dams satisfy the safety requirements for the SEE.

References

[1] ADINA R & D (2008). ADINA User Interface, Command Reference Manual, Vol. I: ADINA Solids & Structures Model Definition, Report ARD 08-2, Watertown, Massachusetts, USA.

[2] Hall, J.F. (2006). Problems encountered from the use (or misuse) of Rayleigh damping. Earthquake Engineering and Structural Dynamics. Vol. 35, pp. 525-545.

[3] Malla, S. and Wieland, M. (2006). Dynamic stability of detached concrete blocks in arch dam subjected to strong ground shaking. Proceedings of the 1st European Conference on Earthquake Engineering and Seismology (ECEES), Geneva, Switzerland, 3-8 September 2006.

[4] Panduri, R., Droz, P., Malla, S., Radogna, R., Wieland, M. and Darbre, G.R. (2012). Ongoing seismic safety assessment of Swiss dams. Proceedings of the 24th International Congress on Large Dams, ICOLD, Kyoto, Japan, 6-8 June 2012.

[5] Shi, B., Anooshehpoor, A., Zeng, Y. and Brune, J.N. (1996). Rocking and overturning of precariously balanced rocks by earthquake. Bulletin of the Seismological Society of America, Vol. 86, No. 5., pp. 1364-1371.

[6] Wieland, M. and Malla, S. (2012). A simple method for seismic stability analysis of detached concrete blocks and estimation of contraction joint openings in large arch dams. Hydropower and Dams, Vol. 19, Issue 3, pp. 113-119.

[7] Zhang, J. and Makris, N. (2001). Rocking response of free-standing blocks under cycloidal pulses. Journal of Engineering Mechanics, ASCE, Vol. 127, No. 5, pp. 473-483.